Characterisation of ion-beam deposited thin-film coating materials for use in future gravitational wave observatories
PhD Thesis

Svetoslava Angelova, PhD Student

Department of Biomedical Engineering
University of Strathclyde, Glasgow

June 15, 2021

This thesis is the result of the author's original research. It has been composed by the author and has not been previously submitted for examination which has led to the award of a degree.

The copyright of this thesis belongs to the author under the terms of the United Kingdom Copyright Acts as qualified by University of Strathclyde Regulation 3.50. Due acknowledgement must always be made of the use of any material contained in, or derived from, this thesis.

Contents

List of Figures

7

9

10

13

14

List of Tables

Preface

In Chapter 1, the nature of gravitational radiation is explained, in addition to the methods utilised within gravitational wave detectors, and the associated limiting factors when using interferometric techniques. Confirmed gravitational wave detections are explained.

Chapter 2 explains the origination of thermal noise and how it can affect and limit gravitational wave detection. Through quantification of factors contributing to the increase in thermal noise, methods can be developed to minimise its effect.

In Chapter 3, coating deposition and characterisation techniques of optical and mechanical properties are covered. A number of quantifying measurements were performed by R. Birney, P. Edwards,and C. Gier. Optical absorption measurements were obtained at the University of Glasgow by S. Tait. The experimental results were obtained and examined by the author.

Chapter 4 focuses on the deposition and characterisation of the internal loss factor of tantulum pentoxide coatings, performed at elevated temperatures using ion-beam sputtering technique, utilising an ECR source. The experiments were performed by the author with the help of R. Birney. The structural study of the deposited films is carried out by S. Macfoy.

In Chapter 5, depositions at room temperature and elevated temperatures of zirconia doped tantulum pentoxide coatings are presented, in addition to characterisation of the internal loss factor associated with these films. Experimental results collected and analysed by the author.

In Chapter 6, depositions of mixed material coatings are covered. The addition of a third composition element is studied, as well as its effect on the internal loss measurements of the deposited films. Spectrophotometry measurements were performed by M. ben Yaala and C. Gier. The experiments and analysis were conducted by the author.

Publications section includes list of published work with contributions from the author of the thesis. Author's contribution associated with each publication:

- [1] - Part of LIGO Scientific Collaboration. No personal contribution;

- [2] - Author has contributed analysis of mechanical dissipation associated with the optical coatings developed on novel ECR IBS system;

- [3] - Author has contributed room temperature and elevated temperature depositions of ZrO_2 doped Ta_2O_5 coatings using ECR IBS deposition. Contribution includes characterisation of optical and mechanical properties of doped optical coatings including mechanical dissipation, elemental composition, crystallisation temperature (maximum thermal annealing), observation of appearance of cracking on coating surface, associated with doping concentrations;

In the Appendix, additional individual results of internal loss are presented. The materials covered are elevated temperature tantulum pentoxide coatings, room temperature and elevated temperature zirconia doped tantulum pentoxide films.

Acknowledgements

I would like to begin by thanking my supervisor Professor S. Reid. Without his guidance, encouragement and support this experience would have been unachievable. Throughout the four years of my PhD, I knew I could always rely on Prof. Reid for assistance and stimulation in successfully completing my goal.

I would also like to recognise my appreciation for the team, I was lucky to work in. Thank you Dr. R. Birney for always being helpful and accommodating; Thank you Dr. D. Vine for introducing me into every experimental aspect of my project; Thank you S. Macfoy, C. Gier, C. Wiseman and Dr. M. ben Yaala for making this process a positive experience.

Lastly, but not in last place, I would like to express my gratitude towards my parents. If it was not for the unending support and their confidence in me, even at the times I did not believe in myself, I could have never even dreamed of not only extending my education abroad, but furthermore being successful in completion of a PhD.

Chapter 1

Introduction to Gravitational Wave Astronomy

1.1   Introduction

In the 1915 paper that describes the Theory of General Relativity [4], Albert Einstein postulated the existence of gravitational waves. They are distortions in spacetime associated with accelerations of asymmetric mass distributions. Gravitational interactions being the weakest of the fundamental forces implied gravitational waves may have such a small amplitude that they could be impossible to directly measure. This evaluation was made based on the state of technology at the beginning of the 20th century. In the 21st century however, or more precisely on September 14th 2015, this postulation was proven wrong. The Advanced Laser Interferometric Gravitational wave Observatory (aLIGO) in the United States of America observed and measured the inspiral and merger of two black holes, thus producing the first direct observation of black holes as well as the propagation of the resulting gravitational wave signal. This event was denoted GW150914 and was heralded as the beginning of the gravitational wave astronomy era.

The nature of gravitational waves results in a weak interaction with matter, thus observable signals on Earth would be associated with massive, highly accelerating, astrophysical systems. Such high mass events can be caused not just by two black holes in orbit with each other and their following mergers, but by other objects and events such as pulsars, supernovae, binary neutron star systems, neutron star - black hole systems and a possible primordial gravitational wave background. Additionally, due to the weak coupling of gravitational waves to matter, the propagating gravitational waves experience extremely low absorption or scatter. The continuation of gravitational wave observation over larger distances will enable the scientific world to observe further back in time, at the early stages of the Universe. Concerning the future, this research field will pro-

vide us with more knowledge on black holes as well as the mass distributions and clusters throughout the Universe. The fact that we have barely emerged into this field also allows for the discovery of new astrophysical objects or events, will enhance our understanding of cosmology and hopefully provide answers for the unknown.

1.2 Gravitational wave radiation

The nature of gravitational waves can be explained through a comparison with electromagnetic (EM) waves, *e.g.* visible light and radio waves are propagating oscillations of the electromagnetic field. EM radiation is associated with positive and negative charges, which produce electric and magnetic dipoles. For gravitational radiation, since mass is conserved and negative mass does not exist, there is no possibility for monopolar radiation. Conservation of momentum prevents dipole gravitational radiation. As a consequence, the only mechanism where gravitational waves can be produced is via qudrapolar radiation, where accelerations of asymmetric matter are required [5]. Candidate sources would include binary systems with high mass objects in orbit with each other, or rotation of a single non-symmetric spherical body. In these two examples, the main frequency component of the gravitational waves will be twice the orbital/rotational frequency of the system, ignoring redshift effects.
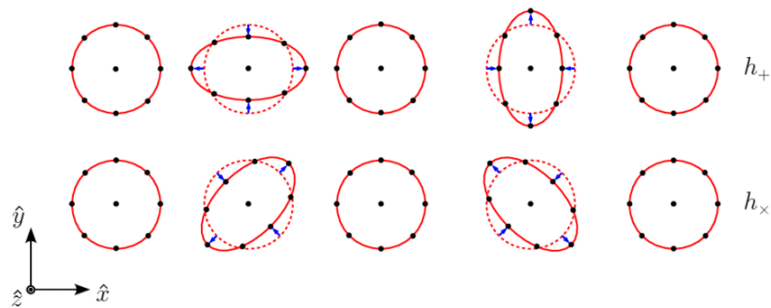
Figure 1.1: h_+ and $h_\times$ polarization states. The effect of the h_+ and $h_\times$ polarization states of a gravitational wave on a ring of free test masses. The propagation direction of the wave is perpendicular to the page. Original image from [6].

As stated, a gravitational wave is a strain in space. The amplitude (strain), h, can be defined as the change in separation between two adjacent masses, such that,

$$h = 2\frac{\Delta L}{L} \tag{1.1}$$

where ΔL is the change in separation of two masses, a distance L apart. h is unit-less quantity.

Possible sources of gravitational radiation are defined in the following section.

1.3   Sources of gravitational waves

1.3.1   Compact binary systems

Coalescing binary systems are one of the most important sources of gravitational waves for ground based detectors. Such systems can consist of different combinations of stellar objects - two black holes, two neutron stars, a black hole-neutron star merger. White dwarfs can also be included within the compact binary system, but since the signal emitted from such an event can only be detected by space based detectors, this section will mostly concentrate at combinations of black holes and/or neutron stars.

The first confirmation of the existence of gravitational waves, as defined by Einstein's theory, was observed by Hulse and Taylor with the system PSR B1913 + 16 [7]. From the radio-frequency emission, this system was shown to consist of a neutron star and another stellar object. Similarly we have acknowledged the fact that the first direct observation of gravitational waves was through the event denoted GW150914. In both cases as the two bodies spiral closer together (*i.e.* their orbit decreases), the gravitational radiation increases in frequency and amplitude over time, leading to a chirp, which represents the final stage of the merger.

The inspiral phase of these stellar objects is simple to computationally predict and accurately model. Considering weak field approximations one can obtain an expression for the signal frequency $f(t)$ such that [8],

$$f(t) \approx 2.1 \text{Hz} \left(\frac{\frac{1\text{day}}{\tau}}{M} \right)^{3\!/\!8}, \tag{1.2}$$

where M is the product of $m_{\text{T}}^{\frac{2}{3}}\mu$, μ being the reduced mass and m_{T} the total mass; τ is the time until collision occurs. Furthermore $m_{\text{T}} = m_1 + m_2$ and $\mu = (m_1 m_2)/(m_1 + m_2)$ where m_1 and m_2 are the masses of the two spiralling stellar objects. Using the standard quadruple formula of general relativity shows that the wave strain (amplitude) then becomes [8]

$$h \propto 10^{-23} m_{\text{T}}^{\frac{2}{3}} \mu f(t)^{\frac{2}{3}} r^{-1} \tag{1.3}$$

r representing the distance from the observer.

Approximations and parameter estimations lead to the final result, where

$$h \approx 10^{-23} \left(\frac{f(t)}{100\text{Hz}} \right)^{\frac{2}{3}} \left(\frac{100\text{Mpc}}{r} \right) \left(\frac{M}{1.1 M_\odot} \right). \qquad (1.4)$$

Binary neutron star and neutron star-black hole binaries are the leading candidates for the central engine of gamma ray bursts (GRBs). Binary neutron star mergers have been predicted to be simultaneously observed in the electromagnetic radiation spectrum, thus leading to an emission of gamma rays. The delay between the two signals (GW and GRB) can reflect on the time the binary components came into contact, leading to the remnant black hole and resulting jet. Through observations of coalescing compact binary systems one can estimate the value of the Hubble constant if the redshift is known, either through the electromagnetic counterpart, or by identifying the host galaxy. The current value is estimated to be $H_0 = 70\text{kms}^{-1}\text{Mpc}^{-1}$ [9].

1.3.2 Pulsars

A pulsar is a rotating neutron star, which as it settles down into its final state can solidify its crust in an asymmetric shape. Asymmetry with respect to its rotational axis can be achieved by different mechanisms - from an extremely strong misaligned magnetic field to elastic deformations in the star's crust. Such mechanisms generally result in a neutron star which in the quadruple approximation and with rotational and angular momentum axes aligned would produce gravitational waves. These waves would be emitted at twice the star's rotational frequency. The resulting waves would have a characteristic strain amplitude such that [10],

$$h_0 = \frac{16 G \pi^2}{c^4} \frac{I_{zz} \epsilon f_{\text{rot}}^2}{r} \qquad (1.5)$$

where f_{rot} is the neutron star's rotational frequency, I_{zz} is the principal moment of inertia, usually with a value of 10^{38}kgm^2, $\epsilon = (I_{xx} - I_{yy})/I_{zz}$, where ϵ is the ellipticity, r represents the distance from the source to Earth.

Many known pulsars have well-defined frequency evolutions and sky positions, making them ideal targets as gravitational wave sources. If a pulsar is observed regularly through electromagnetic radiation it can lead to a coherent phase model. If data is gathered over long periods of time, a gravitational wave can be integrated from those recordings.

Two examples of well known pulsars are the Crab and Vela pulsars. The Crab (PSR B0531+21) has an age of ≈ 945 years with an ellipticity 2.5 times lower

than the maximum ellipticity calculated under the hypothesis that a pulsar's spin down is only due to gravitational wave emission [11]. In the case of the Vela pulsar (PSR B0833-45), its age cannot be exactly determined but consists within a range of 18 - 31 x 10^3 years [12]. Assuming the lower limit, one can estimate $\epsilon \leq 3.3 \times 10^{-4}$, which is 5.5 times lower than the limit solely from gravitational torque. Assuming the higher age value, one estimates $\epsilon \leq 3 \times 10^{-5}$ leading to a value of ≈ 60 times lower than the gravitational limit.

A range of frequencies at which such occurrences are expected is (10 - 100 Hz) where in the lower limit the signal will be limited by the seismic noise in the detectors.

1.3.3   Supernovae

Supernovae are one of the brightest events in the sky. The process through which a star goes prior to reaching its supernova stage can be summarised as follows: Consider the case of a star with a mass several times that of the Sun, the core of which has 'burned' through its nuclear resources reaching the fusion of iron. Above a critical mass, the star will collapse when electron degeneracy and radiation pressure are insufficient to balance the gravitational pull. At this stage the core becomes unstable, and if above $\approx 1.4 M_\odot$ (known as the Chandrasekhar mass) will collapse to form a neutron star. This collapse is reversed once the core has reached nuclear densities (3×10^{14} gm/cm^2). If the resulting collapse is non symmetrical it leads to the release of energy. This energy mostly consists of neutrinos. Approximately 1% of the total energy may get converted into gravitational waves. The remnant of a supernova is a source of gravitational radiation. There are two types of supernovae - type I and II, where most of the gravitational radiation is expected from type II supernova [13].

The collapse of the star's core releases enormous amounts of energy $\sim 0.15 M_\odot c^2$, predominantly in the form of neutrinos. A mechanism reasoned to explain such a burst could be the dynamical instabilities in the rapidly rotating core. The end result of a supernova is either a neutron star or a black hole.

The complexity of the collapse makes it extremely difficult to produce simulations for such event. Another obstruction is also presented due to the fact that the equations used for the estimations do not account for the effect of neutrinos.

An attempt to estimate the (weak) signal can be made using the quadruple estimation formula [14],

$$|h| = \frac{2G\ddot{I}_{ij}}{c^4 D} \simeq 10^{-21} \left(\frac{\varepsilon}{0.1}\right) \left(\frac{10\text{kpc}}{D}\right) \left(\frac{M}{M_\odot}\right) \left(\frac{R_c}{10\text{km}}\right)^2 \left(\frac{T_{\text{dyn}}}{1\text{ms}}\right)^{-2}, \qquad (1.6)$$

where $\ddot{I}_{ij}$ is the second derivative with respect to time of the mass quadruple moment. In turn it decomposes into ϵ, a parameter representing the degree of

24

non-sphericity (where $\epsilon = 0$ is the spherical case), D is the distance from the source to the observer; M is the typical mass, R_c is the radius of the core, and T_{dyn} is the dynamical timescale of the core bounce.

Relating the amplitude of the wave to the frequency of signal leads to the relation [14],

$$f_{GW} \sim \frac{1}{T_{dyn}}, \tag{1.7}$$

stating that the frequency of the gravitational wave produced is inversely proportional to the dynamic timescale.

1.3.4 Stochastic gravitational wave background

Stochastic radiation is considerably different than burst or periodic radiation. Possible sources include: (i) overlapping bursts from collapse and coalescence of massive population III objects [15]; (ii) first order cosmological phase transitions [16]; (iii) speculative objects such as cosmic strings [17] ; (iv) primordial scale-invariant fluctuations generated by quantum effects in inflammatory models [18] and (v) overlapping emission from binary star systems in our own galaxy [19].

The stochastic gravitational wave background (SGWB) is similar to the cosmic microwave background (CMB). Unlike the CMB, SGWB can provide information of up to 10^{-35} seconds after the Big Bang [20]. Relic gravitational waves produced during inflation are of high interest due to the energy spectrum of these waves, as it contains information about the time evolution of the Universe's scale factor [21].

The strength of the signal cannot be easily predicted hence it cannot be established whether such signals will be detected by the current gravitational wave detectors. Since the amplitude of the signal is low, and since the signal will cover a broad range of frequencies, it will be difficult to differentiate from the noise in the detector. This can somewhat be compensated by using multiple detectors simultaneously, thus can distinguish between the baseline noise and the actual signal. In order to predict stochastic background radiation models one has to evaluate it using its power spectrum. This quantity can be described as a dimensionless quantity, Ω_{GW}, which is the gravitational wave energy per unit logarithmic frequency. In order to close the Universe, it also needs to be divided by the critical energy density. Hence, one arrives at the relation [22],

$$\Omega_{GW}(f) = \frac{f}{\rho_c}\frac{d\rho_{GW}}{df}, \tag{1.8}$$

where ρ_c can be expressed as $\rho_{\mathrm{c}} = \frac{3c^2 H_0{}^2}{8\pi G}$ [23] and $\frac{d\rho_{\mathrm{GW}}}{df}$ is the gravitational wave energy density in the frequency range $(f, f + \Delta f)$.

The characteristic strain can be evaluated as [22],

$$h_{\mathrm{GW}} = 4 \times 10^{-22} \sqrt{\Omega_{\mathrm{GW}}} \left(\frac{100\mathrm{Hz}}{f}\right)^{3/2} \mathrm{Hz}^{-\frac{1}{2}}. \qquad (1.9)$$

As it can be seen in the expression for the critical density, the stochastic energy density is proportional to the square of the Hubble constant, which is written as $H_0 = h_0 \times 100 \ \mathrm{km}/(\sec - \mathrm{Mpc})$, where h_0 parametrises the experimental uncertainty. h_0 is given in the range of $0.5 < h_0 < 0.85$ [24].

1.4   Gravitational wave detectors

1.4.1   Resonant bar detectors

The first gravitational wave detectors were proposed by Joseph Weber in the late 1950s [25]. In the 1960s Weber carried out these ground based experiments in the University of Maryland. One way one can describe a resonant mass antenna is a solid body that rings like a bell once 'hit' by a gravitational wave of suitable frequency [26]. These vibrations are then converted into an electrical signal by transducers, as well as amplified by an electrical amplifier. The coupling of the body with the transducer and/or the amplifier, in addition to the thermo-mechanical properties of the body, determine the sensitivity and bandwidth of the detector.

Initially there were two conceptual ideas on the operation of these detectors, based on using free or non-free masses. In the case of a free mass experiment, the measurable quantity is the separation between masses observed, for example, through laser interferometry [27, 28]. In the case of a non-free mass, the atoms and molecules are confined in position due to their binding energies. Since the atoms in the structure try to follow geodesic trajectories produced by any changes in the space-time distortions [28], this could be measured through a varying force or displacement experienced by the mass. Due to the weak interaction of gravitational waves with matter, these effects are extremely small.

The first antenna consisted of an aluminium cylinder suspended through the middle by anti-vibrational suspensions. A 1.2 tonne aluminium cylinder with length of 1.5 m and diameter of 61 cm, is suspended through acoustic wires and held under vacuum. The procedure of operation involved measurements of the fundamental mode excitation caused by a gravitational wave passing through the bar. Weber later used two bar detectors, with a separation between them of approximately 1000 km, to allow coincident detection of signals. The strains

these detectors were able to detect were of the order of 10^{-16} in the ms timescales [29].

The interest in these experiments led to multiple attempts by other groups in the USA, UK, Russia etc. to verify Weber's observations. The Glasgow setup consisted of two split bar detectors separated by 50 m, consisting of two Al half bars of 300 kg mass, 30 cm in diameter, connected together with PZT transducers, resonant at 1020 and 1100 Hz [30].

Through these tests, several noise sources were identified and characterised - seismic noise, thermal noise, etc. The sensitivity limit associated with thermally driven displacements (Brownian thermal noise) eventually led to a second generation of resonant bar detectors where the operation was performed at cryogenic temperatures. Similar to the first generation, these antennas consisted of a cryogenic resonant mass antenna coupled to an electromechanical resonant transducer that has its electrical output pre-amplified by a low noise cryogenic amplifier [28]. When a gravitational wave of appropriate frequency passes through the bar, it will cause it to go into oscillation. The first group to successfully reach a noise temperature in the range of mK was the Stanford group in 1981 [31].

Resonant bar detectors continued to operate, however by 1997 there remained no confirmed detections. The opinion of the scientific community was divided into two distinctive directions - operation at cryogenic temperatures and using laser interferometer technology. Initial km-scale interferometric detectors reached sensitivities in the range of 10^{-21}, hence establishing themselves as the future technique for GW detection.

1.4.2 Laser interferometers

Following the era of resonant bar detectors, scientific community opinions were divided in interest. Whilst operation of bar detectors at cryogenic temperatures was considered, an alternative technique for the detection of gravitational waves was through the use of interferometry in order to measure the distance between two widely separated masses. A passing gravitational wave would produce a strain in space which would result in a change of the intensity of the interference pattern. The use of this technique was first proposed by Gertsenstein and Pustovoit in 1962 [32] and was deemed highly attractive due to its ability to provide high sensitivities at a wide range of frequencies.

The new setup was based on the operation of a Michelson interferometer. Figure 1.2 shows a basic schematic representation of an interferometric detector. Incident light, produced by a laser beam is split into two identical beams by a beam-splitter, which follow paths (L_1 and L_2) perpendicular to one another. At the end of the interferometer arms, mirrors (M_1 and M_2) are suspended through a pendulum system, and each beam gets reflected. The two beams recombine

27

at the beam-splitter and this results in an interference pattern observed by a photodiode.

Gravitational waves can be described by their quadruple nature, which means that as a gravitational wave propagates perpendicularly to the detector, one would observe an extension/compression of each of the interferometer arms by δL. The difference in beam paths results in a relative phase change observed in the intensity of the interference pattern. Feedback systems are used to lock on the interference pattern, primarily at a dark fringe, by controlling the relative positions of the mirrors. Therefore, any information regarding the differential motion of the mirrors, caused by a passing GW, would be encoded in the control system.
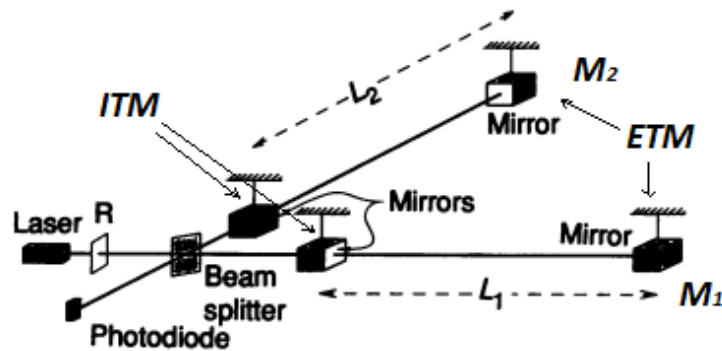
Figure 1.2: A simple schematic of a Michelson interferometer setup utilised in gravitational wave observatories. Light is input through a laser source reaching a beam-splitter, which splits the laser ray in two equivalent components. Each ray travels the same distance, $L_1 = L_2 = L$, to a highly reflective end mirror (M_1 and M_2) which enables the reflection of the light back to the beam splitter. The recombination of the light rays creates an interference pattern observed by a photodiode. The schematic also illustrates the usage of a second set of mirrors placed between the end masses and the beam splitter which allows for part of the light to be reflected. The addition of the ITMs (Input test masses) creates Fabry-Perot cavities in the interferometer. The concept of Fabry-Perot cavities is further discussed in Section 1.5.2. Figure from [33].

GEO600

GEO600 is a British-German detector which was built in 1995. The motivation for this project was based on ongoing work between the UK and Germany. At the University of Glasgow, there was a 10 m interferometer constructed, whereas there was a 30 m interferometer at the Max Planck Institute for Quantum Optics. The GEO600 detector is a folded Michelson interferometer (see Sect 1.5.1) with

Figure 1.3: Worldwide network of gravitational wave observatories. Prior to the beginning of the construction of LIGO India all gravitational wave detectors were located in the Earth's northern hemisphere. The inclusion of a southern hemisphere location would enable a more precise localisation of the gravitational wave signal. Original illustration taken from [34].

600 m arm lengths using dual recycling (see Sect 1.5.3 and 1.5.4) the folded arms effectively doubled at 1200 m [35]. Following several years of collecting data, the detector is currently to be mostly used as a testing site for new innovative technologies, the aim of which is to improve and optimise the current observatories. Once proven effective, those upgrades can be utilised in the larger detectors.

In 2009 a program referred to as GEO-HF (GEO - High Frequency) began. The detector was collecting data at the time, due to other detectors being offline for longer term upgrades, while simultaneously receiving short-timescale upgrades. The primary outcomes were: (i) fixed signal recycling and DC output; (ii) implementation of an output mode cleaner; (iii) injection of squeezed volumes (see Sect 1.5.5) into an anti-symmetric port; (iv) reduction of the signal recycling mirror reflectivity and higher power increase [35].

In 2011 a 35 W laser system was introduced as a replacement of the prior 12 W laser [36]. In comparison to other detectors, the GEO600 observatory does not have Fabry-Perot arm cavities. Therefore, all of the circulating power gets transmitted through the beam-splitter substrate. The absorption of the silica substrate has been measured to have a value of 0.6 ppm cm^{-1} [37].

Following the beginning of the GEO-HF program in 2011, most of the optimisations have been completed and evaluated. Since its original introduction in GEO600, squeezing proves its effectiveness and will be implemented into the further upgrades of the ground-based gravitational wave detectors.

LIGO

The Laser Interferometric Gravitational wave Observatory (LIGO) consists of modified Michelson interferometers spread out to two locations in the United States of America (Fig.1.4). The first location is in Livingston, Louisiana and the detector has a 4 km interferometer (L1) housed within a ultra-high vacuum tube. The second observatory is situated in Hanford, Washington which again consists of a 4 km interferometer (H1).

Construction of the site began in the late 1990s [22], where from the start it was acknowledged that the detectors will need to undergo multiple upgrades in future. The first stage is known as initial LIGO (iLIGO) and was operational until 2007. The detector underwent through an intermediate stage, enhanced LIGO (eLIGO), prior to continuing into major upgrades required for Advanced LIGO(aLIGO).

The iLIGO detector was designed with a detection bandwidth between 40 and 7000 Hz, and the optimal strain amplitude was estimated to be $\sim 10^{-21}$ [38].The test masses within the beam tubes of the interferometers were made of fused silica, weighed 10 kg, and were suspended using a steel piano wire. The mirrors were coated with alternating layers of SiO_2 (silica) and Ta_2O_5 (tantala), which were the chosen materials due to their optical and mechanical properties. A Nd:YAG 10 W laser was used in all the interferometers, operating at a wavelength of 1064 nm, with 10s of W of circulating laser power between the mirrors in the optical cavities.

Figure 1.4: Advanced LIGO observatories. The left image is an aerial photograph of the Hanford, Washington site. The right photograph is the site in Livingston, Louisiana. Images from [39].

The eLIGO intermediate upgrade, operating between 2007 and 2009, aimed to increase the sensitivity of the prior detector as well as estimate the effectiveness of new systems and whether they should be introduced in Advanced LIGO. Multiple upgrades had been performed on the detector in order to enhance its sensitivity. Each arm of the interferometer now contained a Fabry-Perot optical cavity (see Sect 1.5.2), which consisted of a partially transmitting input mirror and a highly reflective end mirror. Additionally, a partially reflecting mirror had

been positioned between the laser and beam-splitter, which was to enable signal recycling (see Sect 1.5.4) [40]. The input laser power had also been changed from the 10 W in iLIGO to 35 W [41].

The second generation of upgrades lead to the Advanced LIGO detector, where construction began in 2011. aLIGO retains the same facilities of the previous generations, but all of the internal components have been replaced. The arm lengths of the interferometers remain the same. The test masses within the system had now been replaced by a 34 cm in diameter, 40 kg in mass, mirrors, which are suspended through a lower stage monolithic suspensions, made of fused silica fibres, utilising a quadruple pendulum. The use of quadruple pendulum as an active isolation system enables the reduction of vibrations within the system. The prior silica/tantala multi-layers had now been replaced by alternating layers of SiO_2 and titania doped Ta_2O_5. Titania was introduced as a dopant due to its optical properties. Post deposition heat treatments have proven to improve not just the mechanical loss of the coating but also its optical absorption. The addition of TiO_2 has proven to reduce the internal friction, whilst maintaining low optical absorption, hence the current optical coatings used consist of a 25 % titania doping in the high index layers.

The next upgrades are referred to Advanced LIGO Plus or 'A+'. The limiting constraint to this upgrade is caused due to the coating Brownian noise, prompting the requirement of alternative coating materials. A key aim of the upgraded Advanced LIGO instrument is to reduce the strain noise associated with said noise.

Advanced Virgo

Advanced Virgo is a second generation gravitational wave detector located in Cascina, Italy (Fig.1.5). The Virgo collaboration has been extended in the past decade to include Holland, Poland and Hungary, as well as France and Italy. The collaboration now includes up to 19 laboratories around Europe [42].

The initial Virgo detector has been upgraded to Advanced Virgo, going through a Virgo+ stage, and took part in the second observation run with the Advanced LIGO detectors. The detector is a Michelson interferometer with Fabry-Perot arm cavities and power recycling (see Sect 1.5.3), where the arm length is 3 km. Transitioning from its initial stage, multiple upgrades have been introduced. Monolithic suspensions, including silica suspension fibres, which were implemented in the Virgo+ stage, are one of the most important upgrades for gravitational wave detectors. Additionally Suprasil 3001/3002 [43] is employed as a substrate to produce the cavity mirror which leads to a 3 times lower optical absorption compared to the value for initial Virgo. New test masses were adopted in Advanced Virgo, where the test mass diameter remained the same, but with a doubled thickness of 20 cm and a weight of $\approx$ 42 kg. Both the initial and end test masses (ITM and

Figure 1.5: Advanced Virgo detector. The gravitational wave detector consists of a Michelson interferometer with arm lengths of 3 km. The site is located in Cascina, Italy. Photograph taken from [44].

ETM) are produced in pairs and are suspended from a steel marionette, which together with the mirrors form a double pendulum system[42].

Upgrades are made to detectors to improve their sensitivity. In the case of AdV the peak sensitivity is expected to be $\sim 3\times 10^{-24}$ Hz$^{-1/2}$ around 300 Hz [44].

Advanced Virgo joined Advanced LIGO into its second observation run. This European observatory joined on August 1$^{\text{st}}$ 2017 and it collected data until the end of the run on August 25$^{\text{th}}$ 2017. Throughout that period Advanced LIGO and Advanced Virgo jointly observed two events - GW170814 and GW170817 [45], the second being the first detection of a gravitational wave signal from a neutron star binary system.

KAGRA

KAGRA is a Japanese gravitational wave observatory recently constructed and now under commissioning (Fig.1.7). Japanese research and involvement in gravitational wave astronomy began around the 1970s - 1980s at the University of Tokyo. The initial detector constructed was TAMA300 - a 300 m interferometric gravitational wave detector. Construction on this detector began in 1995 [47]. By 2004, nine observation runs had been performed, leading to a seismic isolation system installation in order to reduce the seismic noise distributions. The Cryogenic Laser Interferometric Observatory (CLIO) was constructed in 2006. Unlike the other ground-based gravitational wave detectors, it was positioned underground in the Kamioka mine. CLIO is a 100 m interferometer, one of two
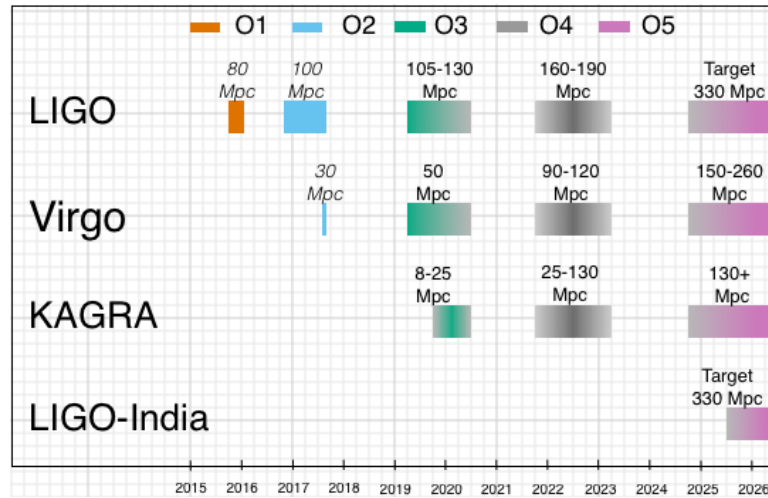
Figure 1.6: Timeline of interferometric gravitational wave detectors. The final generations of the Advanced LIGO+ and Advanced Virgo+ are presented within the fifth observing run as they are expected to be within those specifications by the year 2025. Image reprinted from [46].

Figure 1.7: Artistic impression of the underground interferometer in the Kamioka mine. The KAGRA detector consists of a dual recycled Michelson interferometer with arm lengths of 3 km. The detector operates at cryogenic temperatures hence utilises sapphire test masses unlike the fused silica components within the detectors operating at room temperature. Illustration reprinted from [39].

main purposes of which is to demonstrate thermal noise suppression by cooling mirrors for a future Japanese project, KAGRA, KAmioka GRAvitational wave detector. Similarly to CLIO, the eventual goal of TAMA300 is to test new technologies prior to their inclusion in KAGRA. In the case of TAMA, the main goal is shot noise reduction.

KAGRA is a 3 km underground dual recycled Michelson interferometer using sapphire test masses cooled to cryogenic temperatures, positioned in the Kamioka mine. Construction of KAGRA began in 2010 [48]. The detector has two main differences compared to other gravitational wave observatories. Firstly, the interferometer is located at least 200 m underground [49], hence reducing the levels of seismic noise and gravity gradient noise. Secondly, the test masses for the interferometer are made of sapphire and kept at a temperature of 20 K to further reduce thermal noise fluctuations. Circulating power in each arm cavity will rise to the order of 100 kW [49]. The observatory has gone through 2 stages. Primary stage, initial KAGRA, was conducted until the end of 2015, where the main goal was to develop technologies allowing the operation of an underground gravitational wave site. At the beginning of 2016, the second stage of the development began, baseline KAGRA. During this stage the main events were the replacement of the test masses with sapphire mirrors cooled down to a cryogenic temperature of 20 K. Furthermore, the detector will have both power recycling and signal recycling cavities [49].

Following the progress of the development of the Japanese observatory, KAGRA is expected to join the other detectors during the forth observing run (O4), which is planned to commence early 2021.

1.4.3 Future projects

Einstein Telescope The Einstein telescope is a proposed third generation gravitational wave detector, which is to operate underground (Fig. 1.8). The aim of this project is to further improve upon the current technologies and surpass the present sensitivity limits. The telescope will consist of three detectors which are placed 100 to 200 metres underground, which will consist of dual recycled Michelson interferometers, through 10 km Fabry-Perot cavities tunnels reaching the corner stations. These tunnels will have an inner diameter of 5.5 m throughout most of their length [50]. In order to reduce the quantum noise at high frequencies, very high optical powers are required, thus lowering of the levels of shot noise. To improve the low frequency sensitivity, cryogenically cooled mirror suspensions are proposed for reducing thermal noise [52]. Since the high- and low-frequency requirements are somewhat opposing, particular in relation to high optical powers and the ability to operate at low temperatures, alternative approaches are required to practically meet the intended broadband sensitivities.
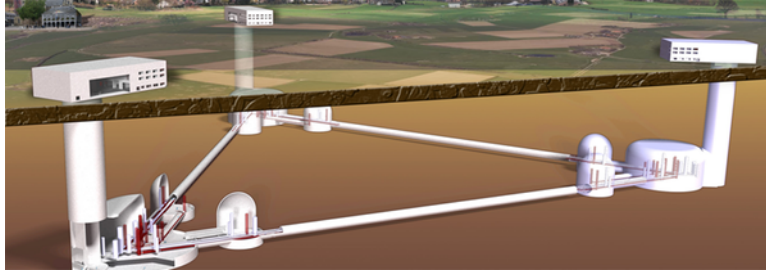
Figure 1.8: Artist impression of Einstein Telescope. The observatory will consist of three detectors, where the overall design can be described as a 2-band xylophone. Original image from [51].

A new design is proposed towards overcoming this issue, and can be described as a 2-band xylophone configuration of two independent interferometers. The xylophone strategy will use the division of each detector into a low and high frequency interferometer, in order to combine the signal bandwidths and maximally optimise the noise sensitivity.

ET-HF (high frequency) will be an interferometer operating at room temperature, using a 1064 nm wavelength. It can be thought of as scaled up version of the current advanced detectors. The frequency range will be between ~ 10 - 10^4 Hz. The test masses throughout the system will be made of fused silica, utilising the same beam shape as ET-LF. As mentioned before, in order to reduce quantum noise at high frequencies, one needs to increase the optical laser power, hence in the case of ET-HF the arm power will be 3 MW.

Table 1.1: Comparison between ET-HF and ET-LF.

Description	ET-HF	ET-LF
Frequency range	10 - 10^4 Hz	1 - 250 Hz
Input power	500 W	3 W
Wavelength	1064 nm	1550 nm
Arm power	3 MW	18 kW
Substrate	TEM_{00}	TEM_{00}
Temperature	291 K	10 - 20 K
Test mass material	Fused silica	Silicon
Test mass diameter	62 cm	> 42 cm
Test mass thickness	30 cm	50 cm
Mirror mass	200 kg	211 kg

ET-LF will be an interferometer operating at cryogenic temperatures, concentrating on the range of frequencies between 1 and 250 Hz. The test masses in this

setup will be fabricated from single crystal silicon, hence the laser wavelength used will be switched from 1064 nm to 1550 nm to prevent bandgap-associated optical absorption, thus silicon becomes highly transmissive at these longer wavelengths [53].

Multiple locations have been investigated for the construction of the detector, taking into account the noise contributions at each area, where the main issue will be the seismic noise. Despite all the research completed for the ET project, multiple areas still require optimisation. Similarly to Advanced Virgo and Advanced LIGO, alternative coating technologies are required to enable the Einstein Telescope to reach its sensitivity limits [54].

LISA

The laser interferometric space antenna (LISA) is to be the first space based gravitational wave detector (Fig.1.9). It is a joint mission by ESA and NASA, which is due to be launched in the 2030s. It will consist of three arms and three identical spacecrafts in a triangular formation, with a separation between them of 2.5 million km. The detector will follow a heliocentric orbit trailing the Earth by 20°, between 50 and 65 million km from Earth [55]. Each vertex of the triangular formation creates a 2 arm Michelson interferometer, the test masses within which are flee-floating. This brings us back to the origin of the theory of General Relativity in the case of which a body is in free fall.

The sensitivity requirements for LISA will be mostly concentrated on frequencies between 20 μHz and 1 Hz. At this frequency range it is expected to observe signals from objects with masses from $10^3 M_\odot$ to $10^6 M_\odot$, as well as observations of the cosmological background. Through this, the antenna will be able to map the structure of space-time around massive black holes which populate centres of galaxies. Due to the fact that some of technological advancements, required for LISA, had not been tested $i.e.$ their effectiveness needs to be verified in a drag-free environment, an intermediate step was undertaken by the launch of LISA Pathfinder on December 3rd 2015. The goal of LISA Pathfinder was to test whether free-falling masses in a space environment will behave as predicted, and their separation measured with sufficient accuracy by interferometry. The LISA Pathfinder project successfully demonstrated all aspects of the proposed technology and has enabled the progress for the launch planning of LISA [57]. The antenna is to be operational for 4 years, where it can be additionally extended to a period of 10 years.

LIGO India

At the initial (first generation) stage, the observatory located at Hanford consisted
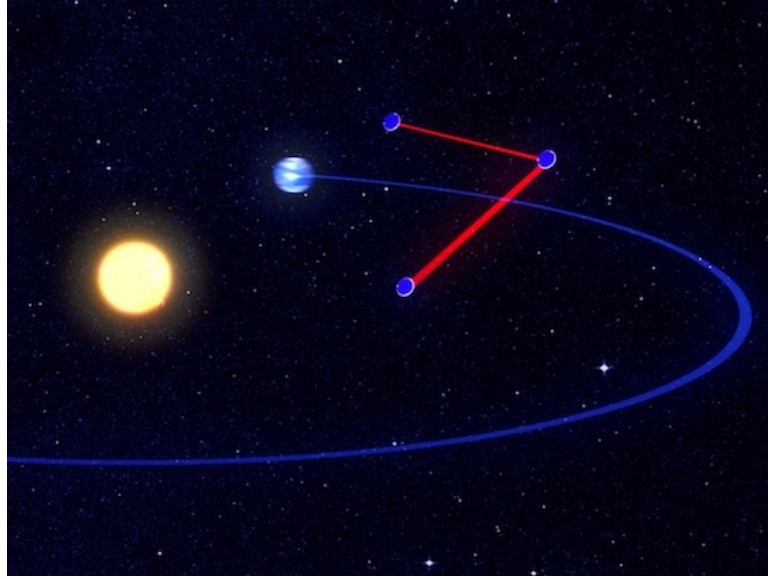
Figure 1.9: Visualisation of LISA in a continuous orbit around Earth. The detector will consist of three identical spacecrafts in a triangular formation, with a separation of 2.5 million kms. Visual representation from [56].

of two interferometers of different arm lengths, 4 km and 2 km. The plan for the second interferometer consisted of lengthening the interferometer arms to match H1 and L1. Eventually, it was decided that in order to obtain more precise measurements of the origins of signals, it is required to have a detector situated in the Southern Hemisphere. The original plan was to transport the already existing (H2), whilst optimising the length of the interferometer, to Perth, Australia. Due to lack of funding, the location of the new detector was switched to India. The proposed observatory will be operated jointly by IndIGO and LIGO and will form a signal network along with the two detectors in USA, Virgo in Italy and KAGRA in Japan [58]. It is evaluated that the most sensitive frequency range will be between 30 and 800 Hz [58]. Furthermore, the detector is to be assembled and operational by 2025 so that it can join the network of detectors.

LIGO Voyager

The next upgrade for the aLIGO detectors as discussed in the A+ stage. Throughout it, two main actions are to be taken - the introduction of frequency depending squeezing (like in GEO600) and improved mirror coatings (still under final investigation). Following that progression, the next step would be to explore the potential of the LIGO facility, known as LIGO Voyager.

In order to further improve the sensitivity of ground based detectors within

the high frequency range, one will have to use much higher laser power, as well as reduce the suspension thermal noise. An obvious route in order to decrease the thermal noise, is to operate the interferometer at very low temperatures, *i.e.* cryogenic temperatures. In order for this to be achieved, both the suspension and test mass substrate material necessitates change, along with the wavelength used throughout. The current phase suggests the replacement of the site's suspensions and test masses with ones made of silicon. The optical and mechanical properties of silicon are up to standard when using cryogenic temperatures. Several more differences can be summarised between the current observatories and LIGO Voyager: (i) the mass of the mirrors is increasing from 40 to 160 kg; (ii) temperature = 120 K; (iii) arm power is expected to be 3.2 MW; (iv) the coating materials suggested are either improved amorphous coatings based on a-Si or SiN_x or crystalline *e.g.* GaAs:AlGaAs, which will replace the 25% $Ti:Ta_2O_5/SiO_2$ [59]. Following the current development, it is estimated that the components of the detector should be ready for installation by early 2030s. [60, 59].

Cosmic Explorer

LIGO Voyager will be the most sensitive ground based observatory at least until the construction of ET and Cosmic Explorer. It is still uncertain whether the detector will be situated above or below ground. The plan for this telescope is to adapt technologies which are used in A+ and Voyager to a much larger interferometer. The arm length in the case of CE will be $\sim$ 40 km. Similarly to LIGO Voyager, the detector will adapt an operation at cryogenic temperatures. Additional changes will be performed on the parameters for the test masses' size and material. The mirrors will be replaced with 80 kg silicon substrates, and the laser wavelength used will be between 1.5 and 2 μm. Compared to the current aLIGO arm power, there will be a significant increase, from 710 kW at aLIGO to 2000 kW in Cosmic Explorer. Once the proposal is optimised and complete, construction should begin, where the current estimation of the observatory commencing operation is by the early 2030s [59].

1.5   Interferometric techniques

1.5.1   Michelson Interferometer

There were two types of detectors. Current gravitational wave detectors consist of a Michelson interferometer (Fig. 1.10). Through a laser source, light is split into the two arms of the interferometer, perpendicular to each other. At the end of each interferometer arm is a suspended mirror, allowing for seismic noise compensation. These suspensions are chosen, such that their pendulums have

longer periods, compared to the periods of the gravitational waves of interest. As a gravitational wave passes, perpendicularly to the plane of the antenna, in order to retain the interference condition, the length of one arm of the interferometer increases, as the other one decreases.
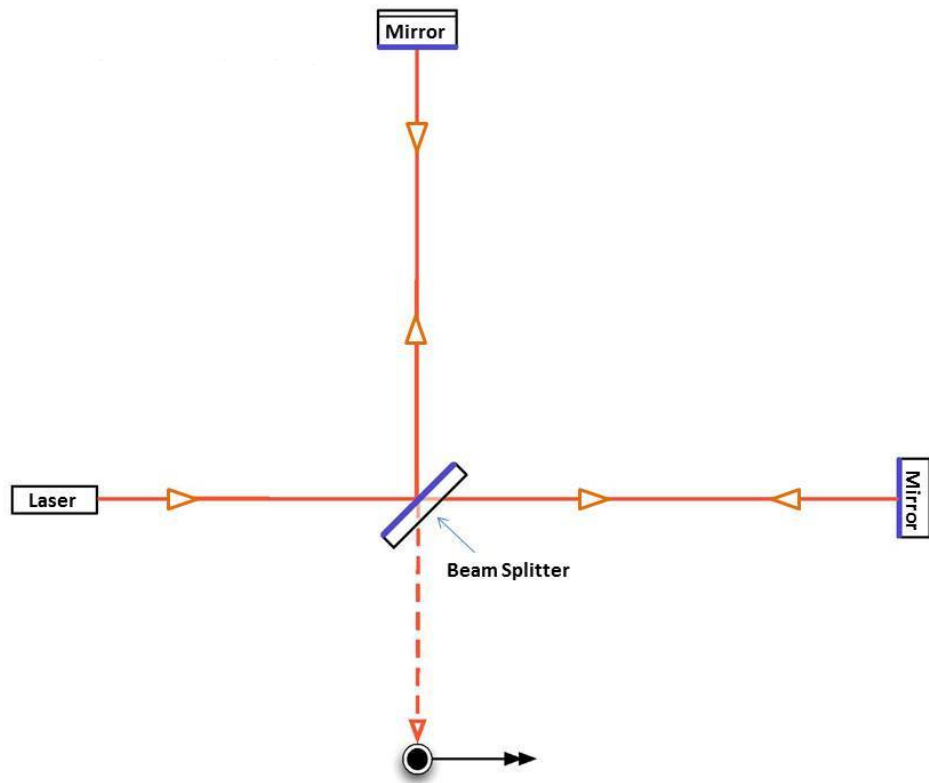
Figure 1.10: Schematic representation of a Michelson interferometer consisting of one beam-splitter and two end mirrors. Original figure from [61].

The first laser interferometric detector was operated by Forward [62]. Through Weiss' influence he constructed the first free mass antenna with laser interferometry. The range of sensitivities this detector was sensitive over was between 1 and 20 kHz [63].

In order to improve the sensitivity of the detector, one resolution is the extension of the arms' length. However, an alternative approach was implemented. The use of a delay line allows for the elongation of the optical path. This technique has been implemented in GEO600, where L=600 m, but through the usage of a delay line it is equivalent to 1.2 km. This line is also known as a folded optical path. With the introduction of intermediate test masses, the light bounces back and forth allowing for the extension of the optical path.

1.5.2 Fabry-Perot Interferometer

In addition to delay lines, another method for increasing the light optical path is through Fabry-Perot (FP) cavities (Fig. 1.11). It can be explained as a result of the addition of two more test masses. The mirrors at the end of the interferometer arms are known as ETMs and have a very high reflectivity. On the other hand, on the path of light from the beam-splitter to the ETMs, a partially transmissive input mirror is placed, causing the light to bounce back and forth, hence increasing the optical length, L. If the length of one of the cavities matches an integral multiple of the laser wavelength, then resonance occurs. The cavity behaves in some way similar to a delay line.

This technique was demonstrated in Glasgow at the 10 m interferometer. The detector consisted of two perpendicular, 10 m long high-finesse FP cavities formed between test masses which are hung as pendulums [64]. The sensitivity of the detector was estimated as $\sim 7\mathrm{x}10^{-19}$ m/$\sqrt{\mathrm{Hz}}$ in the frequency range 500 - 3000 Hz. This configuration is being used throughout all ground-based gravitational wave detectors.
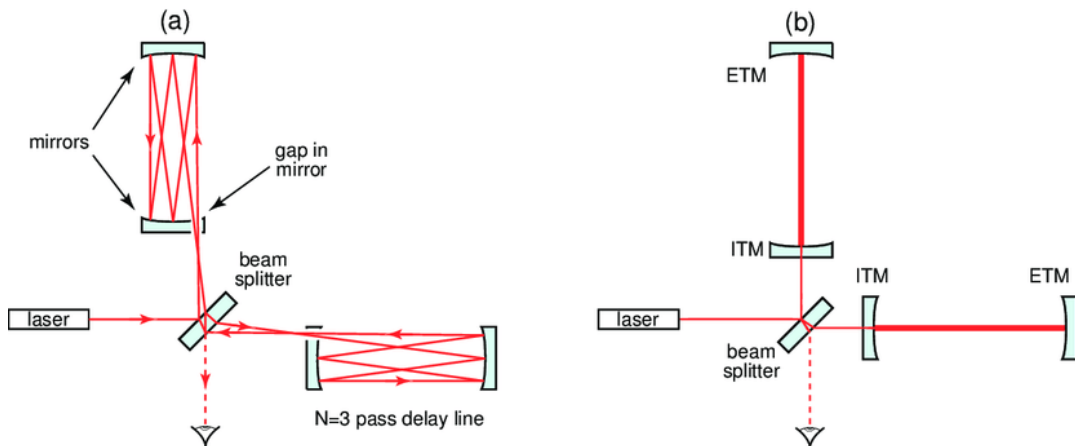
Figure 1.11: Schematic representation of a Michelson interferometer utilisng Fabry-Perot cavities in the interferometer arms in between the ETMs and ITMs. Images' source: [39].

1.5.3 Power recycling

Another technique, which enhances the effectiveness of the detector is known as power recycling. The light, reflected from the interferometer mirrors comes back to the beam-splitter, where light intensity is lost as it reaches the laser input. To overcome this, power recycling is introduced, where it is presented as

an additional concave mirror, placed in between the laser input and the beam-splitter (Fig. 1.12). That way the light coming back can be reflected and hence recycled. This effectively allows an increase in optical power enhancement. One can consider power recycling as the technique, which makes the whole system behave like an optical cavity in which the input laser light is resonant, allowing for it to be coupled in efficiently [65].
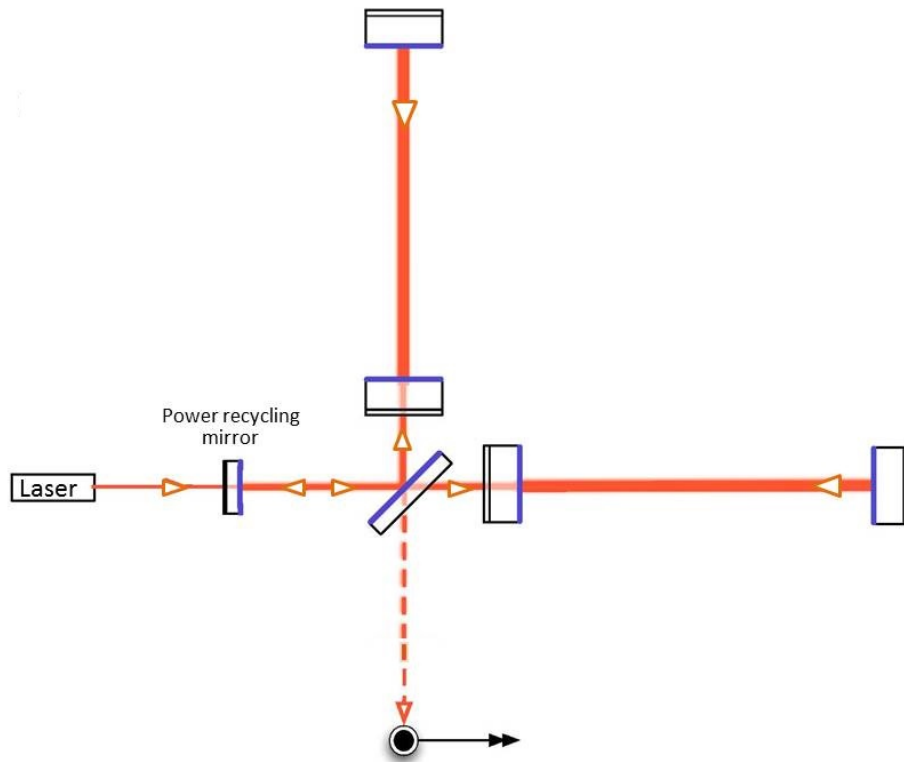
Figure 1.12: Schematic of a Michelson interferometer with an additional power recycling mirror placed between the laser input and beam-splitter. Figure reprinted from [5].

1.5.4 Signal recycling

Similar to the power recycling technique, by placing a mirror in front of the photodetector, the resulting effect is known as signal recycling (Fig. 1.13). In an ideal interferometer, the carrier light and signal side-bands become separated through the beam-splitter and hence leave the interferometer through different ports. The introduction of the addition of a signal-recycling mirror at the anti-symmetric port was suggested by Meers (1993) [40]. This mirror then forms a

signal recycling cavity with the Michelson interferometer. The inclusion of this mirror has the purpose to increase the storage time for the side-bands.

If both recycling techniques are used (power and signal recycling), the method is known as dual recycling, where power recycling is used for the enhancement of the carrier power and the signal recycling method is used in order to increase the interaction time.

Furthermore, the combination of the signal recycling mirror with the arm cavities is known as resonant side extraction [66]. The difference between signal recycling and resonant side extraction (RSE) is such that in the case of RSE the arm cavities posses very high finesse and the signal-recycling mirror is tuned to the anti-resonant operating phase. By performing this, the bandwidth of the detector is increased in the case of the signal side-bands as the storage time is decreased. Theoretically, there is a trade off between signal storage time and bandwidth of a detector, which is defined by Muzino's theorem [67].

1.5.5   Squeezing

An additional technique that has also been introduced is squeezing. Radiation pressure noise and photoelectron shot noise sources arise from the fluctuations in the different quadrature phases of the vacuum entering the unused input port [68]. Cannes *et.al.* [69] proposed that a squeezed state can be injected into the unused port and would therefore reduce one of the two sources of noise, depending on which quadrature gets squeezed (Fig. 1.13). Based on previous work by Cannes, Unruh developed the concepts of a squeezed input interferometer, which contains squeezed vacuum with frequency dependant squeeze angle, which then gets injected into the interferometer's dark port.

The concept of this method can be explained as follows: A squeezed state is a state in which one quadrature phase has less fluctuations, while in the other quadrature phase, there are increased fluctuations. One can use a squeezed state of the oscillator, which unlike the ground state does not have its quantum noise randomly distributed [68], to measure the displacement due to gravitational radiation in the quadrature. Squeezed states are an example of a non-classical light field. For an amplitude a, one has,

$$a = \hat{X}_1 + i\hat{X}_2, \tag{1.10}$$

where X_1 and X_2 are commuting Hermitian operators for the amplitude and phase quadratures of the field. These variances obey the Heisengberg Principle relation $\Delta^2 \hat{X}_1 . \Delta^2 \hat{X}_2 \geq \frac{1}{16}$, where its normalised value is higher or equal to $1/4$. The family of minimum uncertainty is characterised by the equal sign. Unruh and fellow researchers [70], acquired that by using squeezed vacuum states, the
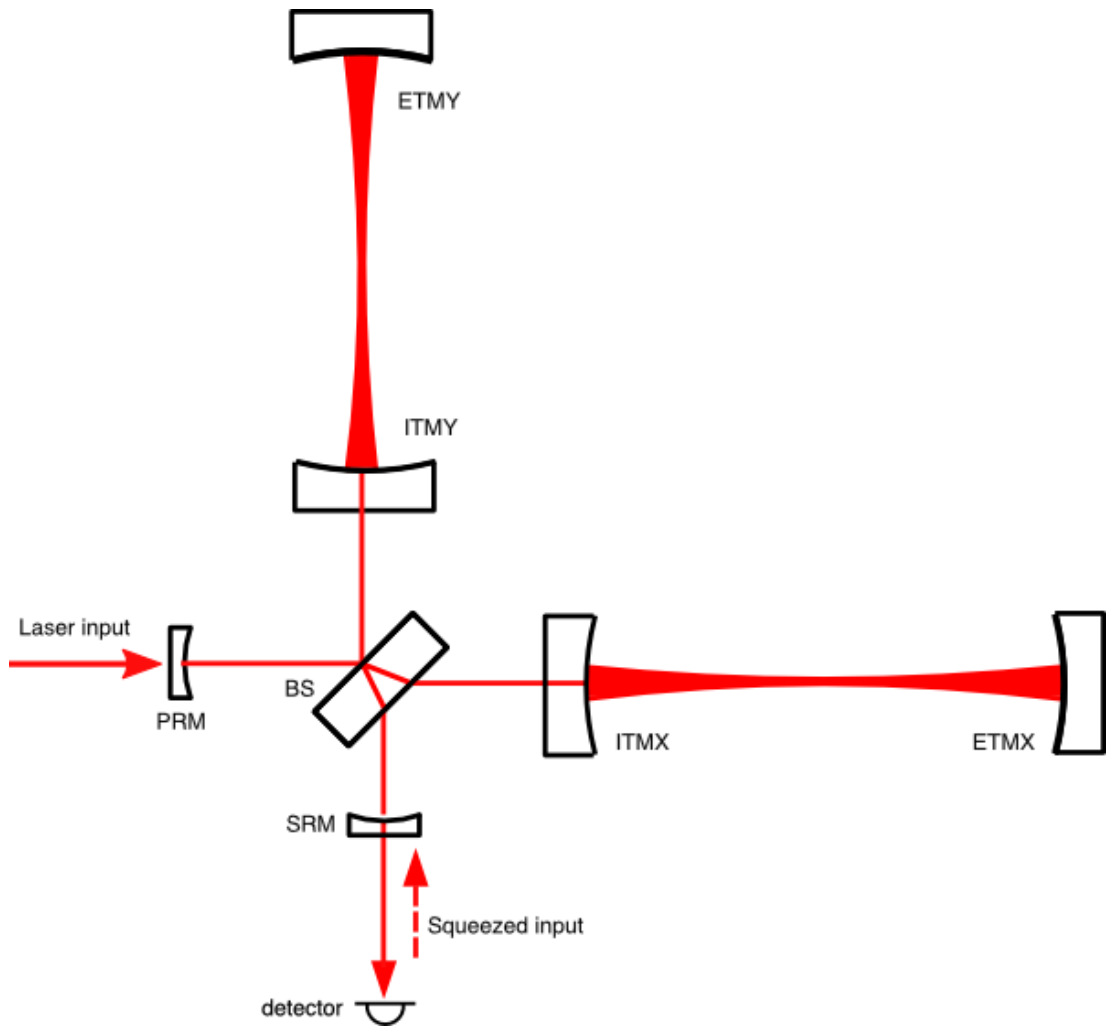
Figure 1.13: Schematic representation of a Michelson interferometer with the inclusion of signal recycling and squeezing techniques. Figure taken from [39].

results were lower than the standard quantum limit and were limited by the mirror damping.

This technique has already been introduced in the German-British detector, where a reduction of up to 6 dB in shot noise can be achieved [71]. Other similar projects are under way [72, 73].
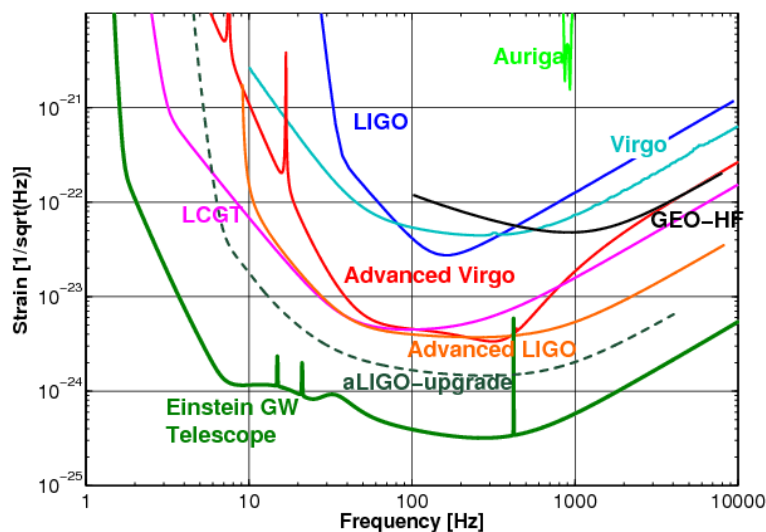
Figure 1.14: Sensitivity of aLIGO following upgrades in the form of inclusion of signal recycling and squeezing techniques. Source of image: [74]

1.6 Limitations on gravitational wave detectors

1.6.1 Seismic noise

There are multiple reasons why seismic noise can arise. Seismographic measurements establish that the ground is in constant motion, with amplitudes in the order of micrometers [75]. This noise source proves limiting to the sensitivity of gravitational wave detectors at frequencies below 10 Hz. The most common source one can think of is an earthquake. Within different frequency ranges, disparate sources contribute to said noise.

For frequencies between 0.1 and 0.3 Hz, the seismic noise band is dominated by secondary microseisms, which are waves travelling throughout the Earth's crust. Their origin is thought to be due to pressure from counter propagating ocean waves against the ocean bottom [76].

Between 1 and 10 Hz, the noise band is dominated by human activity - from vehicles operating nearby to construction work being performed *etc.*, also known as anthropogenic noise. Even on a 'quiet' place, it is estimated that the level of seismic motion follows $\sim 10^{-7} f^2$ mHz$^{-1/2}$ [11]. Taking a frequency of 30 Hz as an example, it is estimated that the disturbance caused to the test mass is $\sim 3 \times 10^{-20}$ Hz$^{-1/2}$.

In order to overcome this, both vertical and horizontal components need to be considered. In the interest of achieving vertical isolation, one can introduce a spring mechanism, whereas in the case of horizontal displacement the operating

method involves the introduction of a pendulum scheme. It can be shown that for a simple pendulum system, the transfer function of the horizontal motion is inversely proportional to f^2.

Therefore one can obtain the relation [8],

$$\frac{x}{x_\mathrm{g}} = \frac{f_0^2}{f_0^2 - f^2},$$

(1.11)

where x is the displacement of the mass at the end of the pendulum, x_g is the displacement from the clamping point of the pendulum, f_0 is the resonant frequency of the pendulum ($f_0 = \frac{1}{2\pi}\sqrt{\frac{g}{L}}$, L is the length from the pivot point to the centre of mass) and f is the frequency of the ground motion. In cases where $f \gg f_0$, i.e. the ground motion frequency far exceed the pendulum frequency: $\frac{x}{x_\mathrm{g}} \approx \frac{f_0^2}{f^2}$.

In order to further enhance this attenuation , a multistage pendulum can be constructed where for a number of pendulum stages, N, the relation becomes [8],

$$\frac{x}{x_\mathrm{g}} = \left(\frac{f_0^2}{f^2}\right)^N.$$

(1.12)

In this result the approximation of $f \gg f_0$ is maintained. In the case of a pendulum, vertical and horizontal planes operate differently. Therefore, above the vertical resonance frequency, this relation implies a factor of $(f_{0,vert}, f_{0,hor})^{2N}$ worse for the vertical isolator in comparison to the horizontal isolator [8].

In the case of frequencies larger than the resonance, the inertia of the mass presents itself from the movement in response to the kx_g force. On the other hand, for low frequencies, $x/x_\mathrm{g} \approx 1$, the spring effectively becomes rigid.

Considering the vertical isolation, the vertical motion of the mass will dominate the noise budget in cases where it exceeds the horizontal motion by more than α^{-1} where α is a variable approximated as $L/R_\odot$ where L is the length of the interferometer arm and $R_\odot$ is the radius of the Earth. In that case the vertical noise dominates. In order to overcome this, the solution is to introduce a vibration isolation stage, which consists of alternating layers of springs and hence compact masses.

1.6.2 Gravity gradient noise

Gravity gradient noise (also known as Newtonian noise) is caused by the direct gravitational coupling of seismic motions and other fluctuations to a gravitational wave detector's test mirrors. This noise source dominates at low frequencies, *i.e.*

below 10 Hz [77]. The occurrence of this noise happens when ambient seismic waves pass close to or underneath the interferometer. They prompt density fluctuations in the earth, which in turn produce gravitational forces upon the interferometer mirrors.

Ray Weiss [78] was the first to postulate gravity gradients as a potential noise source in gravitational wave detectors. This idea was subsequently discussed by Saulson [77] and Spero [79]. The conclusion Saulson reached concluded that the most significant source of Newtonian noise will be the fluctuating density of the earth beneath or near each of the interferometer's test masses [80]. These fluctuations are due to seismic waves, from which the detector cannot be shielded in principle. Additionally, gravity gradient noise can be caused due to human activity around the detector. Other sources have been identified such as wind-borne objects, temperature perturbations and atmospheric shock waves (ones generated by an explosion or the passage of a supersonic aircraft) *etc* [81, 82].

In order to overcome these issues, some detectors are placed underground - like KAGRA and ET. Another option is the use of a space-based detector (LISA). It was determined that effectively in order to eliminate this noise, direct observations of the fluctuations these waves create are made and subtracted. In order for that to be achieved, a network of seismometers is needed around the detector.

1.6.3 Quantum noise

Photoelectron shot noise

Photoelectron shot noise (PSN) originates from photoelectric current due to vibrations of the incident photons. The obvious approach to ensure an interference condition is halfway through a fringe. In fact interferometers operate at/or near a dark fringe. At this condition all common mode effects produce a minimum output signal at the output port whilst differential effects in the interferometer arms are maximised[15]. In order for the interferometer to remain in such condition, the output signal needs monitored through a photodetector. With the use of a transducer, the position of one of the interferometer mirrors may be adjusted to retain the locking of the condition.

The number of photons creating a photoelectric current at the photodetector is noted as N. The number of photons arriving during a measurement interval is equivalent to measuring the optical power. Furthermore, the photons follow a Poisson distribution.

One can consider the case of an interferometer with arm length L, and an input power P. If brightness fluctuations can be interpreted in terms of the

equivalent gravitational wave, then σ_h, is [83],

$$\sigma_\mathrm{h} = \frac{1}{L}\sqrt{\frac{\hbar c\lambda}{4\pi P\tau}}. \tag{1.13}$$

In this equation $\hbar$ is Planck's constant, P is the input laser power, τ is the observational time, where $\Delta f = \frac{1}{2\tau}$ is the bandwidth.

In this frequency scale, each photon arrives independently of the other ones. Using this fact in combination with equation (1.13), one can obtain the relation for the photon shot noise in h, described by [8],

$$h_\mathrm{shot}(f) = \frac{1}{L}\sqrt{\frac{\hbar c\lambda}{2\pi P}}. \tag{1.14}$$

In order to retain photoelectron noise as low as possible, both values of L and P can be adjusted. Due to the inverse proportionality of h_shot to L, increasing the length of the interferometer arms decreases the strain. However that is only sustainable up to a certain point, since for $L = 1000$ km, this is the nearly optimum length for a burst of duration 10^{-6} s [11]. The alternative is increasing the input laser power. However, performing this leads to the arising of another noise contribution.

Radiation pressure noise

The origin of photoelectron shot noise is known. Things are a bit different in the case of radiation pressure noise (RPN). An explanation of the arising of this noise is due to the uncertainty in the photons at the beam-splitter, *i.e.* each interferometer arm will receive a different number of photons at any moment in time. Due to the fact that each photon settles on it own, anti-correlated binomial distribution in the number of light particles in the arms of the interferometer occurs. This distribution attributes to a $\sqrt{N}$ fluctuating force, originating from the radiation pressure [11]. This uncorrelated settlement results in additional light entering through the dark port of the beam-splitter, hence there will be a light intensity increase in one arm, while the intensity will decrease though the other one [5].

Photoelectron shot noise and radiation pressure noise have their similarities. Shot noise arises due to uncertainty in the phase component (quadrature) of the interferometer's laser field, resulting in fluctuations in detection at the output. On the other hand, radiation pressure noise is caused by the uncertainty in the amplitude component (quadrature) of the interferometer's laser field [11]. The fluctuation radiation pressure causes each test mass to move with a spectrum [8],

$$x(f) = \frac{1}{m(2\pi f)^2}F(f) = \frac{1}{mf^2}\sqrt{\frac{\hbar P}{8\pi^3 c\lambda}}, \tag{1.15}$$

where $F(f)$ is the amplitude spectral density, P is the input power, m is the mass of the mirror and f is the frequency of detection.

This correlates to,

$$h_{\rm rp} = \frac{2}{L} x(f), \tag{1.16}$$

where L is the length of the interferometer's arm.

Substituting the expression for $x(f)$, one obtains,

$$h_{\rm rp} = \frac{2}{L} \frac{1}{m f^2} \sqrt{\frac{\hbar P}{8\pi^3 c\lambda}} \tag{1.17}$$

i.e.

$$h_{\rm rp} = \frac{1}{L m f^2} \sqrt{\frac{\hbar P}{2\pi^3 c\lambda}}. \tag{1.18}$$

Photoelectron shot noise and radiation pressure noise can be combined into a single noise contributor, known as optical readout noise [8],

$$h_{\rm or} = \sqrt{h_{\rm shot}^2(f) + h_{\rm rp}^2(f)}. \tag{1.19}$$

Standard Quantum limit

Radiation pressure noise and photoelectron noise are counteractive concepts. As the radiation power increases, $h_{\rm shot}$ decreases while $h_{\rm rp}$ increases. Therefore, there needs to be an optimum power at which these effects are minimised. At the optimum power, the photon coupling and the radiation pressure noise are equal [69]. This sensitivity limit is known as the standard quantum limit. The sensitivity limit is known as the standard quantum limit, and corresponds to the Heisenberg uncertainty principle in its position and momentum formulation.

The difference between the positions of the end mirrors in the interferometer can be expressed as z, where $z = z_2 - z_1$. z_1 and z_2 are the values of the position displacement of the mirrors. The intensity in either of the output ports can be measured with a photodiode, and will enable the measurement of the phase difference between the two arms. $\delta\Phi$ is related to z by $\delta\Phi = \frac{2b\omega z}{c}$, where b is the number of reflections at each mirror and ω is the angular frequency.

Obtaining data for a duration of time τ leads to a determination of the minimal possible error in z, the standard quantum limit [84],

$$(\Delta z)_{\rm SQL} = \left(\frac{2\pi\tau}{m}\right)^{\frac{1}{2}}, \tag{1.20}$$

which is a limit obeying the Heisenberg Uncertainty Principle [85].

One can relate the standard quantum limit to the gravitational wave amplitude, which can be detected as $h_{\mathrm{SQL}} \sim \frac{(\Delta z)_{\mathrm{SQL}}}{L}$ [84].

Another way of obtaining the nature of this limit can be performed by balancing the error due to PSN against the disruption of the positions of the test masses due to RPN.

From the previous two sections, once can further recognise a relation between the frequency and noise amplitude. In the case of RPN, it will dominate at the lower frequencies region, whereas PSN will dominate the higher frequencies.

In order to overcome this limit, various technologies can be applied. A Michelson laser interferometer is also known as a position meter [86]. The variable which is measured is the position of the end mirrors, which does not commute with itself at subsequent position measurements. The non-vanishing commutator poses an uncertainty for the following position measurement, which enforces the standard quantum limit. Braginsky *et. al.* determined that this limit can be surpassed by implementing a quantum non-demolition (QND) measurement [87]. One alternative to the position meters are speed meters. In their case the measurable quantity is the momentum of the test mass [88]. These meters enable a broadband beating of the SQL using homodyne readout of the optimally chosen light quadrature of the dark port [86].

Further information of speed meter can be obtained through [89, 90, 86, 91, 92].

1.6.4 Thermal noise

Thermal noise is one of the most fundamental limits to gravitational wave detectors' sensitivity [93]. It arises due to the thermal energy of the atoms and molecules of the test masses and the mirror suspensions. Thermal noise can be expressed in two components - Brownian and thermoelastic noise.

Brownian noise originates from the $3/2 \; k_{\mathrm{B}}T$ of thermal energy in each atom of a solid in thermal equilibrium, *i.e.* $1/2 \; k_{\mathrm{B}}T$ in each degree of freedom, where k_{B} is Boltzmann's constant and T is the temperature. It is dependant on the internal friction of the system. In order to achieve better loss performance, a low mechanical loss system is required. Mechanical loss can be described as a material property which ascertains the energy storage characterisation around the resonant frequencies. Mechanical loss can also be expressed as a value inversely proportional to the quality factor, Q.

Thermoelastic noise emerges due to thermodynamic fluctuations of the temperature of a substrate material, which result in displacements in the system.

The topic of thermal noise, sources,contributions, *etc.* will be covered more

thoroughly in Chapter 2.

1.7 Detections

1.7.1 Black hole binaries

A hundred years after Einstein's General Theory of Relativity was published, gravitational waves were detected, which made it the first gravitational wave radiation event and also the first direct measurement of the in-spiral and coalition on black holes in a binary system. This occurrence was the beginning of a new era. The first detection, noted GW150914 occurred on September 14$^{\text{th}}$ at 09:50:45 UTC and was detected at both LIGO observatories. The signal arrived first at the Livingston Observatory, L1, and $6.9^{+0.5}_{-0.4}$ ms later at the Hanford observatory, H1. The nature of the origin was evaluated based on mass estimations through the frequency measurements. Two black holes were in an orbit around each other. They reached a peak velocity of 180000 kms^{-1} before merging and producing a single final black hole. During that time the LIGO sites were the only detectors operating. The signal-to-noise ratio obtained for the coincidental signal was 24. Due to the limited number of operating detectors, the origin of the signal could only be estimated within an area of 600 deg^2.

The signal that was detected occurred within 8 cycles over 0.2 second,s where the frequency and amplitude increased from 35 Hz to 150 Hz [94]. Using these values, a mass estimation can be performed. The combined mass of the two black holes known as the chirp mass, can be estimated as,

$$M = \frac{(m_1 m_2)^{\frac{3}{5}}}{(m_1 + m_2)^{\frac{1}{5}}} = \frac{c^3}{G} \left(\frac{5}{96} \pi^{-\frac{8}{3}} f^{-\frac{11}{3}} \dot{f} \right)^{\frac{3}{5}}, \qquad (1.21)$$

where m_1 and m_2 are the masses of the primary objects, c is the speed of light, G is the gravitational constant, f is the observed frequency and $\dot{f}$ is its derivative with respect to time. Using the detection parameters it was deduced that $M \simeq 30 M_\odot$. which implied $m_1 + m_2$ higher or equal to 70 $M_\odot$. This therefore bounds the Schwarzschild radius to 210 km. The approximated distance between the orbiting objects was estimated as $\sim$ 350 km. Through further investigation and data analysis, approximate values were deduced for the primary black hole, m_1, secondary black hole, m_2, and the final black hole, $m_1 + m_2 = 62$; the luminosity distance was evaluated as 410^{+160}_{-180} Mpc [94].

This event as well as the following observations encouraged the continuation of gravitational wave research. Binary black holes being one of the sources of gravitational radiation, opened the way for new phenomena. Numerous black hole binary systems were detected during O1 and O2, where during O2 the LIGO

observatories were joined in observation by Virgo. During O2 a remarkable detection was made, the coalescence of two neutron stars, which is further explained in the next subsection. As a note it can be stated that for the purpose of compactness and clearance only the first detection of its kind is mentioned. Further information about following detections can be found in [95, 96, 1, 23].

1.7.2 Neutron star binary

The first neutron star binary system was observed on August 17$^{\text{th}}$, 2017. The event GW170817 was observed at 12:41:04 UTC and was detected at both Advanced LIGO and Advanced Virgo observatories with a combined signal-to-noise ratio of 32.4. 1.7 s after the coalescence a gamma ray burst was observed by Fermi GBM. The detection of GRB170817A and the subsequent electromagnetic emission demonstrate the presence of matter [1].

This was the first detection, where the signal was observed by more than one telescope. Advanced LIGO started its second operational run on November 30$^{\text{th}}$ 2016 and was joined by Advanced Virgo on August 1$^{\text{st}}$ 2017, where the run ended on August 31$^{\text{st}}$ 2017. During that time, two observations were detected, however the likelihood of the first probable neutron star binary detection lead to increased interest in the event. GEO600 was also operational during this period but on the grounds that its sensitivity was not as good, it was unable to observe the event. The measured chirp mass was estimated to $M = 1.188^{+0.004}_{-0.002}M_\odot$. Using the information about the nature of the origin the component spins can be restricted and a limit of $\chi \leq 0.89$ can be assumed. Through that estimation the component masses were estimated as $m_1 = 1.36 - 2.26M_\odot$, $m_2 = 0.86 - 1.36M_\odot$ and the localisation of the event was within 28 deg^2. By comparison to GW150914, one can acknowledge a huge difference in localisation limit by the introduction of the additional observatory.

Through the measurement of the luminosity distance, in this case 40^{+8}_{-14} Mpc, combined with the estimation of the redshift, the possibility of inferal of cosmological principles increases [70, 97]. In the case of GW170817, the luminosity distance in addition to the estimation of the Hubble flow velocity near NGC 4993, provide an evaluation of Hubble's constant as 67.90 ± 0.55 kms^{-1}Mpc^{-1} [98]. GW170817 has been the only neutron star binary system observed so far but the future is bright and with the improvement of the sensitivity of the detectors more and more events are expected to be observed.

1.8 Conclusion

The direct observation of gravitational waves has further validated Einstein's Theory of General Relativity. The progress in technological advances has enabled the

evolution of ground-based gravitational wave detectors - from the resonant bar detectors in the 1960s to the current advanced technology observatories. At present, aLIGO has successfully measured separation differences between the suspended mirrors in the orders of $\sim 10^{-23}$ $\sqrt{Hz}$ around a frequency of 100 Hz [99]. An expansion of the network of detectors is in progress and it will allow for better pinpointing of origins of signals.

A severe limitation to these ground-based detectors is mostly caused by thermal noise associated with the mirror coatings. For future generations of gravitational wave detectors either alternative coating materials will be developed or there will be an alteration in operation temperature. Following the example of KAGRA, ground-based detectors can evolve into operation at cryogenic temperatures. This has already been the plan for next ground-based projects, like ET, LV and CE. Following the success of LISA Pathfinder, the LISA project has progressed and is expected to ensue in the near future.

The important objective at this stage is to limit the noise contributions in the frequency regions where the detections are most likely to happen. Since currently that limit is imposed due to thermally driven displacements, Chapter 2 will concentrate on establishing the causes of thermal noise as well as how it affects the system and its components. By exploring the originators of thermal noise, a course of improvement is more likely to be identified.
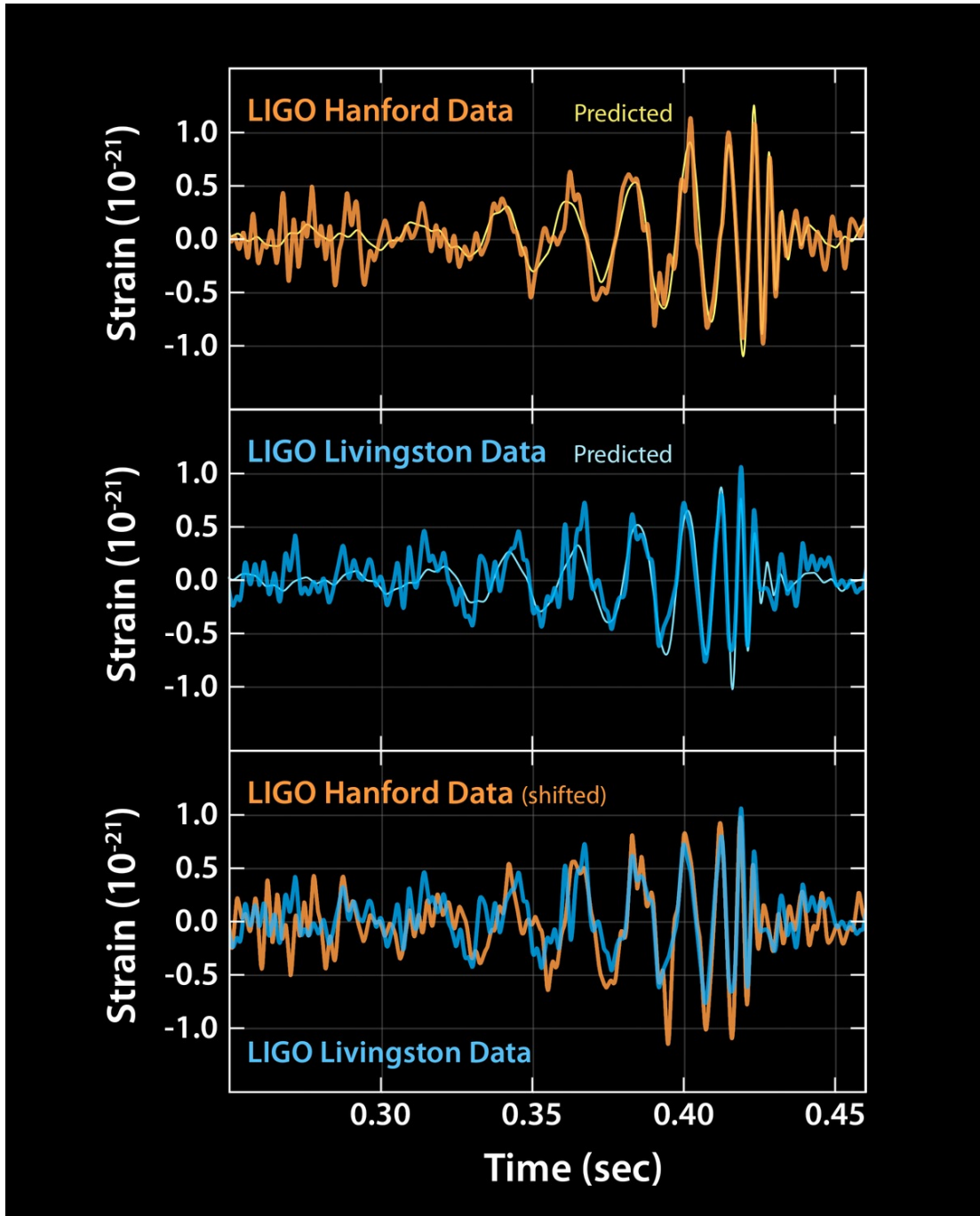
Figure 1.15: Signal GW150914 detected at both aLIGO observatories - Hanford and Livingston. This was the first recorded gravitational wave signal, which resulted due to the merge of two black holes into a final black hole of mass 62 $M_\odot$. Image reprinted from [94].
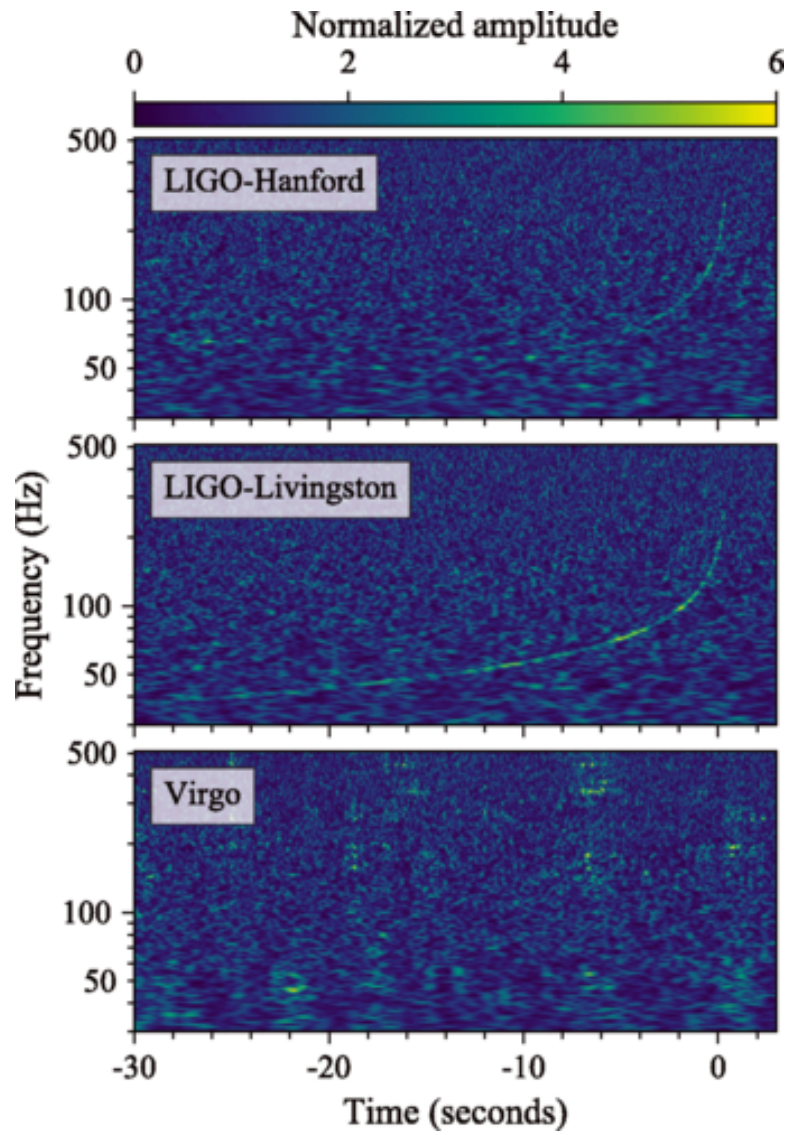
Figure 1.16: Event GW170817 detected at both aLIGO observatories and the aVirgo detector. This is the first recorded signal resulting for the merge of two neutron stars. Image source: [1]

Chapter 2

Thermal noise

2.1 Introduction

A limitation is imposed on the sensitivity of interferometric gravitational wave detectors due to thermally driven motions of the test masses, mirror suspension fibres and mirror coatings. The equipartition theorem states that the motion within the test mass components emerges from the mean $\frac{1}{2}k_{\mathrm{B}}T$ of thermal energy per degree of freedom of molecules in the mechanical system, where k_{B} is Boltzmann's constant and T is the temperature in Kelvin. This thermal energy is stored within the atoms of the mechanical system and hence has an effect over the entirety of the system. This thermally driven movement, known as Brownian thermal noise, is typically in amplitude larger than the expected gravitational wave signal across the acoustic band. The dominant source of thermal noise within the most sensitive frequency band of ground based detectors is associated with the mirror coatings - referred to as coating Brownian thermal noise.

The totality of thermal noise is typically presented as a combination of Brownian coating noise, thermoelastic and thermorefractive noise. All noise contributors vary depending on the thermo-mechanical properties of the materials used to fabricate the coatings as well as the test masses' composite material. Despite their common origin, thermoelastic and thermorefractive noise have not been treated coherently [100, 101] the predicted amplitude of their mean is regarded as thermo-optic noise. One option to reduce the total thermal energy in the mirrors and the lower-stage suspensions is the reduction of the operation temperature of the mechanical system. This approach has now been undertaken within the KAGRA collaboration and it is under consideration for third generation ground based gravitational wave detectors.

2.2 Brownian motion

The concept of Brownian motion was discovered by botanist Robert Brown around 1828 [102]. Observations were performed on pollen grains on a surface of water in random and irregular motion. Brown's hypothesis was that this motion was the result of a universal vital force. It was not until 1916 that Einstein related that motion to the stochastic collision of water molecules interacting with the pollen grains. It was realised that these molecular impacts were the roots of dissipation of the grains' kinetic energy.

2.3 The Fluctuation Dissipation Theorem

The fluctuation dissipation theorem establishes the relationship between fluctuation and dissipation. The relation applies to any linear system (one in which the response is linearly proportional to the applied force [5]) which is also in thermal equilibrium.

Due to the linearity of the system, the frequency domain equation of motion can be written in terms of the amplitude of the externally applied force F_{ext}, which has caused the movement with sinusoidal velocity $v(f)$. Therefore,

$$F_{\text{ext}} = Zv, \tag{2.1}$$

or equivalently

$$v = YF_{\text{ext}}, \tag{2.2}$$

where $Z(f)$ is the function called impedance, and it is associated to the admittance $Y(f)$ by the relation $Z^{-1}(f) = Y(f)$.

The fluctuation dissipation theorem was derived by H.B.Callen *et. al.* in 1951 [103]. Formulation of the power spectrum density ,$F^2_{\text{therm}}(f)$, can be defined by,

$$S_{F(f)} = F^2_{\text{therm}}(f) = 4k_B T \Re\{Z(f)\}, \tag{2.3}$$

where $\Re\{Z(f)\}$ indicates the dissipative part of the impedance.

Alternatively, through the theorem, a relation can be obtained for the power spectrum of the system's fluctuating motion as,

$$S_x(f) = x^2_{\text{therm}}(f) = \frac{k_B T}{\pi^2 f^2} \Re\{Y(f)\} = \frac{4k_B T}{\omega^2} \Re\{Y(\omega)\}, \tag{2.4}$$

where $\Re\{Y(\omega)\}$ is the real part of the mechanical admittance and ω is the angular frequency.

The equation for the power spectral density of the displacement can be used to show that in cases where $Q \gg 1$, then $S_x(f) \propto \phi(\omega)$, where Q is the quality factor

and $\phi(\omega)$ is the mechanical loss. Both of these terms will be further investigated in the following sections. A requirement for a system is then low dissipation, since for high degree of dissipation the spectral densities in displacement noise will be lower and broader. Therefore, within interferometric detectors, the materials used for the composition of the test masses and the suspension pendulums, have been chosen to be ones with a low loss, $\phi(f)$. Current room temperature ground based detectors use fused silica as their substrate material, due to its mechanical dissipation being very low at such temperatures. Fused silica is implemented within the interferometer mirrors and their suspensions. Additional verification of this is provided in the following sections of this chapter.

2.4 External sources of motion

Multiple external sources can contribute to the amount of thermal noise in an interferometric gravitational wave detector:

- Gas damping as a result of the residual gas molecules colliding with the mirrors and suspensions;

- Recoil damping occurs when the dissipation energy from the suspensions transmits into the suspension support;

- Frictional damping arises at points of contact, for example - where the suspensions adjoin the test mass and at the suspending point.

2.5 Internal mechanical dissipation

Once all the external sources of dissipation have been suitably diminished, the contribution is dominated by internal sources. This internal dissipation can be separated into two kinds - viscous dissipation and structural dissipation.

Internal dissipation arises within a material as it experiences an applied force, to which it does not react in the ideal elastic way. The ideal elastic body will follow Hooke's law. However, real bodies respond inelastically.

Let's consider the case of an ideal material. Once a stress , σ, is applied to a material, it experiences a strain , ε, where the two quantities have the relation $\sigma = \varepsilon Y$, where Y is the Young's modulus of the material. In an elastic response, the stress and strain are directly related.

In an inelastic situation, the strain response gets delayed over a finite relaxation time. This delay can be expressed with the use of a phase lag , ϕ. For a periodic stress , σ, with frequency f, it can be written that,

$$\sigma = \sigma_0 \exp(i2\pi ft) = \sigma_0 \exp(i\omega t), \tag{2.5}$$

where σ_0 is the initial amplitude and $2\pi f$ is the angular frequency.

The resulting strain is therefore,

$$\varepsilon = \varepsilon_0 \exp(i(2\pi ft - \phi)) = \varepsilon_0 \exp(i(\omega t - \phi)), \qquad (2.6)$$

where ε_0 is the initial strain amplitude, and ϕ is the phase lag also referred to as the loss angle. In the case of an ideal elastic material this loss angle is $\phi = 0$.

The strain response exhibits the same frequency as the excitation but will have an offset of ϕ which represents the fraction of energy dissipated due to each oscillation of the system [104]. If the stress and strain couple within the system, the result is a heat exchange. This internal dissipation can then be observed through Debye peaks, occurring as broad peaks at certain frequencies. These peaks can occur depending on the frequency range and can be separated by several orders of magnitude.

Internal dissipation can arise from disturbances causing changes in the crystalline structure of the material. Multiple authors have taken this into consideration [105, 106, 107, 108] and have obtained the origin of disturbances to be due to friction caused by lattice dynamics.

Thermal dissipation arises due to two-level systems (TLS) which may be associated with specific properties associated with atomic disorder, *e.g.* crystalline, polycrystalline and amorphous [109, 110, 111, 112].

2.6 Thermal noise associated with a resonant mode

An elastic oscillation of a periodic system can be presented in terms of the phase lag ϕ, force F and displacement x of mass m. For a simple harmonic oscillator, one obtains a complex spring constant for an anelastic spring. The resonant modes of the suspended optics can be modelled as simple harmonic oscillators using a version of Hooke's law, where the system is subject to internal friction. Hooke's law is extended in order to account for periodic damping [104] and hence becomes,

$$m\ddot{x} = -k(1 + i\phi(\omega))x + F(\omega), \qquad (2.7)$$

where $k(1+i\phi(\omega))$ is the complex spring constant, ω is the angular frequency, x is the displacement and $\ddot{x}$ is the acceleration.

Furthermore, both the displacement and acceleration can be written in terms

of the velocity [8], where $x = \frac{\dot{x}}{i\omega}$ and $\ddot{x} = i\omega\dot{x}$. From equation [2.7] one can obtain,

$$F(\omega) = m\ddot{x} + k(1 + i\phi(\omega))x$$

$$= mi\omega\dot{x} + k(1 + i\phi(\omega))\frac{\dot{x}}{i\omega}$$

$$= \dot{x}\left[mi\omega + \frac{k(1 + i\phi(\omega))}{i\omega}\right]$$

$$\Rightarrow F(\omega) = \dot{x}\left[\frac{k(1 + i\phi(\omega)) - m\omega^2}{i\omega}\right]. \quad (2.8)$$

In section 2.3, F was defined in terms of the impedance and velocity, where $F(\omega) = Z(\omega)v(\omega) \Rightarrow Z(\omega) = \frac{F(\omega)}{v(\omega)}$.

Substituting into the expression obtained for F, whilst substituting an expression for the velocity term, the complete impedance formula becomes,

$$Z(\omega) = \frac{k + ki\phi(\omega) - m\omega^2}{i\omega}. \quad (2.9)$$

Furthermore, the impedance is related to the admittance as $Z^{-1}(\omega) = Y(\omega)$.

In order to obtain a relation for the power spectral density, an expression is needed for the real part of the admittance term.

Using the expression for $Z(\omega)$ (Eq. 2.9), the equations for the real and imaginary parts of the admittance become,

$$\Im(Y(\omega)) = \frac{\omega(k - \omega^2 m)}{\left(k - \omega^2 m\right)^2 + \phi^2(\omega)k^2}, \quad (2.10)$$

and,

$$\Re(Y(\omega)) = \frac{k\omega\phi(\omega)}{\left(k - \omega^2 m\right)^2 + \phi^2(\omega)k^2}, \quad (2.11)$$

where the spring constant is equivalent to $m\omega_0^2$ [93]. Substituting in the expressions for the spring constant and the real part of the mechanical admittance gives the frequency dependent power spectral density of an oscillator with mechanical loss $\phi(\omega)$, such that,

$$S = \frac{4k_{\mathrm{B}}T}{\omega^2}\Re(Y(\omega))$$

$$= \frac{4k_{\mathrm{B}}T}{\omega^2}\frac{k\omega\phi(\omega)}{(k - \omega^2 m)^2 + \phi^2(\omega)k^2}$$

$$= \frac{4k_{\mathrm{B}}T}{\omega^2}\phi(\omega)\frac{1}{(m\omega_0^2 - \omega^2 m)^2 + \phi^2(\omega)m^2\omega_0^4}$$

$$\Rightarrow S_x(\omega) = \frac{4k_{\mathrm{B}}T\phi(\omega)}{\omega m}\frac{\omega_0^2}{(\omega_0^2 - \omega^2) + \phi^2(\omega)\omega_0^4} \quad (2.12)$$

Converting the expression from angular frequency gives,

$$S_x(f) = \frac{k_B T}{2\pi^3 f m}\frac{f_0^2\phi(f)}{(f_0^2 - f^2)^2 + f_0^4\phi^2(f)}, \quad (2.13)$$

where $\phi(f)$ is the mechanical loss in terms of the frequency and f_0 is the resonance frequency.

Let us assume that the materials have very low mechanical loss, $i.e.$ $\phi^2(f) \ll 1$.

In the case of a frequency much greater than the resonant frequency, $f \ll f_0$, the equation for $S_x(f)$ becomes,

$$S_x(f) = \frac{k_{\mathrm{B}}T f_0^2}{2\pi^3 m}\frac{\phi(f)}{f^5}. \quad (2.14)$$

Considering the other extreme, where the measured frequency is very low compared to f_0,

$$S_x(f) = \frac{k_{\mathrm{B}}T}{2\pi^3 m f_0^2}\frac{\phi(f)}{f}. \quad (2.15)$$

What is deduced from both limits is that the thermal displacement noise is directly proportional to the mechanical loss. Mechanical loss is quantified through the measurement of the mechanical loss angle, a reduction in said loss angle will lead to a reduction of $\phi(f)$. A reduction in $\phi(f)$ will directly decrease the thermal noise at frequencies different than f_0.

The total thermal motion within the system at constant temperature remains the same due to conservation of energy. Therefore, if the mirrors and suspensions in the interferometer are modelled as harmonic oscillators with a single resonant mode, the thermal noise is directly proportional to the mechanical loss angle away from resonance. Using equation 2.15, it can be demonstrated that the power spectral density is measured in m^2/Hz. Analogously, the amplitude spectral density (mechanical loss) is simply the square root of the density expressions, hence evaluated in $\text{m}/\sqrt{\text{Hz}}$. The mirrors and suspensions have many vibrational resonances such as the combination of the internal mirror modes, suspension fibre modes, and pendulum and bounce modes of the suspended system [113]. Precise construction is then required in order to push the resonant frequencies out of the most sensitive bandwidth of the detectors.

2.7   Mechanical loss

Mechanical loss of a material is an important parameter due to its inclusion into the expression for power spectrum density. It is essential for estimating the levels of thermal noise. Mechanical loss is obtained through measurement of the quality factor, Q, of an oscillator. It is a dimensionless measure of the proportional dissipation at the resonance frequency. The quantity is estimated through,

$$Q \equiv \frac{f_0}{\Delta f}, \tag{2.16}$$

where f_0 is the resonant frequency and Δf is the width of the resonance peak measured at half of its maximum power.

From this relation, it is visible that the quality factor is inversely proportional to the width of the resonant peak. In the case of a broad peak, the system will have a low quality factor, whereas in the case where the peak is narrow, a large Q is obtained.

To calculate how the quality factor affects the damping of the system, one can start with the extended version of Hooke's law which accounts for internal damping, such that,

$$F = m\ddot{x} + k(1 + i\phi(\omega))x. \tag{2.17}$$

Noting again that $\ddot{x} = i\omega\dot{x}$ and $x = \frac{\dot{x}}{i\omega}$, expanding and substituting into the expression gives,

$$F = m\ddot{x} + kx + ik\phi(\omega)x$$

$$= m\ddot{x} + kx + ik\phi(\omega)\frac{\dot{x}}{i\omega}$$

$$= m\ddot{x} + kx + \frac{k}{\omega}\phi(\omega)\dot{x}. \quad (2.18)$$

The resonant frequency is defined as $\omega_0 = \sqrt{\frac{k}{m}}$, therefore the equation becomes,

$$F = m\left(\ddot{x} + \frac{\omega_0^2}{\omega}\phi(\omega)\dot{x} + \omega_0^2 x\right)$$

$$= m\left(\ddot{x} + \frac{\gamma}{m}\dot{x} + \omega_0^2 x\right)$$

$$= m\left(\ddot{x} + \frac{\omega_0}{Q(\omega)}\dot{x} + \omega_0^2 x\right), \quad (2.19)$$

where $\frac{\omega_0^2}{\omega}\phi$ is the damping coefficient, usually denoted as γ.

The quality factor is obtained as inversely proportional to the coating loss angle, *i.e.* $Q = \frac{1}{\phi(\omega)}$. Therefore, the lower the mechanical loss is, the larger the value of the quality factor.

The relation between $Q(\omega)$ and $\phi(\omega)$ means that the loss angle of a material can be obtained by measuring the full width at half maximum of the resonant peaks of the system.

A more detailed and involved characterisation of the Q value is provided in the following chapters. The interpretation and measurement of this parameter is further explored and expanded for different materials.

2.8 Thermal noise assuming no light penetration into the coating

In order to compute an expression for the coating Brownian noise, one begins by assuming there is no light penetrating the coating, *i.e.* all of the light gets reflected at the coating surface, also known as the coating-air interface. Hong *et.al.* [114]

acquired an expression, jointly representing the phase noise and amplitude noise, *i.e.*

$$\xi\left(\vec{x}\right) - i\zeta\left(\vec{x}\right) = -\delta z_s\left(\vec{x}\right) - \sum_{j=1}^{N}\delta l_j\left(\vec{x}\right) - \sum_{j=1}^{N}\frac{i}{2k_0}\left[\frac{\partial\log\rho}{\partial\phi_j}\cdot\delta\phi_j\left(\vec{x}\right)\right]$$

$$-\sum_{p=0}^{N}\frac{i}{2k_0}\left[\frac{\partial\log\rho}{\partial r_p}\cdot\delta r_p\left(\vec{x}\right)\right],\quad(2.20)$$

where $\xi\left(\vec{x}\right)$ corresponds to the phase noise contribution and $\zeta\left(\vec{x}\right)$ to the amplitude noise. The first two terms within the equation are due to motion at the coating-air interface at a coordinate $\vec{x}$ and the fluctuation of the thickness of the coating layers. The remaining two terms represent the light penetration within the coating layers. As in this case it is assumed that all the light is reflected, only the first two terms of equation 2.20 are kept, which additionally implies $\zeta = 0$. This means one only considers the coating phase noise, across the mirror surface, $\bar{\xi}$, expressed by [114]

$$\bar{\xi} = \frac{\int\xi\left(\vec{x}\right)I\left(\vec{x}\right)d^2\vec{x}}{\int I\left(\vec{x}\right)d^2\vec{x}},\qquad(2.21)$$

$$\bar{\zeta} = \frac{\int\zeta\left(\vec{x}\right)I\left(\vec{x}\right)d^2\vec{x}}{\int I\left(\vec{x}\right)d^2\vec{x}}.\qquad(2.22)$$

Equation 2.3 presented an expression for the power spectrum density, relating it to the real part of the mechanical impedance. Furthermore, $Z(f)$ can be expressed as

$$Z\left(f\right) = -2\pi i f x\left(f\right)/F\left(f\right),\qquad(2.23)$$

where the force function is formed as a sinusoidal force,

$$F\left(t\right) = F_0\cos\left(2\pi f t\right).\qquad(2.24)$$

Combining Eq 2.23 and 2.24 and assuming amplitude F_0 acting directly upon coordinate $\vec{x}$, the expression for the power spectral density becomes

$$S_x \left(f \right) = \frac{2k_B T}{\pi^2 f^2} \frac{W_{\text{diss}}}{F_0^2} = \frac{4k_B T}{\pi f} \frac{U}{F_0^2} \phi, \tag{2.25}$$

where W_{diss} is the energy lost per cycle of oscillation divided by 2π, U represents the stored energy within the system, and ϕ is the loss angle.

The elastic energy within the coating can be represented as the sum of the bulk energy U_{B} and shear energy U_{S}, *i.e.*

$$U_{\text{coat}} = U_{\text{B}} + U_{\text{S}}. \tag{2.26}$$

Further expansion of this expression includes proportionality to K and μ, where K is the real part of the bulk modulus and μ is the real part of the shear modulus. This can be expressed in imaginary form as

$$\tilde{K} = K \left(1 + i\phi_{\text{B}} \right), \tag{2.27}$$

$$\tilde{\mu} = \mu \left(1 + i\phi_{\text{S}} \right). \tag{2.28}$$

Furthermore, K and μ can be expressed in terms of the widely used Young's modulus and Poisson's ratio, as

$$K = \frac{Y}{3 \left(1 - 2\sigma \right)}, \tag{2.29}$$

$$\mu = \frac{Y}{2 \left(1 + \sigma \right)}. \tag{2.30}$$

Similarly to expressions for $\tilde{K}$ and $\tilde{\mu}$, $\tilde{Y}$ can be expressed as

$$\tilde{Y} = Y \left(1 + i\phi_{\text{Y}} \right), \tag{2.31}$$

where ϕ_Y is related to ϕ_B and ϕ_S as

$$\phi_Y = \frac{\left(1 - 2\sigma \right) \phi_{\text{B}} + 2 \left(1 + \sigma \right) \phi_{\text{S}}}{3} \tag{2.32}$$

and

$$\tilde{\sigma} = \sigma + \frac{i}{3} \left(1 - 2\sigma \right) \left(1 + \sigma \right) \left(\phi_{\text{B}} - \phi_{\text{S}} \right). \tag{2.33}$$

In the case where $\phi_B = \phi_S$ *i.e.* the loss angles are equal to each other, the Poisson's ratio function only contains real parts and therefore only loss angle required is ϕ_Y. However, there is no particular reason as to why the two angles would be equal to one another.

In order to obtain an expression for the coating Brownian noise, one can even consider a mirror surface coated with a thin single layer of coating. Comparing the thickness of this coating layer to the overall area of the mirror surface, it can be stated that the coating has a negligible effect on the substrate. We had defined $\bar{S}_x(f) \propto W_{\mathrm{diss}}$ [Eq. 2.25], which can be expressed as

$$W_{\mathrm{diss}} = \phi_{\mathrm{sub}}U_{\mathrm{sub}} + \phi_B U_B + \phi_S U_S, \tag{2.34}$$

where ϕ_{sub} is the loss angle associated with the substrate and U_{sub} is the energy stored in the substrate. Furthermore, W_{diss} can be expressed as

$$W_{\mathrm{diss}} \approx \left(\phi_{\mathrm{sub}} + \frac{U_B}{U_{\mathrm{sub}}}\phi_B + \frac{U_S}{U_{\mathrm{sub}}}\phi_{\mathrm{sub}} \right) U_{\mathrm{sub}}. \tag{2.35}$$

Since the thickness of the coating is very small in comparison to the substrate, the mirror can be approximated as a half-infinite surface. This means that U_{sub} can be approximated as equal to the total strain energy stored in the sample. As the coating adds on to the substrate loss angle, ϕ_{coat} can be defined as

$$\phi_{\mathrm{coat}} = \phi_{\mathrm{sub}} + \frac{U_B}{U_{\mathrm{sub}}}\phi_B + \frac{U_S}{U_{\mathrm{sub}}}\phi_S. \tag{2.36}$$

In order to evaluate these energy rations, one needs to apply a pressure profile onto the coating-air interface. Levin [115] proposed that the profile of the applied pressure should match the profile of the laser beam intensity, and since the laser beam intensity follows a Gaussian distribution, a Gaussian pressure distribution is applied.

$$p\left(\vec{r},t\right) = p\left(r,t\right) = \frac{2F_0}{\pi\omega^2} \exp\left(-\frac{2r^2}{\omega_0^2}\right) \sin\left(2\pi ft\right), \tag{2.37}$$

or

$$= F_0 \omega\left(\vec{x}\right), \tag{2.38}$$

where $\omega(\vec{x})$ is expressed as

$$\int \omega\left(\vec{x}\right) = \frac{\int d^2\vec{x} I^2\left(\vec{x}\right)}{\left[\int d^2\vec{x} I\left(\vec{x}\right)\right]^2}, \tag{2.39}$$

65

where $I(\vec{x})$ represents the light intensity.

For a Gaussian pressure distribution, constant in time, expression becomes

$$p\left(r\right) = \frac{2F_0}{\pi\omega^2} \exp\left(-\frac{2r^2}{\omega^2}\right). \tag{2.40}$$

Straightforward calculations give

$$\frac{U_{\mathrm{B}}}{F_0^2} = \frac{(1-2\sigma_{\mathrm{c}})\,l}{3}\left[\frac{Y_{\mathrm{c}}}{Y_{\mathrm{s}}^2}\frac{(1-2\sigma_{\mathrm{s}})^2(1+\sigma_{\mathrm{s}})^2}{(1-\sigma_{\mathrm{c}})}\right.$$

$$+\frac{1}{Y_{\mathrm{s}}}\frac{2\left(1-2\sigma_{\mathrm{s}}\right)\left(1+\sigma_{\mathrm{s}}\right)\left(1+\sigma_{\mathrm{c}}\right)}{(1-\sigma_{\mathrm{c}})^2}$$

$$+\frac{1}{Y_{\mathrm{c}}}\frac{(1+\sigma_{\mathrm{c}})^2}{(1-\sigma_{\mathrm{c}})^2}\int \omega^2\left(\vec{x}\right)d^2\vec{x} \tag{2.41}$$

and

$$\frac{U_{\mathrm{S}}}{F_0^2} = \frac{2l}{3}\left[\frac{Y_{\mathrm{c}}}{Y_{\mathrm{s}}}\frac{\left(1-\sigma_{\mathrm{c}}+\sigma_{\mathrm{c}}^2\right)\left(1+\sigma_{\mathrm{s}}\right)^2(1-2\sigma_{\mathrm{s}})^2}{(1-\sigma_{\mathrm{c}})^2\left(1+\sigma_{\mathrm{c}}\right)}\right.$$

$$-\frac{1}{Y_{\mathrm{s}}}\frac{\left(1+\sigma_{\mathrm{c}}\right)\left(1-2\sigma_{\mathrm{c}}\right)\left(1-2\sigma_{\mathrm{s}}\right)\left(1+\sigma_{\mathrm{s}}\right)}{(1-\sigma_{\mathrm{c}})^2}+$$

$$\frac{1}{Y_{\mathrm{c}}}\frac{(1-2\sigma_{\mathrm{c}})^2\left(1+\sigma_{\mathrm{c}}\right)}{(1-\sigma_{\mathrm{c}})^2}\int \omega^2\left(\vec{x}\right)d^2\vec{x}, \tag{2.42}$$

where l represents the coating thickness.

For a rectangular plate with dimensions $(a \times b \times c)$ and thickness of coating l, one can express $\frac{U_{\mathrm{B}}}{U}$ and $\frac{U_{\mathrm{S}}}{U}$ as

$$\frac{U_{\mathrm{B}}}{U} = \frac{l}{c}\frac{Y_{\mathrm{c}}}{Y_{\mathrm{s}}}\left(\frac{(1-\sigma_{\mathrm{s}})^2\left(1-2\sigma_{\mathrm{c}}\right)}{(1-\sigma_{\mathrm{c}})^2}\right) \tag{2.43}$$

and

$$\frac{U_{\mathrm{S}}}{U} = \frac{2l}{c}\frac{Y_{\mathrm{c}}}{Y_{\mathrm{s}}}\left(\frac{(1-\sigma_{\mathrm{s}})^2\left(1-\sigma_{\mathrm{c}}+\sigma_{\mathrm{c}}^2\right)}{(1-\sigma_{\mathrm{c}})^2\left(1+\sigma_{\mathrm{c}}\right)}\right). \tag{2.44}$$

Substituting these expressions into Eq.(2.36) gives

$$\phi = \phi_{\text{sub}} + \frac{l}{c}\frac{Y_{\text{c}}}{Y_{\text{s}}}\frac{(1-\sigma_{\text{s}}{}^2)}{(1-\sigma_{\text{c}})^2}\left[\phi_{\text{B}}\left(1-2\sigma_{\text{c}}\right) + 2\phi_{\text{S}}\frac{(1-\sigma_{\text{c}}+\sigma_{\text{c}}{}^2)}{(1+\sigma_{\text{c}})}\right]. \tag{2.45}$$

Equation 2.25 provided with an expression for the power spectral density of the Brownian motion. Therefore, substituting Eq.2.45 into 2.25 gives a full expression of the spectral density.

Independently, said spectral density has also been defined as

$$S_x\left(f\right) = \frac{2k_BT}{\pi^{\frac{3}{2}}f}\frac{1}{\omega Y_s}\left\{\phi_{sub} + \frac{1}{\sqrt{\pi}}\frac{l}{\omega}\left(\frac{Y_c}{Y_s}\phi_{\parallel} + \frac{Y_s}{Y_c}\phi_{\perp}\right)\right\} \tag{2.46}$$

as shown in [116].

2.9   Coating thermo-optic noise

Thermal fluctuations within the coatings, used for the production of highly reflective surfaces are becoming of higher significance in optical measurements. Thermo-optic noise can be considered as the coherent sum of contributions from thermo-refractive and thermo-elastic noise. These two noise sources arise due to temperature gradients within the test mass and more precisely within the coatings of the mirror. These temperature gradients equivalently contribute to fluctuations in the physical parameters of the coating. In the case of thermo-elastic noise, this parameter is known as the thermal expansion coefficient, and is denoted by α. Similarly, for thermo-refractive noise the fluctuating parameter is the thermo-refractive coefficient, denoted by β and evaluated as $\frac{dn}{dT}$, where n is the refractive index [117].

An expression is obtained by Gorodetsky $et.$ $al.$ representing the spectrum of thermoelastic contributions [118],

$$S^{\text{TE}}(\omega) = \frac{8}{\sqrt{2}\pi}\frac{k_BT^2\alpha^2(1+\sigma)^2\kappa}{(\rho C)^2r_0^3\omega^2}, \tag{2.47}$$

where k_B is Boltzmann's constant, T is the temperature, α is the thermal expansion coefficient which is evaluated as $\frac{1}{l}\frac{dl}{dT}$, σ is Poisson's ratio, κ is the thermal conductivity, ρ is density, C is specific heat capacity and r_0 is the radius of the beam and l is the length of a test piece at temperature T.

In the scenario of thermo-elastic noise, the equivalent displacements are quantified within the change of the length l, occurring due to temperature differences, resulting in expansion and shrinkage of l. In the case of thermo-refractive noise

the equivalent displacements show a proportionality to the thermo-refractive coefficient, which is expressed as [118]

$$\beta_{\text{eff}} = \frac{n_2^2 \beta_1 + n_1^2 \beta_2}{4\left(n_1^2 - n_2^2\right)}, \tag{2.48}$$

where $\beta_1 = \frac{dn_1}{dT}$, $\beta_2 = \frac{dn_2}{dT}$ and the spectrum density can be computed to describe fluctuations of surface displacements -

$$S^{\text{TD}}(\omega) = \frac{\sqrt{2}\beta_{eff}^2 \lambda^2 \kappa T^2}{\pi r_0^2 \sqrt{\omega \rho C \lambda^*}}. \tag{2.49}$$

By comparing the two expressions, it is of interest to observe that the expression for thermo-elastic noise involves a proportionality to the coating thickness, whereas in the case of thermo-refractive noise this dependence does not exist.

2.10 Conclusions

Thermally induced displacement noise is the primary dominating factor limiting the sensitivity of gravitational wave detectors. In order to estimate the overall contribution of temperature fluctuations it is necessary to combine the contribution of different effects. These will include thermo-optic noise as well as Brownian coating noise and many more concerned not just with the thermal fluctuations within the optical coatings, but within the substrates themselves. One of high importance is Brownian coating noise, limiting the detector sensitivity, which is the effect this thesis will mainly concentrate on by investigating the possibility of improvement on mechanical loss values which have not yet reached any fundamental limits.

An alternative can be observed through the Fluctuation Dissipation Theorem, where it is established that the power spectral density is proportional to the temperature. This is the reason multiple detectors are to operate at cryogenic temperatures. Throughout the experiments which are to be described in the following chapters, the optical coatings analysed and characterised are intended for room temperature gravitational wave detectors.

Chapter 3

Coating development and characterisation

3.1 Introduction

Chapter 2 establishes the motivation for the experimental investigations, primarily related to thermally driven displacement noise. In this chapter, those principles and theories will be connected to various experimental setups used to verify or estimate different material properties. The main objective will be the deposition of optical coatings, which could be used as highly reflective layers on test masses, as well as the estimation of mechanical loss associated with the optical coatings.

In order to estimate the mechanical dissipation of optical coatings, the vibrational modes of the coated resonator substrates are excited, and the natural decay of these excitations are monitored. By comparing the uncoated mechanical loss measurements with ones acquired post deposition, the value of the coating loss can be calculated.

Substrates used throughout these experiments have gone through several stages of heat treatment, as in some cases it was observed to maximise the optical properties of the coating material, $i.e.$ lowering in ϕ, decrease min absorption, $etc.$ Compositional and characteristic analysis has been performed to inspect the deposited material as well as its compatibility with being used as a highly reflective optical coating for interferometric test masses.

3.2 Methods

3.2.1 Coatings

There are many deposition technologies that can be utilised for the formation of materials. The alternating structure of optical coatings on the surface of gravitational wave test masses requires thin films therefore such deposition methods are of high importance. A thin film forms a layer in the thickness range from several nanometres to about ten micrometers.

In general thin film deposition techniques can be categorised as either purely physical, for example, evaporative methods, or purely chemical, such as liquid-phase chemical processes. Alternatively multiple processes rely on a combination of both processes as it is in the case of glow discharges or reactive sputtering.

Thin film deposition techniques can be categorised in four groups [119]:

- Evaporative methods, such as Molecular Beam Epitaxy (MBE);

- Glow discharge processes, such as Magnetron sputtering and Ion-beam sputtering;

- Gas phase chemical processes, such as Chemical vapour deposition;

- Liquid phase chemical processes, such as electroplating.

The choice of deposition technique is correlated with the desired material characteristics of the deposited thin film. Furthermore, the discrepancy between thin films and bulk materials can appear as differences in the morphology, structure and properties in comparison to bulk properties.

Three deposition techniques are considered here, where the main utilised method is a glow discharge process represented by a combination of ion-beam sputtering with the usage of a microwave ECR source. The additional two approaches (Magnetron sputtering and Ion-beam deposition using a DC/Kaufman source) were utilised at collaborating institutions, aiming to directly compare elevated temperature depositions of tantala coatings.

Ion beam deposition

Ion-beam sputtering (IBS) deposition is a form of physical vapour deposition. Gas is injected through a source which causes the ionisation of the atomic or molecular species. The ions get extracted and accelerated towards a target which through transfer of momentum cause the sputtering of the target material. These atoms and molecules then adhere onto a substrate thus resulting in a thin film on the surface of the substrate (Fig. 3.1).

In universal terms coatings, developed by the use of IBS, are achieved at room temperature, although the substrates may reach up to a temperature of 100° C. Such a deposition system is useful for cases where the targets used may be solely consisting of a metallic element but oxygen or other gas can be used to generate a mix of elements.

Ion-beam sputtering deposition is the technique of choice for depositions of highly reflective optical coatings due to the fact that during such deposition the atoms impinging the substrate have higher kinetic energy which contributes to the growth of a thin film in a more densely packed amorphous structure [120]. Additionally, ion-beam deposition produces compact and smooth films, and is currently the only technique that can meet the scatter loss requirements of gravitational wave detectors [59].

Kaufman DC/RF source   The general method employed for the generation of an ion-beam is the use of a Kaufman source. Figure 3.1 shows a schematic representation of different ion-beam/plasma sources. The basis of operation consists of the emission of electrons from a hot cathode colliding with gas atoms, resulting in the production of positive ions and electrons [121]. The shape of the generated beam is dependent on many factors, including grid separation, plasma density, *etc.*, which can result in an alternating beam shape and current density. Furthermore, the use of a Kaufman source has an additional drawback due to the hot filament of the source which requires frequent maintenance. In order to avoid the use of filaments for plasma generation two separate alternatives have been developed - inductively coupled RF type source and microwave ECR source. For the plasma generation using a RF source, RF power with frequency 13.56 MHz is fed through a coil (flat or solenoid) which is embedded in a dielectric shield. Due to the generated field electrons experience oscillations which in turn collide with gas atoms and thus form a plasma [121].

The current gravitational wave mirrors are coated at LMA, Laboratoire des Materiáux Avancés, where their setup consists of two chambers [123]. Chamber 1 contains the conventional Kaufman source, whereas chamber 2 is equipped by 2 radio frequency sources for co-sputtering. They are currently the only corporation which has the ability to perform high quality highly reflective coatings on substrates large enough for gravitational wave detectors.

Microwave ECR source   A key difference between an RF source and an ECR source is the presence of a screen grid onto the source, which is not present in the case of an ECR source. All of the coatings which are going to be accounted for in this thesis were formed by ion-beam deposition however the particular systems used were different to common IBS systems. The novel IBS apparatus uses a single electron cyclotron resonance (ECR) source, developed by Polygon Physics
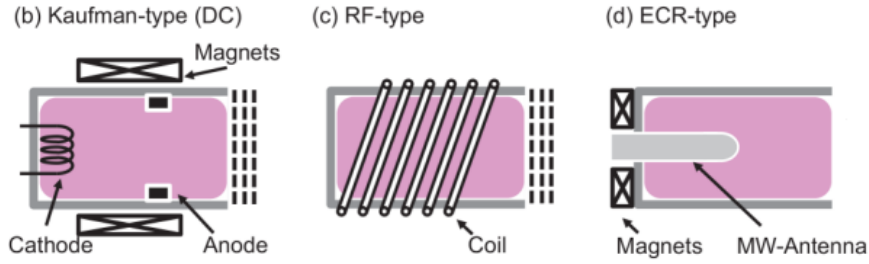
Figure 3.1: Ion beam deposition processes. Representation of ion beam deposition processes utilising different ion/plasma sources. Generally, the most commonly utilised in industry are the hot filament Kaufman type (DC type) and inductively coupled RF-type of plasma generation. The grid-less nature of the ECR-type has potential for the production of thin films with minimum contamination. Images taken from [122].

in Grenoble, France [124].

As mentioned, one main difference evident in the ECR source is the lack of extraction grids, present in RF-IBS sources. Instead, through the usage of magnets and electrostatic potentials, ions are driven out of the plasma cavity. Magnets are placed around the plasma cavity, generating a magnetic field, whereas the electromagnetic field is generated in microwaves introduced into the cavity.

This ECR source contains a small $\lambda/4$ microwave cavity tuned to 2.45 GHz, which can operate for a range of extraction potentials ranging from 0 to 20 kV. Argon gas is injected into the extraction cavity and as the cavity itself would be held at a positive potential , would lead to the repelling of the atoms through a small aperture. The atoms are then directed through the focus plate, and depending on the voltage at which the plate is held, the shape of the beam can be controlled. These atoms are then focused in a near-parallel beam, and electrostatic optics are used to control the focus of the beam.

Such an IBS system is considered cleaner than commercially operated processes. The advantages of the use of this ECR source include the fact that this component is grid-less and also allows a range of extraction potentials ranging from 0 to 20 kV, in comparison to RF-IBS, which only allows for potentials of up to 2 kV [125]. However, in comparison with RF standard IBS systems, the deposition rate is considerably slower within a range of 0.2 - 0.5 mA which increases the duration of coating runs in order to achieve similar thicknesses to RF sources.

Magnetron sputtering

Magnetron sputtering is a beam sputtering process developed in the 1970s. The basic sputtering process of operation consists of the "bombardment of the target" with ions. These ions are generated in a glow discharge plasma, where once it reaches the target surface the target material gets stripped and forms a coating on the substrate surface. Magnetron sputtering is further enhanced through the use of magnetic fields, which constrain the motion of the secondary electrons in the vicinity of the target [126]. The magnets arrangement is such that the position of one pole is at the central axis of the target, whereas the second one is composed of multiple magnets surrounding the outer edges of the target. The use of these magnetic fields traps these electrons, hence increasing the probability of an ionising electron-atom collision. This results in a denser plasma, which in turn increases the coating deposition rate.

3.2.2 Characterisation techniques

All the characterisation techniques which are covered in the following sections have been performed on two types of substrates, both of which have been simultaneously coated. First type is a JGS-1 disc, made of fused silica and mainly exploited as initial characterisation. Second type of substrate is a fused silica cantilever with varying thickness, which was utilised as the primary substrate. Further information regarding the production and treatment of the two substrates is to be provided in section 3.3.1.

Thickness

Profilometry An indirect thin film estimation was performed on coated substrates by using Dektak 3T which is a surface profilometer capable of estimating thin film thickness in the range from 0.001 μm to 131 μm. Measurements are obtained through electromagnetically driven diamond-tipped stylus scanning over the surface of the sample. The detected electrical signals are converted through a Linear Variable Differential transformer producing information about the surface variation of the sample. This is solely performed on JGS-1 witness pieces, as it involves direct contact, which may lead to scratching of the surface, as well as regions which have remained uncoated. This way the apparatus evaluates the difference in vertical amplitude and hence gives a corresponding film thickness. This technique is considerable inadequate as the thickness of the coating on the surface of the witness piece and cantilever need not be the same. This method is mainly utilised for samples prepared in the smaller coating system (Section 3.3.2) as the uniformity of coating depended on repeatability of deposition as well as position with respect to beam and target.

Ellipsometry Coating thickness measurements were performed using a Sentech SE850 spectroscopic ellipsometer. This non-destructive optical technique simultaneously characterises thin film thickness as well as refractive indices. The system operates through the emission of polarised light in the UV-Vis-NIR spectral ranges at a known incidence angle and the measured quantities are the ellipsometric angles which specify the change in amplitude and phase. Through angle measurements and curve fitting models, the thickness of a thin film, in this case a single layer, is therefore obtained. For the samples characterised within this thesis, the wavelength range varied from 320 to 790 nm, and the same incident angle of 70° was used, where optimal angles for maximum possible sensitivity are expected in the range 55 and 70°.

Cross section SEM The final technique for measuring the thickness of the optical coatings is through the use of a SEM scanning electron microscope. The microscope was a Hitachi Cold Cathode field Emission electro microscope consisting of a backscatter detector, inner dispersive X-ray analysis detector and secondary electron detector. For the performance of the analysis, electrons, which are generated by a cathode, are focused/accelarated by applied electric fields. The interaction of this electron beam with the atoms on the surface of the sample results in the generation of secondary electrons, backscattered electrons and X-ray photons. The energy of the secondary electrons is dependant on the accelerating voltage and can be between 1 and 13000 eV.This in turn presents magnified images with a resolution of up to 1.5 nm. The composition can be assessed from observing the backscatter electrons.

This method requires the breaking of the cantilever in order to perform multiple measurements of the thin film thickness and additionally evaluate the uniformity of the coating. Since this method involves the destruction of the samples, it was chosen as a final evaluation due to the fact that post measurements the remaining pieces are unusable. The main goal was to obtain an accurate reading of the film thickness on the surface of the cantilever, due to poor coating uniformity, which would not allow for a correlation between film thickness on witness sample and cantilever, hence necessitating a direct measurement on the cantilever surface.

Furthermore, at starting point of coating depositions using ECR sources, compositional analysis was performed to investigate the possibility of contamination during deposition and therefore how to overcome this problem.

Elemental composition

In order to successfully deduce the elemental composition of the deposited films, compositional analysis is required, which also enables a contamination investigation. Additionally, as multiple materials would be added as dopants to create

mixed material coatings, the ratio of different elements needs monitored to correctly investigate the newly developed materials. The targets utilised within the deposition processes did not have a fixed position within the coating chambers, which further enables a possible discrepancy of the coatings.

Electron probe microanalyser   The compositional analysis of the coating is done with a JXA-8530F electron probe microanalyser (EPMA) consisting of a Schotty field emission electron gun, enhancing the analysis capability [127]. EPMA is a non-destructive method for characterising chemical compositions of solid materials. A high energy beam of electrons is used to generate X-ray characteristics of elements within an analytical area of 0.1 μm across in size. The chemical composition of the sample is determined through comparison of the X-ray intensity from provided standards with the measured specimen whilst correcting for absorption and fluorescence effects. The electron beam current varies from 10 nA to 100 nA, providing a greater precision over standard scanning electron microscope (SEM) measurements.

Energy Dispersive X-ray Spectroscopy   Electron microscopes have the ability to provide compositional quantification of materials through the addition of an X-ray energy dispersive spectrum detector in an analytical electron microscope. Within the microscope, high energy electrons are generated in the electron gun. These electrons can ionise atoms within the sample leading to the ejection of an inner shell electron. Subsequently, this ejected electron is replaced by a higher energy electron, which has lost a portion of its energy through the emission of an X-ray photon. The released photon contains energies characteristic of specific electronic transitions within the target atoms, therefore the X-ray emitted can be recorded as an X-ray energy dispersive spectrum (EDS) which contains elemental information about the sample. The different X-ray wavelength emissions correspond to different atomic structures of the elements and can be used as a identification of the elements present in the sample. Through the analysis of the areas under the X-ray emission peaks, either by using Cliff-Lorimer k-factor method [128] or the Watanabe-Williams ξ-factor method [129], a quantitative measure of the composition can be obtained.

The apparatus utilised within the characterisations of the coatings composition is a Hitachi TM1000 Tabletop Microscope, with an Oxford Instruments EDS detector attachment. Elements heavier than sodium were measured, as Na imposes a limitation on the sensitivity of the detector [130]. Therefore it was unable to measure the oxygen content and it could only provide the composition of the heavier elements. However, the Ar content within the coatings was measurable as it was a key component within the thin film depositions. As a result, the elemental ratio between base and dopant could be obtained, however, it cannot

be determined whether deposited coating is an oxide or a metal composite, and further investigations are required to quantify the oxygen contents within the sample.

Optical characterisation

Reflectance and transmission A photon RT UV-Vis-IR spectrophotometer is used in the characterisation of optical properties of coatings. This instrument is adopted for the direct measurement of reflectance and transmittance of the material as well as the thickness of coating layer. For the coatings within this thesis, the measurements were performed on JGS-1 samples, which were utilized as witness samples throughout the deposition processes/runs. The quantities necessary include the reflectance and transmission of optical coatings at a selected wavelength range, where the ranges can be from 380 - 1700 nm up to 190 - 5200 nm. The optical coatings for gravitational wave detectors are required to be highly reflective hence a condition implying a minimum transmission emerges. The system is calibrated through transmission (without sample) and the absolute transmission of the sample is calculated as the ratio between sample transmitted intensity and calibrated blank transmission (100%). If one assumes no optical losses, energy conservation implies $1 - R = T$, where R is the reflectance and T is the transmittance, and can both be presented as a function of the real and imaginary parts of the complex refractive index. Once the reflectance and transmittance spectra are obtained, model fitting allows for the estimation of the refractive index and extinction coefficient, associated with the coating, as well as the thickness of the thin film.

The procedure at which a spectrophotometer operates includes the measurement of the intensity of electromagnetic energy at each wavelength. Electromagnetic energy, which is collected from the sample is separated into its primary components through a grating. The separate light components are then focused onto an array detector where each intensity measurement corresponds to a pixel from the array. The obtained data is further analysed providing a spectrum displaying the intensity at each wavelength.

Optical absorption The optical requirement for coatings for gravitational wave mirrors insists not just on materials characterised by low mechanical dissipation, required to limit light scattering, but also on highly reflective surfaces. Hence an additional requirement for the materials is low optical absorption, in addition to reduced scattering of light. All the optical absorption characterisation was performed at the University of Glasgow through the use of a technique known as Photo-thermal Common-path Interferometer (PCI). The PCI technique, which is a modification of photo-thermal spectroscopy has largely been developed at the University of Stanford. The concept of this method is based on a pump/probe

technique where a probe beam with a low power is used to establish the heating effect of an absorbed pump. A focused high power pump beam is then used for establishing the modulations of the heating effect at specific frequencies. The probe profile is distorted due to $\frac{dn}{dT}$, causing an alteration from the Gaussian beam profile due to interference [131]. The maximum of this interference is correlated to the absorption coefficient, thus providing the measurement of the optical absorption. Current gravitational wave detectors operate at a wavelength of 1064 nm, though alternative wavelengths at 1550 nm and 2 μm are considered for future detector upgrades. Therefore, the majority of measurements were estimated at these three wavelengths.

Mechanical

Young's modulus Young's modulus is a quantity required as known for the qualification of mechanical properties of materials used as thin film coatings. It can be expressed as the relation between the stress and strain, within the material. The Young's modulus of different materials, utilised in gravitational wave research, has been widely studied, however within this thesis, pre-established values for said parameter cannot be used. The alternative coating apparatus, in addition to the deposition setup may result in a variation in the quantity, hence direct estimation of Young's modulus is necessary. The acquisition of this parameter is performed by using a Harrison Triboscope retrofitted to a digital instruments Multimode AFM with Nano-scope 3 controller.

The estimations are obtained through the use of an indenter in contact with material surface. The indentation left from the non-ideally conical tip is analysed thus providing an approximation of the ratio of the nominal hardness/reduced Young's modulus as well as the ratio of elastic work/total work. This ratio corresponds to different values depending on the shape of the conical tip of the indenter [132].

Using this information, as well as defining the nominal hardness as the ratio of the maximum indentation load per cross section area of the indenter, enable the calculation of Young's modulus. Measurements vary slightly due to non-uniformity of coating hence a reasonable mean value is used.

Mechanical loss Mechanical loss can be defined as the fraction of energy dissipated in an oscillating system per cycle of motion. Oscillations within the system are induced through excitation of the eigenfrequencies which are determined depending on the geometry of the substrate. The evaluation of the mechanical loss can be achieved through the measurement of the amplitude of oscillation during decay. This takes the form

$$A(\omega_0) = A_0 \exp\left(-\frac{\phi(\omega_0)\,\omega_0 t}{2}\right), \tag{3.1}$$

where ω_0 is the angular frequency of a freely resonating eigenmode, A is the amplitude at time t, and A_0 is respectively the amplitude at time t=0. Through the measurement of the time τ, time it takes the amplitude to decay to $\frac{1}{e}A_0$, the mechanical loss can be determined.

Cantilevers have both bending and torsional modes. The bending modes of a cantilever of frequency f are [133]

$$f_n = (k_n L)^2 \frac{t_s}{4\pi\sqrt{3}L^2}\sqrt{\left(\frac{Y}{\rho}\right)}, \tag{3.2}$$

where t_s is the thickness of the substrate ribbon with length L, Y and ρ are the Young's modulus and density of material respectively. $(k_n L)$ is a mode-dependent constant which takes the values of 1.875, 4.694, 7.853, 10.996 and 14.137 for modes one to five. For cases where n is larger than 5, the constant can be written as $k_n L = \frac{\pi}{2}(2n-1)$. The process of measurement of mechanical loss requires the excitation of these modes.

The main goal is determining the mechanical loss of the optical coatings. This is evaluated through the measurement of both coated and uncoated stages. Prior to a coating deposition on the surface of the cantilever, the mechanical loss of said cantilever is measured. After a coating has been deposited the mechanical loss of the sample is again measured. As the amplitude caused by the excitation of vibration decays, energy is lost which is a combination of energy lost in the substrate and the coating

$$E_{\text{lost,total}} = E_{\text{lost,substrate}} + E_{\text{lost,coating}}. \tag{3.3}$$

By dividing through $2\pi E_{\text{stored,total}}$, an expression is obtained for the mechanical loss of a coated cantilever

$$\phi_{\text{total}} = \frac{E_{\text{lost,subsrate}}}{2\pi E_{\text{stored,total}}} + \frac{E_{\text{lost,coating}}}{2\pi E_{\text{stored,total}}}. \tag{3.4}$$

Since the thickness of the coating is significantly thinner than the thickness of the cantilever ribbon, it can be approximated that $E_{\text{stored,substrate}} \approx E_{\text{stored,total}}$. Equation (3.4) becomes

$$\phi_{\text{total}} \simeq \phi_{\text{substrate}} + \frac{E_{\text{lost,coating}}}{2\pi E_{\text{stored,substrate}}}. \tag{3.5}$$

The term consisting of the energy ratios is equivalent to ϕ_{coating} multiplied by the ratio of energy stored in the coating to energy stored in the cantilever. Hence,

$$\phi_{\text{total}} \simeq \phi_{\text{substrate}} + \frac{E_{\text{stored,coating}}}{E_{\text{stored,substrate}}} \phi_{\text{coating}}. \tag{3.6}$$

This enables the estimation of the mechanical loss of the coating, through the measurements of uncoated and coated samples. The expression can be written as,

$$\phi_{\text{coating}} \simeq \frac{E_{\text{stored,substrate}}}{E_{\text{stored,coating}}} \left(\phi_{\text{total}} - \phi_{\text{substrate}} \right). \tag{3.7}$$

In order to appropriately evaluate Eq.(3.7), an expression for the ratio term is needed. In order to define such a relation consider a beam of thickness t_s and length L and width y with a thin coating of thickness t_c [Fig. 3.2]. The beam is bent at an angle θ, and the radius of the arc of the circle is defined as R. The elastic strain energy is stored in both the substrate and the coating. The elastic energy stored within the coating can be shown to be,

$$E_c = \frac{Y_c t_c y}{2L} \Delta L^2, \tag{3.8}$$

where Y_c is the Young's modulus of the coating and ΔL is the change in length and it can be shown that it is equal to $\frac{1}{2} t_s \theta$ [134].

The energy stored within the beam substrate can be estimated through the approximation stating that when the shorter half of the beam is compressed, its stored energy equals to that stored in the longer half when it is under tension. Therefore it can be shown that,

$$dE = \frac{Y_s y \Delta L^2}{2L} dr, \tag{3.9}$$

where ΔL can be expressed as $\Delta L = (r - R)\theta$ and Y_s is the Young's modulus of the substrate material.

Evaluating for half of the detected beam whilst substituting in for the expression for ΔL gives,
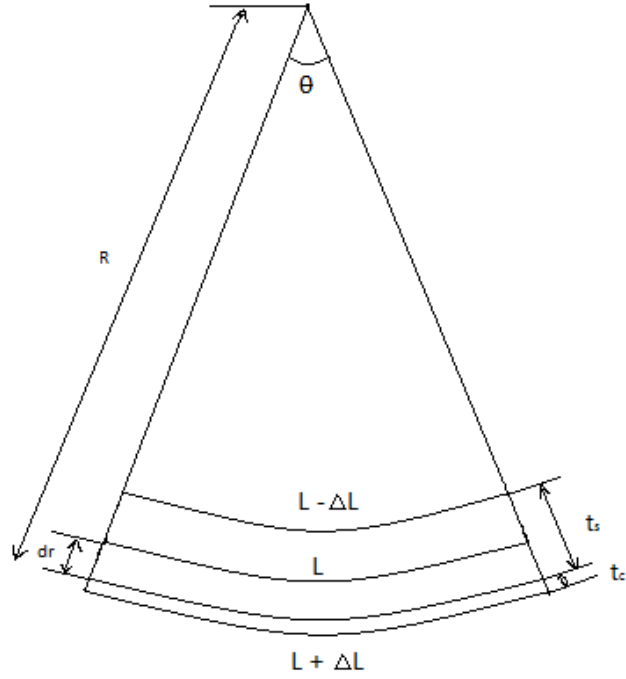
Figure 3.2: A beam of width y and thickness t_s with a thin coating of thickness t_c applied to one face. The beam is bent into the arc of a circle of radius R. Original figure from [135].

$$\frac{E_s}{2} = \int_{R}^{R+\frac{t_s}{2}} \frac{Y_s y \theta^2}{2L}(r-R)^2 dr = \frac{1}{48}\frac{Y_s y \theta^2 t_s^3}{L}. \tag{3.10}$$

Combining Eq.(3.8) and (3.10) leads to the expression,

$$\frac{E_s}{E_c} = \frac{Y_s t_s}{3Y_c t_c}. \tag{3.11}$$

Substituting Eq.(3.11) into (3.7) gives,

$$\phi_{\text{coating}} = \frac{Y_s t_s}{3Y_c t_c}\left(\phi_{\text{total}} - \phi_{\text{substrate}}\right). \tag{3.12}$$

3.3 Experimental setup and methods

3.3.1 Substrate preparation

The choice of substrate is deduced based on appropriateness towards the coating material measured. Different materials can be used depending on the measurement conditions for example. A requirement for these samples is extremely low mechanical loss which allows a sufficient portion of the total energy stored within the resonant modes of the sample to be stored in the coating. Hence, in this case SiO_2 was chosen due to its low mechanical dissipation at room temperature measurements ≈ 1 - 5×10^{-6} rad. Silicon on the other hand is the choice for operation at cryogenic temperatures due to its ultra low losses at low temperatures. The concept of a cantilever as a substrate was proposed by Berry and Pritchett in 1975 [104]. Nowadays a cantilever consists of two individual pieces, a ribbon and a clamping block, which are subsequently welded together creating the cantilever standard. In order to assemble these substrates, a sample preparation is performed. Silica discs of diameter 76.2 mm in diameter and thickness varying between 80 - 180 μm are diced into rectangular pieces with dimensions 45 mm x 5 mm, producing ribbon sections. Similarly, for the other component of a cantilever, silica blocks are used with dimensions 12 mm x 12 mm x 3 mm. Each of the ribbons are individually connected onto a clamping block through an oxyhydrogen flame-welding process, with the use of an AQUARIUS 200 welding apparatus. After welding, each of the cantilevers is cleaned through immersion in a boiling solution of hydrogen peroxide (H_2O_2, 30% w/w H_2O) and potassium hydroxide (KOH). The reasoning behind the choice of these cleaning solutions is due to the fact that both are echants which clean the surface of the sample as well as remove residual material remnant from the welding process. Due to the non-repeatability of the welding process however, the lengths of the cantilevers vary. In some cases the edges of the cantilever are flame polished. This is done as a consequence of the chopping of the silica disc, as it leaves uneven edges which obstruct loss measurements. Depending on the thickness of the ribbon it can both have a positive and negative contribution. Post cleaning all samples are annealed on a Carbolite CSF 1200 oven, utilising an Eurotherm 808 temperature controller, at 950° C for 5 hours.

The use of a clamping block originates due to the fragility of the substrates. The block is used as a clamping component hence reducing the slip-stick losses associated with the clamp. Furthermore, the employment of a clamping block simplifies the handing of the samples reducing the risk of breaking, due to the fragility of the ribbon component. Whilst the silica block is clamped in a stainless steel clamp, the ribbon is electrostatically driven in attempt to excite resonance which then decays uninterrupted whilst mechanical dissipation measurements are executed. According to Quinn [136], the use of a clamping block with thickness

exceeding the ribbon thickness by a large factor, ensure that the bending points occur outwith the clamp.

In general, the losses observed on uncoated silica cantilevers range between 9×10^{-7} - 6×10^{-6} depending on the quality of the material as well as the surface roughness.

For gravitational wave detectors operating at cryogenic temperatures, the material of choice for the cantilevers is silicon due to its optical properties at very low temperatures, *i.e* low optical absorption and low mechanical dissipation. Such samples are not covered within this thesis as all the depositions and analysis performed here are on silica samples.

Heat treatment is a procedure used in cases for uncoated and coated samples. For each of these cases a different argumentation stands behind the annealing. All heat treatments were performed in a Carbolite CSF 1200 oven, and the samples were covered by a silica disc close to the surface of the cantilever to minimise particles on the sample surfaces. In cases of uncoated samples, heat treatment involves annealing at 950°C for five hours. The temperature value and the duration of 'baking' are based on the substrate material as in this case the values presented are used for treating silica. 950°C is chosen as an optimum temperature, due to silica's melting temperature of ≈ 1000°C. Multiple durations have been tested, from annealing for one hour up to annealing for 24 hours. The pre-deposition heat treatment reduces the possibility of contaminants upon the substrate surface, hence once a coating is deposited, there would not be defects due to dust particles, *etc*. The period of five hours was the optimum time for which substrates were annealed, since ϕ_{uncoated} measurements were more consistent and the substrates exhibited lower loss.

3.3.2   Deposition

Within the University of Strathclyde there are two ion-beam deposition systems and both contributed to the production of the optical coatings covered in this thesis. The prototype IBS system (Fig. 3.3) is contained within a 400 mm in diameter cylinder where the ionised beam hits a target at approximately 45 °, in respect to which the substrates are placed at an angle of 60 °, onto a substrate holder. The distance from the ground plate to the target position is ≈ 125 mm, and the separation between target and substrate is ≈ 85 mm. The substrate holder is a copper holder which contains a ceramic heater and furthermore has a PT1000 resistor connected, used to monitor the temperature at which the samples are treated. The addition of the heating element implements higher temperature depositions which in some cases affects the optical properties of the coatings in a positive manner. A maximum deposition temperature successfully achieved was 500° C, where the stability of the coating process was not sufficiently stable,

hence further depositions were limited to temperatures up to 400° C.

The second ECR IBS system (Fig. 3.4) within the University of Strathclyde differs from the prototype system, yet it still employs the same ion source but consists of multiple ion guns. The shape of the chamber is modified from the previous cylindrical form and takes the shape of a cube with dimensions 600 ×600 × 600 mm (length, height and depth), with 2×2 ion guns connected on opposing walls. The substrates, which are to be coated are mounted on a circular rotational stage on the inside of the door of the chamber. Due to the introduction of a rotational motion, the coatings produced are more uniform in comparison to the prototype system. Furthermore, the dimensions of the vacuum chamber, enable the use of multiple targets through a single deposition process. In order to compensate for discharging during deposition, one of the ECR sources is used as an electron gun, prior to the purchase and instalment of neutralizing components. The processes are still performed under high vacuum ($approx$ 10^{-6} mbar), but unlike the initial system, it is not possible to perform elevated temperature depositions. Schematics of both structures are presented in Figures 3.3 and 3.4. The possibility of multiple target materials allows for a more controlled doping of materials, since in the single ion gun chamber, the coating composition is unverifiable prior to the completion of the process. Additional characterisation of coatings produced by both systems is also performed to account for repeatability and uniformity.

IBS makes higher quality films than magnetron sputtering but ECR IBS is not a common technique for coating. It was shown to produce a-Si (amorphous silicon) with low optical absorption [137] and it is a promising technique to improve the quality of coatings, hence the employment of this development technique.

Several alternative techniques have been utilised in the goal of estimating the thickness of the coatings deposited on the cantilevers. These methods include both non-destructive and destructive approaches. The reason multiple methods are used is to decrease the uncertainty in thickness estimation. It is known that $t_c \ll t_s$, where t_c is the thickness of the coating and t_s is the thickness of the substrate. As the thickness of the coating is in the order of nanometres having additional estimations allow for a more definite value of the thickness. These techniques use direct and indirect measurements, and the final value is the mean of all the measurements. These techniques include ellipsometry measurements, based on reflection, Dektak measurements, through evaluation of witness samples and the invasive cross section SEM measurement, which requires the breaking of the substrate to enable estimations of coating thickness as well as thin film uniformity. All of the mentioned techniques are covered in Section 3.2.2.
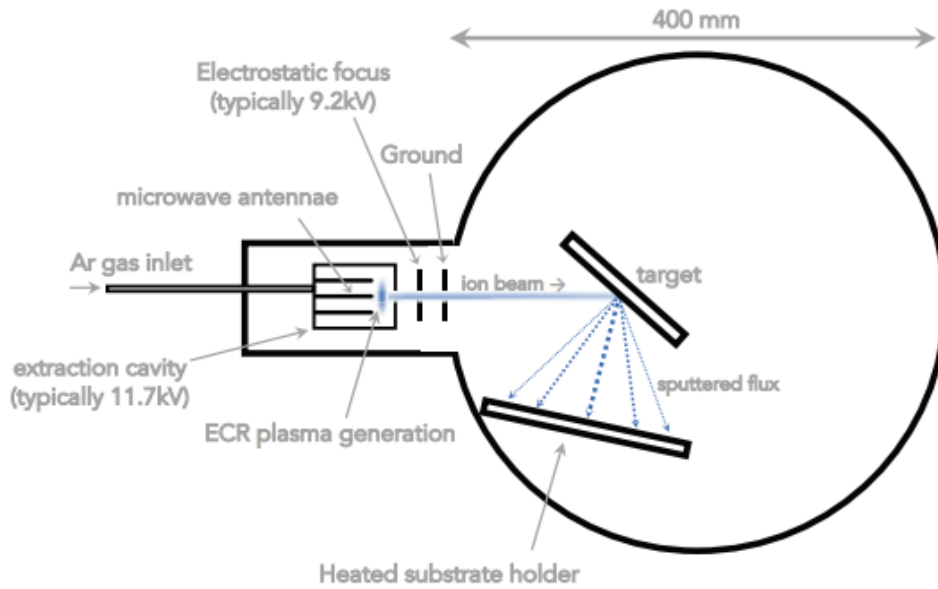
Figure 3.3: Prototype ECR system. Image shows a schematic representation of the components and geometry of the prototype ECR system. Images property of Dr. Ross Birney.

3.3.3 Post-deposition thermal treatment

For coated samples, the verification of heat treatment differs slightly, and through the use of reduced density function (RDF) analysis a correlation is established between the mechanical dissipation and distribution of atom-atom distances [135]. The observations indicated that as the post deposition heat treatment is increased, the distribution of the bond lengths decreased and in turn the mechanical dissipation at room temperature decreased [138]. Previous studies have shown that annealing at a temperature of 600°C (for example Ta_2O_5) has an apparent effect on the atomic structure of the material, larger than achieved through annealing at lower temperatures (300°C, 400°C). This heat treatment enables a further reduction of homogeneity which can be explained as the structure beginning to organise into regions of higher order [139]. Post deposition heat treatment has proven experimentally as well as theoretically its contribution in reducing the coating mechanical loss.

3.3.4 Mechanical loss measurements

This subsection will contain information about the apparatus used for mechanical loss estimations as well as a verification of its utilisation. Figure 3.5 shows the
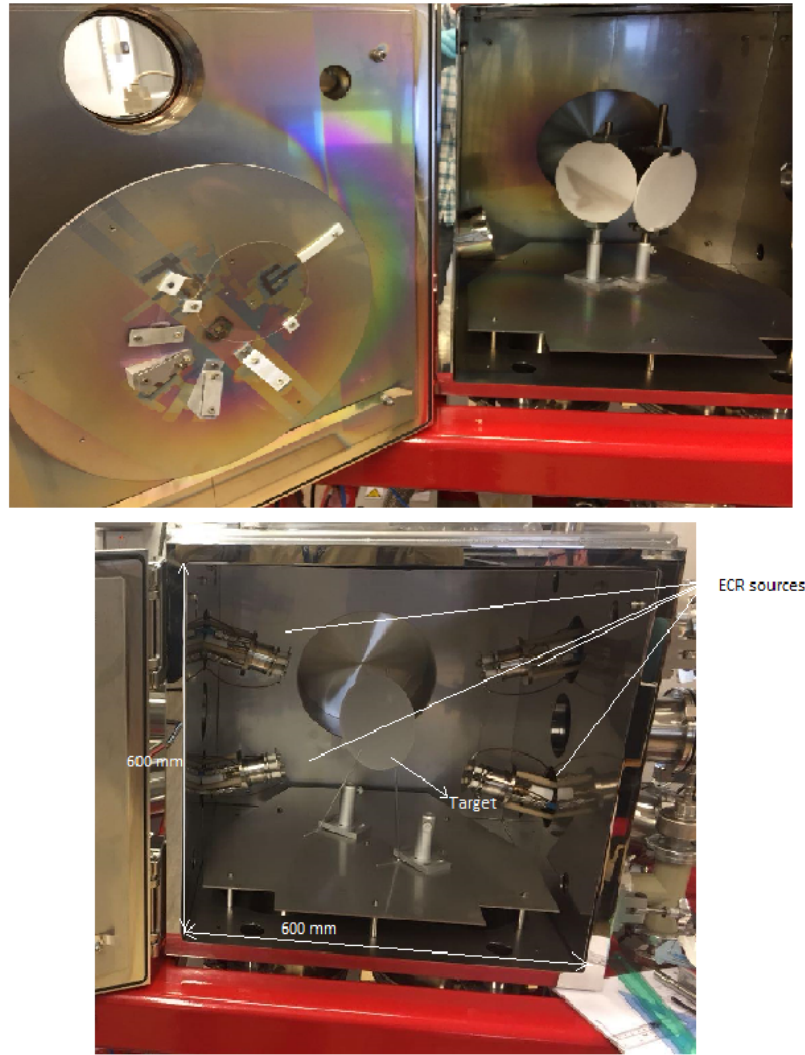
Figure 3.4: Cuboid chamber IBS system, consisting of four ECR sources. The left image includes a visual representation of the coating chamber and substrate holder. The samples are mounted on a circular rotational stage operated by an external motor. The right image shows the setup within the coating chamber with dimensions 600 ×600 × 600 mm. The ion sources are mounted on opposing walls and are at an angle to one another to allow for the simultaneous deposition of different materials.

design of the apparatus used for measurements of the mechanical loss factors of the bending modes of the cantilevers.

A cantilever is clamped to a stainless steel clamp inside a vacuum chamber.
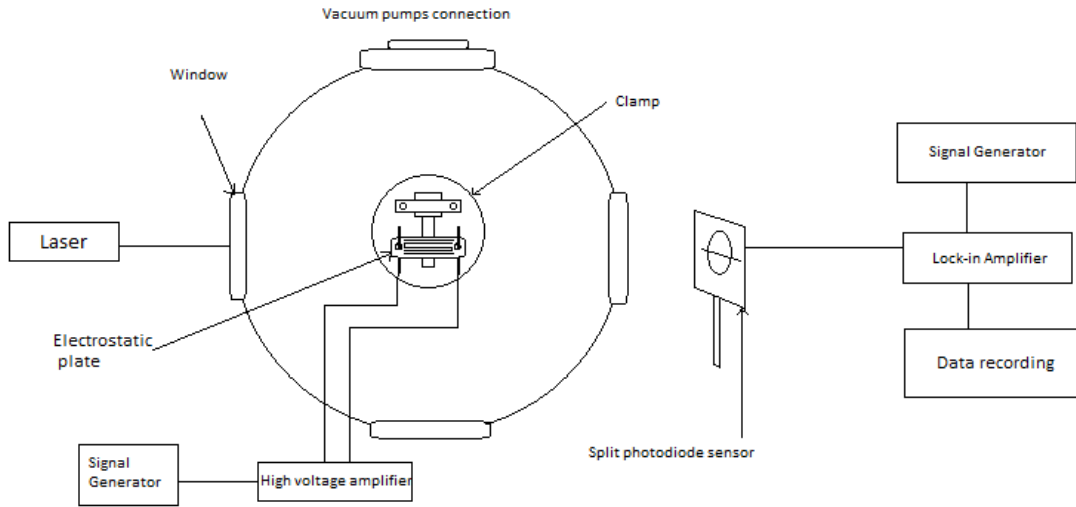
Figure 3.5: Schematic representation of setup used for measuring the mechanical loss of silica cantilever resonators. A silica cantilever is clamped onto a stainless steel clamp. An electrostatic drive plate is used to excite the cantilever bending modes. This excitation force acts on the sample, resulting in the polarisation of the atoms in the cantilever. The split photodiode sensor measures the ring-down amplitude of the excitation by tracking the motion of the cantilever shadow, which is aligned with the split of the photodiode.

The clamp enables the easier handling of the samples, as well as a reduction of slip-stick losses, however the tightness of the clamp is reflective on the measurements. If the cantilever has been overly tightened there is a high possibility of the clamping block breaking. If the clamp is too loose, this enables the movement of the sample and energy due to the oscillations may be dissipated through the clamping surface. After the clamping of the cantilever has been successful, the component is placed inside a vacuum tank and evacuated to a high vacuum state. A Triboscroll Dry Vacuum pump is used to reduce the pressure within the vacuum chamber, where the pressure is monitored using a Grainlike-Phillips Vacuum Gauge controller. Once the pressure within the chamber had reached values ≈ 1 mbar, the vacuum chamber is further pumped down using a Turbo-vac 450i turbo pump. The use of said turbo pump requires pressures lower than atmospheric value, hence it was necessary to employ both pumping systems. With the use of the turbo pump, vacuum chamber is evacuated to a pressure $\approx 2 \times 10^{-5}$ mbar. of An electrostatic drive plate, placed in close proximity to the cantilever surface, is used to excite the bending modes of the cantilever as an oscillating high voltage signal is applied at the frequency of the resonant mode 3.7. The excitation force acts on the cantilever, leading to the polarisation of the atoms in the cantilever.
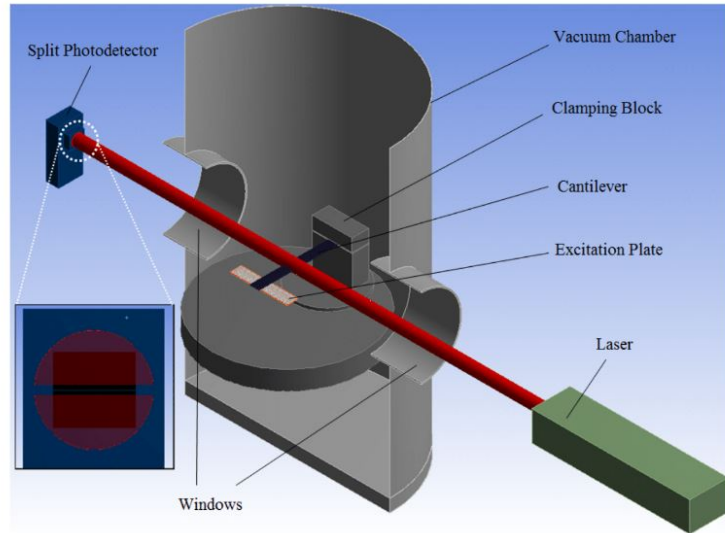
Figure 3.6: Visual representation of 3.5. The image shows the geometry of the individual components , including the path of the laser light. Image reprinted from [140].

The ring-down amplitude is recorded with the use of a shadow sensors technique. This method traces the motion of the shadow of the cantilever as the edge of it is illuminated by a laser beam. The equilibrium point of the shadow is aligned with the split between the two photodiodes. As the cantilever oscillates, the shadow moves from its equilibrium position. The signals the photodiodes are subtracted and amplified. A Stanford Research systems SR560 Low Noise Voltage Preamplifier is used to multiply the measured signal with a generated sine wave[141]. Additionally, lock in amplifiers use a technique known as phase selective detection, through the use of which very small signals can be detected and measured, even in cases where the level of noise exceeds overwhelmingly the power of the signal.

The sum of the sinusoidal waves can be deconstructed enabling the recording of the frequencies of excitation. A high voltage signal ±5 Hz around the mode frequency was sent through the electrostatic plate, leading to the detection of a peak in amplitude caused by the excitation. As the peak frequency is deduced, voltage signal is dropped to 0 V and the resonance is left to freely decay. The mechanical dissipation is therefore evaluated from the exponential fit of the amplitude decay with respect to time 3.9.

87
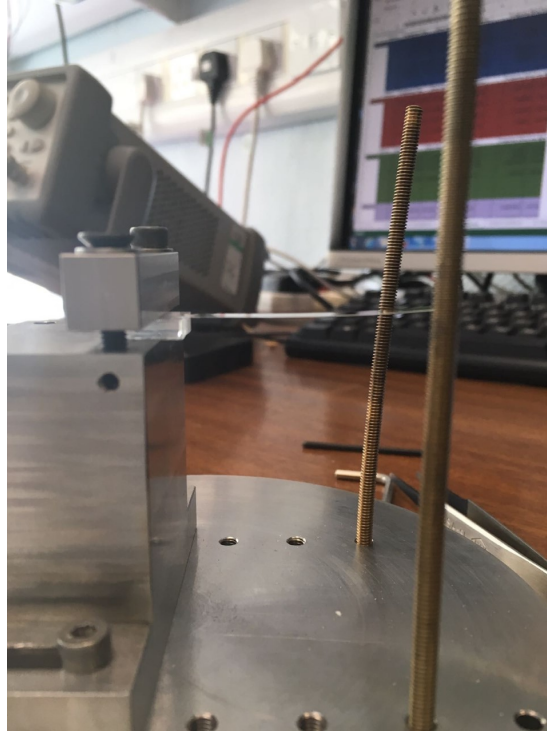
Figure 3.7: Image of stainless steel clamp utilised in the measurement of mechanical loss. The clamping block of the cantilever sample was placed under a smaller steel piece, attached to the clamp with two screws. By tightening the screws, the sample was positioned and levelled within the clamp. Two copper rods were placed accordingly to the length of the cantilever ribbon. The electrostatic plate was fixed on the two rods, at an approximate distance of 2-3 mm to the ribbon.

3.4 Conclusions

Current gravitational wave detectors have been limited by coating Brownian noise, imposing a limitation on the sensitivity of the detector, at frequencies of interest. Research has been focused on developing new optical coatings for the test mass mirrors, which are simultaneously characterised by low mechanical dissipation and low optical absorption. Alternatively, operations at lower (cryogenic) temperatures have been considered. Throughout this study all materials, developed and characterised, have been aimed to be utilised within detectors operating at room temperature.

The temperature of operation of the observatories affects not just the HR coating, but the nature of the mirror substrate. For room temperature experiments, the material chosen as substrate material is fused silica, where two different sam-
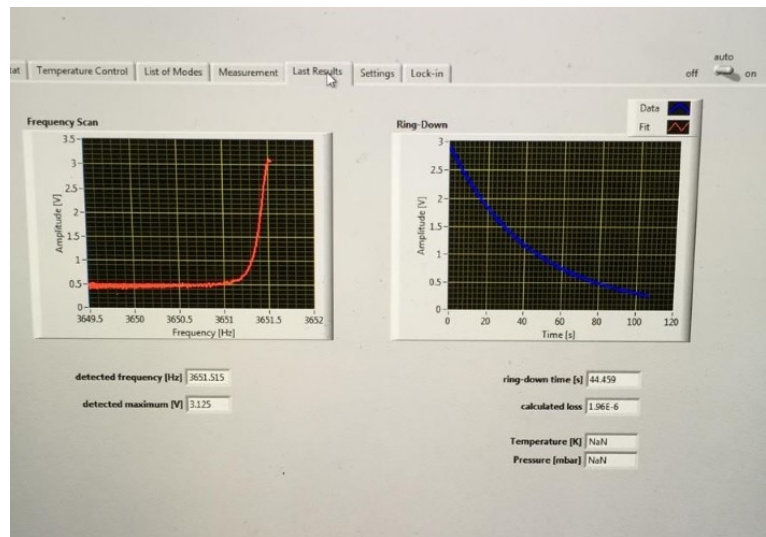
Figure 3.8: Screenshot of a single mode excitation and its following ringdown, monitored and controlled through programming software LabView. The left graph shows the detection of the excitation and the respective frequency. The right graph shows the measured ringdown of said excitation. Through the measurement of the ring-down duration, the mechanical loss associated with the mode is calculated within the program.
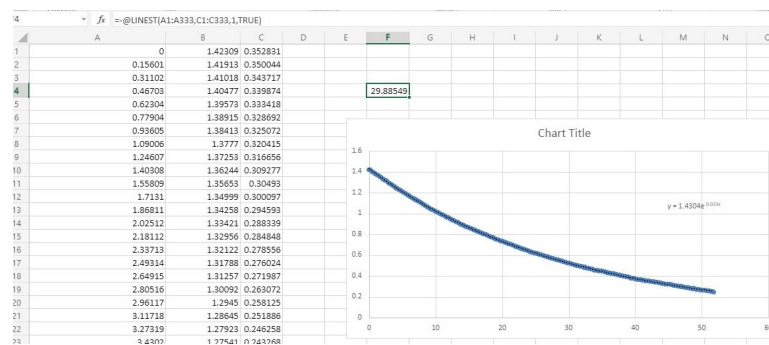
Figure 3.9: An Excel worksheet is utilised for the analysis of the recorded ringdowns. An exponential decay trendline is fit onto the amplitude decay, leading to the deduction of the loss of the specific ringdown of the specific mode. As each clamp contained multiple measurements of individual decays, the averaged value of all measurements per mode per clamp is used in the following analysis.

ples are used for specific characterisations. Fused silica cantilever samples are fabricated through flame welding, and are subsequently utilised in the measurement of mechanical dissipation, characteristic for the thin film coating. Fused silica JGS-11 discs are used for the determination of material properties, which

89

include coating elemental composition, amorphous-to-crystalline phase transition temperature, optical absorption and complex refractive index.

A new method of ion-beam deposition has been developed, utilising a novel ECR source, which allows for production of improved optical coatings in comparison to similar deposition methods. Two IBS systems had been constructed, one operating with a single ECR source, and the second one operating with up to four sources. Additionally, the single ECR source system enables the deposition of thin films at elevated temperatures, which has been considered of interest for improving current optical coatings. The multi-sourced system, though only operating at room temperature, allows for the simultaneous deposition of mixed material films, and it improves monitoring and control of the deposition process. During deposition in both ECR systems, coating was deposited on both a silica cantilever and a JGS-1 witness piece.

For each deposited film, using the JGS-1 fused silica disc, optical and mechanical properties are obtained. The cantilever sample is primarily used in measuring the mechanical dissipation, characteristic for the coating. Heat treatments prior and post-deposition have been proven advantageous to the coating characteristics. Pre-deposition annealing improves the consistency of the substrate material, whereas the post-deposition heat treatment reduces the mechanical dissipation and optical absorption of the coating.

Utilising this novel deposition technique and analysing the subsequently developed optical coatings can potentially lead to the improvement of coating properties and hence overall reduction of coating thermal noise.

Chapter 4

Mechanical characterisation of ion-beam sputtered tantala coatings

4.1 Introduction

Ion-beam sputtered coatings have been utilised in all ground based gravitational wave detectors. The thermo-mechanical properties of typical coating materials will vary and will have different temperature dependences, which can lead to different optimum coating choices for different operational temperatures. The coatings studied here will be characterised at room temperature only, however further work would be required to assess for use at lower temperatures.

As discussed previously, the optical coatings for gravitational wave detector mirrors require high reflectivity, low optical loss and scatter, in addition to low thermal noise. The reflectance of the multilayer coatings is enhanced through increasing the number of quarterwave optical thickness layer pairs and choosing materials with higher refractive index contrast. The greater the difference in refractive index, the fewer layers needed to achieve the same reflectivity. Since coating thermal noise is proportional to the thickness of the optical coatings, reducing the number of layers will lower the level of thermal noise, for a given mechanical dissipation. The low refractive index layer, n_{L}, is currently composed of amorphous silica, where $n_{\mathrm{L}} = 1.45$. The high index material employed is titania doped tantala, with concentration of 25% TiO_2 to 75% Ta_2O_5, with a value of $n_{\mathrm{H}} = 2.03$ [142]. Prior to the introduction of the dopant material, tantala was the sole component of the high n layer, however it is also the dominating source of mechanical loss comparatively to amorphous silica hence an adjustment was required to reduce said dissipation [143]. This was achieved through the addition of a dopant, in this case TiO_2, which not only contributed to a reduction in

mechanical loss, but due to TiO_2's high refractive index ($n_H = 2.61$), increased the overall reflectivity of the high index layers. Even with this reduction, the high index layers remain the dominating source of mechanical dissipation and of Brownian thermal noise, hence the most important constituent within the coating layers to be improved or replaced.

It is important to highlight that the mechanical loss depends on various factors, including the composition and the atomic structure, as described by the two-level system (TLS) model mentioned in Chapter 2. The atomic structure can vary depending on the deposition parameters (synthesis conditions) and the post-deposition heat treatment and annealing [2]. It is therefore important to consider optimised deposition conditions and annealing regimes of existing coating materials, in addition to new potential coating materials including new alloys of tantala.

The first reported investigation of elevated temperature ion-beam deposition of pure tantala films is described in the following sections, in addition to investigating the difference when sputtering from a pure oxide and pure metal targets. Results will inform the wider gravitational wave detection community regarding methods by which the current mirror coatings can be fabricated with lower thermal noise without the need to change the coating materials used.

4.2 Experimental procedure

4.2.1 Substrate preparation

The characterisation of the deposited thin film materials was carried out using two different types of fused silica samples. Fused silica (JGS-1 type) cantilevers were used as mechanical resonators in order to estimate the mechanical dissipation. The same silica material was used to fabricate 20 mm diameter, 1 mm thickness, disks used for optical characterisation in addition to mechanical/compositional analysis by XRD (X-ray diffraction), EDX (energy-dispersive X-ray spectroscopy) and WDX (wavelength dispersive X-ray spectroscopy). Cantilevers of different thickness were evaluated between $\sim 100 \rightarrow 200$ μm, showing that thinner substrates exhibited lower levels of mechanical loss. This could be due to the surface quality being improved as the silica material was polished down further [144], or else could be consistent with recoil losses in the clamp for thicker resonators [145]. No further investigations were carried out, however thinner cantilevers were chosen in order to more precisely estimate the mechanical dissipation of the film, as shown in Equation 3.11. Prior to any measurements or depositions, all cantilever substrates were annealed at a temperature of 950° C for approximately 5 hours. In the case of the witness samples, there is no prior treatment before deposition.

In order to assess the mechanical loss of the coatings, it was necessary to

measure all of the relevant resonant modes of the uncoated cantilevers. This was important as each mode can have different mechanical dissipation due to intrinsic frequency-dependant loss mechanisms and/or due to inhomogeniety in the cantilever thickness and surface quality. The freely-decaying ringdowns of each more was measured between $3 \rightarrow 6$ times for at least 4 separate clampings of the sample. The average mechanical loss was evaluated for each mode for each clamp, and the minimum values were taken to be the intrinsic dissipation of the cantilever. Note that it is not possible to measure a mechanical loss below that of the intrinsic material.

For each coating deposition, a disk and cantilever sample were mounted on the surface of a substrate holder/clamp. The cantilever was position to be in the centre of the deposition plume, resulting in the JGS-1 disk being located off-centre and thus receiving a thinner coating. Previous studies [137] have presented a relation between the thickness of the deposited coating on the surface of the witness sample and cantilever in the form of a multiplication constant. In this study, for accuracy, the thickness of the witness sample coating was evaluated using profilography, whereas the cantilever coating was estimated through a cross-sectional image. For the study of Ta_2O_5 this interconnection was further investigated through additional SEM measurements, showing a significant uncertainty in the previous scaling factor due to the manual placement of samples within the deposition system.

4.2.2   Deposition parameters

Elevated temperature depositions were performed on silica cantilevers in the temperature range from $25°$ C to $500°$ C, where two different targets were utilised for the deposition of the same thin film, *i.e.* a pure Ta metallic target and a Ta_2O_5 target, with the goal of depositing tantulum pentoxide in both cases. Performing the complete study utilising a single deposition apparatus enables the comparison between room temperature and elevated temperature depositions, and furthermore will provide a direct comparison on how the optical properties of the coatings may differ under different deposition conditions. It is important to note that standard ion-beam deposition will use quartz radiative heaters to reach substrate temperatures in the range $200 \rightarrow 250°$ C [146], however the motivation is typically for improving refractive index stability during long deposition runs that are strongly affected by temperature. The depositions were performed on the cylindrical (prototype) deposition system, and the deposition parameters were kept as constant as possible excluding the deposition temperature. The ion gun was set at 11.720 kV for all runs, and the sputtering was performed on a 4 inch target, Ta or Ta_2O_5, positioned at 45 degrees to the beam. Throughout each coating run, additional to the cantilever, a witness silica sample is placed in close

proximity to the thin substrate.

The deposition parameters for the separate coating sets are summarised in tables 4.1 and 4.2. Despite the consistency of deposition parameters, a variation was still exhibited in the deposition rates and therefore coating thicknesses. Since no clear relationship was found between deposition rate and key parameters, such as the extractor current, it was assumed that this variation arises from the manual placement of the targets and samples in each run.

Table 4.1: Parameters of tantalum pentoxide elevated temperature runs, deposited from a metallic Ta target

Deposition temperature (°C)	25	100	200	300	400
Average deposition temperature (°C)	33.0	100.5	205.7	311.8	413.4
Extractor current (mA)	0.31	0.30	0.31	0.28	0.27
Duration (hrs)	23.9	26.5	27.0	29.5	29.5
Coating thickness witness sample (nm)	290	327	N/A	N/A	N/A
Coating thickness cantilever (nm)	489.5	535.0	588.0	786.3	751.0
Deposition rate (nm/hr)	20.47	20.19	21.78	26.69	25.56

Table 4.2: Parameters of tantalum pentoxide elevated temperature runs, deposited from a Ta_2O_5 target. Depositions are presented in order of coating.

Deposition temperature °C	25	400	300	200	100	500
Average deposition temperature (° C)	32.6	421.3	323.5	217.9	115.1	527.0
Extractor current (mA)	0.19	0.21	0.22	0.21	0.21	0.21
Duration (hrs)	30.0	30.0	31.4	29.5	30.0	26.5
Coating thickness witness sample (nm)	198.0	228.0	265.0	270.0	278.0	271.0
Coating thickness cantilever (nm)	342.4	394.3	458.5	467.1	480.9	468.8
Deposition rate (nm/hr)	11.4	13.1	14.6	15.8	16.0	17.7

In order for the sputtering to be achieved, injection of gases is required. In the case of this set of optical coatings the gases used were argon and oxygen, where the gas flow was kept under the same parameters. For all depositions, the base pressure of the chamber was approximately 6.8×10^{-6} Torr. Prior to deposition, vacuum chamber was baked at a temperature of 200° C for ≈ 1 hour to minimise the probability of contaminations within the chamber as no gas composition measurements were performed before or after the completion of coating process. Argon gas was inserted through the ECR source reaching a pressure of 6.0×10^{-5} Torr. Oxygen gas is released in the background, increasing the system pressure to 1.0×10^{-4} Torr. The oxygen content was approximately 3 times

higher whilst using the oxide target, in respect to the sputtering using the metal target. It was expected for less oxygen gas to be required throughout the depositions, however coupling of currents, associated with the extractor and focus plate of the ion gun, could only be averted through the increase of the oxygen content. The occurrence was problematic and requires further investigation, regarding the vacuum system atmosphere, visual access to the deposition process.

For the set of coatings sputtered from the Ta target, the sequence of depositions was 25° C, 100° C, 200° C, 300° C and 400° C. A deposition at 500° C was attempted, however the excessive temperature caused instabilities in the coating process, disrupting the plasma flow and therefore the uniformity was poor and composition was non-stoichiometric. Due to this, the 500° C sample was analysed but not included in the average estimations of the optical and mechanical properties of the material. The duration of coating deposition varied independently for each run. The goal was to deposit for approximately 24 hours, where in some cases, lower currents implied slower deposition rates, hence the deposition time was increased. On average the deposition process continued for 27 hours. There was no obvious trend regarding the deposition rate between coating runs. On average there was a variation in deposition rate of 6%, where the average deposition was estimated as 22.8 nm/hr $\pm$ 13%.

For the coatings directly deposited from the Ta_2O_5 target, the order of depositions was 25° C, 400° C, 300° C, 200° C, 100° C and 500° C. Based on initial comparisons of mechanical losses from the coatings deposited from the metal target, it was deduced that a Ta_2O_5 deposition at 400° C was most promising. Therefore the 400° C deposition was performed immediately after the room temperature. Furthermore, an additional coating was developed at a temperature of 500° C. The coating system remained stable during this deposition, however multiple air fans were directed at the coating chamber to reduce the outer surface temperature of the chamber. Based on previous research conducted, it was established that depositing using an oxide target is slower compared to a deposition from a metal target irrespective of the deposition technique [147], hence duration of depositions was aimed at $\approx$ 30 hours. In the case of coating deposited at 500°C, the deposition time was reduced to 26.5 hours, to reduce the risk of safety hazard, since the system could not be monitored continuously. With each subsequent run the deposition rate increased. On average the deposition rate was approximated as 14.79 nm/hr $\pm$ 020%. The average increase in between sputtering runs was estimated as $\approx$ 9%. This was consistent with the known relationship between the deposition rate and the target material [147]. By directly comparing the deposition rate of the two sets of coatings, it was deduced that using a Ta target enabled 35% faster deposition than utilising the Ta_2O_5 target.

The main goal of this study was to explore new deposition parameters for the fabrication of tantala-based optical coatings with lower mechanical dissipation,

and thus thermal noise. It is important to note that, despite best efforts, other deposition parameter varied between deposition runs due to the challenge of finding conditions that allowed the stable operation of the ion source. In particular, the rate of sputtering is a possible factor affecting the coating loss angle of the films. It has been theorised [148] that slower depositions allow for a more densely packed structure, however, it also enables the possibility of contamination on the surface of the substrate. Therefore, the next step required the direct characterisation of the coating loss angle for the slower deposited coatings, which would directly relate the sputtering rate to the mechanical loss of the coatings.

4.3 Results

4.3.1 Film thickness

As mentioned, two samples were coated in each run, with the intention of using the JGS-1 silica disk for carrying out optical and thickness characterisation of the films. The initial thickness of the cantilever coatings was taken from these disks and applying a scaling factor, since the cantilevers were centred within the deposition plume [2]. Once the mechanical loss of the coated cantilevers was fully characterised, SEM cross sectional imaging was used to measure the coating thickness and thus reduce the uncertainty in the coating loss calculations.

Furthermore, based on the evaluations of the coating thicknesses, it was observed that each coating did not experience the same deposition rate. For the depositions from the oxide targer, each subsequent coating deposition showed an increased rate. As all the deposition parameters were kept nominally identical between runs, it could be assumed that an uncontrolled variable within the deposition process was responsible. One possibility was that the target became increasingly metallic between deposition runs, and therefore the deposition rate was observed to increase [149]. The slow rate of deposition associated with these ECR sources could also allow a higher degree of contamination incorporation, which could vary between the deposition runs. Further investigation is required.

4.3.2 Optical properties

Transmission

The optical transmission of the tantala coatings was obtained for each deposition. The number of interference extrema in a given spectral region is correlated to the films optical thickness, and thus associated with the physical thickness and the refractive index. The measured transmittance is evaluated as the ratio of transmission of the substrate and the transmittance across the back face of the
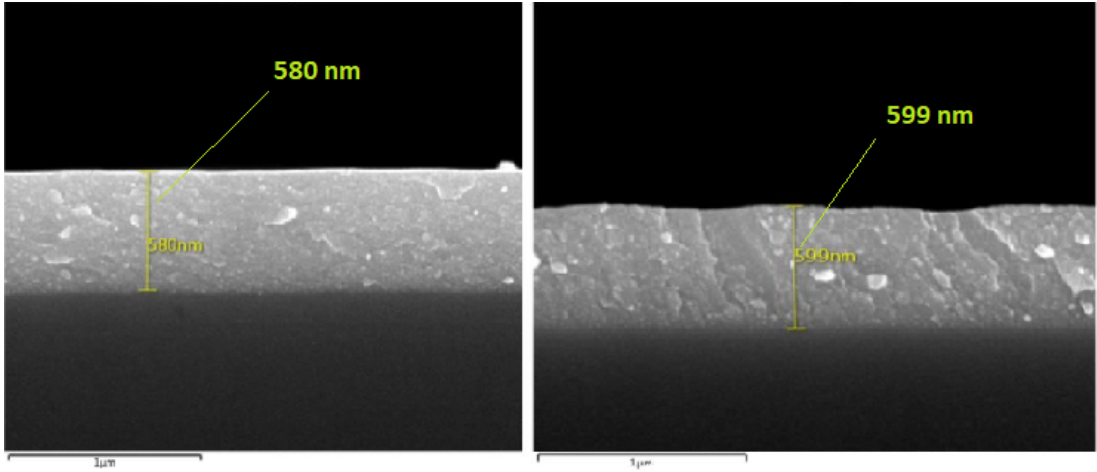
Figure 4.1: Cross-sectional image of cantilever as measured on a SEM. Images represent the visual boundary separation between the substrate material and the deposited coating. Left image shows a coating with thickness of 580 nm. Right image shows coating with thickness 599 nm. These images were used as a direct evaluation of the coating thickness variation upon the surface of the cantilever. Such evaluation was necessary to study the coating uniformity and surface roughness.

substrate, usually annotated T_s, and is evaluated as $\dfrac{4n_0n_2}{(n_0 + n_2)^2}$, where n_0 is the refractive index of air and n_2 is the refractive index of the substrate, in this case SiO_2.

As shown in Figure 4.2, the transmission spectra, T, can be obtained from the various coated substrates within the studies detailed here. The optical reflectance, R, can also be obtained, which provides a more accurate estimation of the films refractive index, and the ability to measure optical absorptions down to around $k \geq 1 \times 10^{-4}$. Optical modelling software, SCOUT, was used to simulate and fit modelled T and R spectra to the measured data, and provide estimates for n, k, and physical thickness of the film. Multiple measurements of each film were taken to assess the variation in film thickness. As discussed previously, the film thicknesses calculated from the optical spectra were used to assess the mechanical loss of the coatings, since the thickness plays an important role in the energy ratio, until the direct film thicknesses were measured at the end of each study.

n and k fitting

The refractive index of the developed tantala coatings also plays an important role in defining the number of bi-layers to achieve the required reflectivity in a gravitational wave detector, since the reflectivity is defined from the refractive
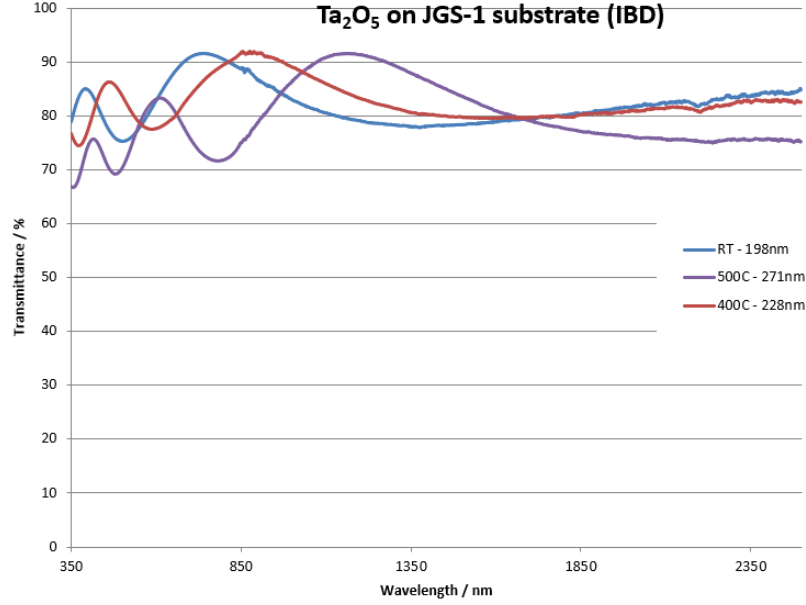
Figure 4.2: Transmittance of Ta_2O_5 coatings using a metallic Ta target deposited at 25° C, 400° C and 500° C on prototype ECR IBS system. The number of peaks in each spectra can be used to additionally determine the film thickness of the coating. Image taken from [2].

index contrast between the high- and low-index materials.

The determination of the real and complex parts of the refractive index are determined using the Kramers-Kronig method [150], which requires the reflectance or transmission of the combined substrate-film sample to be known for a range of wavelengths. Using the measured spectra enables the calculation of the phase changes as a function of wavelength. Figure 4.3 presents the calculated n and k as a function of wavelength, which have been modelled from the obtained transmittance spectrum, T.

In order to obtain the optical constants for the thin film, curve fitting models are required for the multi-wavelength spectrum, where the dispersion of said optical constants is represented by the dispersion equations [150].

Figure 4.3 presents the real and imaginary parts of the complex refractive index of a tantulum pentoxide coating fabricated in the ECR IBS system. The increase in n at lower wavelengths is due to the absorption associated with the mobility gap in the film, however the wavelengths of interest in this case, 1064 nm and 1550 nm, are far away from the mobility gap and associated Urbach tail. Optical parameters for ion beam deposited tantala coatings, presented by Demiryot $et.al.$ 1985 [151], were similarly calculated using the transmittance spectra of each film. By comparing the data obtained for the two different deposition techniques

98
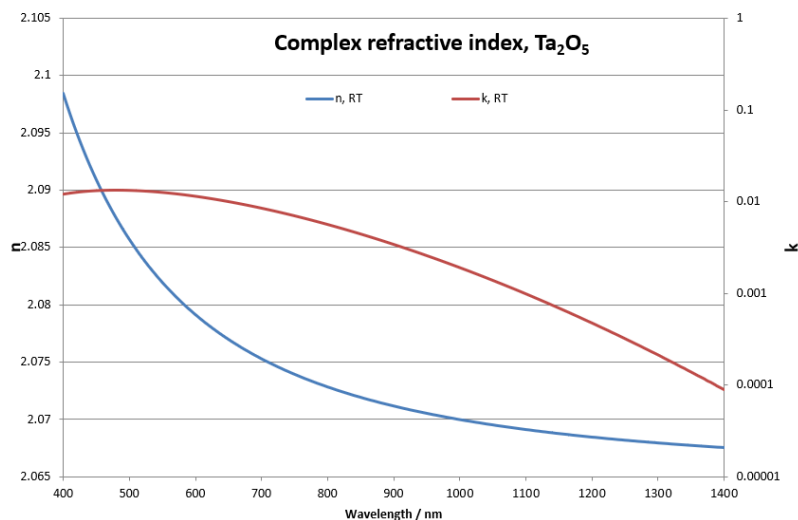
Figure 4.3: n,k. By using a modelling software, measured data is compared to pre-calculated models. The matching of a measurement to a model enables the evaluation of the refractive index and extinction coefficients as a function of wavelength. Image from [2].

for coatings of the same nature, it is shown that optical properties of ECR developed coatings do not deviate significantly as compared to standard Kaufmann or DC ion-beam sputtering.

Despite the previous successes of fabricating ultra-low optical absorption a-Si films using the ECR ion-beam deposition process [137], it is important to verify that low optical absorption can also be achieved in oxide films. For example, the low deposition rate will increase the probability of contaminations being incorporated due to residual gas species in the vacuum chamber. Furthermore, through the characterisation of the absorption coefficient of the optical coatings, the stoichiometry of the thin films can be confirmed. Suboxide-composite films or oxygen deficient films are expected to be absorbing and dispersive unlike the stoichiometric Ta_2O_5 films. The absorption spectrum as a function of wavelength can further be related to the mobility gap.

Optical absorption

Absorption of light induces a thermal lens within the mirrors of gravitational wave detectors, creating instability within the optical cavities that required thermal compensation [152]. Diagnostics performed on the Fabry-Perot cavities deduced an optical absorption and scatter of 1.5 ∓ 0.8 ppm (parts per million) at a wavelength of 1064 nm [153]. At this wavelength, tantulum pentoxide has been known to exhibit very low optical absorption, justifying it as a suitable coating mate-

99

rial. Furthermore, this material has been observed to have scattering lower than 10 ppm [154], additionally to a sub-ppm optical absorption upon annealing [142]. A constraint was imposed on the absorption and scattering levels of optical coatings, restricting the absorption to values lower than 5 ppm and scattering lower than 5 ppm. Multiple techniques can be utilised, however, the characterisations here were performed using the PCI technique, employed at Stanford University and University of Glasgow.
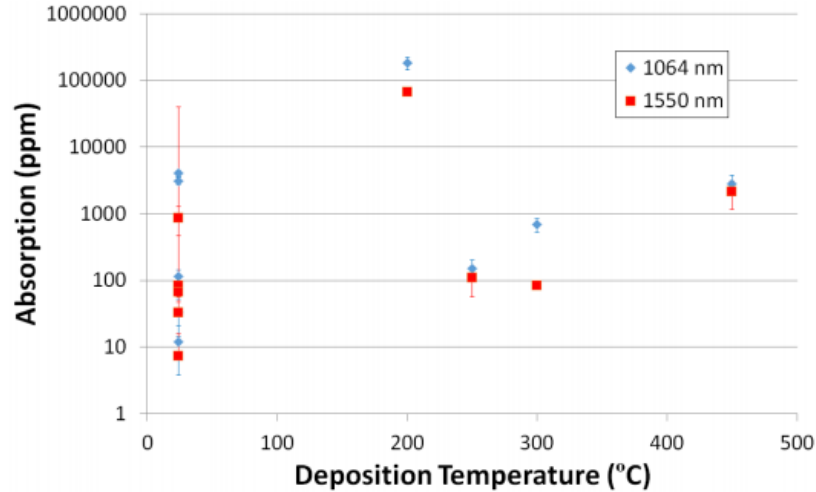
Figure 4.4: Optical absorption as a function of deposition temperature for tantulum pentoxide coating developed via IBS using an ECR source. For completeness absorption was estimated at both 1064 and 1550 nm. There is no apparent correlation between the deposition temperature and the optical absorption, however, a wide range of values was observed for the RT deposited coatings. The lowest measured optical absorption value appeared as 12.1 ppm at 1064 nm and 7.4 ppm at 1550 nm. Original plot by [140]

Furthermore, it was deduced that the coating deposition technique affected the absorption of the optical coatings. Even though DC magnetron sputtered Ta_5O_2 coatings exhibited a lower mechanical loss after heat treatments in comparison with literature [2, 155, 156], the optical absorption averaged at 85 ppm [135].

Figure 4.4 presents the characterisation of optical absorption of pure tantala coatings deposited using via IBS for wavelengths of 1064 nm and 1550 nm, where the data presented was acquired prior to heat treatment of the thin films. The lowest optical absorption at a wavelength of 1064 nm was measured as 12.1 ppm, similar to the lowest values of absorption in as-deposited films [157]. The greater range of values observed at room temperature may simply be associated with the larger sample set, and further study is required to understand potential trends. It is interesting to note that the majority of values at room temperature lie between

100

10 and 100 ppm (Figure 4.4), again consistent with high quality standard IBS coatings.

Optical absorption has been shown to reduce following post deposition heat treatment. However, such treatment typically entails a well-defined maximum temperature limitation due to the possibility of structural/phase changes within the coating. The ECR tantala coatings remained amorphous up to heat treatments at 600° C. Since the optical properties of Ta_2O_5 films have been well studied, with absorptions routinely observed below 1 ppm [142], no additional optical absorption characterisation was performed. The aim here is to investigate the reduction of mechanical dissipation associated with elevated temperature deposition.

4.3.3 Structure

Elevated temperature deposition and post-deposition annealing treatment have been considered as important steps in the development of lower mechanical loss, highly reflective optical coatings [158]. However, a limitation is imposed on both the deposition and annealing temperature set up by phase change of the material from amorphous to crystalline. For the coating developed using the ECR ion source, thin films remained amorphous up to temperatures of 650° C, above this temperature, Ta_2O_5 will undergo a phase change and become poly-crystalline. Poly-crystalline coatings, due to grain boundaries within the materials, can exhibit high levels of optical scatter, in addition to exhibiting higher levels of mechanical loss due to friction and the grain boundaries [135]. It can be seen in Figure 4.5, that coatings developed using the prototype IBS system showed peaks which are indicative of crystallisation within the material structure when heat treated at 700° C. As higher temperature depositions reached a temperature of 500° C it was necessary to verify that the optical coatings remained in an amorphous state up to such temperatures. If post-heat treatment, the structure is crystallised, it is characterised as a $\beta - Ta_2O_5$, *i.e.* it is in its orthorhombic phase [159].

Heat treatments were performed pre- and post-deposition, as well as in further treatment cycles. Heat treatment has been proven to improve optical and mechanical properties of materials, hence it has been implemented as a follow up procedure after deposition. Since coatings are required to remain in an amorphous state, crystallisation temperature is limiting the thermal processing. As the coating needs to remain amorphous, XRD (X-ray diffraction) scans were performed on witness samples as deposited and after subsequent heat treatments. Both cantilever and witness sample were annealed at temperatures up to 600°C. Subsequently, cantilever samples were used for the obtaining of mechanical loss measurements, whereas the JGS-1 discs were utilised in XRD scans used for de-

101
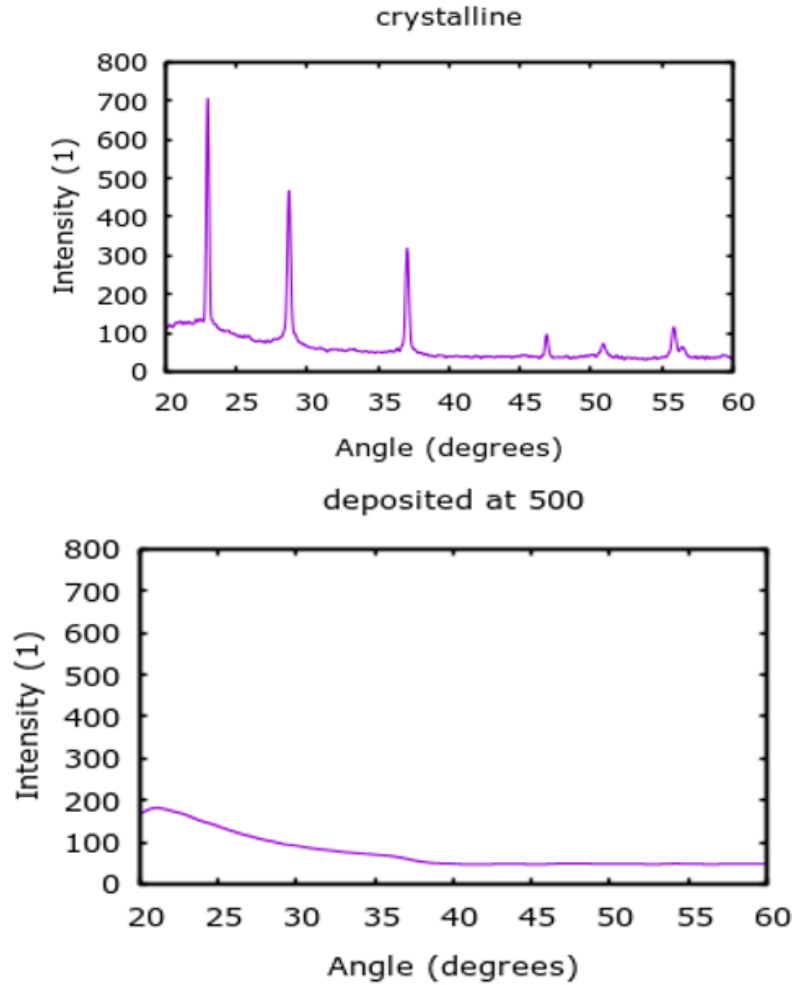
Figure 4.5: XRD spectra of IBS ECR coatings. (Top) Figure presents data of a Ta_2O_5 coating deposited at 300° C, after a heat treatment at 700° C. Post heat treatments at 700° C, coating was no longer amorphous and had crystallised. The crystalline feature are shown on the plot. (Bottom) Tantala coating deposited at 500° C. The sample had not been heat treated, showing that prior to any thermal processing the coating showed no crystalline features and remained in an amorphous state. From the two plots it is evident that ECR deposited tantalum pentoxide coatings remain amorphous above 500° C.

duction of state of material, *i.e.* to determine the temperatures where the optical coating remain amorphous. In the case of Ta_2O_5 optimum annealing temperature was established as 600° C, since at temperatures at, or above, 700° C, the coatings appeared crystallised. Regarding deposition temperature, it is interesting to
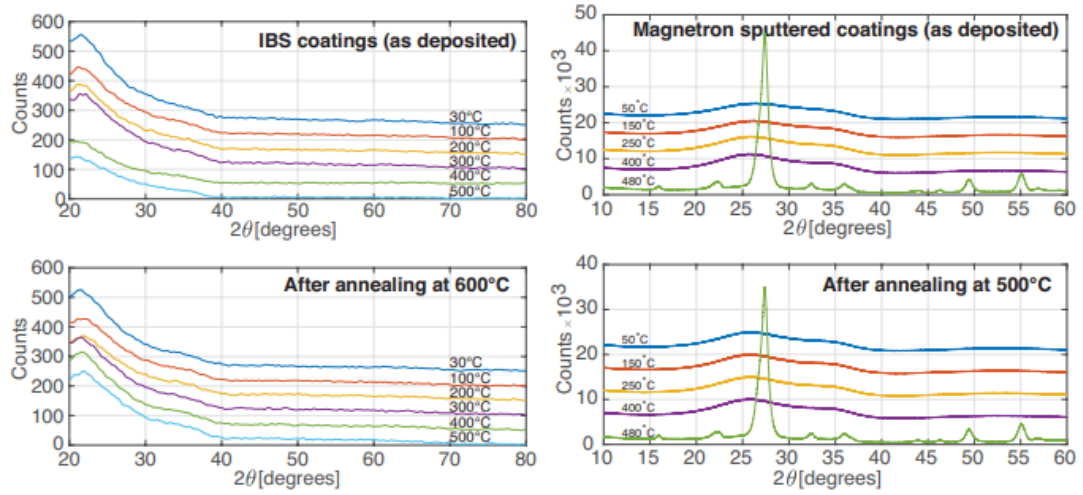
Figure 4.6: XRD diffraction patterns for ion beam deposited tantalum pentoxide films, sputtered from an oxide target. Before (top) and after (bottom) annealing at 600° C. The temperatures listed in the graph correspond to the different substrate temperatures during deposition. XRD scans were carried out using a Siemens D5000 X- ray diffractometer at room temperature with Cu K radiation ($\lambda = 0.154$ nm) in the range of 2θ between 20° and 80°. Images reprinted from [2].

note that the ECR IBS coatings remained amorphous at up to 500° C, whereas DC sputtered materials showed signs of crystallisation at temperatures of 480° C [2] (Figure 4.6). It is likely that this is due to IBS coatings being more densely packed, hence suppressing crystallisation [160]. Additionally, coatings deposited using magnetron reactive sputtering [161], and RF sputtered thin films [159], remained amorphous after thermal processing at temperatures higher than 600° C. Therefore, the transitional temperature separating the amorphous and crystalline stage of ECR IBS coatings is consistent with the specified alternative deposition methods (Magnetron sputtering and RF sputtering) for pure tantala.

4.3.4 Mechanical properties

Young's modulus

Young's moduli of both the substrate material and coating are required for the characterisation of the mechanical dissipation, in addition to the estimation of the thermal noise performance, of the optical coatings. The Young's modulus of silica has been extensively studied by other authors, and an average value of 72 GPa was used for the calculations [162, 163, 164]. In the case of the

tantulum pentoxide coatings, a pre-established value cannot be easily used, since this material does not naturally exist in an amorphous state. In the studies detailed here, witness samples for each deposition run were analysed using a nano-indenter, which provided multiple measurements of Young's modulus. As an average for the tantulum pentoxide coatings, Young's modulus was evaluated as 140±10 GPa.

Mechanical loss

Mechanical loss measurements were performed using the technique described in Chapter 3. All uncoated cantilevers had been heat treated simultaneously, reducing the variability of thermal conditions. The substrates had been coated in nominally identical conditions where the only difference was the deposition temperature.

In order for the coating mechanical loss to be calculated, knowledge of multiple properties are required, as shown in Equation 3.12. As stated, the thickness of the deposited coatings were assessed through a variety of non-destructive techniqus, followed by a final direct measurement which was destructive but had the lowest uncertainties. The thickness of the silica cantilever substrates is also required, and was estimated through both analytical [165] and computational techniques, through least squares or incremental fitting between the measured and modelled resonant frequencies. For the computational simulations, the cantilever was modelled using Ansys Finite Element software, using the modal analysis technique [5]. The measured modal frequencies were found by exciting the resonances of the cantilevers by using a frequency-sweep in the electrostatic driving potential, and identifying the resonant peaks in the FFT of the optical displacement readout signal, as described in Chapter 3.

The mechanical ringdowns of each mode, from ~ 100 Hz $\rightarrow 10$ kHz, were measured around 5 times, for each clamping of the sample. The samples were typically re-clamped six times, which involved breaking the vacuum. This was important because the clamping condition could affect the resonant coupling to the cantilever, in addiiton to changing the friction between the clamping block and the clamp [145]. Therefore the lowest mechanical loss values could be taken from the individual sets of ringdowns, as these would represent measurements where the external sources of dissipation were minimised. This methodology was followed for all the steps of the study, *i.e.* where the cantilever was uncoated, coated and following each annealing step.

As shown in Figure 4.3.4, the mechanical loss reduces for all coatings after annealing at 600° C. The lowest obtained loss value for a deposition using the Ta metal target was performed at 200° C and it was estimated as 2×10^{-4} rad. Across all deposition temperatures, the post heat treatment allowed all measured mechanical losses to become lower than 5×10^{-4} rad.
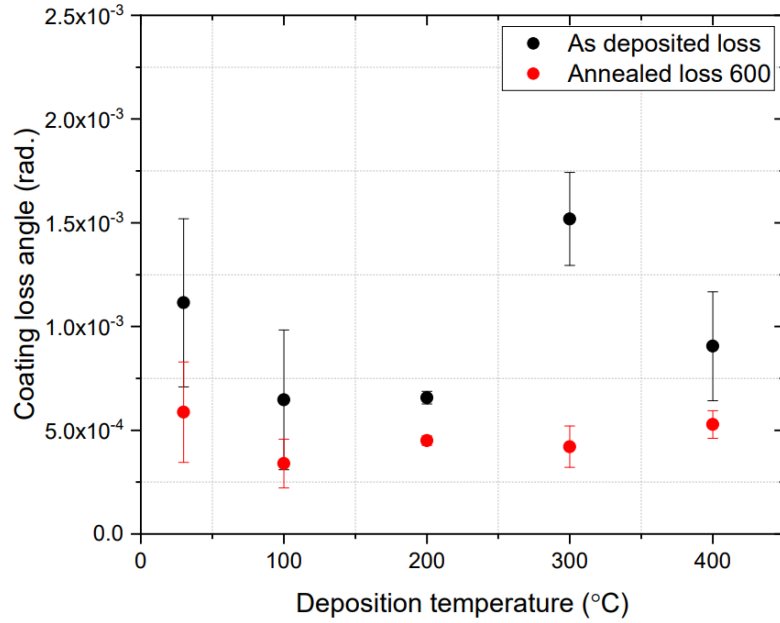
Figure 4.7: Mechanical loss angle for Ta_2O_5 deposited using a Ta target. Films were deposited at a range of temperatures - from 25° C to 500° C. Due to contamination upon the surface of the 500° C study, said sample was excluded from the data set. Lowest loss was obtained for coating deposited at 200° C, following a heat treatment at 600° C. On average, all losses decreased to an average value of 5×10^{-4} rad post heat treatment.

The coating showing the lowest loss for the depositions using an oxide target was the coating deposited at 200° C. An overall evaluation provides an average loss of 7×10^{-4} rad pre-annealing and 3.5×10^{-4} rad post heat treatment. There is a factor of two improvement.

4.4 Conclusion

In total two sets of six samples had been coated with a Ta_2O_5 coating at elevated temperatures, individual sets differing solely on target composition used during deposition. They will be referred to based on the nature of the coating material, *i.e.* in set 1 the target used was a Ta metal target, whereas in set 2, the target utilised was a Ta_2O_5 oxide target, hence the sets will be referred to as metal and oxide, correspondingly. The substrates used in both sets had been prepared simultaneously. Each set of depositions included coatings performed at room temperature (25° C), 100° C, 200° C, 300° C, 400° C, and 500° C, where only one coating performed at a temperature of 500° C was successful. All 12 can-
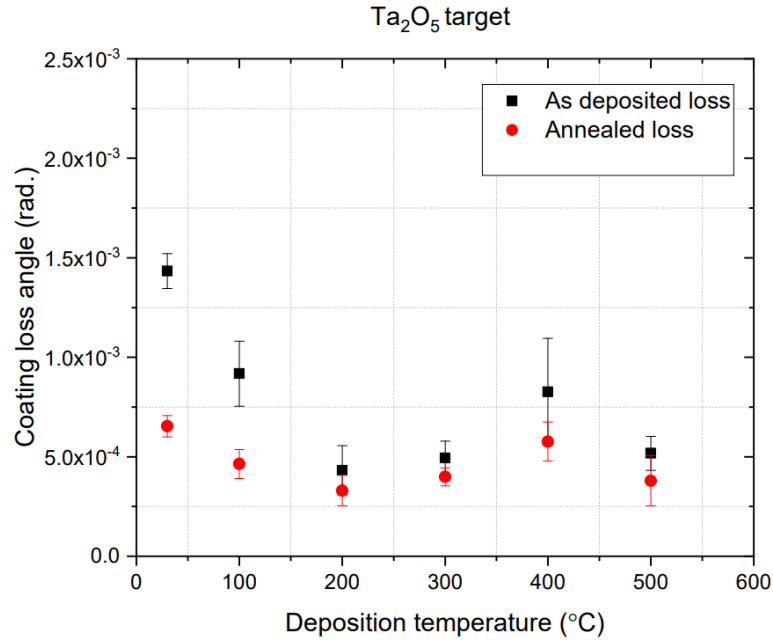
Figure 4.8: Mechanical loss angle for Ta_2O_5 deposited using a Ta_2O_5 target. Films were deposited at a range of temperatures from 25° C to 500° C. The lowest loss was obtained for coatings deposited at 200° C with an average loss of 3.5×10^{-4} rad following a 600° C heat treatment.

tilevers were used for estimation of mechanical loss angle, therefore the samples were measured pre-deposition, post-deposition and following a heat treatment, in order to accurately estimate the mechanical loss of the coating material and its dependence on thermal processing.

The oxide set had depositions longer in duration compared to the metal set, as it is known that using an oxide target imposes a slower deposition rate. All deposition parameters were kept constant to limit the number of variables and hence enable a comparison between two target materials. Through the use of the metal target, however, remained a risk of not injecting enough oxygen gas during the process and hence coated substrates would appear oxygen deficient. The amounts of gas used in both set was kept constant and following the analyses of both sets, there were no signs of oxygen deficiency. It was observed that coatings deposited at higher temperature, i.e. 100 and 200 demonstrated the lowest average mechanical losses for both sets. It is evident from the previous two sections that the two sets of coating differed in coating thickness. It is observed that using a metal target allows a 1.54 faster deposition rate compared to the use an oxide target. The thickness of the deposited films was not the only difference between the samples.

Mechanical loss is the main subject under question for new thin film materials used as optical coating. Figure 4.9 shows a comparison between the metal and oxide set, including both data regarding the as deposited losses and following a heat treatment. It is evident that in the metal set the majority of as deposited losses remained in the order of 10^{-3} rad, where for the second set those values were closer to the order of 10^{-4} radians. However, following the thermal annealing, it can be observed that the data spread shrinks, showing average mechanical loss estimations at a similar value. Furthermore, it is known that heat treatment affects mechanical loss in a positive manner, *i.e.* reduces the dissipation, which can also be noted from Figure 4.9. In both cases it was deduced that heat treating coated samples leads to a reduction in mechanical loss in the order of 2. Following the heat treatment, lowest loss for coatings from metal target was estimated as 9.82×10^{-5} for a deposition at 100° C, and a minimum loss of 2.00×10^{-4} for coatings developed using the oxide target deposited at a temperature of 200° C.
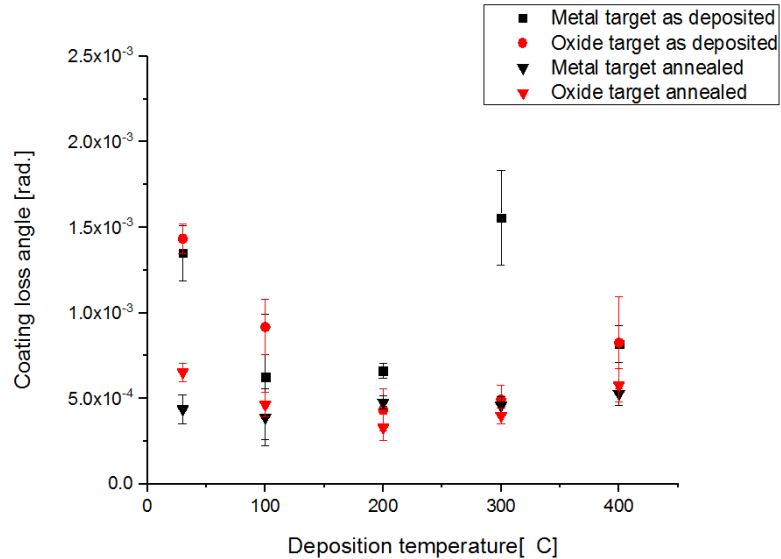
Figure 4.9: Mechanical loss angle for both metal and oxide deposited sets. Square shape represents the as deposited losses, whereas triangular symbol represents data post heat treatment. In both sets, thermal treating of the coated samples has lead to a factor of 2 reduction in average mechanical loss angle.

Theoretically speaking, mechanical loss is caused by low energy excitations which can be modelled as two level systems. The structure of the energy landscape in glasses depends on the fabrication history: a detectable change in the glass structure is expected to happen when the deposition is carried out at a significant fraction (85%) of the glass transition temperature. This was indeed

observed in amorphous silicon. If, as expected from experiments and models, the fraction of the glass transition temperature at which the density of TLS reduces is universal, we might expect any effect to be visible in tantala for temperatures much higher than those explored in this study, which was limited by the incipient crystallization of the thin film. It is possible that the glass transition temperature of tantala is too high to be practically reachable before crystallization of the coating is induced [2]. In order to prevent crystallisation an alternative suggested is through the addition of a dopant to tantala, for example TiO_2 (titania) or ZrO_2 (zirconia). Following chapters look more in detail at the effects of the addition of dopant(s) can have on the tantala coatings produced using an ECR ion source.

Chapter 5

Characterisation of zirconia doped tantala coatings

5.1   Introduction

The Advanced LIGO upgrade, called Advanced LIGO Plus or 'A+', will complete installation by the end of 2023 and potentially be ready for observations from mid-2024. The detector will maintain similar operational parameters, for example with use of 1064 nm laser wavelength and 34 cm diameter test mass mirrors. Lower suspension thermal noise will be achieved through use of thinner silica suspension fibres, in addition to lower quantum noise through use of frequency dependant squeezing [166, 167]. In order to exploit these noise reductions, the thermal noise associated with the mirror coatings should be reduced by a factor of *circa* 2. This requires a reduction in the loss-thickness product, $\phi_{\mathrm{coating}}d_{\mathrm{coating}}$, by a factor of 4.

Chapter 4 covered the deposition and analysis of pure tantulum pentoxide coatings, introducing for the first time deposition temperature as a variable for ion-beam deposition. However, the coatings developed, even though the lowest reported mechanical dissipation for pure tantalum pentoxide, were not lower than titania-doped tantalum pentoxide currently used in Advanced LIGO [168]. In Chapter 4, the positive effect of post-deposition heat treatments was presented, resulting in a progressive reduction in mechanical loss. However, the thermal treatment of the samples was limited by the crystallisation temperature of tantala, after which the coating would no longer remain amorphous. Investigating the use of alternative dopants, that have similar benefits to reducing mechanical dissipation as observed for titania, in addition to increasing the crystalisation temperature, would be highly attractive.

It has been shown that doping tantala with ZrO_2 enables the suppression of the crystallisation of the thin film up to higher temperatures of the order of 800° C [166]. The structure of the new doped material will be dependant on

dopant concentration as studied in [169]. Not only will it affect the crystallisation temperature of the film, but it will also have an effect on the crystal structure of the material. The addition of a dopant interferes the alignment of the tantala molecules, leading to a suppression in crystallisation [170]. The dopant concentration should not exceed a concentration of 30% [3], however, as it may lead to ZrO_2 forming a separate crystalline phase [169].

This chapter covers the deposition of multiple zirconia doped tantala coatings. Comparatively to the prior coating sets, these data acquisitions contained multiple variable conditions in the search of discovering the optimum deposition parameters. Elevated temperature depositions were performed on the prototype IBS system, where the target used was a tantulum pentoxide target with the addition of 99.9% pure Zr foil, positioned in the line of the ion beam, onto the surface of the target.

In conjunction with the prototype system described before, additional depositions were performed on the new IBS deposition system based on four individual ECR sources. The increased size of the system also enables the use of multiple targets, hence during deposition of a zirconia doped tantala coatings, two separate targets were utilised - ZrO_2 and Ta_2O_5. In attempt to further investigate the change in deposition rate, different angled placements were attempted to deduce whether a rotational stage in constant motion provides a more uniform coating, irrespective of the deposition angle.

Through the comparison of the collected data from both deposition systems, one will be able to not only provide an estimation of the mechanical and optical properties of doped tantala coatings, but also investigate how different dopant concentrations can affect the optical coating.

5.2 Zirconia doped tantala coatings

5.2.1 Substrate preparation

All substrates utilised during the deposition of zirconia-doped tantala were composed of fused silica. The two types of samples used were rectangular silica cantilevers and JGS-1 discs, where the cantilevers were mainly used in the characterisation of the mechanical loss of the deposited coatings, and the discs were utilised in the attainment of optical and mechanical properties of the coatings. Cantilevers were manufactured to be as similar to one another as possible, however, depending on the silica disc used for their fabrication, there was a variation in the thicknesses of the ribbons of the cantilevers, ranging between 100 μm and 200 μm.

Prior to deposition and analysis all substrates underwent a thermal treatment at 950°C for a duration of 5 hours. This was performed in order to remove any

residual organic material onto the surface of the cantilevers which would have an effect on the mechanical loss evaluations pre and post coating as well as disrupt the uniformity of the deposited films.

Throughout depositions, at least one JGS-1 and one cantilever were coated, where in the case of the prototype system, the JGS-1 disc was placed in close proximity to the cantilever. In the case of the larger deposition system, all samples were attached to a vertically held circular rotational stage, where the distance from the targets to the substrates remained the same, hence both cantilever and witness piece were expected to have the same coating thickness. This will be further examined within the chapter.

5.2.2   Coating processes

Prototype ECR ion source system

Elevated temperature depositions were performed on the prototype single ion source system. Deposition temperatures ranged between room temperature and 500°C. The optical coating deposited was ZrO_2 doped Ta_2O_5. Due to the small size of the vacuum chamber and the parallel beam size, it was impossible to include more than one targets during deposition. In order to introduce the dopant material into the thin film coating, pure Zr foil was attached to the surface of the Ta_2O_5 target. Based on the imprint of the beam from previous depositions onto the surface of the target, the appropriate position of the metal foil was estimated. The foil used was of width of 9 mm and was positioned at an angle of 40° to the normal of the plane of the target. On the left side it was measured that the distance between the foil and the edge of the target was 55 mm, whereas on the left side the distance was estimated as 35 mm (Figure 5.1). The geometry of the

Table 5.1:   Parameters of zirconia doped tantalum pentoxide coating runs.

Deposition temperature	RT	200	400	500
Average deposition temperature (° C)	41.1	220.4	409.9	509.2
Extractor current (mA)	0.45	0.51	0.45	0.37
Duration (hrs)	26.8	24.5	24.4	23.8
Coating thickness cantilever (nm)	453.0±10.0	340.0±10.0	442.5±10.0	525.0±10.0
Deposition rate (nm/hr)	16.7	13.8	18.1	22.1

setup was identical to the pure tantala coatings. The ion gun had been kept at 11.720 kV for all deposition runs. A variation from 0.37 to 0.51 mA in extractor currents, associated with the current density of the ions within the plasma, was

observed, and the reason behind said discrepancy remained unknown and could be further investigated.

Majority of coating deposition had a duration of 24 hours. Also from the data summarised in table 5.1, it was observed that the average deposition rate was approximately 18 nm/hr, where outliers would exhibit an approximate 20% deviation. This deviation from the average deposition rate was subsequently contributed to contaminations and instabilities present during these depositions.

Similarly to the pure tantala study, oxygen and argon were introduced in the system. The chamber pressure was elevated from $\approx 10^{-6}$ mbar to 8×10^{-5} mbar with Ar and 4×10^{-4} mbar with O_2, where the Ar gas was introduced directly through the plasma source and oxygen was released in the background of the system. These specific quantities were chosen due to prior parameter testings, explained in section 4.5 of the previous chapter.

Multi-sourced ion system

Further development of coatings depositions lead to the construction of a cuboid vacuum chamber with four ECR ion sources connected on opposite walls (as seen in Figure 3.4). Unlike the prototype system, the larger size of the chamber not only enabled the use of multiple guns but also individual targets for the dopants, as in the case of these coating sets. Coatings were deposited in three individual runs using a tantala and zirconia targets, where two of the guns were aimed at the Ta_2O_5 target and one at the dopant material. For two of the deposition runs only three ECR sources were utilised, whereas subsequently the fourth gun was ran as an electron gun in order to neutralise sparking due to currents, and therefore stabilise the system. All of the deposition parameters are summarised in table 5.2.

Table 5.2: Parameters of zirconia doped tantala coating runs, deposited at room temperature, within the multi-sourced ion-beam system

Deposition run	B18H1716	B18J0409	B19B0817
Extractor current Gun 1(mA)	0.21	0.25	0.63
Extractor current Gun 2(mA)	0.15	0.15	0.21
Extractor current Gun 4(mA)	0.13	0.17	0.23
Duration (hrs)	42	360	384
Coating thickness (nm)	261	398	1390
Deposition rate (nm/hr)	6.21	1.11	3.62

Identically to the prototype system, argon and oxygen gasses were introduced during the process, where the average base pressure of the chamber was 1×10^{-5} mbar, rising to 8×10^{-5} mbar with argon injected through the ion source
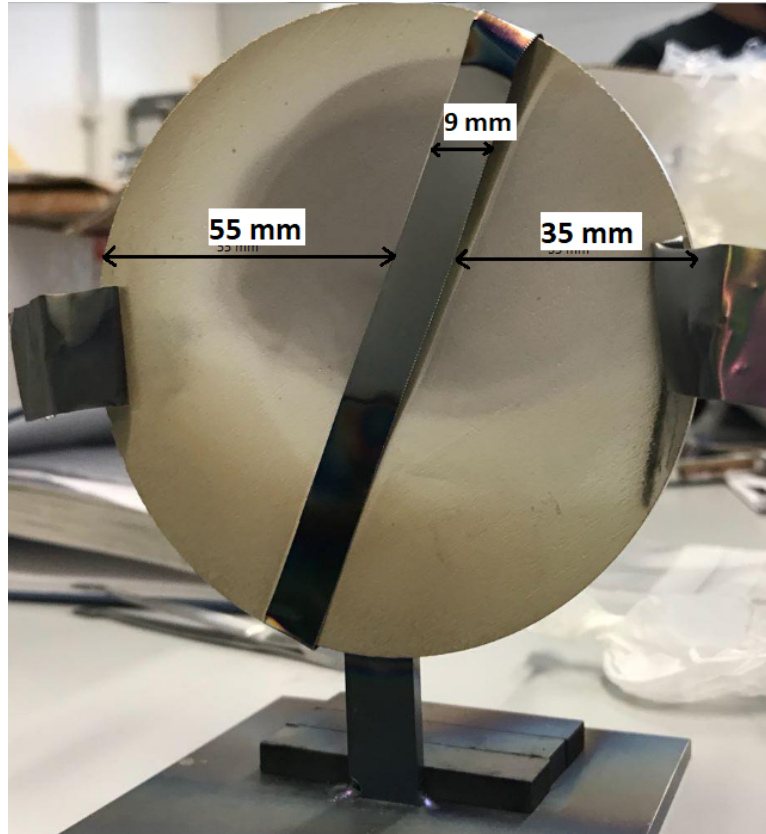
Figure 5.1: Setup of the target used for coatings within the prototype system. The Zr foil was attached to the surface of the tantala target at approximately 40°, intercepting the plume of the beam on the surface of the target. The position at which the beam would hit the target was visible through the darker appearing spot, which had arisen due to previous depositions. Additionally, the side clamps, holding the target in place, were covered in tantulum foil to intercept any contamination from the steel components of the target holder.

and reaching a final pressure of 1.2×10^{-4} mbar with oxygen released in the background of the process.

Prior to the conversion of the fourth source into a neutraliser, the deposition rate of the coatings was inconsistent, ranging from 6.2 to 1.1 nm/hr. This variation was subsequently attributed to discharging during sputtering process causing abruptions leading to the instability of the process consistency.

Additionally, the rotational stage, containing all the uncoated samples was moved closer to the positions of the targets, decreasing the distance between substrate and target. It was deduced that these two alterations lead to an increased stability of the deposition system and the tripling of the deposition rate (also observed in difference in extractor current values between runs).

5.3 Results/Discussion

5.3.1 Zirconium dioxide as a dopant for tantulum pentoxide

The addition of ZrO_2 as a dopant to Ta_2O_5 coatings is beneficial in terms of increasing the amorphous-to-crystalline temperature, allowing for heat treatments above 600°C. The ratio of zirconia to tantala is calculated as $Zr/(Zr+Ta)$. Prasai *et. al.* [3] conducted an assessment of the $Zr/(Zr+Ta)$ atomic ratio, and how it affects the final coating material and deduced that even though Zr is beneficial as a dopant, if the concentration of it is too high (≥ 0.48), it can form a separate ZrO_2 crystalline form. The concentration of the dopant material within the coatings developed in the prototype system was of high interest, due to the uncertainty of the atomic ratio of the two materials. In the case of the multiple ion source system, the use of multiple targets, as well as the appropriately chosen deposition parameters for each gun had enabled a predictable ratio. In this case it could be estimated as 33% ZrO_2 to 67% Ta_2O_5 (two operational ECR sources on the tantala target and one on the zirconia target, running at the same deposition parameters).

Coatings deposited on the prototype system had compositional analysis performed on them using an Electron Probe Microanalyser (EPMA). Different temperature depositions' substrates were tested and the results concluded a composition of 72 ±1% Ta, 15±1% O and 9± 1% Zr. Visibly the sum does not add up to 100% of the total mass. Due to an issue with the calibration of the instrument, an accurate estimate could not be conducted. It was speculated that those remaining 4% could be attributed to argon as it was the main ingredient during the depositions, however, that was not verified. Alternatively, the coatings from the larger system were measured using an electron microscope. Similarly to the EPMA, the full picture of the deposited coatings could not be painted as the EDS setup did not have the ability to measure element concentration for element with a lower atomic number than sodium. Therefore, the oxygen content could not be estimated. However, it was observed that within several coatings Ta $\approx$ 62% of the material, Zr was 34±0.5% and Ar was $\approx$3.5%. These measurements proved the prior 33% ZrO_2 : 67% Ta_2O_5 estimation within 10% of the actual composition.

Due to the calibration issue with the EPMA, only an estimate was available for the composition of the coatings developed within the prototype system. However, their consistency verified the repeatability of the coating runs, irrespective of the mobility of the target. Therefore, it was deduced that the $Zr/(Zr+Ta)$ atomic ratio of the elevated temperature depositions was approximately 0.21±0.05. For the case of the multiple target depositions, that ratio was estimated to a value

of $\approx 0.36 \pm 0.05$.

Through these results it was deduced that levels of doping material within both coating sets did in fact contain zirconia and furthermore the concentration of the dopant material had not exceeded the concentration limit. Therefore, the developed coatings were expected to remain amorphous when annealed at temperatures higher than 600°C.

5.3.2 Deposition angle impact on Q factor
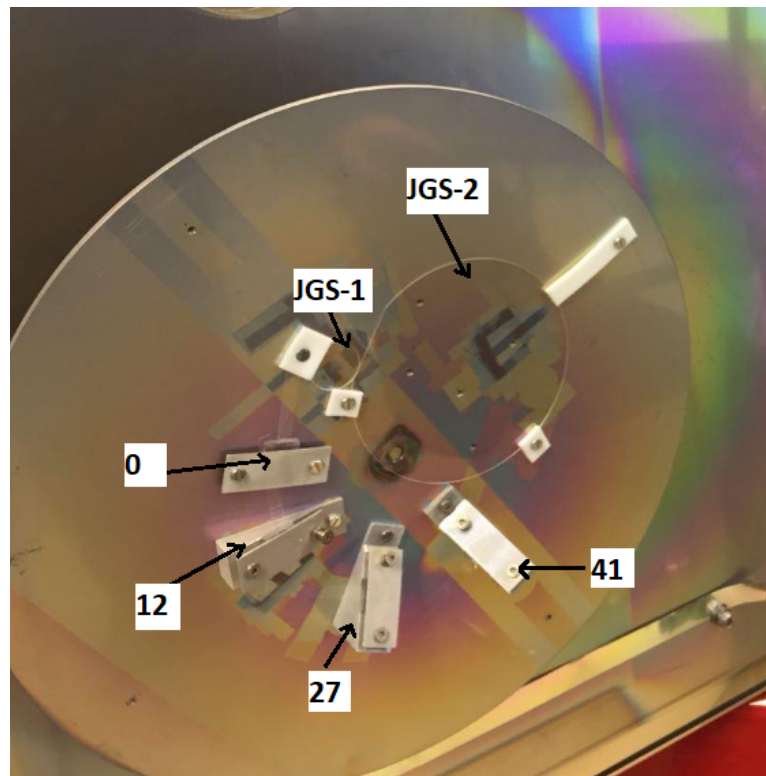
Figure 5.2: Visual representation of deposition setup on multi-sourced ECR system. The rotational stage was attached to the door of the vacuum chamber, such that once closed, it was in close proximity to the two targets. As deduced, the angles were not as pre-decided, but were at 0°, 12°, 27° and 41° with relation to the plate. At the higher angles, lower deposition rates were detected, which can also be attributed to the decrease in uniformity of the optical coatings.

The system utilising multiple ECR ion sources had been newly developed, hence the deposition parameters set had not been compared to the deposition rates. Furthermore, uncoated substrates were placed on a rotational stage in order

to improve uniformity of the new coatings, something which was not achievable in the prototype system.
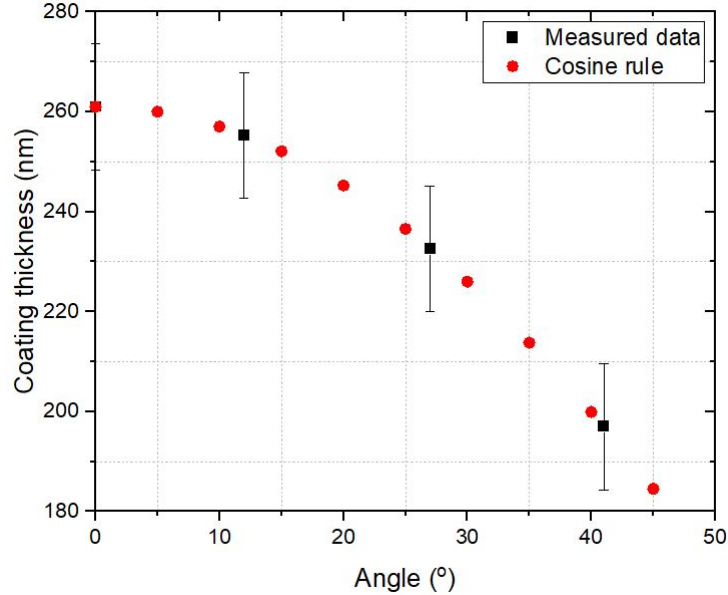
Figure 5.3: Characterisation of the deposition rate in respect to the alternative clamping angles. As expected the thickest coating (highest deposition rate) was exhibited in the sample, clamped normal to the plane. With increasing angle, the coating thickness decreased as expected. Red points present expected coating thicknesses based on the cosine rule.

The ultimate positions of the target with respect to the beams and the un-coated substrates, as well as the position of the clamping block in relation to the target, had been determined for the single sourced system. In the case of the new system, the addition of more than one gun as well as the multiple targets complicate the positioning of the target holders. Since several guns were positioned on a single wall of the system, they had been placed at an angle to one another to allow for all beams to successfully deposit using the same target. Since the multiple gun system is one of a kind, no prior research had been obtained relative to the alignment of the coating setup. For that reason, an experiment was conducted using four cantilever samples and a JGS-1 and JGS-2 discs. All substrates were attached to a circular stage connected to a motor, which enables the rotational movement. The angles at which the cantilevers were attached to the plate were 0° (parallel to the surface of the plate), 15°, 30° and 45°. Previous studies performed on coatings produced via magnetron sputtering [**magnetronangle**], which had shown that alternative deposition angles cause an effect on the material properties of the coating. In order for the substrates to be held at an angle

POINT SOURCE   SURFACE SOURCE
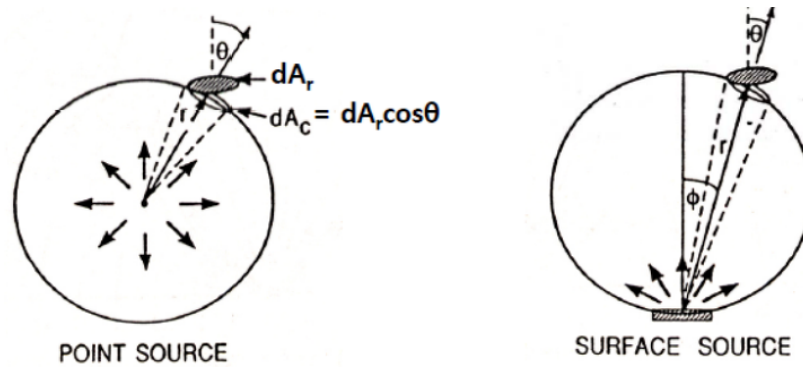
Figure 5.4: Deposition geometry. Thin film deposition involves consideration of both the source of atoms and substrate upon which they impinge. Different deposition geometry affects the film uniformity. Considering the simplest case of a point source, the evaporated particles are imagined to originate from an infinitesimally small region (dA_r) with a uniform mass evaporation rate. This in turn results in deposition being a function of the geometric orientation of the substrate. This technique is usually utilised in physical vapour deposition (PVD) processes. This approach was undertaken for depositions at different angles using IBS technique to deduce if the same relation as in PVD processes apply. Image reprinted from [171].

in relation to the plate, special clamps were designed, increasing the incline of the clamping block with respect to the plane of the plate. Figure 5.2 shows an image of the pre-deposition substrate setup. The values of the angles were chosen such that through the measurement of the coating thicknesses, using the cosine rule (Fig. 5.4), the exact inclination of the clamping blocks can easily be determined. In order to deduce whether an alternative deposition angle would provide a more uniform coating which in turn in to be less lossy, zirconia doped tantala coatings were produced using two oxide targets. Two of the guns, positioned on top of each other, were aimed at a tantala target, and the remaining one gun was aimed at a zirconia target. At the time of the test, only three ECR sources were properly operating. A coating run using Ar/O_2 sputtering was conducted with a duration of 42 hours. Following the completion of the deposition process, the coating thickness on each of the cantilevers was measured directly using cross-sectional SEM measurements. Figure 5.3 shows the relationship between the deposition angle and the estimated thickness of the coating. It was observed that with the increase of the incline with respect to the stage plate, the thickness of the coatings decreased, hence each cantilever exhibited a different deposition rate. Through those measurements it was deduced, however, that the samples were not at the assigned angles. Using the evaluations of the coating thicknesses, it was calculated that the corrected angles corresponded to 12°, 27° and 41°,

considering the 0 degree remaining unchanged. This might have occurred due to the preciseness of the clamping components.

Additionally to the deposition rate study, mechanical loss characterisations were performed on the four cantilevers to study whether different deposition angles lead to an improvement of the quality of the coating. The difference in deposition rates, combined with the similarity in mechanical loss concluded that altering the deposition angle has such a small contribution to the loss of the coatings, that preserving the prior, normal to the plate, attachment was deemed acceptable and hence was not further altered.

5.3.3   Absorption

Ta_2O_5 deposited using ECR ion sources has already validated its ability to reach sub ppm levels of absorption. The addition of the dopant ZrO_2 enables the higher temperature heat treatment proven to have a positive outcome on the optical and mechanical properties of materials. Even though zirconia-doped tantala was expected to produce highly reflective coatings, absorption measurements were performed to ensure the usability of said materials for gravitational wave detectors.

The characterisations were performed on the witness samples, coated simultaneously with the cantilevers using a Photo-thermal Common-Path Interferometer at the University of Glasgow, performed by Simon Tait. The absorption was measured as deposited and following heat treatments limited to temperatures lower than 800°C, following an analogous heat treatment procedure to the annealing of the cantilever samples. It was observed that for coatings deposited at room temperature, the absorption measurements had a wide variation between 10 and 40 ppm, where the minimum value measured was 12.4 ± 3.1 ppm for a wavelength of 1064 nm. Additional measurements were performed on coatings of higher deposition temperature (up to 400° C), showing an average absorption value of 25 ± 1.6 ppm for samples with no additional heat treatment. Following a thermal processing at 750°C it was deduced that irrespective of the deposition temperature, the average value of the absorption increased, however, variation between values decreased. This reduction of uncertainty can be attributed to the stress relaxation of the coating, providing better coating uniformity of the surface, hence reducing the uncertainty. It has been previously thought that due to low deposition rates of ion-beam sputtering using ECR ion sources, their use leads to the production of lower absorption coatings.

Measurements, obtained at room temperature and elevated temperature depositions of $ZrO_2 : Ta_2O_5$ showed similar absorption levels to alternatively deposited oxide coatings [3, 172]. A more detailed study can be performed to further investigate how the absorption varies as a function of the coating deposition rate.

5.3.4 Thermal treatment

Unlike crystalline materials, amorphous materials lack an overall structural description, which makes these materials more difficult to optimise structurally. However, thermal annealing had been shown to reduce the residual stress of the sputtered films. Furthermore, thermal treatment can induce a slow amorphous-to-crystalline transition, a process which can be associated with additional oxidation during annealing. Undoped tantala coatings have been determined to remain amorphous up to temperatures of 600°C (see Sect 4.3.3), however, higher annealing temperatures have shown to further induce deviation from homogeneity which can be attributed to the structure beginning to organise itself into regions of higher order [139]. It has also been suggested that this increased ordering affects the number and magnitude of defects forming double well potentials at boundaries between para-crystallites [139]. It is deduced that the energy barrier between two metastable states appears low for such defects, therefore it is expected for elevated temperature deposited films to exhibit a lower overall loss compared to room temperature depositions. Using zirconia as a dopant for tantala has been shown to suppress crystallisation allowing for thin films to be annealed up to temperatures of 800°C [169].

To test these findings, different zirconia/tantala deposition ratios were studied, where the variations in parameters further included deposition temperature and heat treatments.

Pre-annealing

The mechanical loss of the Zr doped coatings was measured prior to any annealing treatment as well as following each annealing step. It is known that doping with Zr enables the suppression of the crystallization but also affects the polyhedra structure of the material. In general, the atomic structure of amorphous materials can be described in terms of short and intermediate range order (SRO and IRO), where SRO generally describes the structural order up to the first coordination sphere, and IRO describes the structural organisation that is intermediate between the discrete chemical bonds described in the SRO and the periodic lattice of the long range order, characteristic of crystals [3]. The structure of the doped material can also be described as a system of metal centred coordination polyhedra that have oxygen atoms at their corners. The difference in Ta-O and Zr-O bond lengths is contributory to the frustration of the crystallisation of tantala [173]. Annealing affects both SRO and IRO, however, whilst in SRO there are miniscule changes, in IRO there is a significant change, observed in the increase in the M-M (metal-metal) correlation lengths.

A corner-shared polyhedra such as silica [3], has very low mechanical loss at room temperature measurements and high loss measurements at low tempera-

tures. Zr, however, leads to the increase in the fraction of edge-sharing polyhedra, which leads to an increase in mechanical loss at high temperatures. Therefore, the doping percentage of zirconia within the coating, can affect the overall loss. If the zirconia content within the coating is too high that leads to an increase mechanical loss even at room temperature measurements. The compositional analysis of the coating was already conducted, yet it remained unknown whether the doping percentage exceeded the required to keep the mechanical loss low. In order to investigate whether the doping percentage is low enough, before any heat treatments are performed on the coatings, the ring-downs of the cantilever vibrational modes were measured to compare with prior un-doped tantala coatings. The samples were measured between ≈ 1 Hz and 20 kHz, where this range varied depending on the individual cantilever. Figure 5.5 shows the averaged results for each coated sample, where the error bars are a representation of the standard deviation between losses for each mode. It was discovered that the losses appeared consistently between high 10^{-4} order and 1×10^{-3}, which matched prior results obtained by alternative groups [3]. In comparison to the pure tantalum pentoxide coatings from Chapter 4, the losses appear approximately two times lower at an approximated value of $\approx 3 \times 10^{-4}$ rad. Additionally, the set of coatings presented
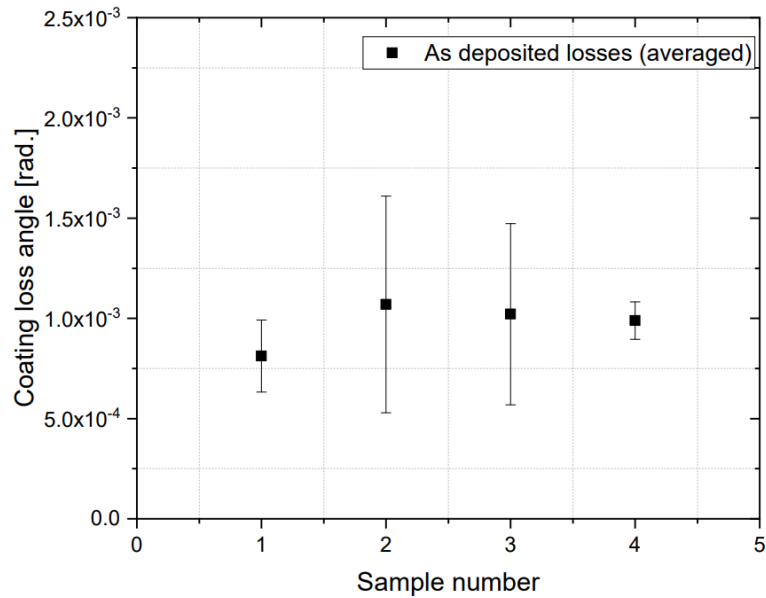
Figure 5.5: Mechanical loss angle for ZrO_2 doped Ta_2O_5 deposited at room temperature using a Ta_2O_5 and ZrO_2 targets. Averaged data presented on plot, confirming a consistency in the loss prior to any thermal processing. Error bars represent the standard deviation for the losses for all the modes. For samples 2 and 3, there is a larger error bar spread due to the larger number of modes which were detected and measured.

here were coated by the multiple source system, which utilized a tantala and a zirconia target. The prior pure Ta_2O_5 coatings had been deposited on the prototype system. Therefore, comparing the two deposition rates might explain the factor of 2. For the pure coatings at room temperature, the deposition rate was averagely approximated at 11 nm/hr, whereas in the multi-sourced system that rate was averaging as $\approx$ 6 nm/hr. Therefore, the deposition on the multi-sourced system was two times slower than the prototype system, which can be correlated to the factor of 2 in averaged pre-annealing losses.

Elevated temperature depositions
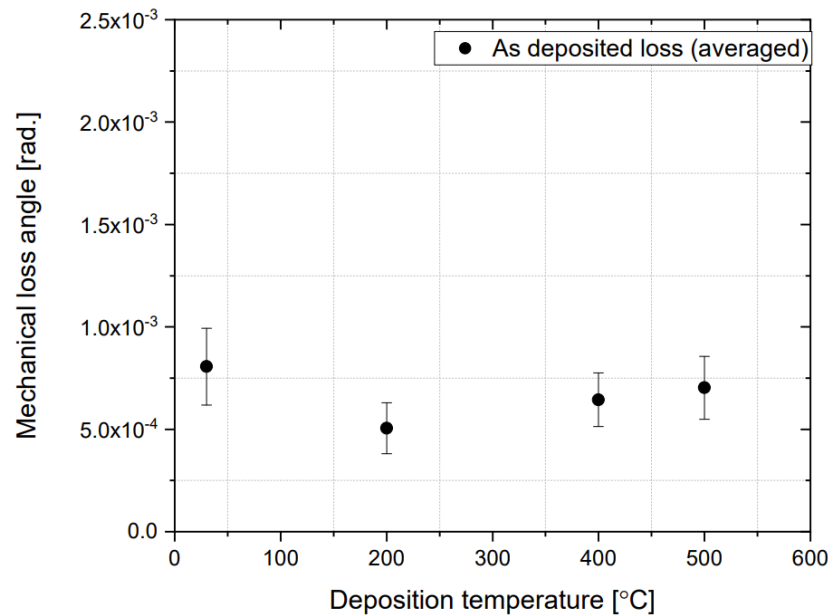
Figure 5.6: Mechanical loss angle for ZrO_2 doped Ta_2O_5 deposited at alternating temperatures using a Ta_2O_5 target with Zr foil attached to it. Expected ratio of Zr/(Zr+Ta)$\approx$0.33. The data plotted are the averaged result for each deposition temperature, where at each step there were 2 or more samples. Modes measured varied in frequency from $\approx$ 1 Hz up to 15 kHz. Error bars were estimated based on the losses for all the modes for samples deposited at the specific temperature. Overall, as deposited losses remain between 5×10^{-4} and 1×10^{-3} rad. Average loss decreases between room temperature and 200°C, similarly to the case of un-doped tantala coatings.

Analogously to the pure tantala coatings discussed in the previous chapter, elevated temperature depositions were tested for the doped coating material. The temperatures at which depositions were performed were room temperature,

200°C, 400°C and 500°C. Due to the inability of both system to perform elevated depositions, all higher temperature coatings were developed in the prototype system, utilising a single ECR ion source. Even though all deposition parameters were kept constant, from the inflows of both argon and oxygen, to the current density of the ions within the plasma, there was a variation within the coating rates. The deposition rates ranged from $\approx$ 11 nm/hr to 22 nm/hr, where the lowest and highest rate were a room temperature and a 500°C respectively.

Figure 5.6 shows the averaged mechanical loss data characterised prior to any post-deposition heat treatment, where each data point represents the averaged loss for that deposition temperature and the error bars represent the standard deviation of that data set. At first glance, it is noticeable that the lowest loss was obtained for the coatings performed at 200°C. For higher temperatures the average loss gradually increases. Secondly, one can compare this set of doped coatings to the pure tantala coatings in chapter 4 (Figure 4.9), the losses appear to be following the same trend-line with increasing deposition temperature, *i.e.* a decrease in mechanical loss as the deposition temperature increased. In the case of the pure material, a drop in the mechanical loss angle was observed at 200°C. Similarly, for the elevated temperature depositions of zirconia doped tantala, there is a lowering of the average mechanical loss observed at the depositions at 200°C. On average, the as deposited losses for the doped tantala coatings varied from low 10^{-3} orders to 10^{-4} orders. Furthermore, similarly to pure Ta_2O_5 elevated temperature depositions, a decreasing trend was observed in between losses for coatings developed at RT and at 200° C, with the higher temperature deposited films showing a decrease in average mechanical loss. The average loss determined for the tantulum pentoxide coating derived from an oxide target at 200°C averaged on $\approx 2.5 \times 10^{-4}$, where in the case of the zirconia doped coatings deposited at the same temperature, that loss was estimated as $\approx 5 \times 10^{-4}$. The difference between the losses, factor of 2, could be explained due to the addition of zirconia as a dopant in the coating. *Prasai et. al.* [3] reported that the addition of zirconia leads to the increase of the fraction of the edge-shared polyhedra, which leads to an increase in the mechanical loss for measurements at room temperature. However, the inclusion of ZrO_2 enables the suppression of the crystallisation of the coating, allowing for heat treatments at higher temperatures, speculated to reduce the mechanical dissipation.

Post-heat treatment

Zirconia-doped tantulum pentoxide coatings were developed on two IBS systems utilising (an) ECR source(s). The smaller system, often referenced as the prototype, employs an ECR ion source, and the coatings are deposited from a tantulum pentoxide target with a Zr foil attached to its surface (Figure 5.1). The foil was placed in the centre of the beam spot, created from previous depositions. It was

expected that the Zr would contribute a fifth of the coating composition. The larger system, employed three ECR sources, where two were aimed at a tantala target and the third one was aimed at a ZrO_2 target. This increases the aspect ratio of Zr/Ta, in comparison to the smaller system, where in this case a ration of $\approx 30\%$ was expected. Room temperature depositions were performed in both systems, which allowed for a comparison of the quality of production of each system.

It was known that after the introduction of ZrO_2 as a dopant, the temperature at which the samples could be treated whilst remaining in an amorphous state, would increase. However, prior to this study, ZrO_2/Ta_2O_5 had not been deposited using an ECR ion source IBS. This alternative technique of deposition differs in respect to the deposition rate of the sputtered coatings, in comparison to alternative deposition techniques, therefore affected the packing density of the thin films. In addition, it was unknown what the elemental composition of the coatings was, *i.e.* what was the ratio between tantulum pentoxide and zirconium dioxide. Therefore, previous research concerning the crystallisation temperature of such coating were deemed irrelevant, and an additional study had to be done to determine the highest annealing point prior to the thin film reaching a crystallised state. It was deduced that after thermal processing at 825°C, the coatings no longer remained amorphous. Therefore, it was established that the amorphous to crystalline transition temperature was at values lower than 825° C, and higher than temperatures of 800° C. For the following studies, lower temperature increments were utilised to enable a more exact diagnosis of the transition temperature limit. The annealing study surmised that up to temperatures of 810°C, coatings remained amorphous, therefore for the purpose of this thesis, the maximum annealing point was taken as 800°C for coatings deposited on both systems.

Figures [5.6] and [5.7] present the averaged results of the mechanical loss of the coatings post annealing. For the system using the foil as a dopant, the lowest average losses were obtained following a heat treatment at 600°C. However, once the individual modes were explored, it was deduced that at temperatures of 750°C, the data point had a larger variation which is visible in the range of the error bars. Following this assortment, the temperature showing the lowest losses was deduced to be 750°C. Similarly, the coatings developed in the double-targeted system underwent higher temperature treatments, and the lowest average loss was deduced to be at 750°C.

Based on initial analysis, there is no obvious trend with increasing temperature in the case of the prototype system. It was expected for the coating loss angle to decrease with the increase of the annealing temperature, with an optimum heat treatment at 750° C. For the larger system, the data follows an exponential parabola, with the lowest average loss angle obtained at 750°C. Therefore, if the

measurements from the two sets of coatings are imposed upon another, they differ only at their dipping points, *i.e.* 600°C and 750°C.

This discrepancy can be attributed to multiple factors - the target utilised in the system, the geometry of the setup, the addition of rotation to the substrates. The difference in target materials had been acknowledged, therefore there is a high possibility that there difference between the two sets arises from the different material ratios.
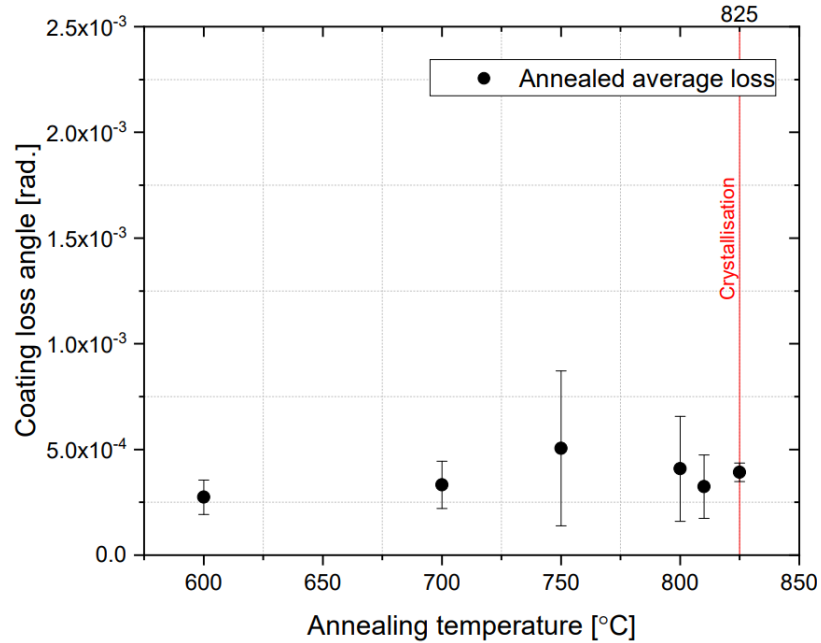
Figure 5.7: Estimation of the mechanical loss of zirconia doped tantala, deposited on the prototype singular ECR ion source system, following heat treatments up to 825°C. On average, the lowest loss detected was obtained following thermal processing at 600°C, which is the maximum annealing temperature for un-doped tantala. However, inspecting the data enabled the conclusion that lowest losses were obtained following heat treatments at 750°C, which also explains the larger error variation on that data set. Initially annealing was performed at increments of 50 °C. Crystallisation was expected to appear at temperatures larger than 800°C [169], therefore once that temperature was reached, following increments were every 25 °C, which proved to be a value at which the coatings no longer remain amorphous. An intermediate step at 810°C was taken for the remaining samples, and it was deduced that all coating remained amorphous.
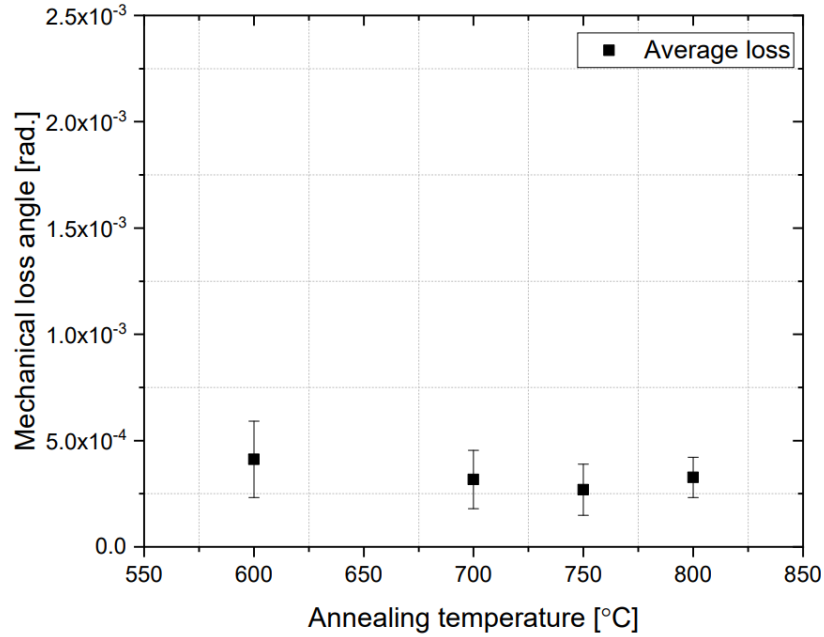
Figure 5.8: Estimation of the mechanical loss of zirconia doped tantala, deposited using multiple ECR ion sources, following heat treatments up to 800°C. The coatings were deposited from a tantala and a zirconia target, where two of the three guns were aligned with the Ta_2O_5 target, and one was on the ZrO_2 target, producing a 33% doping. On average, the lowest loss detected was obtained following thermal processing at 750°C. Using the priorly deduced crystallisation temperature, the samples were treated at 50°C increments up to a temperature of 800°C. All losses appear lower than $5x10^{-4}$, which is an improvement comparatively to the doped coating using the prototype system. Furthermore, the data spread had decreased, therefore, leading to smaller error bars, where the error bars represent the standard deviation of the loss measurements.

Incremental annealing

Once the maximum annealing temperature for zirconia-doped tantala coatings was obtained, a new study was initiated to understand how this maximum heating point alternated for different depositions. In order for that to be achieved, two silica cantilevers, and two JGS 1 discs were simultaneously coated using the multi-sourced ion-beam system for a duration of ≈ 16 days. The two witness pieces enabled the measurement of the coating thickness without directly damaging the surfaces of the cantilevers. Mechanical loss measurements were performed on both cantilevers before any thermal treatment. Furthermore, both substrates were heat treated at the same time, minimising the risk of discrepancy. The thermal processing was performed at 100°C increments, up to a temperature

125
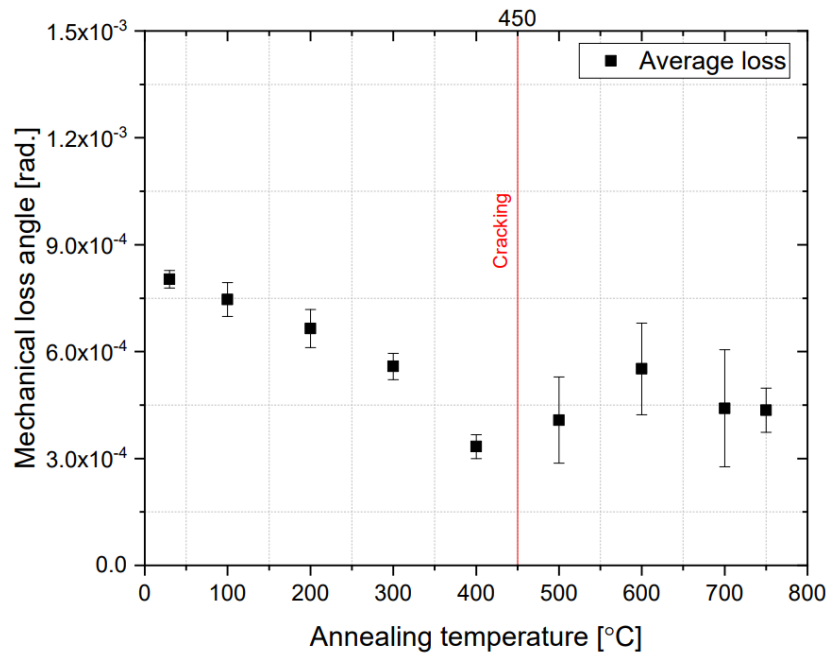
Figure 5.9: Mechanical loss of zirconia doped tantala, deposited using multiple ECR sources. Two substrates were simultaneously coated, and then heat treated at 100°C increments (at the same time), until a maximum annealing temperature of 750°C. The annealing was not continued for higher temperatures as from Figure 5.8 it was deduced that the lowest loss appears following a heat treatment at 750°C. Following the thermal processing at 500°C, the surface of the substrates appeared disturbed, where cracks had appeared. It was deduced afterwards, that this lead to a less concentrated set of loss values, thus larger deviation between measurements. Furthermore, the vibrational modes' ring-downs became more difficult to obtain, which resulted in fewer data points. The losses followed a decreasing trend, until the point at which the coating surface had been damaged.

of 700°C. The remaining two heat treatments were performed at 750 and 800°C respectively. Figure 5.9 presents the evaluated mechanical loss of the two coatings, where up to a temperature of 400°C the loss values followed a declining in loss trend.

It had previously been observed that for coatings deposited on cantilevers, after annealing at 500°C, the stress on the surface of the cantilever, due to the thin film coating, relaxes. Figure 5.10 shows the same sample, before any heating had been performed onto it (top), where the bottom picture demonstrates how post annealing, the ribbon of the cantilever no longer appears curved. However, the change in stress distribution was accompanied with micro-cracks appearing on the surface of the cantilevers (Figure 5.11). As the heat treatments progressed,

126

the cracks appeared to propagate further throughout the coating. Concurrently, the evaluation of the mechanical loss became troublesome, which was attributed to the scattering of the laser light hitting the edge of the cantilever. For the previous ZrO_2:Ta_2O_5 coatings no such event was observed.

Previous reports showed that the introduction of zirconia into the tantala coatings can improve the composite strength in terms of high temperature performance [174]. The improvement in mechanical properties is attributed to the martensitic phase transformation of the zirconia particles from the tetragonal to the monoclinic phase, which is generated at temperatures between 500°C and 750°C due to a volume change. This change in volume causes an expansion of the zirconia crystals that hinder the propagation of cracks[175]. Furthermore, micro-defects had also been observed in pure Ta_2O_5 coatings [176]. It was deduced that as the annealing temperature was increased, micro-defects appeared due to densification of the tantulum oxide [176]. It was not deduced whether those micro-defects in the doped coatings appeared due to the higher zirconia content, the annealing rate, or cool down rate. Further investigations are required to clarify the origin of the cracking of the optical coatings.

Figure 5.10: Side-view images illustrating the changes in thin film stress on the silica cantilever resonators. The upper image represents the stress on the cantilever due to the deposited coating with no heat treatment. The bottom image illustrates the change in stress after a heat treatment at 500° C.

5.4   Summary

The coatings currently employed within the Advanced LIGO detectors consist of TiO_2/Ta_2O_5. The requirement for the next upgrade for the observatory requires the optimisation of the coating loss by a factor of 4, or by a factor of 2 reduction in the strain noise. Previous coatings deposited using the two systems at the University of Strathclyde had shown improved optical and mechanical properties.
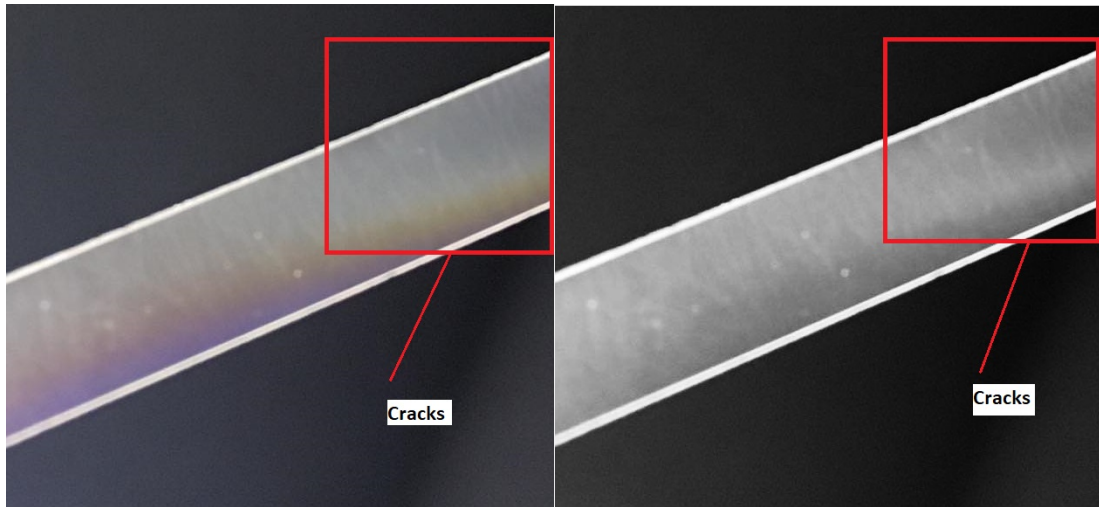
Figure 5.11: Micro cracks visible on the surface of a coated silica cantilever following a heat treatment at 500° . Left picture is original image of sample. Right image is a black-white version of picture with an increased contrast to enable the visibility of the micro cracks. These micro cracks appeared as a result of the change in stress distribution post heat treatment. Further heat treatments lead to further propagation of said cracks, resulting in increased light scattering which obstructed mechanical loss measurements.

Hence it was deemed reasonable to attempt the deposition of a doped coating material on the two systems. The use of both systems allowed for the exploration of elevated temperature depositions, alternative deposition angles and various material ratios. Instead of using titania as a dopant however, zirconia was chosen as the additive material. It had been proven that the addition of zirconia into the tantala coatings enabled the heat treatments of the coatings to a higher temperature, which has been proven to reduce the optical absorption in thin film coatings. Furthermore, previous thermal processing of the tantala coatings had been limited by the crystalisation temperature of tantulum pentoxide at 600° C, whereas the doped coatings had been successfully annealed up to temperatures of 800° C whilst remaining amorphous.

Elevated temperature depositions were performed on the prototype system, up to temperatures of 500. The zirconia doped tantala coatings were deposited from an oxide tantala target, with zirconium foil attached to the surface. Upon analysis it was deduced that estimated doping ratio averaged at 0.3. The addition of a dopant allowed for higher annealing temperatures, reaching a maximum of 800° C. Above such temperatures, coatings no longer remained in amorphous state. Similar to pure tantala coatings, higher deposition temperatures contributed to less lossy materials, with an optimum deposition temperature of 200° C. Post thermal

treatment, coatings exhibited average losses $\approx 1.89 \times 10^{-4}$, with an minimum loss measurement of 1.59×10^{-4} per individual mode.

Depositions performed on multi-sourced system incorporated the use of separate oxide target to achieve an approximate 33% zirconia doping. Two of the ion guns were aimed at a Ta_2O_5 target, and one was aimed at zirconia target. Following elemental analysis, the estimated material ratio was below 0.48 as implied in [3], therefore there was no expected crystalline phase change. Analogous to coatings developed in prototype system, deposited films remained amorphous when treated at temperatures up to 800° C. Post thermal treatment, coatings were estimated to exhibit losses of $\approx 2.68 \times 10^{-4}$, with a minimum loss measurement of 4.00×10^{-5}. The difference observed in the losses from the two systems originate due to difference in coating deposition rates in each system, with prototype system exhibiting 4.6 times faster deposition rate. Slower deposition rates are likely to produce more densely packed structures, leading to a lower loss. The difference in deposition rates between two systems could also be responsible for cracks appearing on sample surface 5.9, 5.11, which had not been observed for coatings deposited on the prototype system.

Comparing the measured losses form both systems, it is evident that elevated temperature depositions lead to coatings exhibiting lower loss, which is 1.33 lower than coatings currently employed at the LIGO observatories. In order for a reduction of a factor of 4 to be achieved, as is required for the next detector upgrade, coatings exhibiting losses app $6 - 9 \times 10^{-5}$ are required. Throughout the characterisation of the coatings developed on multi-sourced system some modes experienced losses in the order of $\times 10^{-5}$ which would be an appropriate reduction 5.12. For the future of gravitational detector mirror coatings it is highly likely that an alternative material would need to be selected, which coincidently has a high refractive index, as well as low mechanical loss and optical absorption at the required wavelength.
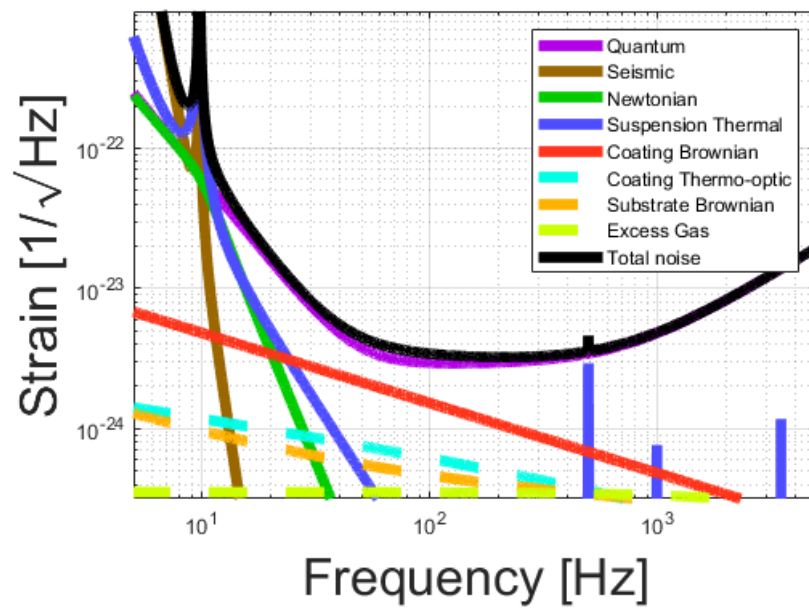
Figure 5.12: Modelling of the coating thermal noise, considering a loss of 4×10^{-5} rad. If this can be successfully implemented, coating Brownian noise will no longer be the limitation to the sensitivity of the detectors at low frequencies.

Chapter 6

Mixed material coatings

6.1 Introduction

Brownian thermal noise is the current obstruction limiting the sensitivity of gravitational wave detectors at frequencies from 10 Hz to *approx* 200 Hz. The currently employed optical coatings within the Advanced LIGO detectors are estimated to have a coating loss of 3.6×10^{-4} rad [177], where the thin films consist of alternating layers of SiO_2 and $TiO_2{:}Ta_2O_5$. For the Advanced LIGO Plus (A+) update, however, the required loss target is estimated between $6 \times 10^{-5} \rightarrow 9 \times 10^{-5}$ rad, which is a value still to be reached by amorphous thin film coatings with appropriate optical performances. The introduction of a dopant into the high index layer material has proven beneficial, as seen in the case of titania [157], which has encouraged the research of multiple materials as dopants into the Ta_2O_5 coatings. The requirement of low mechanical loss is not the only condition limiting the choice of dopant material. High refractive index, higher annealing temperatures and lowering of the optical absorption are still requirements for the Bragg reflector coatings.

The introduction of multiple dopants is a possible alternative to the current high index optical coating. The previous chapter explored the addition of zirconia as a dopant to tantala, which had allowed for the thin films to be heat treated at higher temperatures, whilst the coatings remained in an amorphous state, leading to a reduction in the mechanical loss, reducing the potential coating thermal noise. On the other hand, the inclusion of ZrO_2 had led to an increase in the optical absorption of the coating hence doping ratio was deemed of high importance. Titania was introduced as a dopant following results presented by G. Harry *et. al.* , where the motivation for the material mixing arose due to the high index of TiO_2, and where the Ti atomic size allowed for a more densely packed Ta, Ti and O matrix [157]. Furthermore, the introduction of Ti increased the melting point of the material, allowing the thin film to retain a more stable amorphous

state upon heat treatment, as well as contributing to the increase of the refractive index.

The doping of Ta_2O_5 with both ZrO_2 and TiO_2 was considered. The addition of both materials has proven beneficial for the reduction of the coating loss angle, however their inclusion also leads to an increase in the optical absorption, therefore, low concentrations of dopants are needed for optimum improvements. The choice of material ratio will aim to simultaneously reduce the mechanical loss of the high index material whilst retaining a low optical absorption.

This chapter covers the deposition of ZrO_2:TiO_2 doped Ta_2O_5 coatings produced through the usage of multiple ECR ion sources. The depositions were sputtered from a Ta_2O_5 target with, two guns aimed at its surface, and a ZrO_2 target with the addition of two sectons of titanium foil on the surface, where only one gun was utilised on the dopant materials. The addition of Ti was performed in a similar manner to the production of a doped coating on the prototype system. The mechanical and optical properties of the new materials were investigated, including the monitoring of the composition of the thin films, which can lead to a modification in the refractive index of the material as well as the shift in the amorphous-to-crystalline transition temperature.

By comparing the newly developed dually doped material to priorly deposited pure and mixed materials, this chapter will not only provide an insight into development of multi-material mixtures but furthermore will deduce the suitability of a multi-doped coating material for the A+ detector update.

6.2   Thin film deposition

Two deposition runs were performed on the multi-sourced ion-beam system. The first run (B19D2614) contained two cantilevers, a JGS-1 witness piece and a JGS-2 disc. The second run (B19E1615) contained only one cantilever, 2 JGS-1 discs, and 1 JGS-2 disc. During the depositions all 4 ECR sources were utilised. Two of the sources were aimed at the Ta_2O_5, one source was aimed at the doping target, and one was employed in the form of a neutraliser, *i.e.* an electron gun. High current ion beams contain low energy electrons which are generated by collisions with neutral particles, vacuum chamber walls and the target(s). The electrons neutralise the ion beam charge and help keep them from diverging. Therefore, if not supplied with negative voltage, low energy electrons would get discharged in the plasma cavity and the ejected ion beam will strongly diverge. Hence, the utilisation of one of the ECR sources as attentive to the discharging during the coating process [178]. Since there was only ZrO_2 and Ta_2O_5 targets, a similar approach to section 5.2.2 was taken, where the second dopant was added via an attachment of Ti foil on to the surface of the zirconia target. Based on the deposition setup, films were expected to consist of $\approx 67\%$ Ta_2O_5, and $\approx 33\%$ of

ZrO$_2$ and TiO$_2$. This elemental ratio was expected due to the sputtering yield of the coating materials. It was deduced [179, 180] that a sputtering rate expected for a tantulum pentoxide is 0.195 nmm$^{-1}\mu$Acm^{-2}, whereas for zirconium dioxide the sputtering rate was 0.120 nmm$^{-1}\mu$Acm^{-2}. These sputtering rates entails a 17% difference in sputtering yield between the two oxides. However, for the titanium dioxide contribution, pure Ti was used, studied to have a sputtering rate of 0.235 nmm$^{-1}\mu$Acm^{-2} [180], which is expected as metals exhibit a larger sputtering rate in comparison to oxides. Figure 6.1 shows the setup for both depositions, where the positions of the targets were not changed between the two coating runs. In both coating runs the substrates were attached onto the

Table 6.1: Parameters of ZrO$_2$:TiO$_2$ doped Ta$_2$O$_5$, deposited at room temperature, within the multi-sourced ion beam system

Deposition run	B19D2614	B19E1615
Extractor current Gun 1(mA)	0.67	0.68
Extractor current Gun 2(mA)	0.25	0.20
Extractor current Gun 4(mA)	0.19	0.19
Duration (hrs)	384	356
Coating thickness (nm)	1440	1162
Deposition rate (nm/hr)	3.75	3.26

rotational stage at the door of the vacuum chamber. The deposition parameters were kept constant for both runs and a summary of them is detailed in table 6.1. The base pressure of the vacuum chamber for both coating runs was $\approx 1 \times 10^{-5}$ mbar, where after the injection of argon through the ion sources and the neutraliser that pressure rose to $\approx 8 \times 10^{-5}$ and reached its highest point of 1.3×10^{-4} mbar with the addition of oxygen in the background. The thicknesses of the coatings had been directly measured on the surfaces of the JGS 1 discs, using a DekTak technique, establishing an average deposition rate of ≈ 3.5 nm per hour. The deposition rate was similar to the rate of coating run B19B0817, proving the improved consistency and repeatability of the coating runs on the larger coating system, following the employment of one of the ECR sources as an electron gun.

6.3 Results/Discussion

6.3.1 Composition

Doping Ta$_2$O$_5$ with both ZrO$_2$ and TiO$_2$ has been proven beneficial to the mechanical and optical properties of the material. However, an increased doping

Figure 6.1: Target setup for deposition of ZrO_2:TiO_2 doped Ta_2O_5 coatings within the multi-sourced ECR ion beam system. On the left is a tantulum pentoxide target, positioned such that two guns can simultaneously meet the target. The two darker spots on the target surface present the positions at which each gun hits the target. On the right, is a ZrO_2 with two Ti foil pieces attached in close proximity to the position at which the beam collides with the target. Despite the lower indentation on the target including a partial position on the target holder element, no additional contamination by holder was determined.

ratio has been shown to lead to increased absorption [3, 157] in the thin film coating, therefore a doping limitation is implied. The mixing ratio boundary has not been examined, therefore following each of the deposition runs, elemental analysis was performed on the doped coating. It not only enabled the verification of deposition repeatability but furthermore provided an actual limitation to the doping percentage for potential GW mirror coatings. All analysis was performed through energy dispersive X-ray spectroscopy (EDS) using an scanning electron microscope.

The verification of the coating composition was performed on the witness JGS 1 samples present in each coating run. To impose an easy comparison all ratios are presented in the form $(Zr+Ti)/(Zr+Ti+Ta)$, omitting the oxygen quantification. These ratios were then compared to the doping ratio, presented in the previous chapter, which characterises the differences due to the addition of TiO_2. It was deduced that within both coating runs, the elemental ratios were approximately 0.12 ± 0.01, where on average the Zr attributed to $7.5 \pm 0.5\%$ of the atomic

mass and Ti attributed to 3.8 $\pm$ 0.1% of the total atomic mass. The previous doping with ZrO_2 had shown a three times higher atomic ratio (See Chapter 5), presenting differentiations in the doping percentages. Even though in both setups, the multi-gun system had been operated at the exact same conditions, a difference arises due to the utilisation of fourth ECR source as a neutraliser. The usage as a neutraliser improved the stability of the deposition runs, and since we are unable to monitor the process 24 hours a day, it is unknown whether there were disruptions when system not monitored. Furthermore, for the zirconia doped tantala coatings, Zr was estimated as $\approx$ 33% of the total atomic mass, which was within the doping boundary, as estimated in [3].

By conducting elemental compositional analysis of the dually doped tantala coatings one can not only establish the doping ratio within the thin films, but furthermore it allows for the investigation of changes in the optical and mechanical properties of the material, which can be attributed either to the additional dopant material or the change in ZrO_2 concentration. Since TiO_2 possesses a higher refractive index, comparatively to both zirconia and tantala, the next step of the investigation would be the estimation of said refractive index as a function of not only the doping concentrations but furthermore, how post-depositional heat treatments affect the optical properties of the thin film.

6.3.2   Optical properties

The coating loss angle is not the exclusive concern for newly developed optical coatings. Even though it is acknowledged to have a high impact, requirements cannot be limited to low mechanical loss. The proposal by Harry *et, al* [157], suggested the mixing of tantala with titania would not just lead to a more densely pack coating but also to induce an increase in the refractive index of the doped coating. A higher refractive index would allow the reduction of the total thickness of the coating, decreasing the total coating thermal noise.

Following the elemental analysis of the coatings, one needs to deduce how the addition of the second dopant (TiO_2) affected the refractive index as a function of wavelength. Furthermore, due to the prior depositions of pure tantala coatings as well as zirconia doped tantala coatings, measuring the spectra of the coatings, enables the determination of the optimum conditions, including doping and annealing. The transmittance and reflectance spectra were measured by a photon RT, which spectra was then used in the refractive index fitting, performed by Chalisa Gier at the University of Strathclyde.

Optical transmission

A Photon RT spectrophotometer was used for transmission and reflection measurements on the JGS-1 witness pieces from each coating run. Each sample was
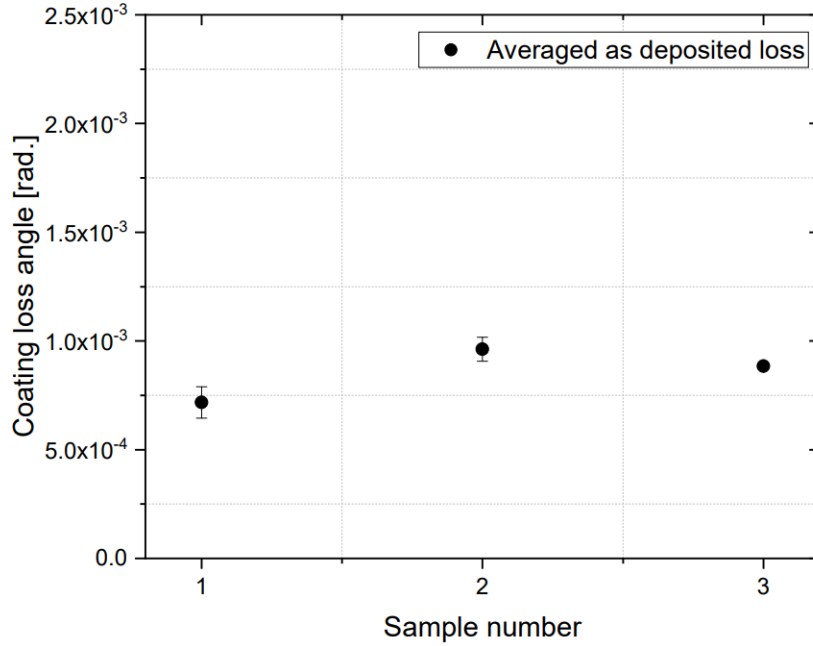
Figure 6.2: Mechanical loss measurements on ZrO_2:TiO_2 doped tantulum pentoxide optical coatings. Figure 6.2 presents the averaged data points for each coated sample, before any thermal practice had been performed on the samples. Similar to previous as deposited studies, losses appear within a reasonable and expected range.

attached to a rotational stage. The sample was then rotated at different angles in accordance to the detector. By choosing a low angle of incidence,close to the near normal angle (0 - 10°), the reflection spectrum of the surface was measured. The angle utilised in this case was 8°. As the position of the light source and the detector cannot be at the same position, the smallest angle possible for the detector was 8 degrees, whereas the sample was rotated to 4 degrees, also known as the specular Fresnel direction [181]. Furthermore, by changing the position of the detector in relation to the incident light, the transmission spectrum of the sample was obtained. Both acquired spectra are representative of the whole disc (substrate + coating). This data was then used to determine the thickness of the coating on the surface of the disc (t_c), the refractive index (n), the extinction coefficient (k) and the absorption coefficient of the coating (α).

The Advanced LIGO A+ coatings are required to be highly reflective, therefore the reflection from the coated discs was of interest. However, the spectrum obtained was corresponding of the full sample, coating and substrate, and since the coating was a lot thinner in comparison to the thickness of the substrate, low reflection and high transmission were deduced. Through the transmission data,
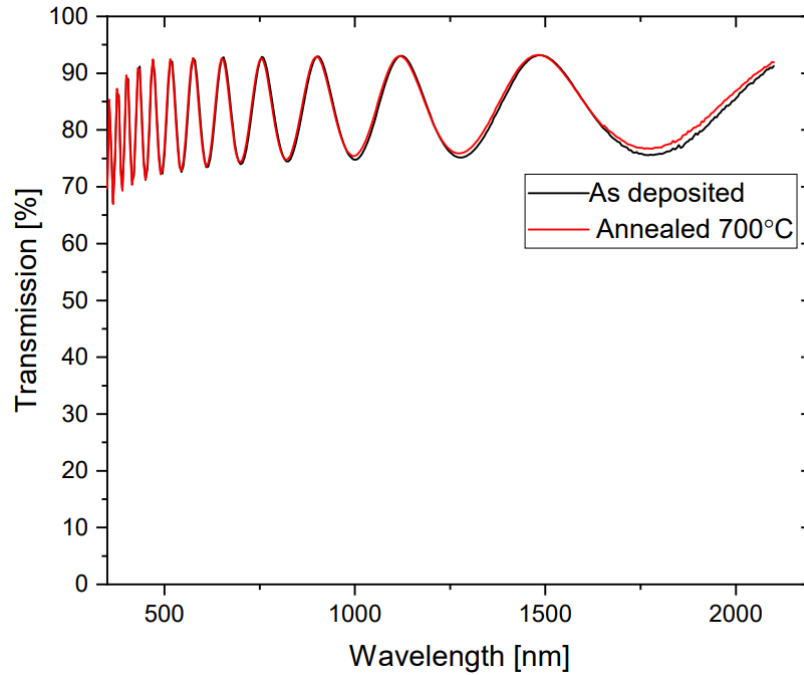
Figure 6.3: Transmission curves as a function of wavelength for a $ZrO_2 : TiO_2 :$ Ta_2O_5 film before and after annealing at a temperature of 700°C. It was deduced that as a consequence of to the heat treatment the transmission of the sample had increased by $\approx 1\%$. One has to consider the multiple reflections within the films. The overall transmission had increased by 1% however, this could be also be attributed to the systematic error of the apparatus. Furthermore, the uniformity of the coating can additionally affect the RT measurements.

one was able to determine the thickness of the coating, and furthermore investigate the effect post-deposition heat treatments have on the optical properties of the coatings.

The variation of the transmission spectrum following a thermal treatment was studied. Figure 6.3 shows the difference between the two measurements. For a wavelength of 1064 nm, pre-annealing the transmittance was corresponding to 84.76%. Following a 5 hour heat treatment at 700°C, at 1064 nm, the transmission percentage was evaluated as 85.64%. Therefore, after annealing the absorption coefficient of the full sample had increased, and since SiO_2 has very low optical absorption, it was deduced that the decrease in reflectance was due to the optical coating, as postulated in the previous chapter. Absorption coefficient is inversely proportional to the transmission percentage, however, as the transmission spectrum measured accounted for the entire sample (substrate and thin film), in order to establish the absorptivity of the film, additional PCI measurements are needed.

137

The transmission and reflection spectra were analysed through SCOUT programme using the OJL2 model [182]. The transmission spectrum acquired was compared to a calculated model, enabling the estimation of the coating thickness and complex refractive index, which is a function of the refractive index and the extinction coefficient of the material, due to multiple variables. Since the refractive index is a function of the reflection property of the coating, the next section will study the evolution of the refractive index due to variations in the elemental composition of the coatings as well as heat treatments.

Refractive index

Through the measurements of the overall reflectance and transmittance of the samples, one has the ability to model and evaluate the refractive index of the coating as a function of wavelength. The reflectance of the coating is dependent on the complex refractive index, which varies as a function of the refractive index and extinction coefficient. However due to the multiple refractions transpiring through the distinct layers of the substrate, including the coating, one cannot simply distinguish the refractive index, exclusive for the thin film. In order for the reflectivity of the coating to be estimated, the acquired transmittance data had to be analysed through the SCOUT Operating language, employing model OJL 2. The measured spectrum was compared to a pre-modelled spectrum, and once a matching model was determined, the refractive index and extinction coefficient of that condition were equated with the values for our coatings. Furthermore, the matching of model additionally allowed for an indirect evaluation of the coating thickness. Previous research has shown that post-deposition heat treatments are beneficial for the reduction of the optical absorption of the coatings [183]. In cases of coatings experiencing low level of oxygen, the additional annealing allows for the oxygenation of the coating, which in turn increases the coating density [184]. However, in cases where there are defects in the structure of the coating, known as voids, the additional thermal processing might enable the enlargement of said voids [185]. For amorphous oxide coatings, the effect of the heat treatments depends on the stoichiometry of the structures. Furthermore, the absorption coefficient is proportional to $ln(T)$, therefore if there is an increase in the coating transmittance, there would be a corresponding increase in the absorption coefficient. Different research groups have acquired opposing data in regards to the variability of the refractive index as a function of annealing temperature. In cases of ion-beam sputtered alternating layers of Ta_2O_5 and SiO_2 deposited using an RF ion-beam deposition technique (Veeco IonTech - Spector), post-deposition anneal affects the coating stress, stoichiometry and density. Coatings generally processed using IBS sputtering experience high levels of compressive stress, which get decreased through post-deposition annealing, however, it was observed that the stress in the tantala did not reduce but inverted to tensile stress [186]. Dif-
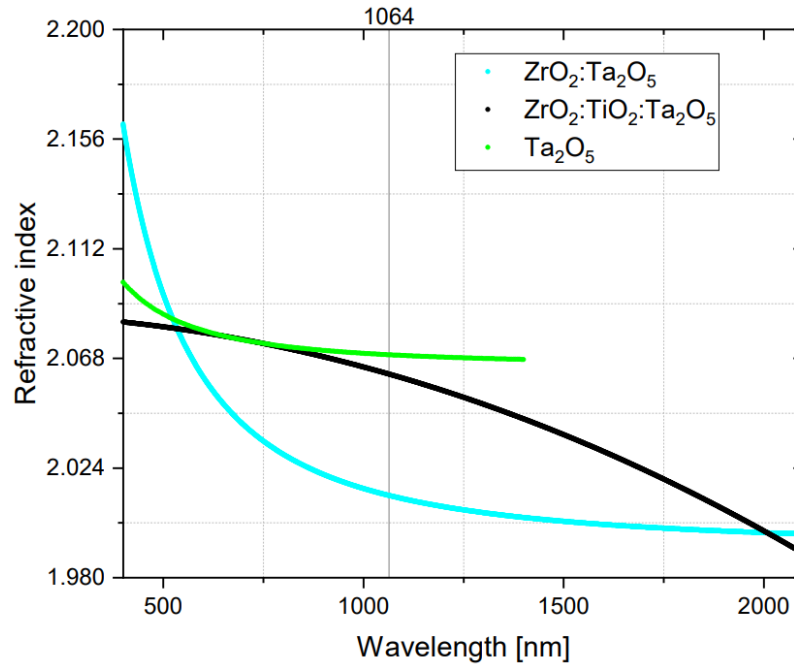
Figure 6.4: Comparison in the refractive index values, between pure tantala, zirconia doped tantala and zirconia:titania doped tantala, deposited using ECR ion-beam deposition. The optimum magnitude was deduced for un-doped Ta_2O_5. The addition of zirconia and titania had been shown to increase the fraction of the edge-shared polyhedra within the structure of the coatings. There was a noticeable difference in the curve associated with the ZrO_2:Ta_2O_5 coating. The minor atomic percentage of titania within the dually doped coating could not have attributed such a large effect on the refractive index, in comparison to the zirconia-doped-tantala. This variation due to coating compositions required further investigation, which had not been performed throughout the project covered in this thesis.

ferent researchers had arrived at the conclusion that heat treatments decrease the stress, and decrease the optical absorption [187]. Nichelatti [188], derived a relation allowing for the direct calculation of the refractive index and the extinction coefficient though analysis of the reflection and transmittance data. In the paper, it was shown that the extinction coefficient, k, is proportional to the natural logarithm of the ratio of the intensity reflectance and the overall reflectance, where for the refractive index, n, that expression had a direct proportionality to the intensity reflectance. Therefore, one would expect an increase in the refractive index as the reflectance increases, or transmittance decreases. However, the transmittance and reflectance spectra obtained characterise the combination of substrate and coating. In order for a conclusion to be made on the evolution of
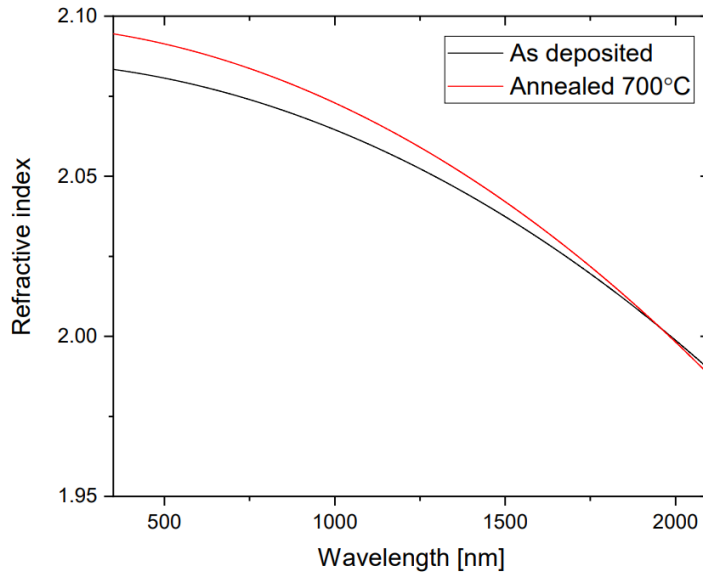
Figure 6.5: Change in refractive index due to post-deposition heat treatment at a temperature of 700°C for a ZrO_2 : TiO_2 : Ta_2O_5 coatings. As there was an increase in the transmittance of the coating, 1%, an alteration was expected in the refractive index function. That increase was characterised by less than half a percent, making the change in value miniscule and deemed to be caused by systematic errors. Therefore, it can be assumed that the refractive index did not experience a change following thermal processing at 700°C, which was consistent with the compositional analysis of the coatings.

the refractive index, the coating transmittance and reflectance needs separated from the full stack.

Figure 6.3 presented the transmittance data acquired for the same sample pre and post heat treatments at 700°C. The increase in the transmittance percentage was estimated as 1%, which is almost a negligible difference. However, one would expect that since the transmittance percentage increased as a function of annealing, the refractive index of said coating should decrease. Figure 6.5 shows the distribution of the refractive index values as a function of wavelength. It can be observed that in the case of the ZrO_2:TiO_2:Ta_2O_5 coating, thermal processing resulted in a refractive index gain. The results presented in Figures 6.3 and 6.5 are conflicting, which could be explained due to low uniformity of the coating on the surface of the substrate.

To summarise, the addition of TiO_2 aimed to increase the Young's modulus and refractive index of the dually doped coating, however the low titania composition ($\approx$3%) within the threefold thin film, could not explain the increase in refractive index in comparison to the prior zirconia-doped coatings. Additional

140

characterisation in regards to the film stoichiometry required to pinpoint the reason for change in refractive index. Furthermore, post-deposition heat treatment had been previously shown to be beneficial to the reduction of optical absorption [183]. However, the acquired transmittance spectra (Figure 6.3) were in contradiction with the results for the refractive index. The conflicting data sets would require additional characterisation in order to produce an explanation to the inconsistency in the two models.

6.3.3   Heat treatment

The addition of ZrO_2 has enabled the thermal treating of optical coatings to higher temperatures, suppressing the amorphous to crystalline transition. The dual doping of the Ta_2O_5 IBS thin films, aimed to not only retain the low level of coating loss angle obtained after heat treatments at high temperatures but to furthermore increase the density of the coating, leading to a corresponding higher refractive index enabling the reduction of number of alternating low and high refractive index layers. In a discussion presented previously [3], there exists a limitation of the dopant ratio within the coating. Even though, zirconia enables higher heat treatments and titania contributes to an increase in the Young's modulus, the excessive addition of oxides could eventually lead to the forming of separate crystalline phases. Therefore, the goal for the two depositions was to allow for a maximum of 25% doping, whereas the remaining 75% were to remain tantulum pentoxide. However, as discussed in section 6.3.1 the doping concentrations were substantially lower than expected.

The forming of cracks on the coated surface had been a pre-existing issue. In order to deduce the origination of this effect, two of the three coated cantilevers had been directly compared, where one was annealed in 100°C increments and its identical companion was directly heat treated at 600°C, and then in 100°C steps, both reaching a maximum anneal temperature of 750°C. The temperature of 600° C was chosen as a result on the uncertainty in elemental composition of the coating at this point, therefore to ensure the thin film remains in an amorphous state, coatings were annealed only up to a temperature which has been previously proven to be below the crystallisation point of tantala coatings. For the case of the dually doped coatings, cracks on the surface of the coating were not present, independent of the annealing temperature, as long as it remained under a crystallisation amplitude. Therefore, evaluations of the coating loss angle were deemed acceptable, as the uniformity of the coated surface had not been disturbed. Figure 6.2 presented the averaged mechanical loss evaluations before any heat treatment had been performed. The measured values were as expected considering that for all the IBS ECR deposited coatings before any thermal annealing, the as deposited loss was approximately at the order of $1 - 2 \times 10^{-3}$
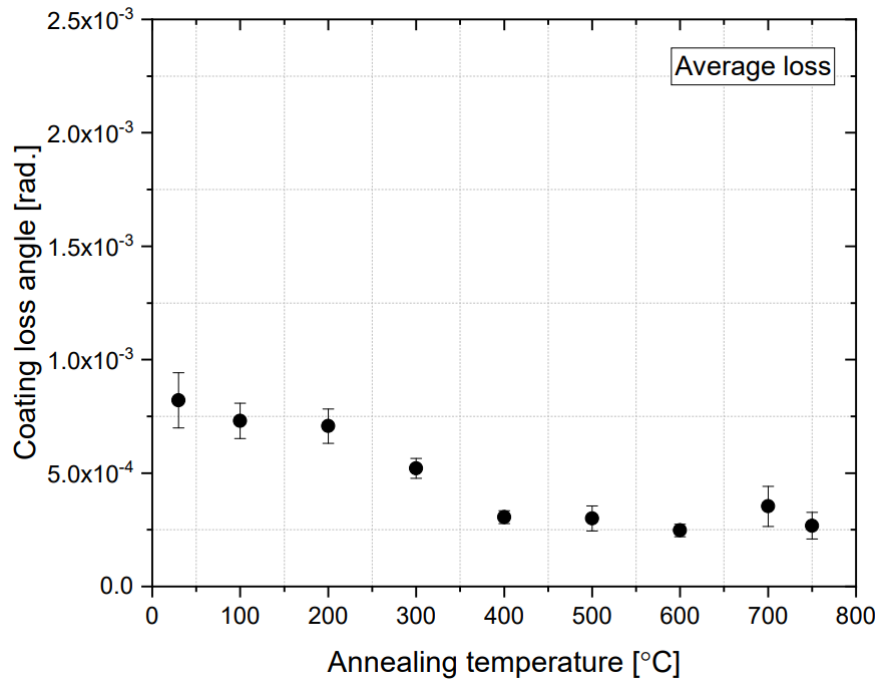
Figure 6.6: Characterisation of the mechanical loss of zirconia/titania doped tantala coatings as a function of annealing temperature. Optimum annealing temperature was at 750°C, which simultaneously allowed the coatings to remain in an amorphous state and exhibit a low coating loss angle. In comparison to the ZrO_2 doped Ta_2O_5 coatings, there was a factor of 2 reduction in the average coating loss angle.

rad. Figure 6.6 demonstrates the variation of the average coating loss angle as a function of increasing annealing temperature, which manifested the same trend of loss angle decrease at a temperature of 400°C as the ZrO_2 doped tantulum pentoxide thin films. The dip in loss at the 400 point of annealing coincided with the change of orientation of the stress on the coated sample. The lowest average loss was detected post annealing at 600°C at 2.47×10^{-4} rad, however, the average loss detected at 750°C was only 8% higher in comparison. As there was a larger spread in loss estimations following the heat treatment at the higher temperature, the variation between the two averaged losses could be conspired equivalent, since a similar trend was observed for the twofold coatings covered in the previous chapter. The identical declination of the mechanical loss with the increase of the annealing temperature for both the single and dually doped coatings were in correspondence with the low titania concentration.

In order to deduce whether the contribution of the second dopant is substantial enough to improve the currently employed Bragg refractor coatings, the three

sets were compared (elevated ZrO_2:Ta_2O_5, multi-sourced ECR system using individual oxide targets and the dually doped titania/zirconia/tantala thin films). In comparison with the three individual sets, the dually doped coatings exhibited a middle position, with an improvement in loss of 60% in comparison to the deposition of zirconia/tantala using oxide target, however it still remained 35% higher than the lowest average coating loss for elevated temperature deposited ZrO_2 doped Ta_2O_5, using a oxide target, with the addition of a metal foil section.

6.4   Summary

The mixture of multiple materials has ben currently implemented as the high-refractive (HR) optical layer of the Bragg refractors' coatings, in the form of titania doped tantulum pentoxide. However, the next step of the development of gravitational wave observatories requires an improvement in regards to the optical coatings of the test masses. Doping of the HR coating layer has aimed to increase the amorphous-to-crystalline transition temperature, as well as increase the Young's modulus of the coating. Independent dopants contribute to different characteristic improvements. The addition of zirconia has increased the thermal treatment limit, whereas the mixture with titania aims to decrease the number of layer required in the coating stack, both of which would contribute to a decrease in the limiting coating thermal noise trend.

Dual doping was performed on a multi-source ECR IBS system, using two oxide targets, Ta_2O_5 and ZrO_2, where a Ti foil was attached to the surface of the latter one, enabling the addition of the second material. The aim was to introduce a 25% mixture of zirconia and titania, to the high n coating layer. However, it was deduced that the ratio between tantala and the dopants was lower than expected, leading to the assumption that there was no change in the corner-shared polyhedra structure of the coating due to the doping [3]. Therefore, compositionally the developed coatings remained within the imposed doping ratio boundary.

The inclusion of TiO_2 was expected to increase the overall refractive index of the coating, however the low atomic ratio of the element within the composition of the thin films could not provide sufficient evidence of modification. Nevertheless, optical properties of the developed coatings were studied, showing a minimal increase in transmittance percentage following thermal annealing. This effect could be attributed to an inhomogeneity of the coating surface, or a structural void, enhanced by the heat treatments. The increase of the transmittance contradicted the diagnosed increase in refractive index. The justification of said increase could not be accredited to the titania doping, and would require further investigation.

Furthermore, the mechanical loss of the coatings, even though lower than pure tantala, was $\approx 35\%$ higher than the single doped optical coatings. These

results may have several explanations, including the doping concentration, nature of doping material (oxide or metal), deposition temperature, uniformity of the film, *etc.* If the coating loss angle is directly compared to the identical sputtering of ZrO_2 doped Ta_2O_5 covered in the previous chapter, the mechanical loss associated with the dually doped material is almost 30% lower than the single doped material. Speculations suggest that this de-escalation in the internal friction factor was due to the lower zirconia content and almost negligible titania content, resulting in higher fraction of the corner-shared polyhedra, which provided the lower loss measurements at higher temperatures. In order to better understand how multi material doping affects the deposited film, an investigation is required, which should investigate different $ZrO_2/$ $TiO_2/$ Ta_2O_5 ratios.

To summarise, multi-doped coatings suggest improving optical and mechanical properties of mirror coatings, however further investigation is necessary into the doping concentrations of the individual elements. The reduction of number of variables would allow for an optimum doping ratio, and therefore an optimum threefold thin film. Currently, based on the results presented in this chapter, the ZrO_2:TiO_2:Ta_2O_5 mix does not fulfil the requirements for Advanced LIGO A+, and is still a factor of two higher than demanded.

Chapter 7

Conclusions

The detection of gravitational waves, caused by the merger of two black holes, on September 14th 2015 at the LIGO detectors, introduced a whole new era of gravitational wave astronomy. All these years following Einstein's publication, researchers had been investigating various possibilities to prove the validity of the theory. By implementing and researching new technologies, with the observation of the gravitational wave signal, the legitimacy of the speculation was confirmed. Subsequent observing runs, accompanied by the Advanced Virgo detector, increased the number of observations, including the originators of such events. As both detectors have reached their sensitivity limits, improvement of the current noise limitations is required, especially in regards to the coating thermal noise and quantum noise. Advancements in the decrease of the quantum noise amplitude have been obtained in the form of squeezing, and are to be introduced during the next detector sensitivity improvement, *i.e.* Advanced LIGO +. The remaining dominating noise contributor will then be coating Brownian noise which is attributed to the optical coatings on the surface of the Bragg reflectors, within the gravitational wave interferometers, and is the main research topic covered within this thesis presentation. Different approaches have been taken in aim to reduce the boundary due to coating thermal noise and a summary of the results presented within this thesis work will be condensed in the following sections.

Substrates Throughout the studies, both silica cantilevers and JGS 1 silica pieces were utilised. Whilst the cantilever substrates contributed to the evaluation of the mechanical loss of the optical coatings, the silica discs were used for deduction of optical properties including Young's modulus, coating thicknesses, *etc.* All the SiO_2 cantilevers have been separately made from base components *i.e.* glass block and rectangular μm thick ribbon, which were then welded together. The variation in substrate thickness was understood to originate within the ultra thin silica disc from which the cantilever ribbons were diced. It was deduced that cantilever produced from lower thickness discs showed lower mechanical loss prior

to any coating deposition and furthermore, exhibited a wider spread of measurable vibrational modes. In order to decrease variability in surface parameters of coating substrates, all samples were heat treated at 950°C for a duration of 5 hours, prior to any characterisations.

Coating deposition Ion-beam sputtering has been acknowledged as an ultimate deposition technique. The two deposition apparatuses utilised for the development of the optical coatings covered in this thesis employed an ECR/ multiple ECR source/s instead of the commonly use RF sources. Due to the grid less nature of the ECR sources structure, they produce lesser contaminated films. Furthermore, it has been proven that the slower deposition rate, attributed to the two apparatuses, enables higher packing density of the coating elements, hence decrease the amount of internal friction causing mechanical loss. The low deposition rate further affects the levels of optical absorption and reflection, providing optimum optical coatings.

The prototype system, containing a single ECR ion source, allowed for elevated temperature depositions with a maximum temperature of 500°C, alongside room temperature depositions. The size of the vacuum chamber enabled the use of a single sputtering target, limiting the incorporation of additional dopants. Nevertheless, the addition of up to two dopants was achievable.

The multi-sourced deposition system, utilising up to four ECR sources, enabled the usage of multiple sputtering targets as long as composition was set up in accordance to the positions of the ion guns. Furthermore, the inclusion of a rotational stage, containing the uncoated substrates, improved on the coating uniformity. The alteration of the separation between the substrates and the targets allowed for modification of the deposition rate. One of the ion sources was subsequently utilised as a neutralising electron gun, diminishing the effect of discharging during deposition runs.

The production of thin films on the two IBS systems, provided variability in the deposition parameters, which further expanded the coating research area and allowed for the direct comparison of independently produced coatings from the two apparatuses.

Tantulum pentoxide coatings Pure tantulum pentoxide coatings were deposited on the prototype system, sputtering from an oxide and a metal target. Unlike typical depositions, the thin films produced were developed at different temperatures, ranging from room temperature to 500°C. The instability of the system for the highest temperature deposition affected the quality of optical coatings, hence they had been excluded. Depositions at 100°C and 200°C demonstrated the lowest average mechanical losses, implying a proposition of further elevated depositions using alternative coating materials. The low deposition rate

of IBS ECR systems contributes to higher packing density films, which leads to better optical and mechanical properties. Sputtering from the metal target was deduced to have a higher deposition rate in comparison to the Ta_2O_5 target, which in turn explains the lower mechanical loss characterised for the coatings deposited from the oxide target. All coated substrates had went through thermal processing at 600°C, allowing the coatings to remain amorphous after the heat treatment. It was observed that on average, coatings deposited at 200°C using the oxide target, had a $\approx 35\%$ reduction in loss, in comparison to the identical coating, deposited from a metal target.

Overall, the use of oxide target lead to the production of less lossy materials. Instead of using averaged data, the lowest measured mode ring-down for the metal target coatings showed a loss of 9.82×10^{-5} rad, whereas the lowest value obtained accordingly for the oxide target coatings was 2.00×10^{-4} rad. The loss in the order of 10^{-5} was correspondent to a 100°C deposition, whereas the low 10^{-4} loss corresponded to a 200°C deposition.

Post-deposition annealing showed improvement in the mechanical loss in both cases. For the coatings deposited with the metal target, after heat treatments at 600°C, the average loss improved by $\approx 75\%$. In the case of the oxide target depositions, the reduction in loss post the same heat treatment was estimated as $\approx 30\%$. Coatings, deposited from the Ta target had the risk of being oxygen deficient, which was corrected with the post depositional thermal processing. This in turn explains the larger decrease in losses in the metal target coatings in comparison to the oxide target coatings. Higher temperature anneals have improved the mechanical and optical properties of thin films, reducing the mechanical loss and the absorption coefficient of the coating. In order for tantulum pentoxide coatings to be heat treated to a higher temperature, the introduction of a dopant is required, which enables the suppression of the crystallisation of the material. As the current dopant (TiO_2) does not affect the amorphous to crystalline transition, an alternative material is required to enable higher temperature annealing. Zirconia was chosen as a doping candidate, as it has been shown to increase the packing density of the Ta and O matrix and furthermore increase the melting point of the deposited material.

Zirconia doped tantulum pentoxide coatings   Zirconia doped tantala coatings were deposited on both the prototype and the multi-sources system. Whilst the prototype system utilised a Ta_2O_5 with Zr foil attached to its surface, the larger system successfully employed a tantala and a zirconia target, where two of the ECR sources were aimed at the Ta_2O_5 target and one on the dopant. The depositions performed on the single-sourced system allowed for higher coating temperatures, whereas the multi-sourced system provided a more controlled doping environment, allowing for an exact choice of atomic ratio between elements.

Depositions on the prototype system, using a Zr foil, produced a doping ratio of Zr/(Zr+Ta)=0.3. Depositions up to temperatures of 500°C were performed. In order for the optimum annealing temperature to be deduced each coating had been annealed at 600°C, 700°C, 750°C and 800°C. Higher temperatures were not achievable as the coating crystallised. Based on multiple depositions at each temperature, it was gathered that the deposition temperature leading to the lowest loss material was at 200°C which is analogous to what was deduced for the pure tantala coatings. On average the lowest loss obtained was after a heat treatment at 800°C, estimated as 1.89×10^{-4} rad, or per individual ringdown 1.59×10^{-4} rad after the same temperature thermal treatment. In comparison to the currently employed titania doped tantala coatings, the ones developed on the ECR system showed a factor of two improvement. However, there is an overall reduction of a factor of 4 in mechanical loss required for the Advanced LIGO + optical coatings.

The coatings, produced on the multi-sourced IBS system, contained a similar dopant to base atomic ratio as the coatings developed in the prototype system. The alignment of the three guns suggested a $\approx 33\%$ ZrO_2 doping ratio. The use of a ZrO_2 target also decreased the probability of oxygen deficiency within the optical coatings. Variation was introduced in the deposition angle for some of the coatings, investigating the optimal deposition conditions characterised with the best uniformity and lowest loss, confirming a position normal to the substrate plate as the most efficient. Furthermore on inspection it was deduced that deposition on this system was ≈ 4.6 times slower in comparison to the prototype system. Slower deposition rates are expected to produce more densely packed coatings with lower loss. The average loss was estimated as 2.68×10^{-4} rad after a heat treatment at 750°C, which matches the expectancy of loss for the Advanced LIGO titania doped tantala coatings. The lower optimum temperature is presumed to be due to elemental composition of coatings, *i.e.* lower zirconia content, lower crystallisation temperature. However, the lowest detected loss was 4.26×10^{-5}, which is three times lower than the average mechanical loss, but within limitations for the requirements for the Advanced LIGO + coatings. This is the lowest loss measured at this point in time of a zirconia doped tantala film deposited using ion-beam sputtering. Further investigation of doping ratios could identify a mixture with an overall loss in the 10^{-5} range.

It was deduced that in both coating setups, the absorption coefficient of the thin films was sufficiently larger than expected, *i.e.* the coatings were not as reflective as anticipated. Therefore, in attempt to coincidently maintain a low mechanical loss and improve reflectivity of optical coatings, a second dopant, TiO_2 was interpolated.

Titania and zirconia doped tantulum pentoxide coatings   The addition of ZrO_2 and TiO_2 to tantulum pentoxide envisioned ultra low loss optical coatings with a high refractive index. Multiple coatings were deposited on the multi-beam IBS system, as the dual doping imposed limitations of the choice of system. Similar to the zirconia doped coatings, two of the ECR sources were pointed at the Ta_2O_5 target, and on was aimed at the ZrO_2, where Ti foil was attached to its surface, incorporating it in the final mixture. It was deduced that the overall achieved doping was $\approx 12\%$, where Ti represented only 0.03 parts of the complete mixture.

The presence of ZrO_2 enabled the thermal treatment of deposited films up to a temperature of 750°C, whereas TiO_2 was expected to affect the optical properties of the coating. The implementation of titania into the mixture did not alter the reflectance or transmittance of the thin film, which is attributed to the limited doping concentration. Upon inspection, it was established that post heat treatment, the refractive index of the coating increased, which was attributed to the densification of the thin film following additional oxygenation. In order for the addition of titanium to enable the decrease of number of coating layers, higher doping concentrations are required, which will enable the improvement in film reflectivity.

On average, the dually doped thin films experienced a loss of $\approx 2.46 \times 10^{-4}$ rad, where the ultimate mechanical loss estimated as $\approx 1.85 \times 10^{-4}$ rad. In comparison to the zirconia doped coatings, there was an 8% improvement in the average loss, however, independent ringdowns did not de-escalate correspondingly.

The dual doping was an attempt to provide an option for the Advanced LIGO+ stage, however, it did not fulfil the optical requirements for the next enhancement. Studies demonstrated an overall improvement, however, further investigations into the doping concentrations are required to complete the review of TiO_2:ZrO_2 doped Ta_2O_5.

Future work   Depositions utilising ECR ion-beam sources presented a major qualitative advantage over alternative deposition techniques. The two IBS systems demonstrated an improvement in optical and mechanical properties of mixed or pure materials, however, due to the only recent employment of these plasma sources, there is high unpredictability in the resulting thin films. Continuous usage will enable the improvement in repeatability.

The production of less lossy, highly reflective materials has been successfully achieved. The introduction of multiple doping mixtures showed diversity in possible compound materials, with improved mechanical and optical properties. Even though the dually doped materials did not attain to the required parameters, higher doping percentage zirconia/tantala coatings provided an excellent example of future possible conglomerations.

Bibliography

[1] B. P. Abbott et al. "GW170817: Observation of Gravitational Waves from a Binary Neutron Star Inspiral". In: *Physical Review Letters* 119.16 (2017). ISSN: 10797114. DOI: `10.1103/PhysRevLett.119.161101`.

[2] G. Vajente et al. "Effect of elevated substrate temperature deposition on the mechanical losses in tantala thin film coatings". In: *Classical and Quantum Gravity* (2018). ISSN: 13616382. DOI: `10.1088/1361-6382/aaad7c`.

[3] K. Prasai et al. "High Precision Detection of Change in Intermediate Range Order of Amorphous Zirconia-Doped Tantala Thin Films Due to Annealing". In: *Physical Review Letters* 123.4 (2019), pp. 1–6. ISSN: 10797114. DOI: `10.1103/PhysRevLett.123.045501`.

[4] A. Einstein. "A. Prinzipielle Ernllgungen zum Postulat der Relativitllt". In: *Annalen der Physik,* 354(7) (1916), 354(7):769–822.

[5] S. Reid. "Studies of materials for future ground-based and space-based interferometric gravitational wave detectors". PhD thesis. University of Glasgow, 2006.

[6] A. Tiec and J. Novak. "Theory of gravitational waves". In: *Overview of Gravitational Waves: Theory, Sources and Detection.* 2017. ISBN: 9789813141766. DOI: `10.1142/9789813141766_0001`.

[7] R. A. Hulse and J. H. Taylor. "Discovery of a pulsar in a binary system". In: *The Astrophysical Journal* (1975). ISSN: 0004-637X. DOI: `10.1086/181708`.

[8] P. R. Saulson. *Fundamentals of Interferometric Gravitational Wave Detectors.* 2011. DOI: `10.1142/9789814350235`.

[9] W. L. Freedman et al. "Final Results from the Hubble Space Telescope Key Project to Measure the Hubble Constant". In: *The Astrophysical Journal* (2001). ISSN: 0004-637X. DOI: `10.1086/320638`.

[10] B. Abbott et al. "Upper limits on gravitational wave emission from 78 radio pulsars". In: *Physical Review D - Particles, Fields, Gravitation and Cosmology* (2007). ISSN: 15502368. DOI: `10.1103/PhysRevD.76.042001`.

[11] M. Pitkin et al. *Gravitational wave detection by Interferometry (Ground and Space)*. 2011. DOI: 10.12942/lrr-2011-5. arXiv: 1102.3355.

[12] B. Aschenbach, R. Egger, and J. Trémper. "Discovery of explosion fragments outside the Vela supernova remnant shock-wave boundary". In: *Nature* (1995). ISSN: 00280836. DOI: 10.1038/373587a0.

[13] E. Seidel, E. S. Myra, and T. Moore. "Gravitational radiation from type-II supernovae: The effect of the high-density equation of state". In: *Physical Review D* (1988). ISSN: 05562821. DOI: 10.1103/PhysRevD.38.2349.

[14] T. Kuroda et al. "Correlated Signatures of Gravitational-wave and Neutrino Emission in Three-dimensional General-relativistic Core-collapse Supernova Simulations". In: *The Astrophysical Journal* 851.1 (2017), p. 62. ISSN: 1538-4357. DOI: 10.3847/1538-4357/aa988d.

[15] J. R. Bond and B. J. Carr. "Gravitational waves from a population of binary black holes". In: *Monthly Notices of the Royal Astronomical Society* (1984). ISSN: 0035-8711. DOI: 10.1093/mnras/207.3.585.

[16] E. Witten. "Cosmic separation of phases". In: *Physical Review D* (1984). ISSN: 05562821. DOI: 10.1103/PhysRevD.30.272.

[17] A. Vilenkin. *Cosmic strings and domain walls*. May 1985. DOI: 10.1016/0370-1573(85)90033-X.

[18] A. A. Starobinskiĭ. "Spectrum of relict gravitational radiation and the early state of the universe". In: *JETP Lett.* 30 (1979), pp. 682–685. DOI: 10.1142/9789814317344_0078.

[19] L. A. Rosi and R. L. Zimmerman. "A maximal background spectrum of gravitational radiation". In: *Astrophysics and Space Science* (1976). ISSN: 0004640X. DOI: 10.1007/BF00642679.

[20] B. F. Schutz. "Gravitational-wave sources". In: *Classical and Quantum Gravity* (1996). ISSN: 02649381. DOI: 10.1088/0264-9381/13/11A/031.

[21] L. P. Grishchuk and M. Solokhin. "Spectra of relic gravitons and the early history of the Hubble parameter". In: *Physical Review D* (1991). ISSN: 05562821. DOI: 10.1103/PhysRevD.43.2566.

[22] B. P. Abbott et al. "LIGO: The laser interferometer gravitational-wave observatory". In: *Reports on Progress in Physics* 72.7 (2009). ISSN: 00344885. DOI: 10.1088/0034-4885/72/7/076901.

[23] B. P. Abbott et al. "GW170814: A Three-Detector Observation of Gravitational Waves from a Binary Black Hole Coalescence". In: *Physical Review Letters* 119.14 (2017). ISSN: 10797114. DOI: 10.1103/PhysRevLett.119.141101.

[24] M. Maggiore. *Gravitational wave experiments and early universe cosmology.* 2000. DOI: 10.1016/S0370-1573(99)00102-7.

[25] J. Weber. "Detection and generation of gravitational waves". In: *Physical Review* 117.1 (1960), pp. 306–313. ISSN: 0031899X. DOI: 10.1103/PhysRev.117.306.

[26] Global plan. *The Gravitational Wave Internationl Committee Roadmap The future of gravitational wave astronomy.* Tech. rep. 2010. URL: https://gwic.ligo.org/.

[27] G. E. Moss, L. R. Miller, and R. L. Forward. "Photon-Noise-Limited Laser Transducer for Gravitational Antenna". In: *Applied Optics* 10.11 (1971), p. 2495. ISSN: 0003-6935. DOI: 10.1364/ao.10.002495.

[28] O. D. Aguiar. *Past, present and future of the Resonant-Mass gravitational wave detectors.* Tech. rep. 1. 2011, pp. 1–42. URL: http://www.raa-journal.orghttp//www.iop.org/journals/raa.

[29] L. Rezzolla et al. "The Final Spin from the Coalescence of Aligned-Spin Black Hole Binaries". In: *The Astrophysical Journal* 674.1 (2008), pp. L29–L32. ISSN: 0004-637X. DOI: 10.1086/528935.

[30] R .W .P. Dreyer et al. *Search for Short Bursts of Gravitational Radiation.* Tech. rep. 1973.

[31] S. P. Boughn et al. "Observations with a low-temperature, resonant mass, gravitational radiation detector". In: *The Astrophysical Journal* 261 (1982), p. L19. ISSN: 0004-637X. DOI: 10.1086/183881.

[32] M. E. Gertsenshtein and V. I Pustovoit. "On the detection of low frequency gravitational waves". In: *Journal of Experimental and Theoretical Physics (U.S.S.R.)* (1962).

[33] A. Abramovici et al. *LIGO: The Laser Interferometer Gravitational-Wave Observatory.* 1992. DOI: 10.1126/science.256.5055.325.

[34] É. Chassande-Mottin. "Data analysis challenges in transient gravitational-wave astronomy". In: *AIP Conference Proceedings.* 2013. ISBN: 9780735411593. DOI: 10.1063/1.4807558.

[35] H. Lück et al. "The upgrade of GEO 600". In: *Journal of Physics: Conference Series.* Vol. 228. Institute of Physics Publishing, 2010. DOI: 10.1088/1742-6596/228/1/012012.

[36] K. L. Dooley. "Status of GEO 600". In: *Journal of Physics: Conference Series.* Vol. 610. 1. Institute of Physics Publishing, 2015. DOI: 10.1088/1742-6596/610/1/012015.

[37] V. Loriette and C. Boccara. "Absorption of low-loss optical materials measured at 1064 nm by a position-modulated collinear photothermal detection technique". In: *Applied Optics* (2003). ISSN: 0003-6935. DOI: `10.1364/ao.42.000649`.

[38] G. Attractor et al. *Cepheids in M81 and NGC 2403.* Tech. rep. 22. 1988, p. 530. URL: `http://science.sciencemag.org/`.

[39] *Advanced LIGO Observatories.* URL: `www.ligo.caltech.edu`.

[40] B. J. Meers. "Recycling in laser-interferometric gravitational-wave detectors". In: *Physical Review D* 38.8 (1988), pp. 2317–2326. ISSN: 05562821. DOI: `10.1103/PhysRevD.38.2317`.

[41] R. Adhikari. "Enhanced LIGO". In: *AAS/High Energy Astrophysics Division* 9.225 (2006), p. 21.03.

[42] F. Acernese et al. "The Advanced Virgo detector". In: *Journal of Physics: Conference Series.* Vol. 610. 1. Institute of Physics Publishing, 2015. DOI: `10.1088/1742-6596/610/1/012014`.

[43] Technical File. *Suprasil 3001/3002.* Tech. rep. Heraeus.

[44] *Advanced Virgo detector.* URL: `www.virgo-gw.eu`.

[45] M. Razzano. *Observing run news.* URL: `http://public.virgo-gw.eu/exciting-ligo-virgo-observing-run-draws-close-25th-august/`.

[46] *Observing capabilities of detectors.* URL: `https://emfollow.docs.ligo.org/userguide/capabilities.html`.

[47] K. Yamamoto. "Current status of KAGRA". In: August (2016).

[48] T. Uchiyama et al. "Reduction of thermal fluctuations in a cryogenic laser interferometric gravitational wave detector". In: *Physical Review Letters* 108.14 (2012). ISSN: 00319007. DOI: `10.1103/PhysRevLett.108.141101`. arXiv: `1202.3558`.

[49] T. Akutsu. "Large-scale cryogenic gravitational-wave telescope in Japan: KAGRA". In: *Journal of Physics: Conference Series.* Vol. 610. 1. Institute of Physics Publishing, 2015. DOI: `10.1088/1742-6596/610/1/012016`.

[50] M. Punturo et al. "The Einstein Telescope: A third-generation gravitational wave observatory". In: *Classical and Quantum Gravity* 27.19 (2010). ISSN: 13616382. DOI: `10.1088/0264-9381/27/19/194002`.

[51] *ET.* URL: `www.et-gw.eu`.

[52] S. Hild et al. "A xylophone configuration for a third-generation gravitational wave detector". In: *Classical and Quantum Gravity* 27.1 (2010). ISSN: 02649381. DOI: `10.1088/0264-9381/27/1/015003`.

[53] M. A. Green and M. J. Keevers. "Optical properties of intrinsic silicon at 300 K". In: *Progress in Photovoltaics: Research and Applications* (1995). ISSN: 1099159X. DOI: `10.1002/pip.4670030303`.

[54] M. Evans et al. "Thermo-optic noise in coated mirrors for high-precision optical measurements". In: *Physical Review D - Particles, Fields, Gravitation and Cosmology* 78.10 (2008), pp. 1–10. ISSN: 15507998. DOI: `10.1103/PhysRevD.78.102003`.

[55] K. Danzmann. *LISA Laser Interferometer Space Antenna A proposal in response to the ESA call for L3 mission concepts.* Tech. rep.

[56] *LISA*. URL: `www.lisa.nasa.gov`.

[57] P. McNamara, S. Vitale, and K. Danzmann. "LISA pathfinder". In: *Classical and Quantum Gravity*. Vol. 25. 11. 2008. DOI: `10.1088/0264-9381/25/11/114034`.

[58] "Gravitational waves send ripples of joy for LIGO-India". In: *Nature India* (2016). DOI: `10.1038/nindia.2016.20`.

[59] LIGO. *Instrument Science White Paper 2018*. Tech. rep. 225. 2018, p. 125.

[60] R. X. Adhikari et al. "A cryogenic silicon interferometer for gravitational-wave detection". In: *Classical and Quantum Gravity* (2020). ISSN: 13616382. DOI: `10.1088/1361-6382/ab9143`.

[61] P. Giacomo. "The Michelson interferometer". In: *Mikrochimica Acta* (1987). ISSN: 00263672. DOI: `10.1007/BF01201680`.

[62] R. L. Forward et al. "Upper limit for interstellar millicycle gravitational radiation". In: *Nature* (1961). ISSN: 00280836. DOI: `10.1038/189473a0`.

[63] R. L. Forward. "Wideband laser-interferometer graviational-radiation experiment". In: *Physical Review D* 17.2 (1978), pp. 379–390. ISSN: 05562821. DOI: `10.1103/PhysRevD.17.379`.

[64] D. I. Robertson et al. "The Glasgow 10 m prototype laser interferometric gravitational wave detector". In: *Review of Scientific Instruments* 66.9 (1995), pp. 4447–4452. ISSN: 00346748. DOI: `10.1063/1.1145339`.

[65] K. A. Strain and B. J. Meers. "Experimental demonstration of dual recycling for interferometric gravitational-wave detectors". In: *Physical Review Letters* 66.11 (1991), pp. 1391–1394. ISSN: 00319007. DOI: `10.1103/PhysRevLett.66.1391`.

[66] J. Mizuno et al. "Resonant sideband extraction: a new configuration for interferometric gravitational wave detectors". In: *Physics Letters A* 175.5 (1993), pp. 273–276. ISSN: 03759601. DOI: `10.1016/0375-9601(93)90620-F`.

[67] J. Mizuno. "Mizuno, PhD Thesis". PhD thesis. University of Hannover, 1995. URL: http://worldcat.org/oclc/76698836.

[68] D. F. Walls. *Squeezed states of light.* Tech. rep. 1983.

[69] C. M. Caves. "Quantum-mechanical noise in an interferometer". In: *Physical Review D* 23.8 (1981), pp. 1693–1708. ISSN: 05562821. DOI: 10.1103/PhysRevD.23.1693.

[70] A. F. Pace, M. J. Collett, and D. F. Walls. "Quantum limits in interferometric detection of gravitational radiation". In: *Physical Review A* 47.4 (1993), pp. 3173–3189. ISSN: 10502947. DOI: 10.1103/PhysRevA.47.3173.

[71] J. Lough et al. *First demonstration of 6 dB quantum noise reduction in a kilometer scale gravitational wave observatory.* 2020.

[72] T. Corbitt et al. "Measurement of radiation-pressure-induced optomechanical dynamics in a suspended Fabry-Perot cavity". In: *Physical Review A - Atomic, Molecular, and Optical Physics* 74.2 (2006). ISSN: 10502947. DOI: 10.1103/PhysRevA.74.021802.

[73] DeSalvo R. "Gravitational waves and Experimental Gravity". In: 1999.

[74] B. P. Abbott et al. "A gravitational-wave standard siren measurement of the Hubble constant". In: *Nature* 551.7678 (2017), pp. 85–98. ISSN: 14764687. DOI: 10.1038/nature24471.

[75] V. A. Dubrovskiy and N. N. Smirnov. "Correlation of the earth microseism background with space objects distribution and gravity waves velocity". In: *AIAA 57th International Astronautical Congress, IAC 2006.* 2006. ISBN: 9781605600390. DOI: 10.2514/6.iac-06-a2.1.05.

[76] E. J. Daw et al. "Long-term study of the seismic environment at LIGO". In: *Classical and Quantum Gravity* 21.9 (2004), pp. 2255–2273. ISSN: 02649381. DOI: 10.1088/0264-9381/21/9/003.

[77] P. Saulson. "Terrestrial gravitational noise on a gravitational wave antenna". In: *Physical Review D* 30.4 (1984).

[78] R. Weiss. "Electromagnetically Coupled Broadband Gravitational Antenna". In: *LIGO DCC* (1972). URL: http://www.ligo.caltech.edu/.

[79] R. Spero. "Prospects for ground based detectors of low frequency gravitational radiation". In: AIP Publishing, 2008, pp. 347–350. DOI: 10.1063/1.33916.

[80] K. Thorne. "Seismic gravity-gradient noise in interferometric gravitational-wave detectors". In: *Physical Review D - Particles, Fields, Gravitation and Cosmology* 58.12 (1998). ISSN: 15502368. DOI: 10.1103/PhysRevD.58.122002.

[81] M. G. Beker et al. "Improving the sensitivity of future GW observatories in the 1-10 Hz band: Newtonian and seismic noise". In: *General Relativity and Gravitation* 43.2 (2011). ISSN: 15729532. DOI: 10.1007/s10714-010-1011-7.

[82] T. Creighton. "Tumbleweeds and airborne gravitational noise sources for LIGO". In: *Classical and Quantum Gravity* 25.12 (2008). ISSN: 02649381. DOI: 10.1088/0264-9381/25/12/125011.

[83] A. Polnarev. "Radiation of gravitational waves by a cluster of superdense stars". In: *Soviet Astronomy* 18 (1974), p. 17.

[84] C. M. Caves. "Quantum Mechanical Radiation-Pressure fluctuations in an interferometer". In: *Physical Review Letters* 45.2 (1980), pp. 75–79.

[85] R. W.P. Drever et al. "Laser phase and frequency stabilization using an optical resonator". In: *Applied Physics B Photophysics and Laser Chemistry* (1983). ISSN: 14320649. DOI: 10.1007/BF00702605.

[86] C. Gräf et al. "Design of a speed meter interferometer proof-of-principle experiment". In: *Classical and Quantum Gravity* 31.21 (2014). ISSN: 13616382. DOI: 10.1088/0264-9381/31/21/215009.

[87] V. B. Braginsky et al. "Quantum Nondemolition Measurements". In: *Science* 209.4456 (1980), pp. 547–557.

[88] V. B. Braginskii. "Gravitational radiation and the prospect of its experimental discovery". In: *Uspekhi Fizicheskih Nauk* 86.7 (1965), pp. 433–446. ISSN: 0042-1294. DOI: 10.3367/ufnr.0086.196507e.0433.

[89] W. A. Edelstein et al. *Limits to the measurement of displacement in an interferometric gravitational radiation detector.* 1978. DOI: 10.1088/0022-3735/11/7/030.

[90] Y. Ma et al. "Proposal for Gravitational-Wave Detection Beyond the Standard Quantum Limit via EPR Entanglement". In: *Nature* 13 (2016), pp. 776–780. DOI: 10.1038/nphys4118.

[91] V. B. Braginsky and F. Ja Khalili. "Gravitational wave antenna with QND speed meter". In: *Physics Letters A* (1990). ISSN: 03759601. DOI: 10.1016/0375-9601(90)90442-Q.

[92] S. H. Huttner et al. "Candidates for a possible third-generation gravitational wave detector: Comparison of ring-Sagnac and sloshing-Sagnac speedmeter interferometers". In: *Classical and Quantum Gravity* 34.2 (2017). ISSN: 13616382. DOI: 10.1088/1361-6382/34/2/024001.

[93] P. R. Saulson. *Thermal noise in mechanical experiments.* Tech. rep. 1990, p. 15.

[94]   B. P. Abbott et al. "Observation of gravitational waves from a binary black hole merger". In: *Physical Review Letters* 116.6 (2016). ISSN: 10797114. DOI: `10.1103/PhysRevLett.116.061102`.

[95]   B. P. Abbott et al. "GW151226: Observation of Gravitational Waves from a 22-Solar-Mass Binary Black Hole Coalescence". In: *Physical Review Letters* 116.24 (2016). ISSN: 10797114. DOI: `10.1103/PhysRevLett.116.241103`.

[96]   B. P. Abbott et al. "GW170104: Observation of a 50-Solar-Mass Binary Black Hole Coalescence at Redshift 0.2". In: *Physical Review Letters* 118.22 (2017). ISSN: 10797114. DOI: `10.1103/PhysRevLett.118.221101`.

[97]   B. F. Schutz. "Determining the Hubble constant from gravitational wave observations". In: *Nature* 323.6086 (1986), pp. 310–311. ISSN: 00280836. DOI: `10.1038/323310a0`.

[98]   P. A.R. Ade et al. "Planck 2015 results: XIII. Cosmological parameters". In: *Astronomy and Astrophysics* 594 (2016). ISSN: 14320746. DOI: `10.1051/0004-6361/201525830`.

[99]   D. V. Martynov et al. "Sensitivity of the Advanced LIGO detectors at the beginning of gravitational wave astronomy". In: *Physical Review D* 93.11 (2016). ISSN: 24700029. DOI: `10.1103/PhysRevD.93.112004`.

[100]   V. B. Braginsky and S. P. Vyatchanin. "Thermodynamical fluctuations in optical mirror coatings". In: *Physics Letters, Section A: General, Atomic and Solid State Physics* 312.3-4 (2003), pp. 244–255. ISSN: 03759601. DOI: `10.1016/S0375-9601(03)00473-0`.

[101]   Y. Levin. "Fluctuation-dissipation theorem for thermo-refractive noise". In: *Physics Letters, Section A: General, Atomic and Solid State Physics* 372.12 (2008), pp. 1941–1944. ISSN: 03759601. DOI: `10.1016/j.physleta.2007.11.007`.

[102]   R. Brown. "A brief account of microscopical observations made in the months of June, July and August 1827, on the particles contained in the pollen of plants; and on the general existence of active molecules in organic and inorganic bodies". In: *The Philosophical Magazine* 4.21 (1828), pp. 161–173. ISSN: 1941-5850. DOI: `10.1080/14786442808674769`.

[103]   J. L. Jackson. "Irreversibility and generalized noise". In: *Physical Review* 87.3 (1952), pp. 471–472. ISSN: 0031899X. DOI: `10.1103/PhysRev.87.471`.

[104]   A. S. Nowick, B. S. Berry, and J. Lawrence Katz. "Anelastic Relaxation in Crystalline Solids". In: *Journal of Applied Mechanics* (1975). ISSN: 0021-8936. DOI: `10.1115/1.3423694`.

[105] L. Kimball and D. E. Lovell. *Mathematical Theory of Elasticity*. Tech. rep. 1923, pp. 397–438.

[106] Y. Huang and P. R. Saulson. "A method for measuring the dependence of internal friction on strain". In: *Review of Scientific Instruments* 65.6 (1994), pp. 2102–2106. ISSN: 00346748. DOI: 10.1063/1.1144819.

[107] G. I. Gonzalez and P. R. Saulson. "Brownian motion of a mass suspended by an anelastic wire". In: *Journal of the Acoustical Society of America* 96.1 (1994), pp. 207–212. ISSN: NA. DOI: 10.1121/1.410467.

[108] K. Yuki et al. "Measuring the anelasticity of Cu-Be film under tensile stress using the X-pendulum". In: *Physics Letters, Section A: General, Atomic and Solid State Physics* (1996). ISSN: 03759601. DOI: 10.1016/S0375-9601(96)00723-2.

[109] O.L. Anderson and H. E. Bommel. "Ultrasonic Absorption in Fused Silica at Low Temperatures and High Frequencies". In: *Journal of the American Ceramic Society* 38.4 (1955), pp. 125–131. ISSN: 15512916. DOI: 10.1111/j.1151-2916.1955.tb14914.x.

[110] C. M. Varma. *Quantum Mechanics in Glasses*. Tech. rep. 1988.

[111] J. P. Trinastic et al. "Unified interatomic potential and energy barrier distributions for amorphous oxides". In: *Journal of Chemical Physics* 139.15 (2013). ISSN: 00219606. DOI: 10.1063/1.4825197.

[112] C. R. Billman et al. "Origin of the second peak in the mechanical loss function of amorphous silica". In: *Physical Review B* 95.1 (2017). ISSN: 24699969. DOI: 10.1103/PhysRevB.95.014109.

[113] R. Robie. "Characterisation of the mechanical properties of thin-film mirror coating materials for use in future interferometric gravitational wave detectors". PhD thesis. 2018.

[114] T. Hong et al. "Brownian thermal noise in multilayer coated mirrors". In: *Physical Review D - Particles, Fields, Gravitation and Cosmology* 87.8 (2013), pp. 1–26. ISSN: 15507998. DOI: 10.1103/PhysRevD.87.082001.

[115] Y. Levin. "Internal thermal noise in the LIGO test masses: A direct approach". In: *Physical Review D - Particles, Fields, Gravitation and Cosmology* 57.2 (1998), pp. 1–4. DOI: 10.1103/PhysRevE.67.046106.

[116] G. M. Harry et al. "Thermal noise in interferometric gravitational wave detectors due to dielectric optical coatings". In: *Classical and Quantum Gravity* 19.5 (2002), pp. 897–917. ISSN: 02649381. DOI: 10.1088/0264-9381/19/5/305.

[117] A. M. Gretarsson, E. Jesse, and B. Nollet. "Problems measuring the thermo-optic parameters for tantala / silica coatings". In: *LIGO DCC* (), G080151–00.

[118] V. B. Braginsky, M. L. Gorodetsky, and S. P. Vyatchanin. "Thermo-refractive noise in gravitational wave antennae". In: *Physics Letters, Section A: General, Atomic and Solid State Physics* 271.5-6 (2000), pp. 303–307. ISSN: 03759601. DOI: 10.1016/S0375-9601(00)00389-3.

[119] K. Seshan. *Handbook of Thin Film Deposition Techniques Principles, Methods, Equipment and Applications, Second Editon.* 2002. DOI: 10.1201/9781482269680.

[120] N. K. Sahoo et al. *Ion Assisted Deposition of Refractory Oxide Thin Film Coatings for Improved Optical and Structural Properties.* Tech. rep. 1999.

[121] G. M. Harry, T. P. Bodiya, and R. DeSalvo. *Optical coatings and thermal noise in precision measurement.* Cambridge University Press, 2012. ISBN: 9781107003385.

[122] C. Bundesmann and H. Neumann. "Tutorial: The systematics of ion beam sputtering for deposition of thin films with tailored properties". In: *Journal of Applied Physics* 124.23 (2018). ISSN: 10897550. DOI: 10.1063/1.5054046. URL: http://dx.doi.org/10.1063/1.5054046.

[123] *Laboratoire des Matériaux Avancés.* URL: http://lma.in2p3.fr/.

[124] *Polygon Physics.* URL: https://polygonphysics.com/.

[125] R. Lossy and J. Engemann. "Rf-broad-beam ion source for reactive sputtering". In: *Vacuum* (1986). ISSN: 0042207X. DOI: 10.1016/0042-207X(86)90150-8.

[126] P. J. Kelly and R. D. Arnell. *Magnetron sputtering: A review of recent developments and applications.* 2000. DOI: 10.1016/S0042-207X(99)00189-X.

[127] N. Mori. "Micro Area Analysis with JXA-8530F (FE-EPMA)". In: *JEOL News* 45 (2010).

[128] G. Cliff and G. W. Lorimer. "The quantitative analysis of thin specimens". In: *Journal of Microscopy* 103.2 (1975), pp. 203–207. ISSN: 13652818. DOI: 10.1111/j.1365-2818.1975.tb03895.x.

[129] M. Watanabe and D. B. Williams. *The quantitative analysis of thin specimens: A review of progress from the Cliff-Lorimer to the new ζ-factor methods.* 2006. DOI: 10.1111/j.1365-2818.2006.01549.x.

[130] C. Van Hoek and M. Koolwijk. "Conventional wavelength dispersive spectroscopy versus parallel beam spectroscopy - A basic overview". In: *Microchimica Acta.* 2008. DOI: 10.1007/s00604-007-0865-1.

[131] A. Alexandrovski et al. "Photothermal common-path interferometry (PCI): new developments". In: *Solid State Lasers XVIII: Technology and Devices* 7193 (2009), p. 71930D. ISSN: 0277786X. DOI: 10.1117/12.814813.

[132] D. Ma et al. "Determination of Young's modulus by nanoindentation". In: *Science in China, Series E: Technological Sciences* 47.4 (2004). ISSN: 10069321. DOI: 10.1360/03ye0590.

[133] M. Wiercigroch. "Mechanical Vibrations: Theory and Application to Structural Dynamics – 3rd Edition M. Geradin and D. J. Rixen John Wiley and Sons, The Atrium, Southern Gate, Chichester, West Sussex, PO19 8SQ, UK. 2015. 598pp. Illustrated. £83.95. ISBN 978-1-118-90020 8." In: *The Aeronautical Journal* 122.1251 (2018). ISSN: 0001-9240. DOI: 10.1017/aer.2018.27.

[134] D. R. M. Crooks. "Mechanical Loss and its Significance in the Test Mass Mirrors of Gravitational Wave Detectors". PhD thesis. 2002.

[135] I. W. Martin et al. "Effect of heat treatment on mechanical dissipation in Ta2O 5 coatings". In: *Classical and Quantum Gravity* 27.22 (2010). ISSN: 02649381. DOI: 10.1088/0264-9381/27/22/225020. arXiv: 1010.0577.

[136] T. J. Quinn et al. "Stress-dependent damping in Cu-Be torsion and flexure suspensions at stresses up to 1.1 GPa". In: *Physics Letters A* (1995). ISSN: 03759601. DOI: 10.1016/0375-9601(94)00921-B.

[137] R. Birney et al. "Amorphous Silicon with Extremely Low Absorption: Beating Thermal Noise in Gravitational Astronomy". In: *Physical Review Letters* 121.19 (2018). ISSN: 10797114. DOI: 10.1103/PhysRevLett.121.191101.

[138] A. Vinante et al. "Thermal noise in a high Q ultracryogenic resonator". In: *Review of Scientific Instruments* 76.7 (2005). ISSN: 00346748. DOI: 10.1063/1.1947927.

[139] M. J. Hart et al. "Medium range structural order in amorphous tantala spatially resolved with changes to atomic structure by thermal annealing". In: *Journal of Non-Crystalline Solids* 438 (2016), pp. 10–17. ISSN: 00223093. DOI: 10.1016/j.jnoncrysol.2016.02.005.

[140] D. Vine. "Implementation of a Novel Ion Beam Deposition System for the Development of Future Gravitational Wave Mirrors ." PhD thesis. 2019.

[141] I. W. Martin. "Studies of materials for use in future interferometric gravitational wave detectors". PhD thesis. 2009.

[142] M. Granata et al. "Amorphous optical coatings of present gravitational-wave interferometers". In: *Classical and Quantum Gravity* 37.9 (2020). ISSN: 13616382. DOI: 10.1088/1361-6382/ab77e9.

[143] G. M. Harry et al. "Thermal noise from optical coatings". In: *The Tenth Marcel Grossmann Meeting: On Recent Developments in Theoretical and Experimental General Relativity, Gravitation and Relativistic Field Theories.* Vol. 3. World Scientific Publishing Co., 2006, pp. 2003–2005. ISBN: 9789812704030. DOI: `10.1142/9789812704030_0257`.

[144] S. D. Penn et al. "Frequency and surface dependence of the mechanical loss in fused silica". In: *Physics Letters, Section A: General, Atomic and Solid State Physics* 352.1-2 (2006). ISSN: 03759601. DOI: `10.1016/j.physleta.2005.11.046`.

[145] S. Reid et al. "Mechanical dissipation in silicon flexures". In: *Physics Letters, Section A: General, Atomic and Solid State Physics* 351.4-5 (2006). ISSN: 03759601. DOI: `10.1016/j.physleta.2005.10.103`.

[146] Technical Report. *SPECTOR Large Area Ion Beam Deposition System for Optical Coating.* URL: `https://www.veeco.com/products/spector-large-area-ion-beam-deposition-system-for-optical-coating/`.

[147] R. Kukla et al. "High rate sputtering of metals and metal oxides with a moving plasma zone". In: *Thin Solid Films* 228.1-2 (1993), pp. 51–55. ISSN: 00406090. DOI: `10.1016/0040-6090(93)90562-4`.

[148] S. Singh, M. D. Ediger, and J. J. De Pablo. "Ultrastable glasses from in silico vapour deposition". In: *Nature Materials* 12.2 (2013). ISSN: 14764660. DOI: `10.1038/nmat3521`.

[149] Y. Abe et al. "Target surface oxide layer formed by reactive sputtering of Ti target in Ar+O2 mixed gas". In: *Journal of Vacuum Science Technology A: Vacuum, Surfaces, and Films* 23.5 (2005), pp. 1371–1374. ISSN: 0734-2101. DOI: `10.1116/1.2006135`.

[150] J. A. Dobrowolski, F. C. Ho, and A. Waldorf. "Determination of optical constants of thin film coating materials based on inverse synthesis". In: *Applied Optics* 22.20 (1983), p. 3191. ISSN: 0003-6935. DOI: `10.1364/ao.22.003191`.

[151] H. Demiryont, J. R. Sites, and K. Geib. "Effects of oxygen content on the optical properties of tantalum oxide films deposited by ion-beam sputtering". In: *Applied Optics* 24.4 (1985), p. 490. ISSN: 0003-6935. DOI: `10.1364/ao.24.000490`.

[152] A. F. Brooks et al. "Overview of Advanced LIGO adaptive optics". In: *Applied Optics* 55.29 (2016). ISSN: 0003-6935. DOI: `10.1364/ao.55.008256`.

[153] A. Ueda et al. "Ultra-high quality cavity with 1.5 ppm loss at 1064 nm". In: *Optical Review* (1996). ISSN: 13406000. DOI: `10.1007/s10043-996-0369-y`.

[154] G. L. Billingsley, H. Yamamoto, and L. Zhang. "Characterization of advanced ligo core optics". In: *Proceedings - ASPE 2017 Spring Topical Meeting - Precision Engineering and Optics: What are the Limits of Precision, and How to Characterize Them?* 2017. ISBN: 9781887706735.

[155] D. R.M. Crooks et al. "Experimental measurements of mechanical dissipation associated with dielectric coatings formed using SiO2, Ta2O5 and Al2O3". In: *Classical and Quantum Gravity* (2006). ISSN: 02649381. DOI: `10.1088/0264-9381/23/15/014`.

[156] T. Li et al. "Measurements of mechanical thermal noise and energy dissipation in optical dielectric coatings". In: *Physical Review D - Particles, Fields, Gravitation and Cosmology* (2014). ISSN: 15502368. DOI: `10.1103/PhysRevD.89.092004`. arXiv: `1401.0184`.

[157] G. M. Harry et al. "Titania-doped tantala/silica coatings for gravitational-wave detection". In: *Classical and Quantum Gravity* 24.2 (2007), pp. 405–415. ISSN: 02649381. DOI: `10.1088/0264-9381/24/2/008`. arXiv: `0610004 [gr-qc]`.

[158] X. Liu et al. "Hydrogen-free amorphous silicon with no tunneling states". In: *Physical Review Letters* 113.2 (2014). ISSN: 10797114. DOI: `10.1103/PhysRevLett.113.025503`.

[159] E. Atanassova et al. "High temperature-induced crystallization in tantalum pentoxide layers and its influence on the electrical properties". In: *Thin Solid Films* 426.1-2 (2003), pp. 191–199. ISSN: 00406090. DOI: `10.1016/S0040-6090(03)00027-0`.

[160] H. Chen, K. S. Lee, and C. C. Lee. "Residual stress and optical properties of TiO2 thin film during annealing by different deposition methods". In: *Optics InfoBase Conference Papers* (2007), pp. 5–8. ISSN: 21622701. DOI: `10.1364/oic.2007.tua4`.

[161] G. Sethi et al. "Structure and dielectric properties of amorphous tantalum pentoxide thin film capacitors". In: *Annual Report - Conference on Electrical Insulation and Dielectric Phenomena, CEIDP* (2007), pp. 815–818. ISSN: 00849162. DOI: `10.1109/CEIDP.2007.4451491`.

[162] T. Vo et al. "Effect of domain size, boundary, and loading conditions on mechanical properties of amorphous silica: A reactive molecular dynamics study". In: *Nanomaterials* 10.1 (2020). ISSN: 20794991. DOI: `10.3390/nano10010054`.

[163] S.M. Wiederhorn. "Fracture Surface Energy of Glass". In: *Journal of the American Ceramic Society* 52.2 (1969), pp. 99–105. ISSN: 15512916. DOI: `10.1111/j.1151-2916.1969.tb13350.x`.

[164] T. Deschamps et al. "Elastic moduli of permanently densified silica glasses". In: *Scientific Reports* 4 (2014), pp. 1–7. ISSN: 20452322. DOI: 10.1038/srep07193.

[165] N. McLachlan. *Theory of vibrations*. New York: Dover Publications, 1951.

[166] L. Barsotti et al. "The A + design curve". In: 225 ().

[167] E. Oelker et al. "Audio-Band Frequency-Dependent Squeezing for Gravitational-Wave Detectors". In: *Physical Review Letters* 116.4 (2016), pp. 1–6. ISSN: 10797114. DOI: 10.1103/PhysRevLett.116.041102.

[168] J. Aasi et al. "Advanced LIGO". In: *Classical and Quantum Gravity* (2015). ISSN: 13616382. DOI: 10.1088/0264-9381/32/7/074001.

[169] J. Tewg, Y. Kuo, and J. Lu. "Suppression of crystallization of tantalum oxide thin film by doping with zirconium". In: *Electrochemical and Solid-State Letters* 8.1 (2005), pp. 27–30. ISSN: 10990062. DOI: 10.1149/1.1836122.

[170] Y. Cui, L. Zhang, and R. Wang. "Dielectric properties of polycrystalline MgB2". In: *Physica C: Superconductivity and its Applications* 442.1 (2006), pp. 29–32. ISSN: 09214534. DOI: 10.1016/j.physc.2006.03.140.

[171] H. H. Gatzen, V. Saile, and J. Leuthold. "Deposition Technologies". In: *Micro and Nano Fabrication*. 2015. DOI: 10.1007/978-3-662-44395-8_3.

[172] M. A. Fazio et al. "Structure and morphology of low mechanical loss TiO 2 -doped Ta 2 O 5". In: *Optical Materials Express* (2020). ISSN: 2159-3930. DOI: 10.1364/ome.10.001687.

[173] N. Kim and J. F. Stebbins. "Effects of annealing on the structure of ion beam sputtered amorphous tantalum oxide: Oxygen-17 NMR spectra and relaxation times". In: *Journal of Non-Crystalline Solids* (2013). ISSN: 00223093. DOI: 10.1016/j.jnoncrysol.2013.07.003.

[174] C. F. Chan and Y. C. Ko. "Effect of Cr2O3 on Slag Resistance of Al2O3–SiO2 Refractories". In: *Journal of the American Ceramic Society* 75.10 (1992), pp. 2857–2861. ISSN: 15512916. DOI: 10.1111/j.1151-2916.1992.tb05516.x.

[175] T. Chotard et al. "Thermomechanical Characterisation of Mullite Zirconia Composites Sintered from Andalusite for High Temperature Applications". In: *Ceramics* 2.4 (2019), pp. 587–601. DOI: 10.3390/ceramics2040046.

[176] S. V. Jagadeesh Chandra et al. "Structural and electrical properties of radio frequency magnetron sputtered tantalum oxide films: Influence of post-deposition annealing". In: *Materials Science in Semiconductor Processing* 13.4 (2010), pp. 245–251. ISSN: 13698001. DOI: 10.1016/j.mssp.2010.08.002.

[177] S. Gras and M. Evans. "Direct measurement of coating thermal noise in optical resonators". In: *Physical Review D* 98.12 (2018), p. 122001. ISSN: 24700029. DOI: 10.1103/PhysRevD.98.122001. URL: https://doi.org/10.1103/PhysRevD.98.122001.

[178] N. Sakudo et al. "Microwave ion source". In: *Review of Scientific Instruments* 48.7 (1977), pp. 762–766. ISSN: 00346748. DOI: 10.1063/1.1135144.

[179] R. L. Tapping, R. D. Davidson, and T. E. Jackman. "Calibration of argon ion sputter rates using nuclear microanalysis and Auger spectroscopy". In: *Surface and Interface Analysis* 7.2 (1985), pp. 105–108. ISSN: 10969918. DOI: 10.1002/sia.740070209.

[180] M P Seah and T S Nunney. "Sputtering yields of compounds using argon ions". In: *Journal of Physics D: Applied Physics* 43.25 (2011), p. 253001. URL: 10.1088/0022-3727/43/25/253001.

[181] S. Lüth et al. "Fresnel volume migration of multicomponent data". In: *Geophysics* (2005). ISSN: 00168033. DOI: 10.1190/1.2127114.

[182] Ferroli. *SCOUT Technical Manual.* 2019. URL: http://www.act.org/content/dam/act/unsecured/documents/ACT_Technical_Manual.pdf.

[183] H. Nyakotyo, T. S. Sathiaraj, and E. Muchuweni. "Effect of annealing on the optical properties of amorphous Se79Te10Sb4Bi7 thin films". In: *Optics and Laser Technology* (2017). ISSN: 00303992. DOI: 10.1016/j.optlastec.2017.01.023.

[184] Y. Wang et al. "Effect of inter-annealing between two stages of extrusion on the microstructure and mechanical property for spray deposited Al-Cu-Li alloy 2195". In: *Journal of Materials Research and Technology* 8.5 (2019). ISSN: 22387854. DOI: 10.1016/j.jmrt.2019.06.052.

[185] N. R. Mathews et al. "TiO2 thin films - Influence of annealing temperature on structural, optical and photocatalytic properties". In: *Solar Energy* 83.9 (2009), pp. 1499–1508. ISSN: 0038092X. DOI: 10.1016/j.solener.2009.04.008.

[186] R. P. Netterfield et al. "Low mechanical loss coatings for LIGO optics: progress report". In: *Advances in Thin-Film Coatings for Optical Applications II* 5870 (2005). ISSN: 0277786X. DOI: 10.1117/12.618288.

[187] I. W. Martin et al. "Effect of heat treatment on mechanical dissipation in Ta2O 5 coatings". In: *Classical and Quantum Gravity* 27.22 (2010). ISSN: 02649381. DOI: 10.1088/0264-9381/27/22/225020. arXiv: 1010.0577.

[188] E. Nichelatti. "Complex refractive index of a slab from reflectance and transmittance: Analytical solution". In: *Journal of Optics A: Pure and Applied Optics* 4.4 (2002), pp. 400–403. ISSN: 14644258. DOI: 10.1088/1464-4258/4/4/306.

List of publications

[1]   B. P. Abbott et al. "GW170817: Observation of Gravitational Waves from a Binary Neutron Star Inspiral". In: *Physical Review Letters* 119.16 (2017). ISSN: 10797114. DOI: 10.1103/PhysRevLett.119.161101.

[2]   G. Vajente et al. "Effect of elevated substrate temperature deposition on the mechanical losses in tantala thin film coatings". In: *Classical and Quantum Gravity* (2018). ISSN: 13616382. DOI: 10.1088/1361-6382/aaad7c.

[3]   K. Prasai et al. "High Precision Detection of Change in Intermediate Range Order of Amorphous Zirconia-Doped Tantala Thin Films Due to Annealing". In: *Physical Review Letters* 123.4 (2019), pp. 1–6. ISSN: 10797114. DOI: 10.1103/PhysRevLett.123.045501.

꧂

GW170817: Observation of Gravitational Waves from a Binary Neutron Star Inspiral

B. P. Abbott *et al.*[*]

(LIGO Scientific Collaboration and Virgo Collaboration)

On August 17, 2017 at 12:41:04 UTC the Advanced LIGO and Advanced Virgo gravitational-wave detectors made their first observation of a binary neutron star inspiral. The signal, GW170817, was detected with a combined signal-to-noise ratio of 32.4 and a false-alarm-rate estimate of less than one per 8.0×10^4 years. We infer the component masses of the binary to be between 0.86 and 2.26 $M_\odot$, in agreement with masses of known neutron stars. Restricting the component spins to the range inferred in binary neutron stars, we find the component masses to be in the range 1.17–1.60 $M_\odot$, with the total mass of the system $2.74^{+0.04}_{-0.01} M_\odot$. The source was localized within a sky region of 28 deg^2 (90% probability) and had a luminosity distance of 40^{+8}_{-14} Mpc, the closest and most precisely localized gravitational-wave signal yet. The association with the γ-ray burst GRB 170817A, detected by Fermi-GBM 1.7 s after the coalescence, corroborates the hypothesis of a neutron star merger and provides the first direct evidence of a link between these mergers and short γ-ray bursts. Subsequent identification of transient counterparts across the electromagnetic spectrum in the same location further supports the interpretation of this event as a neutron star merger. This unprecedented joint gravitational and electromagnetic observation provides insight into astrophysics, dense matter, gravitation, and cosmology.

I. INTRODUCTION

On August 17, 2017, the LIGO-Virgo detector network observed a gravitational-wave signal from the inspiral of two low-mass compact objects consistent with a binary neutron star (BNS) merger. This discovery comes four decades after Hulse and Taylor discovered the first neutron star binary, PSR B1913+16 [1]. Observations of PSR B1913+16 found that its orbit was losing energy due to the emission of gravitational waves, providing the first indirect evidence of their existence [2]. As the orbit of a BNS system shrinks, the gravitational-wave luminosity increases, accelerating the inspiral. This process has long been predicted to produce a gravitational-wave signal observable by ground-based detectors [3–6] in the final minutes before the stars collide [7].

Since the Hulse-Taylor discovery, radio pulsar surveys have found several more BNS systems in our galaxy [8]. Understanding the orbital dynamics of these systems inspired detailed theoretical predictions for gravitational-wave signals from compact binaries [9–13]. Models of the population of compact binaries, informed by the known binary pulsars, predicted that the network of advanced gravitational-wave detectors operating at design sensitivity

will observe between one BNS merger every few years to hundreds per year [14–21]. This detector network currently includes three Fabry-Perot-Michelson interferometers that measure spacetime strain induced by passing gravitational waves as a varying phase difference between laser light propagating in perpendicular arms: the two Advanced LIGO detectors (Hanford, WA and Livingston, LA) [22] and the Advanced Virgo detector (Cascina, Italy) [23].

Advanced LIGO's first observing run (O1), from September 12, 2015, to January 19, 2016, obtained 49 days of simultaneous observation time in two detectors. While two confirmed binary black hole (BBH) mergers were discovered [24–26], no detections or significant candidates had component masses lower than $5M_\odot$, placing a 90% credible upper limit of 12 600 Gpc^{-3} yr^{-1} on the rate of BNS mergers [27] (credible intervals throughout this Letter contain 90% of the posterior probability unless noted otherwise). This measurement did not impinge on the range of astrophysical predictions, which allow rates as high as $\sim$10 000 Gpc^{-3} yr^{-1} [19].

The second observing run (O2) of Advanced LIGO, from November 30, 2016 to August 25, 2017, collected 117 days of simultaneous LIGO-detector observing time. Advanced Virgo joined the O2 run on August 1, 2017. At the time of this publication, two BBH detections have been announced [28,29] from the O2 run, and analysis is still in progress.

Toward the end of the O2 run a BNS signal, GW170817, was identified by matched filtering [7,30–33] the data against post-Newtonian waveform models [34–37]. This gravitational-wave signal is the loudest yet observed, with a combined signal-to-noise ratio (SNR) of 32.4 [38]. After

---

[*]Full author list given at the end of the Letter.

~100 s (calculated starting from 24 Hz) in the detectors' sensitive band, the inspiral signal ended at 12:41:04.4 UTC. In addition, a γ-ray burst was observed 1.7 s after the coalescence time [39–45]. The combination of data from the LIGO and Virgo detectors allowed a precise sky position localization to an area of 28 deg^2. This measurement enabled an electromagnetic follow-up campaign that identified a counterpart near the galaxy NGC 4993, consistent with the localization and distance inferred from gravitational-wave data [46–50].

From the gravitational-wave signal, the best measured combination of the masses is the chirp mass [51] $\mathcal{M} = 1.188^{+0.004}_{-0.002} M_\odot$. From the union of 90% credible intervals obtained using different waveform models (see Sec. IV for details), the total mass of the system is between 2.73 and 3.29 $M_\odot$. The individual masses are in the broad range of 0.86 to 2.26 $M_\odot$, due to correlations between their uncertainties. This suggests a BNS as the source of the gravitational-wave signal, as the total masses of known BNS systems are between 2.57 and 2.88 $M_\odot$ with components between 1.17 and ~1.6 $M_\odot$ [52]. Neutron stars in general have precisely measured masses as large as 2.01 $\pm$ 0.04 $M_\odot$ [53], whereas stellar-mass black holes found in binaries in our galaxy have masses substantially greater than the components of GW170817 [54–56].

Gravitational-wave observations alone are able to measure the masses of the two objects and set a lower limit on their compactness, but the results presented here do not exclude objects more compact than neutron stars such as quark stars, black holes, or more exotic objects [57–61]. The detection of GRB 170817A and subsequent electromagnetic emission demonstrates the presence of matter. Moreover, although a neutron star–black hole system is not ruled out, the consistency of the mass estimates with the dynamically measured masses of known neutron stars in binaries, and their inconsistency with the masses of known black holes in galactic binary systems, suggests the source was composed of two neutron stars.

II. DATA

At the time of GW170817, the Advanced LIGO detectors and the Advanced Virgo detector were in observing mode. The maximum distances at which the LIGO-Livingston and LIGO-Hanford detectors could detect a BNS system (SNR = 8), known as the detector horizon [32,62,63], were 218 Mpc and 107 Mpc, while for Virgo the horizon was 58 Mpc. The GEO600 detector [64] was also operating at the time, but its sensitivity was insufficient to contribute to the analysis of the inspiral. The configuration of the detectors at the time of GW170817 is summarized in [29].

A time-frequency representation [65] of the data from all three detectors around the time of the signal is shown in Fig 1. The signal is clearly visible in the LIGO-Hanford and LIGO-Livingston data. The signal is not visible
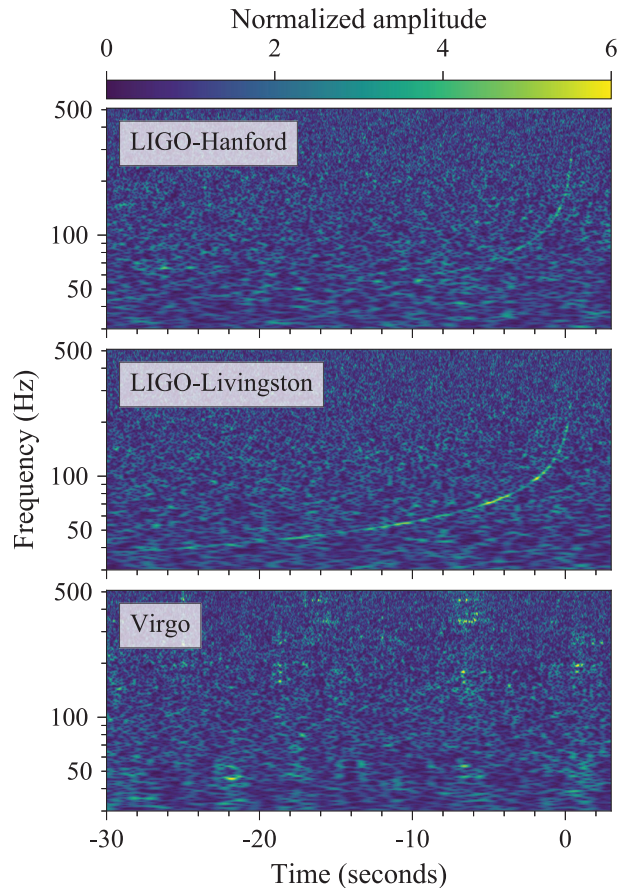
FIG. 1. Time-frequency representations [65] of data containing the gravitational-wave event GW170817, observed by the LIGO-Hanford (top), LIGO-Livingston (middle), and Virgo (bottom) detectors. Times are shown relative to August 17, 2017 12:41:04 UTC. The amplitude scale in each detector is normalized to that detector's noise amplitude spectral density. In the LIGO data, independently observable noise sources and a glitch that occurred in the LIGO-Livingston detector have been subtracted, as described in the text. This noise mitigation is the same as that used for the results presented in Sec. IV.

in the Virgo data due to the lower BNS horizon and the direction of the source with respect to the detector's antenna pattern.

Figure 1 illustrates the data as they were analyzed to determine astrophysical source properties. After data collection, several independently measured terrestrial contributions to the detector noise were subtracted from the LIGO data using Wiener filtering [66], as described in [67–70]. This subtraction removed calibration lines and 60 Hz ac power mains harmonics from both LIGO data streams. The sensitivity of the LIGO-Hanford detector was particularly improved by the subtraction of laser pointing noise; several broad peaks in the 150–800 Hz region were effectively removed, increasing the BNS horizon of that detector by 26%.

Additionally, a short instrumental noise transient appeared in the LIGO-Livingston detector 1.1 s before the coalescence time of GW170817 as shown in Fig. 2. This transient noise, or glitch [71], produced a very brief (less than 5 ms) saturation in the digital-to-analog converter of the feedback signal controlling the position of the test masses. Similar glitches are registered roughly once every few hours in each of the LIGO detectors with no temporal correlation between the LIGO sites. Their cause remains unknown. To mitigate the effect on the results presented in Sec. III, the search analyses applied a window function to zero out the data around the glitch [72,73], following the treatment of other high-amplitude glitches used in the O1 analysis [74]. To accurately determine the properties of GW170817 (as reported in Sec. IV) in addition to the noise subtraction described above, the glitch was modeled with a time-frequency wavelet reconstruction [75] and subtracted from the data, as shown in Fig. 2.

Following the procedures developed for prior gravitational-wave detections [29,78], we conclude there is no environmental disturbance observed by LIGO environmental sensors [79] that could account for the GW170817 signal.

The Virgo data, used for sky localization and an estimation of the source properties, are shown in the bottom panel of Fig. 1. The Virgo data are nonstationary above 150 Hz due to scattered light from the output optics modulated by alignment fluctuations and below 30 Hz due to seismic noise from anthropogenic activity. Occasional noise excess around the European power mains frequency of 50 Hz is also present. No noise subtraction was applied to the Virgo data prior to this analysis. The low signal amplitude observed in Virgo significantly constrained the sky position, but meant that the Virgo data did not contribute significantly to other parameters. As a result, the estimation of the source's parameters reported in Sec. IV is not impacted by the nonstationarity of Virgo data at the time of the event. Moreover, no unusual disturbance was observed by Virgo environmental sensors.

Data used in this study can be found in [80].

III. DETECTION

GW170817 was initially identified as a single-detector event with the LIGO-Hanford detector by a low-latency binary-coalescence search [81–83] using template waveforms computed in post-Newtonian theory [11,13,36,84]. The two LIGO detectors and the Virgo detector were all taking data at the time; however, the saturation at the LIGO-Livingston detector prevented the search from registering a simultaneous event in both LIGO detectors, and the low-latency transfer of Virgo data was delayed.

Visual inspection of the LIGO-Hanford and LIGO-Livingston detector data showed the presence of a clear, long-duration chirp signal in time-frequency representations of the detector strain data. As a result, an initial alert was
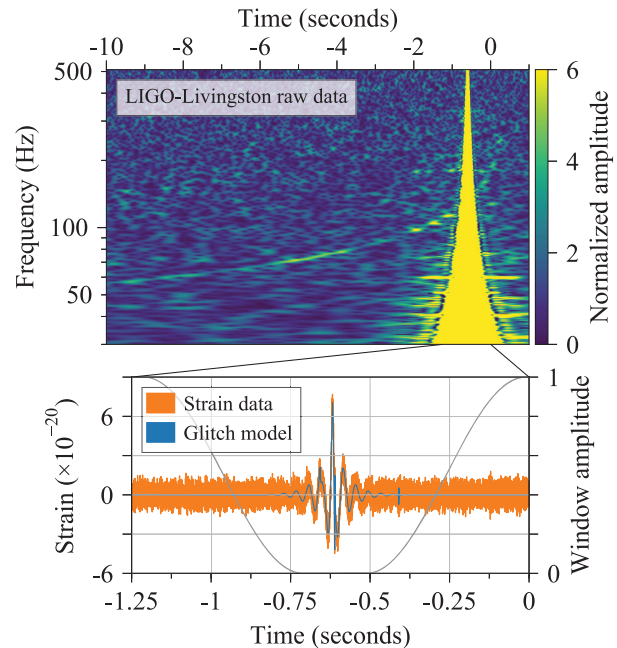
FIG. 2. Mitigation of the glitch in LIGO-Livingston data. Times are shown relative to August 17, 2017 12:41:04 UTC. *Top panel*: A time-frequency representation [65] of the raw LIGO-Livingston data used in the initial identification of GW170817 [76]. The coalescence time reported by the search is at time 0.4 s in this figure and the glitch occurs 1.1 s before this time. The time-frequency track of GW170817 is clearly visible despite the presence of the glitch. *Bottom panel*: The raw LIGO-Livingston strain data (orange curve) showing the glitch in the time domain. To mitigate the glitch in the rapid reanalysis that produced the sky map shown in Fig. 3 [77], the raw detector data were multiplied by an inverse Tukey window (gray curve, right axis) that zeroed out the data around the glitch [73]. To mitigate the glitch in the measurement of the source's properties, a model of the glitch based on a wavelet reconstruction [75] (blue curve) was subtracted from the data. The time-series data visualized in this figure have been bandpassed between 30 Hz and 2 kHz so that the detector's sensitive band is emphasized. The gravitational-wave strain amplitude of GW170817 is of the order of 10^{-22} and so is not visible in the bottom panel.

generated reporting a highly significant detection of a binary neutron star signal [85] in coincidence with the independently observed γ-ray burst GRB 170817A [39–41].

A rapid binary-coalescence reanalysis [86,87], with the time series around the glitch suppressed with a window function [73], as shown in Fig. 2, confirmed the presence of a significant coincident signal in the LIGO detectors. The source was rapidly localized to a region of 31 deg², shown in Fig. 3, using data from all three detectors [88]. This sky map was issued to observing partners, allowing the identification of an electromagnetic counterpart [46,48,50,77].

The combined SNR of GW170817 is estimated to be 32.4, with values 18.8, 26.4, and 2.0 in the LIGO-Hanford,
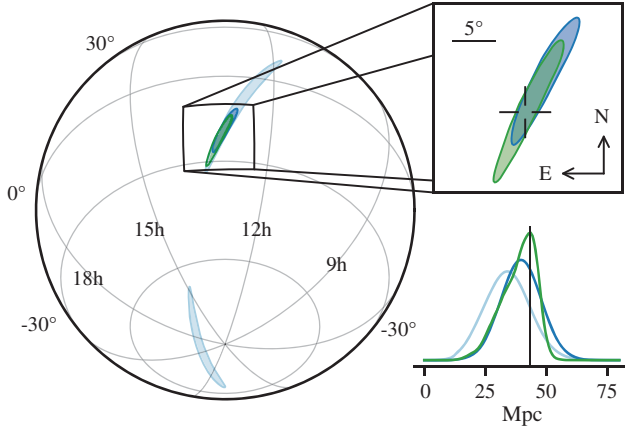
FIG. 3. Sky location reconstructed for GW170817 by a rapid localization algorithm from a Hanford-Livingston (190 deg^2, light blue contours) and Hanford-Livingston-Virgo (31 deg^2, dark blue contours) analysis. A higher latency Hanford-Livingston-Virgo analysis improved the localization (28 deg^2, green contours). In the top-right inset panel, the reticle marks the position of the apparent host galaxy NGC 4993. The bottom-right panel shows the *a posteriori* luminosity distance distribution from the three gravitational-wave localization analyses. The distance of NGC 4993, assuming the redshift from the NASA/IPAC Extragalactic Database [89] and standard cosmological parameters [90], is shown with a vertical line.

LIGO-Livingston, and Virgo data respectively, making it the loudest gravitational-wave signal so far detected. Two matched-filter binary-coalescence searches targeting sources with total mass between 2 and 500 $M_\odot$ in the detector frame were used to estimate the significance of this event [9,12,30,32,73,81–83,86,87,91–97]. The searches analyzed 5.9 days of LIGO data between August 13, 2017 02:00 UTC and August 21, 2017 01:05 UTC. Events are assigned a detection-statistic value that ranks their probability of being a gravitational-wave signal. Each search uses a different method to compute this statistic and measure the search background—the rate at which detector noise produces events with a detection-statistic value equal to or higher than the candidate event.

GW170817 was identified as the most significant event in the 5.9 days of data, with an estimated false alarm rate of one in 1.1×10^6 years with one search [81,83], and a consistent bound of less than one in 8.0×10^4 years for the other [73,86,87]. The second most significant signal in this analysis of 5.9 days of data is GW170814, which has a combined SNR of 18.3 [29]. Virgo data were not used in these significance estimates, but were used in the sky localization of the source and inference of the source properties.

IV. SOURCE PROPERTIES

General relativity makes detailed predictions for the inspiral and coalescence of two compact objects, which

may be neutron stars or black holes. At early times, for low orbital and gravitational-wave frequencies, the chirplike time evolution of the frequency is determined primarily by a specific combination of the component masses m_1 and m_2, the chirp mass $\mathcal{M} = (m_1 m_2)^{3/5}(m_1 + m_2)^{-1/5}$. As the orbit shrinks and the gravitational-wave frequency grows rapidly, the gravitational-wave phase is increasingly influenced by relativistic effects related to the mass ratio $q = m_2/m_1$, where $m_1 \geq m_2$, as well as spin-orbit and spin-spin couplings [98].

The details of the objects' internal structure become important as the orbital separation approaches the size of the bodies. For neutron stars, the tidal field of the companion induces a mass-quadrupole moment [99,100] and accelerates the coalescence [101]. The ratio of the induced quadrupole moment to the external tidal field is proportional to the tidal deformability (or polarizability) $\Lambda = (2/3)k_2[(c^2/G)(R/m)]^5$, where k_2 is the second Love number and R is the stellar radius. Both R and k_2 are fixed for a given stellar mass m by the equation of state (EOS) for neutron-star matter, with $k_2 \simeq 0.05$–0.15 for realistic neutron stars [102–104]. Black holes are expected to have $k_2 = 0$ [99,105–109], so this effect would be absent.

As the gravitational-wave frequency increases, tidal effects in binary neutron stars increasingly affect the phase and become significant above $f_{GW} \simeq 600$ Hz, so they are potentially observable [103,110–116]. Tidal deformabilities correlate with masses and spins, and our measurements are sensitive to the accuracy with which we describe the point-mass, spin, and tidal dynamics [113,117–119]. The point-mass dynamics has been calculated within the post-Newtonian framework [34,36,37], effective-one-body formalism [10,120–125], and with a phenomenological approach [126–131]. Results presented here are obtained using a frequency domain post-Newtonian waveform model [30] that includes dynamical effects from tidal interactions [132], point-mass spin-spin interactions [34,37,133,134], and couplings between the orbital angular momentum and the orbit-aligned dimensionless spin components of the stars χ_z [92].

The properties of gravitational-wave sources are inferred by matching the data with predicted waveforms. We perform a Bayesian analysis in the frequency range 30–2048 Hz that includes the effects of the 1σ calibration uncertainties on the received signal [135,136] ($< 7\%$ in amplitude and 3° in phase for the LIGO detectors [137] and 10% and 10° for Virgo at the time of the event). Unless otherwise specified, bounds on the properties of GW170817 presented in the text and in Table I are 90% posterior probability intervals that enclose systematic differences from currently available waveform models.

To ensure that the applied glitch mitigation procedure previously discussed in Sec. II (see Fig. 2) did not bias the estimated parameters, we added simulated signals with known parameters to data that contained glitches analogous

TABLE I.   Source properties for GW170817: we give ranges encompassing the 90% credible intervals for different assumptions of the waveform model to bound systematic uncertainty. The mass values are quoted in the frame of the source, accounting for uncertainty in the source redshift.

	Low-spin priors ($|\chi| \leq 0.05$)	High-spin priors ($|\chi| \leq 0.89$)
Primary mass m_1	1.36–1.60 $M_\odot$	1.36–2.26 $M_\odot$
Secondary mass m_2	1.17–1.36 $M_\odot$	0.86–1.36 $M_\odot$
Chirp mass $\mathcal{M}$	$1.188^{+0.004}_{-0.002} M_\odot$	$1.188^{+0.004}_{-0.002} M_\odot$
Mass ratio m_2/m_1	0.7–1.0	0.4–1.0
Total mass m_{tot}	$2.74^{+0.04}_{-0.01} M_\odot$	$2.82^{+0.47}_{-0.09} M_\odot$
Radiated energy E_{rad}	$> 0.025 M_\odot c^2$	$> 0.025 M_\odot c^2$
Luminosity distance D_{L}	40^{+8}_{-14} Mpc	40^{+8}_{-14} Mpc
Viewing angle Θ	$\leq 55°$	$\leq 56°$
Using NGC 4993 location	$\leq 28°$	$\leq 28°$
Combined dimensionless tidal deformability $\tilde{\Lambda}$	≤ 800	≤ 700
Dimensionless tidal deformability $\Lambda(1.4M_\odot)$	≤ 800	≤ 1400

to the one observed at the LIGO-Livingston detector during GW170817. After applying the glitch subtraction technique, we found that the bias in recovered parameters relative to their known values was well within their uncertainties. This can be understood by noting that a small time cut out of the coherent integration of the phase evolution has little impact on the recovered parameters. To corroborate these results, the test was also repeated with a window function applied, as shown in Fig. 2 [73].

The source was localized to a region of the sky 28 deg^2 in area, and 380 Mpc^3 in volume, near the southern end of the constellation Hydra, by using a combination of the timing, phase, and amplitude of the source as observed in the three detectors [138,139]. The third detector, Virgo, was essential in localizing the source to a single region of the sky, as shown in Fig. 3. The small sky area triggered a successful follow-up campaign that identified an electromagnetic counterpart [50].

The luminosity distance to the source is 40^{+8}_{-14} Mpc, the closest ever observed gravitational-wave source and, by association, the closest short γ-ray burst with a distance measurement [45]. The distance measurement is correlated with the inclination angle $\cos\theta_{JN} = \hat{\mathbf{J}} \cdot \hat{\mathbf{N}}$, where $\hat{\mathbf{J}}$ is the unit vector in the direction of the total angular momentum of the system and $\hat{\mathbf{N}}$ is that from the source towards the observer [140]. We find that the data are consistent with an antialigned source: $\cos\theta_{JN} \leq -0.54$, and the viewing angle $\Theta \equiv \min(\theta_{JN}, 180° - \theta_{JN})$ is $\Theta \leq 56°$. Since the luminosity distance of this source can be determined independently of the gravitational wave data alone, we can use the association with NGC 4993 to break the distance degeneracy with $\cos\theta_{JN}$. The estimated Hubble flow velocity near NGC 4993 of 3017 ± 166 km s^{-1} [141] provides a redshift, which in a flat cosmology with $H_0 = 67.90 \pm 0.55$ km s^{-1} Mpc^{-1} [90], constrains $\cos\theta_{JN} < -0.88$ and $\Theta < 28°$. The constraint varies with the assumptions made about H_0 [141].

From the gravitational-wave phase and the $\sim$3000 cycles in the frequency range considered, we constrain the chirp mass in the detector frame to be $\mathcal{M}^{\mathrm{det}} = 1.1977^{+0.0008}_{-0.0003} M_\odot$ [51]. The mass parameters in the detector frame are related to the rest-frame masses of the source by its redshift z as $m^{\mathrm{det}} = m(1 + z)$ [142]. Assuming the above cosmology [90], and correcting for the motion of the Solar System Barycenter with respect to the Cosmic Microwave Background [143], the gravitational-wave distance measurement alone implies a cosmological redshift of $0.008^{+0.002}_{-0.003}$, which is consistent with that of NGC 4993 [50,141,144,145]. Without the host galaxy, the uncertainty in the source's chirp mass $\mathcal{M}$ is dominated by the uncertainty in its luminosity distance. Independent of the waveform model or the choice of priors, described below, the source-frame chirp mass is $\mathcal{M} = 1.188^{+0.004}_{-0.002} M_\odot$.

While the chirp mass is well constrained, our estimates of the component masses are affected by the degeneracy between mass ratio q and the aligned spin components χ_{1z} and χ_{2z} [38,146–150]. Therefore, the estimates of q and the component masses depend on assumptions made about the admissible values of the spins. While $\chi < 1$ for black holes, and quark stars allow even larger spin values, realistic NS equations of state typically imply more stringent limits. For the set of EOS studied in [151] $\chi < 0.7$, although other EOS can exceed this bound. We began by assuming $|\chi| \leq 0.89$, a limit imposed by available rapid waveform models, with an isotropic prior on the spin direction. With these priors we recover $q \in (0.4, 1.0)$ and a constraint on the effective aligned spin of the system [127,152] of $\chi_{\mathrm{eff}} \in (-0.01, 0.17)$. The aligned spin components are consistent with zero, with stricter bounds than in previous BBH observations [26,28,29]. Analysis using the effective precessing phenomenological waveforms of [128], which do not contain tidal effects, demonstrates that spin components in the orbital plane are not constrained.
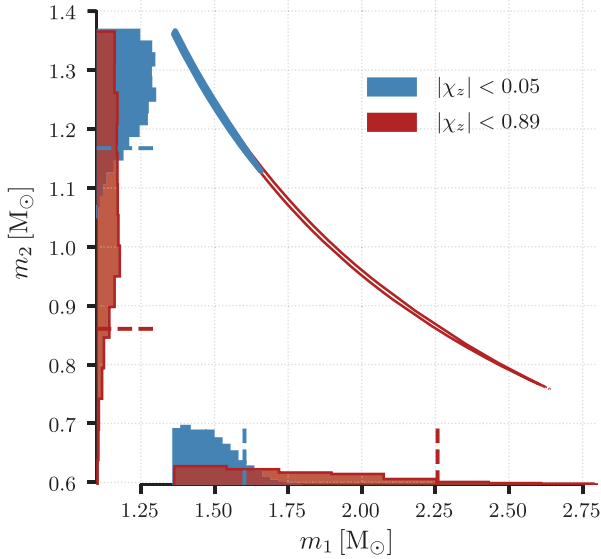
FIG. 4.   Two-dimensional posterior distribution for the component masses m_1 and m_2 in the rest frame of the source for the low-spin scenario ($|\chi| < 0.05$, blue) and the high-spin scenario ($|\chi| < 0.89$, red). The colored contours enclose 90% of the probability from the joint posterior probability density function for m_1 and m_2. The shape of the two dimensional posterior is determined by a line of constant $\mathcal{M}$ and its width is determined by the uncertainty in $\mathcal{M}$. The widths of the marginal distributions (shown on axes, dashed lines enclose 90% probability away from equal mass of $1.36 M_\odot$) is strongly affected by the choice of spin priors. The result using the low-spin prior (blue) is consistent with the masses of all known binary neutron star systems.

From $\mathcal{M}$ and q, we obtain a measure of the component masses $m_1 \in (1.36, 2.26)M_\odot$ and $m_2 \in (0.86, 1.36)M_\odot$, shown in Fig. 4. As discussed in Sec. I, these values are within the range of known neutron-star masses and below those of known black holes. In combination with electromagnetic observations, we regard this as evidence of the BNS nature of GW170817.

The fastest-spinning known neutron star has a dimensionless spin $\lesssim 0.4$ [153], and the possible BNS J1807-2500B has spin $\lesssim 0.2$ [154], after allowing for a broad range of equations of state. However, among BNS that will merge within a Hubble time, PSR J0737-3039A [155] has the most extreme spin, less than ~ 0.04 after spin-down is extrapolated to merger. If we restrict the spin magnitude in our analysis to $|\chi| \leq 0.05$, consistent with the observed population, we recover the mass ratio $q \in (0.7, 1.0)$ and component masses $m_1 \in (1.36, 1.60)M_\odot$ and $m_2 \in (1.17, 1.36)M_\odot$ (see Fig. 4). We also recover $\chi_{\text{eff}} \in (-0.01, 0.02)$, where the upper limit is consistent with the low-spin prior.

Our first analysis allows the tidal deformabilities of the high-mass and low-mass component, Λ_1 and Λ_2, to vary independently. Figure 5 shows the resulting 90% and 50% contours on the posterior distribution with the post-Newtonian waveform model for the high-spin and low-spin priors. As a comparison, we show predictions coming from a set of candidate equations of state for neutron-star matter [156–160], generated using fits from [161]. All EOS support masses of $2.01 \pm 0.04 M_\odot$. Assuming that both components are neutron stars described by the same equation of state, a single function $\Lambda(m)$ is computed from the static $\ell = 2$ perturbation of a Tolman-Oppenheimer-Volkoff solution [103]. The shaded regions in Fig. 5 represent the values of the tidal deformabilities Λ_1 and Λ_2 generated using an equation of state from the 90% most probable fraction of the values of m_1 and m_2, consistent with the posterior shown in Fig. 4. We find that our constraints on Λ_1 and Λ_2 disfavor equations of state that predict less compact stars, since the mass range we recover generates Λ values outside the 90% probability region. This is consistent with radius constraints from x-ray observations of neutron stars [162–166]. Analysis methods, in development, that *a priori* assume the same EOS governs both stars should improve our constraints [167].

To leading order in Λ_1 and Λ_2, the gravitational-wave phase is determined by the parameter

$$\tilde{\Lambda} = \frac{16}{13} \frac{(m_1 + 12m_2)m_1^4 \Lambda_1 + (m_2 + 12m_1)m_2^4 \Lambda_2}{(m_1 + m_2)^5} \quad (1)$$

[101,117]. Assuming a uniform prior on $\tilde{\Lambda}$, we place a 90% upper limit of $\tilde{\Lambda} \leq 800$ in the low-spin case and $\tilde{\Lambda} \leq 700$ in the high-spin case. We can also constrain the function $\Lambda(m)$ more directly by expanding $\Lambda(m)$ linearly about $m = 1.4M_\odot$ (as in [112,115]), which gives $\Lambda(1.4M_\odot) \leq 1400$ for the high-spin prior and $\Lambda(1.4M_\odot) \leq 800$ for the low-spin prior. A 95% upper bound inferred with the low-spin prior, $\Lambda(1.4M_\odot) \leq 970$, begins to compete with the 95% upper bound of 1000 derived from x-ray observations in [168].

Since the energy emitted in gravitational waves depends critically on the EOS of neutron-star matter, with a wide range consistent with constraints above, we are only able to place a lower bound on the energy emitted before the onset of strong tidal effects at $f_{\text{GW}} \sim 600 \text{ Hz}$ as $E_{\text{rad}} > 0.025 M_\odot c^2$. This is consistent with E_{rad} obtained from numerical simulations and fits for BNS systems consistent with GW170817 [114,169–171].

We estimate systematic errors from waveform modeling by comparing the post-Newtonian results with parameters recovered using an effective-one-body model [124] augmented with tidal effects extracted from numerical relativity with hydrodynamics [172]. This does not change the 90% credible intervals for component masses and effective spin under low-spin priors, but in the case of high-spin priors, we obtain the more restrictive $m_1 \in (1.36, 1.93)M_\odot$, $m_2 \in (0.99, 1.36)M_\odot$, and $\chi_{\text{eff}} \in (0.0, 0.09)$. Recovered tidal deformabilities indicate shifts in the posterior distributions towards smaller values, with upper bounds for $\tilde{\Lambda}$ and $\Lambda(1.4M_\odot)$ reduced by a factor of roughly (0.8, 0.8) in the
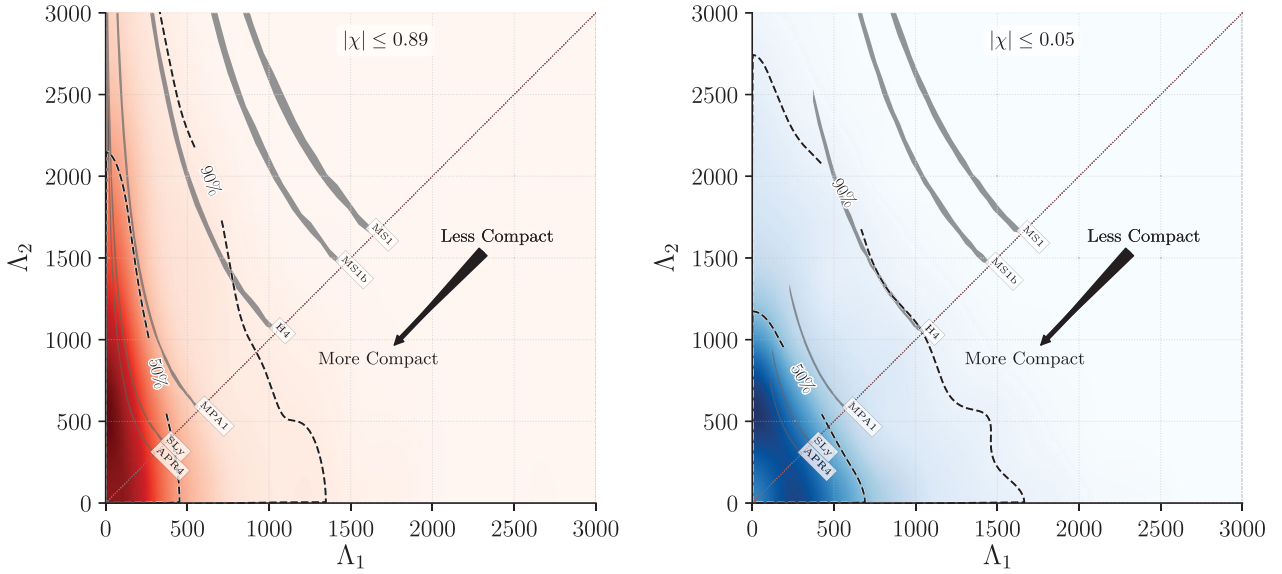
FIG. 5.   Probability density for the tidal deformability parameters of the high and low mass components inferred from the detected signals using the post-Newtonian model. Contours enclosing 90% and 50% of the probability density are overlaid (dashed lines). The diagonal dashed line indicates the $\Lambda_1 = \Lambda_2$ boundary. The Λ_1 and Λ_2 parameters characterize the size of the tidally induced mass deformations of each star and are proportional to $k_2(R/m)^5$. Constraints are shown for the high-spin scenario $|\chi| \leq 0.89$ (left panel) and for the low-spin $|\chi| \leq 0.05$ (right panel). As a comparison, we plot predictions for tidal deformability given by a set of representative equations of state [156–160] (shaded filled regions), with labels following [161], all of which support stars of $2.01 M_\odot$. Under the assumption that both components are neutron stars, we apply the function $\Lambda(m)$ prescribed by that equation of state to the 90% most probable region of the component mass posterior distributions shown in Fig. 4. EOS that produce less compact stars, such as MS1 and MS1b, predict Λ values outside our 90% contour.

low-spin case and (1.0, 0.7) in the high-spin case. Further analysis is required to establish the uncertainties of these tighter bounds, and a detailed study of systematics is a subject of ongoing work.

Preliminary comparisons with waveform models under development [171,173–177] also suggest the post-Newtonian model used will systematically overestimate the value of the tidal deformabilities. Therefore, based on our current understanding of the physics of neutron stars, we consider the post-Newtonian results presented in this Letter to be conservative upper limits on tidal deformability. Refinements should be possible as our knowledge and models improve.

V. IMPLICATIONS

A. Astrophysical rate

Our analyses identified GW170817 as the only BNS-mass signal detected in O2 with a false alarm rate below $1/100$ yr. Using a method derived from [27,178,179], and assuming that the mass distribution of the components of BNS systems is flat between 1 and $2\,M_\odot$ and their dimensionless spins are below 0.4, we are able to infer the local coalescence rate density R of BNS systems. Incorporating the upper limit of 12600 Gpc^{-3} yr^{-1} from O1 as a prior, $R = 1540^{+3200}_{-1220}$ Gpc^{-3} yr^{-1}. Our findings are

consistent with the rate inferred from observations of galactic BNS systems [19,20,155,180].

From this inferred rate, the stochastic background of gravitational wave s produced by unresolved BNS mergers throughout the history of the Universe should be comparable in magnitude to the stochastic background produced by BBH mergers [181,182]. As the advanced detector network improves in sensitivity in the coming years, the total stochastic background from BNS and BBH mergers should be detectable [183].

B. Remnant

Binary neutron star mergers may result in a short- or long-lived neutron star remnant that could emit gravitational waves following the merger [184–190]. The ringdown of a black hole formed after the coalescence could also produce gravitational waves, at frequencies around 6 kHz, but the reduced interferometer response at high frequencies makes their observation unfeasible. Consequently, searches have been made for short (tens of ms) and intermediate duration (≤ 500 s) gravitational-wave signals from a neutron star remnant at frequencies up to 4 kHz [75,191,192]. For the latter, the data examined start at the time of the coalescence and extend to the end of the observing run on August 25, 2017. With the time scales and methods considered so far [193], there is no evidence of a postmerger signal of

astrophysical origin. However, upper limits placed on the strength of gravitational-wave emission cannot definitively rule out the existence of a short- or long-lived postmerger neutron star. The implications of various postmerger scenarios are explored in [45,193].

C. Tests of gravity

GRB 170817A was observed 1.7 s after GW170817. Combining this delay with the knowledge of the source luminosity distance, strong constraints are placed on the fundamental physics of gravity. The observed arrival times are used to investigate the speed of gravity, Lorentz invariance, and tests of the equivalence principle through the Shapiro time delay, as reported in [45].

We also expect the much longer duration of the BNS signal compared to previous BBH gravitational-wave sources to yield significantly improved constraints when testing for waveform deviations from general relativity using a parametrized waveform expansion [194], especially at low post-Newtonian orders. Placing these bounds requires a deep understanding of the systematic uncertainties resulting from waveform modeling and data conditioning, and is the subject of ongoing investigations.

D. Cosmology

The gravitational-wave signal gives a direct measurement of the luminosity distance of the source, which, along with a redshift measurement, can be used to infer cosmological parameters independently of the cosmic distance ladder [141,195]. Using the association with the galaxy NGC 4993 and the luminosity distance directly measured from the gravitational-wave signal, the Hubble constant is inferred to be $H_0 = 70^{+12}_{-8}$ km s^{-1} Mpc^{-1} [141] (most probable value and minimum 68.3% probability range, which can be compared to the value from Planck $H_0 = 67.90 \pm 0.55$ km s^{-1} Mpc^{-1} [90]). Alternatively, we may assume the cosmology is known and use the association with NGC 4993 to constrain the luminosity distance of the source, in which case the gravitational-wave measurement of the inclination angle of the source is significantly improved, with consequences for the γ-ray burst opening angle and related physics [45].

VI. CONCLUSIONS

In this Letter we have presented the first detection of gravitational waves from the inspiral of a binary neutron star system. Gravitational-wave event GW170817, observed and localized by the two Advanced LIGO detectors and the Advanced Virgo detector, is the loudest gravitational-wave signal detected to date. This coalescence event was followed by a short burst of γ rays observed with the *Fermi* Gamma-Ray Burst Monitor [39–42] and *INTEGRAL* [43,44]. The coincident observation of a gravitational-wave signal and a γ-ray burst appears to confirm the long-held hypothesis that

BNS mergers are linked to short-γ-ray bursts [196,197]. Subsequent observations have determined the location of the source and followed its evolution through the electromagnetic spectrum [50].

Detailed analyses of the gravitational-wave data, together with observations of electromagnetic emissions, are providing new insights into the astrophysics of compact binary systems and γ-ray bursts, dense matter under extreme conditions, the nature of gravitation, and independent tests of cosmology. Less than two years after the debut of gravitational-wave astronomy, GW170817 marks the beginning of a new era of discovery.

ACKNOWLEDGMENTS

[1] R. A. Hulse and J. H. Taylor, Astrophys. J. **195**, L51 (1975).

[2] J. H. Taylor and J. M. Weisberg, Astrophys. J. **253**, 908 (1982).

[3] R. Weiss, MIT Technical Report No. LIGO-P720002, 1972.

[4] R. W. P. Drever, in *Gravitational Radiation*, edited by N. Deruelle and T. Piran (North-Holland, Amsterdam, 1983), p. 321.

[5] A. Brillet *et al.* (Virgo Collaboration), Technical Report No. VIR-0517A-15, 1989 [https://tds.virgo-gw.eu/?content=3&r=12122].

[6] J. Hough *et al.*, MPQ Technical Report No. 147, 1989 [GWD/137/JH(89)].

[7] K. Thorne, *Three Hundred Years of Gravitation*, edited by S. W. Hawking and W. Israel (Cambridge University Press, Cambridge, U.K., 1987), pp. 330–458.

[8] R. N. Manchester, G. B. Hobbs, A. Teoh, and M. Hobbs, Astron. J. **129**, 1993 (2005).

[9] L. Blanchet, Thibault Damour, Bala R. Iyer, Clifford M. Will, and Alan G. Wiseman, Phys. Rev. Lett. **74**, 3515 (1995).

[10] A. Buonanno and T. Damour, Phys. Rev. D **59**, 084006 (1999).

[11] T. Damour, P. Jaranowski, and G. Schäfer, Phys. Lett. B **513**, 147 (2001).

[12] L. Blanchet, T. Damour, G. Esposito-Farese, and B. R. Iyer, Phys. Rev. Lett. **93**, 091101 (2004).

[13] W. D. Goldberger and I. Z. Rothstein, Phys. Rev. D **73**, 104029 (2006).

[14] B. P. Flannery and E. P. J. van den Heuvel, Astron. Astrophys. **39**, 61 (1975).

[15] A. G. Massevitch, A. V. Tutukov, and L. R. Yungelson, Astrophys. Space Sci. **40**, 115 (1976).

[16] J. P. A. Clark, E. P. J. van den Heuvel, and W. Sutantyo, Astron. Astrophys. **72**, 120 (1979).

[17] E. S. Phinney, Astrophys. J. Lett. **380**, L17 (1991).

[18] V. Kalogera *et al.*, Astrophys. J. Lett. **601**, L179 (2004). V. Kalogera *et al.*, Astrophys. J. Lett. **614**, L137(E) (2004).

[19] J. Abadie *et al.* (LIGO Scientific Collaboration and Virgo Collaboration), Classical Quantum Gravity **27**, 173001 (2010).

[20] C. Kim, B. B. P. Perera, and M. A. McLaughlin, Mon. Not. R. Astron. Soc. **448**, 928 (2015).

[21] B. P. Abbott *et al.* (KAGRA Collaboration, LIGO Scientific Collaboration, Virgo Collaboration), Living Rev. Relativity **19**, 1 (2016).

[22] J. Aasi *et al.* (LIGO Scientific Collaboration), Classical Quantum Gravity **32**, 074001 (2015).

[23] F. Acernese *et al.* (Virgo Collaboration), Classical Quantum Gravity **32**, 024001 (2015).

[24] B. P. Abbott *et al.* (LIGO Scientific Collaboration and Virgo Collaboration), Phys. Rev. Lett. **116**, 061102 (2016).

[25] B. P. Abbott *et al.* (LIGO Scientific Collaboration and Virgo Collaboration), Phys. Rev. Lett. **116**, 241103 (2016).

[26] B. P. Abbott *et al.* (LIGO Scientific Collaboration and Virgo Collaboration), Phys. Rev. X **6**, 041015 (2016).

[27] B. P. Abbott *et al.* (LIGO Scientific Collaboration and Virgo Collaboration), Astrophys. J. Lett. **832**, L21 (2016).

[28] B. P. Abbott *et al.* (LIGO Scientific Collaboration and Virgo Collaboration), Phys. Rev. Lett. **118**, 221101 (2017).

[29] B. P. Abbott *et al.* (LIGO Scientific Collaboration and Virgo Collaboration), Phys. Rev. Lett. **119**, 141101 (2017).

[30] B. S. Sathyaprakash and S. V. Dhurandhar, Phys. Rev. D **44**, 3819 (1991).

[31] C. Cutler *et al.*, Phys. Rev. Lett. **70**, 2984 (1993).

[32] B. Allen, W. G. Anderson, P. R. Brady, D. A. Brown, and J. D. E. Creighton, Phys. Rev. D **85**, 122006 (2012).

[33] D. A. Brown, P. Kumar, and A. H. Nitz, Phys. Rev. D **87**, 082004 (2013).

[34] K. G. Arun, A. Buonanno, G. Faye, and E. Ochsner, Phys. Rev. D **79**, 104023 (2009); **84**, 049901(E) (2011).

[35] A. Buonanno, B. R. Iyer, E. Ochsner, Y. Pan, and B. S. Sathyaprakash, Phys. Rev. D **80**, 084043 (2009).

[36] L. Blanchet, Living Rev. Relativity **17**, 2 (2014).

[37] C. K. Mishra, A. Kela, K. G. Arun, and G. Faye, Phys. Rev. D **93**, 084054 (2016).

[38] C. Cutler and E. E. Flanagan, Phys. Rev. D **49**, 2658 (1994).

[39] A. G. A. von Kienlin, C. Meegan, and the Fermi GBM Team, GCN 21520, 1 (2017).

[40] V. Connaughton *et al.*, GCN 21506, 1 (2017).

[41] A. Goldstein *et al.*, GCN 21528, 1 (2017).

[42] A. Goldstein *et al.*, Astrophys. J. Lett. **848**, L14 (2017).

[43] V. Savchenko *et al.*, GCN 21507, 1 (2017).

[44] V. Savchenko *et al.*, Astrophys. J. Lett. **848**, L15 (2017).

[45] B. P. Abbott *et al.* (LIGO Scientific Collaboration and Virgo Collaboration), Astrophys. J. Lett. **848**, L13 (2017);

[46] D. A. Coulter *et al.*, GCN 21529, 1 (2017).

[47] R. J. Foley *et al.*, GCN 21536, 1 (2017).

[48] D. A. Coulter *et al.*, Science, in press (2017), DOI: 10.1126/science.aap9811.

[49] Y.-C. Pan *et al.*, Astrophys. J. Lett. **848**, L30 (2017).

[50] B. P. Abbott *et al.* (LIGO Scientific Collaboration and Virgo Collaboration), Astrophys. J. Lett. **848**, L12 (2017).

[51] P. C. Peters and J. Mathews, Phys. Rev. **131**, 435 (1963).

[52] T. M. Tauris *et al.*, Astrophys. J. **846**, 170 (2017).

[53] J. Antoniadis *et al.*, Science **340**, 1233232 (2013).

[54] F. Özel, D. Psaltis, R. Narayan, and J. E. McClintock, Astrophys. J. **725**, 1918 (2010).

[55] L. Kreidberg, C. D. Bailyn, W. M. Farr, and V. Kalogera, Astrophys. J. **757**, 36 (2012).

[56] R. Narayan and J. E. McClintock, in *General Relativity and Gravitation: A Centennial Perspective*, edited by A. Ashtekar, B. K. Berger, J. Isenberg, and M. MacCallum (Cambridge University Press, Cambridge, U.K., 2015), Chap. 3.3, pp. 133–147.

[57] D. J. Kaup, Phys. Rev. **172**, 1331 (1968).

[58] P. O. Mazur and E. Mottola, Proc. Natl. Acad. Sci. U.S.A. **101**, 9545 (2004).

[59] N. Itoh, Prog. Theor. Phys. **44**, 291 (1970).

[60] V. Cardoso, S. Hopper, C. F. B. Macedo, C. Palenzuela, and P. Pani, Phys. Rev. D **94**, 084031 (2016).

[61] V. Cardoso, E. Franzin, A. Maselli, P. Pani, and G. Raposo, Phys. Rev. D **95**, 084014 (2017); **95**, 089901 (2017).

[62] L. S. Finn and D. F. Chernoff, Phys. Rev. D **47**, 2198 (1993).

[63] H.-Y. Chen, D. E. Holz, J. Miller, M. Evans, S. Vitale, and J. Creighton, arXiv:1709.08079.

[64] K. L. Dooley et al., Classical Quantum Gravity **33**, 075009 (2016).

[65] S. Chatterji, L Blackburn, G Martin, and E Katsavounidis, Classical Quantum Gravity **21**, S1809 (2004).

[66] R. G. Brown and P. Y. C. Hwang, *Introduction to Random Signals and Applied Kalman Filtering with Matlab Exercises* (Wiley, New York, 2012).

[67] J. C. Driggers et al., Technical Report No. LIGO-P1700260, 2017.

[68] J. C. Driggers, M. Evans, K. Pepper, and R. Adhikari, Rev. Sci. Instrum. **83**, 024501 (2012).

[69] G. D. Meadors, K. Kawabe, and K. Riles, Classical Quantum Gravity **31**, 105014 (2014).

[70] V. Tiwari et al., Classical Quantum Gravity **32**, 165014 (2015).

[71] L. Nuttall et al., Classical Quantum Gravity **32**, 245005 (2015).

[72] B. P. Abbott et al. (LIGO Scientific Collaboration and Virgo Collaboration), Phys. Rev. D **93**, 122003 (2016).

[73] S. A. Usman et al., Classical Quantum Gravity **33**, 215004 (2016).

[74] B. P. Abbott et al. (LIGO Scientific Collaboration and Virgo Collaboration), Technical Report No. LIGO-P1600110, 2017.

[75] N. J. Cornish and T. B. Littenberg, Classical Quantum Gravity **32**, 135012 (2015).

[76] LIGO Scientific Collaboration and Virgo Collaboration, GCN **21509**, 1 (2017).

[77] LIGO Scientific Collaboration and Virgo Collaboration, GCN **21513**, 1 (2017).

[78] B. P. Abbott et al. (LIGO Scientific Collaboration and Virgo Collaboration), Classical Quantum Gravity **33**, 134001 (2016).

[79] A. Effler, R M S Schofield, V V Frolov, G González, K Kawabe, J R Smith, J Birch, and R McCarthy, Classical Quantum Gravity **32**, 035017 (2015).

[80] LIGO Scientific Collaboration and Virgo Collaboration, LIGO Open Science Center (LOSC), 2017 [https://doi.org/10.7935/K5B8566F].

[81] K. Cannon et al., Astrophys. J. **748**, 136 (2012).

[82] S. Privitera, S. R. P. Mohapatra, P. Ajith, K. Cannon, N. Fotopoulos, M. A. Frei, C. Hanna, A. J. Weinstein, and J. T. Whelan, Phys. Rev. D **89**, 024003 (2014).

[83] C. Messick et al., Phys. Rev. D **95**, 042001 (2017).

[84] A. Einstein, L. Infeld, and B. Hoffmann, Ann. Math. **39**, 65 (1938).

[85] LIGO Scientific Collaboration and Virgo Collaboration, GCN **21505**, 1 (2017).

[86] A. H. Nitz, T. Dent, T. Dal Canton, S. Fairhurst, and D. A. Brown, arXiv:1705.01513.

[87] A. Nitz et al., ligo-cbc/pycbc: O2 production release 20, 2017.

[88] L. P. Singer and L. R. Price, Phys. Rev. D **93**, 024013 (2016).

[89] NASA/IPAC Extragalactic Database.

[90] P. A. R. Ade et al. (Planck Collaboration), Astron. Astrophys. **594**, A13 (2016).

[91] L. Blanchet, A. Buonanno, and G. Faye, Phys. Rev. D **74**, 104034 (2006); **75**, 049903(E) (2007); **81**, 089901(E) (2010).

[92] A. Bohé, S. Marsat, and L. Blanchet, Classical Quantum Gravity **30**, 135009 (2013).

[93] B. J. Owen and B. S. Sathyaprakash, Phys. Rev. D **60**, 022002 (1999).

[94] D. A. Brown, I. Harry, A. Lundgren, and A. H. Nitz, Phys. Rev. D **86**, 084017 (2012).

[95] T. Dal Canton and I. W. Harry, arXiv:1705.01845.

[96] B. Allen, Phys. Rev. D **71**, 062001 (2005).

[97] A. H. Nitz, arXiv:1709.08974.

[98] C. Cutler, T. A. Apostolatos, L. Bildsten, L. S. Finn, E. E. Flanagan, D. Kennefick, D. M. Markovic, A. Ori, E. Poisson, G. J. Sussman, and K. S. Thorne, Phys. Rev. Lett. **70**, 2984 (1993).

[99] T. Damour, Lect. Notes Phys., **124**, 59 (1983).

[100] T. Damour, M. Soffel, and C.-m. Xu, Phys. Rev. D **45**, 1017 (1992).

[101] E. E. Flanagan and T. Hinderer, Phys. Rev. D **77**, 021502 (2008).

[102] T. Hinderer, Astrophys. J. **677**, 1216 (2008).

[103] T. Hinderer, B. D. Lackey, R. N. Lang, and J. S. Read, Phys. Rev. D **81**, 123016 (2010).

[104] S. Postnikov, M. Prakash, and J. M. Lattimer, Phys. Rev. D **82**, 024016 (2010).

[105] T. Damour and A. Nagar, Phys. Rev. D **80**, 084035 (2009).

[106] T. Binnington and E. Poisson, Phys. Rev. D **80**, 084018 (2009).

[107] B. Kol and M. Smolkin, J. High Energy Phys. 02 (2012) 010.

[108] P. Pani, L. Gualtieri, A. Maselli, and V. Ferrari, Phys. Rev. D **92**, 024010 (2015).

[109] P. Landry and E. Poisson, Phys. Rev. D **91**, 104018 (2015).

[110] J. S. Read, C. Markakis, M. Shibata, K. Uryu, J. D. E. Creighton, and J. L. Friedman, Phys. Rev. D **79**, 124033 (2009).

[111] T. Damour, A. Nagar, and L. Villain, Phys. Rev. D **85**, 123007 (2012).

[112] W. Del Pozzo, T. G. F. Li, M. Agathos, C. Van Den Broeck, and S. Vitale, Phys. Rev. Lett. **111**, 071101 (2013).

[113] L. Wade, J. D. E. Creighton, E. Ochsner, B. D. Lackey, B. F. Farr, T. B. Littenberg, and V. Raymond, Phys. Rev. D **89**, 103012 (2014).

[114] S. Bernuzzi, A. Nagar, S. Balmelli, T. Dietrich, and M. Ujevic, Phys. Rev. Lett. **112**, 201101 (2014).

[115] M. Agathos, J. Meidam, W. Del Pozzo, T. G. F. Li, M. Tompitak, J. Veitch, S. Vitale, and C. Van Den Broeck, Phys. Rev. D **92**, 023012 (2015).

[116] K. Hotokezaka, K. Kyutoku, Y.-i. Sekiguchi, and M. Shibata, Phys. Rev. D **93**, 064082 (2016).

[117] M. Favata, Phys. Rev. Lett. **112**, 101101 (2014).

[118] K. Yagi and N. Yunes, Phys. Rev. D **89**, 021303 (2014).

[119] T. Cullen, I. Harry, J. Read, and E. Flynn, arXiv: 1708.04359.

[120] A. Buonanno and T. Damour, Phys. Rev. D **62**, 064015 (2000).

[121] T. Damour, P. Jaranowski, and G. Schäfer, Phys. Rev. D **78**, 024009 (2008).

[122] T. Damour and A. Nagar, Phys. Rev. D **79**, 081503 (2009).

[123] E. Barausse and A. Buonanno, Phys. Rev. D **81**, 084024 (2010).

[124] A. Bohé et al., Phys. Rev. D **95**, 044028 (2017).

[125] A. Nagar, G. Riemenschneider, and G. Pratten, arXiv:1703.06814 [Phys. Rev. D (to be published)].

[126] P. Ajith et al., Classical Quantum Gravity **24**, S689 (2007).

[127] P. Ajith et al., Phys. Rev. Lett. **106**, 241101 (2011).

[128] M. Hannam, Patricia Schmidt, Alejandro Bohé, Leïla Haegel, Sascha Husa, Frank Ohme, Geraint Pratten, and Michael Pürrer, Phys. Rev. Lett. **113**, 151101 (2014).

[129] S. Husa, S. Khan, M. Hannam, M. Purrer, F. Ohme, X. J. Forteza, and A. Bohe, Phys. Rev. D **93**, 044006 (2016).

[130] S. Khan, S. Husa, M. Hannam, F. Ohme, M. Purrer, X. J. Forteza, and A. Bohe, Phys. Rev. D **93**, 044007 (2016).

[131] R. Smith, S. E. Field, K. Blackburn, C.-J. Haster, M. Pürrer, V. Raymond, and P. Schmidt, Phys. Rev. D **94**, 044031 (2016).

[132] J. Vines, E. E. Flanagan, and T. Hinderer, Phys. Rev. D **83**, 084051 (2011).

[133] B. Mikoczi, M. Vasuth, and L. A. Gergely, Phys. Rev. D **71**, 124043 (2005).

[134] A. Bohé, G. Faye, S. Marsat, and E. K. Porter, Classical Quantum Gravity **32**, 195010 (2015).

[135] J. Veitch et al., Phys. Rev. D **91**, 042003 (2015).

[136] B. P. Abbott et al. (LIGO Scientific Collaboration and Virgo Collaboration), Phys. Rev. Lett. **116**, 241102 (2016).

[137] C. Cahillane et al., arXiv:1708.03023.

[138] L. P. Singer, H.-Y. Chen, D. E. Holz, W. M. Farr, L. R. Price, V. Raymond, S. B. Cenko, N. Gehrels, J. Cannizzo, M. M. Kasliwal, S. Nissanke, M. Coughlin, B. Farr, A. L. Urban, S. Vitale, J. Veitch, P. Graff, C. P. L. Berry, S. Mohapatra, and I. Mandel, Astrophys. J. Lett. **829**, L15 (2016).

[139] H.-Y. Chen and D. E. Holz, arXiv:1612.01471.

[140] T. A. Apostolatos, C. Cutler, G. J. Sussman, and K. S. Thorne, Phys. Rev. D **49**, 6274 (1994).

[141] B. P. Abbott et al. (LIGO Scientific Collaboration, Virgo Collaboration, IM2H Collaboration, Dark Energy Camera GW-EM Collaboration, DES Collaboration, DLT40 Collaboration, Las Cumbres Observatory Collaboration, VINROUGE Collaboration, and MASTER Collaboration), Nature (London), in press (2017), DOI: 10.1038/nature24471.

[142] A. Krolak and B. F. Schutz, Gen. Relativ. Gravit. **19**, 1163 (1987).

[143] D. J. Fixsen, Astrophys. J. **707**, 916 (2009).

[144] A. C. Crook, J. P. Huchra, N. Martimbeau, K. L. Masters, T. Jarrett, and L. M. Macri, Astrophys. J. **655**, 790 (2007).

[145] A. C. Crook, J. P. Huchra, N. Martimbeau, K. L. Masters, T. Jarrett, and L. M. Macri, Astrophys. J. **685**, 1320 (2008).

[146] M. Hannam, D. A. Brown, S. Fairhurst, C. L. Fryer, and I. W. Harry, Astrophys. J. Lett. **766**, L14 (2013).

[147] F. Ohme, A. B. Nielsen, D. Keppel, and A. Lundgren, Phys. Rev. D **88**, 042002 (2013).

[148] C. P. L. Berry et al., Astrophys. J. **804**, 114 (2015).

[149] M. Pürrer, M. Hannam, and F. Ohme, Phys. Rev. D **93**, 084042 (2016).

[150] B. Farr et al., Astrophys. J. **825**, 116 (2016).

[151] K.-W. Lo and L.-M. Lin, Astrophys. J. **728**, 12 (2011).

[152] E. Racine, Phys. Rev. D **78**, 044021 (2008).

[153] J. W. T. Hessels, S. M. Ransom, I. H. Stairs, P. C. C. Freire, V. M. Kaspi, and F. Camilo, Science **311**, 1901 (2006).

[154] R. S. Lynch, P. C. C. Freire, S. M. Ransom, and B. A. Jacoby, Astrophys. J. **745**, 109 (2012).

[155] M. Burgay et al., Nature (London) **426**, 531 (2003).

[156] H. Müther, M. Prakash, and T. L. Ainsworth, Phys. Lett. B **199**, 469 (1987).

[157] H. Mueller and B. D. Serot, Nucl. Phys. A **A606**, 508 (1996).

[158] F. Douchin and P. Haensel, Astron. Astrophys. **380**, 151 (2001).

[159] A. Akmal, V. R. Pandharipande, and D. G. Ravenhall, Phys. Rev. C **58**, 1804 (1998).

[160] B. D. Lackey, M. Nayyar, and B. J. Owen, Phys. Rev. D **73**, 024021 (2006).

[161] J. S. Read, B. D. Lackey, B. J. Owen, and J. L. Friedman, Phys. Rev. D **79**, 124032 (2009).

[162] J. M. Lattimer and M. Prakash, Phys. Rep. **621**, 127 (2016).

[163] F. Ozel and P. Freire, Annu. Rev. Astron. Astrophys. **54**, 401 (2016).

[164] A. L. Watts et al., Rev. Mod. Phys. **88**, 021001 (2016).

[165] A. W. Steiner, C. O. Heinke, S. Bogdanov, C. Li, W. C. G. Ho, A. Bahramian, and S. Han, arXiv:1709.05013.

[166] J. Nättilä, M. C. Miller, A. W. Steiner, J. J. E. Kajava, V. F. Suleimanov, and J. Poutanen, arXiv:1709.09120.

[167] B. D. Lackey and L. Wade, Phys. Rev. D **91**, 043002 (2015).

[168] A. W. Steiner, S. Gandolfi, F. J. Fattoyev, and W. G. Newton, Phys. Rev. C **91**, 015804 (2015).

[169] R. De Pietri, A. Feo, F. Maione, and F. Löffler, Phys. Rev. D **93**, 064047 (2016).

[170] T. Dietrich, M. Ujevic, W. Tichy, S. Bernuzzi, and B. Brügmann, Phys. Rev. D **95**, 024029 (2017).

[171] T. Dietrich and T. Hinderer, Phys. Rev. D **95**, 124006 (2017).

[172] T. Dietrich, S. Bernuzzi, and W. Tichy, arXiv:1706.02969.

[173] T. Damour and A. Nagar, Phys. Rev. D **81**, 084016 (2010).

[174] B. D. Lackey, S. Bernuzzi, C. R. Galley, J. Meidam, and C. Van Den Broeck, Phys. Rev. D **95**, 104036 (2017).

[175] S. Bernuzzi, A. Nagar, T. Dietrich, and T. Damour, Phys. Rev. Lett. **114**, 161103 (2015).

[176] T. Hinderer *et al.*, Phys. Rev. Lett. **116**, 181101 (2016).

[177] J. Steinhoff, T. Hinderer, A. Buonanno, and A. Taracchini, Phys. Rev. D **94**, 104028 (2016).

[178] B. P. Abbott *et al.* (LIGO Scientific Collaboration and Virgo Collaboration), Astrophys. J. Lett. **833**, L1 (2016).

[179] B. P. Abbott *et al.* (LIGO Scientific Collaboration and Virgo Collaboration), Astrophys. J. Suppl. Ser. **227**, 14 (2016).

[180] C. Kim, V. Kalogera, and D. R. Lorimer, Astrophys. J. **584**, 985 (2003).

[181] B. P. Abbott *et al.* (LIGO Scientific Collaboration and Virgo Collaboration), Phys. Rev. Lett. **118**, 121101 (2017).

[182] B. P. Abbott *et al.* (LIGO Scientific Collaboration and Virgo Collaboration), Phys. Rev. Lett. **116**, 131102 (2016).

[183] LIGO Scientific Collaboration and Virgo Collaboration, Technical Report No. LIGO-P170272, 2017.

[184] N. Andersson, Classical Quantum Gravity **20**, R105 (2003).

[185] A. L. Piro, B. Giacomazzo, and R. Perna, Astrophys. J. **844**, L19 (2017).

[186] J. A. Clark, A. Bauswein, N. Stergioulas, and D. Shoemaker, Classical Quantum Gravity **33**, 085003 (2016).

[187] P. D. Lasky and K. Glampedakis, Mon. Not. R. Astron. Soc. **458**, 1660 (2016).

[188] S. Bose, K. Chakravarti, L. Rezzolla, B. S. Sathyaprakash, and K. Takami, arXiv:1705.10850.

[189] M. Shibata and K. Uryū, Phys. Rev. D **61**, 064001 (2000).

[190] L. Baiotti and L. Rezzolla, Rep. Prog. Phys. **80**, 096901 (2017).

[191] S. Klimenko *et al.*, Phys. Rev. D **93**, 042004 (2016).

[192] B. P. Abbott *et al.* (LIGO Scientific Collaboration and Virgo Collaboration), Phys. Rev. D **93**, 042005 (2016).

[193] LIGO Scientific Collaboration and Virgo Collaboration *et al.*, Technical Report No. LIGO-P1700318, 2017.

[194] B. P. Abbott *et al.* (LIGO Scientific Collaboration and Virgo Collaboration), Phys. Rev. Lett. **116**, 221101 (2016).

[195] B. F. Schutz, Nature (London) **323**, 310 (1986).

[196] D. Eichler, M. Livio, T. Piran, and D. N. Schramm, Nature (London) **340**, 126 (1989).

[197] P. D'Avanzo, J. High Energy Astrophys. **7**, 73 (2015).

B. P. Abbott,[1] R. Abbott,[1] T. D. Abbott,[2] F. Acernese,[3,4] K. Ackley,[5,6] C. Adams,[7] T. Adams,[8] P. Addesso,[9] R. X. Adhikari,[1] V. B. Adya,[10] C. Affeldt,[10] M. Afrough,[11] B. Agarwal,[12] M. Agathos,[13] K. Agatsuma,[14] N. Aggarwal,[15] O. D. Aguiar,[16] L. Aiello,[17,18] A. Ain,[19] P. Ajith,[20] B. Allen,[10,21,22] G. Allen,[12] A. Allocca,[23,24] P. A. Altin,[25] A. Amato,[26] A. Ananyeva,[1] S. B. Anderson,[1] W. G. Anderson,[21] S. V. Angelova,[27] S. Antier,[28] S. Appert,[1] K. Arai,[1] M. C. Araya,[1] J. S. Areeda,[29] N. Arnaud,[28,30] K. G. Arun,[31] S. Ascenzi,[32,33] G. Ashton,[10] M. Ast,[34] S. M. Aston,[7] P. Astone,[35] D. V. Atallah,[36] P. Aufmuth,[22] C. Aulbert,[10] K. AultONeal,[37] C. Austin,[2] A. Avila-Alvarez,[29] S. Babak,[38] P. Bacon,[39] M. K. M. Bader,[14] S. Bae,[40] M. Bailes,[41] P. T. Baker,[42] F. Baldaccini,[43,44] G. Ballardin,[30] S. W. Ballmer,[45] S. Banagiri,[46] J. C. Barayoga,[1] S. E. Barclay,[47] B. C. Barish,[1] D. Barker,[48] K. Barkett,[49] F. Barone,[3,4] B. Barr,[47] L. Barsotti,[15] M. Barsuglia,[39] D. Barta,[50] S. D. Barthelmy,[51] J. Bartlett,[48] I. Bartos,[52,5] R. Bassiri,[53] A. Basti,[23,24] J. C. Batch,[48] M. Bawaj,[54,44] J. C. Bayley,[47] M. Bazzan,[55,56] B. Bécsy,[57] C. Beer,[10] M. Bejger,[58] I. Belahcene,[28] A. S. Bell,[47] B. K. Berger,[1] G. Bergmann,[10] S. Bernuzzi,[59,60] J. J. Bero,[61] C. P. L. Berry,[62] D. Bersanetti,[63] A. Bertolini,[14] J. Betzwieser,[7] S. Bhagwat,[45] R. Bhandare,[64] I. A. Bilenko,[65] G. Billingsley,[1] C. R. Billman,[5] J. Birch,[7] R. Birney,[66] O. Birnholtz,[10] S. Biscans,[1,15] S. Biscoveanu,[67,6] A. Bisht,[22] M. Bitossi,[30,24] C. Biwer,[45] M. A. Bizouard,[28] J. K. Blackburn,[1] J. Blackman,[49] C. D. Blair,[1,68] D. G. Blair,[68] R. M. Blair,[48] S. Bloemen,[69] O. Bock,[10] N. Bode,[10] M. Boer,[70] G. Bogaert,[70] A. Bohe,[38] F. Bondu,[71] E. Bonilla,[53] R. Bonnand,[8] B. A. Boom,[14] R. Bork,[1] V. Boschi,[30,24] S. Bose,[72,19] K. Bossie,[7] Y. Bouffanais,[39] A. Bozzi,[30] C. Bradaschia,[24] P. R. Brady,[21] M. Branchesi,[17,18] J. E. Brau,[73] T. Briant,[74] A. Brillet,[70] M. Brinkmann,[10] V. Brisson,[28] P. Brockill,[21] J. E. Broida,[75] A. F. Brooks,[1] D. A. Brown,[45] D. D. Brown,[76] S. Brunett,[1] C. C. Buchanan,[2] A. Buikema,[15] T. Bulik,[77] H. J. Bulten,[78,14] A. Buonanno,[38,79] D. Buskulic,[8] C. Buy,[39] R. L. Byer,[53] M. Cabero,[10] L. Cadonati,[80] G. Cagnoli,[26,81] C. Cahillane,[1] J. Calderón Bustillo,[80] T. A. Callister,[1] E. Calloni,[82,4] J. B. Camp,[51] M. Canepa,[83,63] P. Canizares,[69] K. C. Cannon,[84] H. Cao,[76] J. Cao,[85] C. D. Capano,[10] E. Capocasa,[39] F. Carbognani,[30] S. Caride,[86] M. F. Carney,[87] G. Carullo,[23,24] J. Casanueva Diaz,[28] C. Casentini,[32,33] S. Caudill,[21,14] M. Cavaglià,[11] F. Cavalier,[28] R. Cavalieri,[30] G. Cella,[24] C. B. Cepeda,[1] P. Cerdá-Durán,[88] G. Cerretani,[23,24] E. Cesarini,[89,33] S. J. Chamberlin,[67] M. Chan,[47] S. Chao,[90] P. Charlton,[91] E. Chase,[92] E. Chassande-Mottin,[39] D. Chatterjee,[21] K. Chatziioannou,[93] B. D. Cheeseboro,[42] H. Y. Chen,[94] X. Chen,[68] Y. Chen,[49] H.-P. Cheng,[5] H. Chia,[5] A. Chincarini,[63] A. Chiummo,[30] T. Chmiel,[87] H. S. Cho,[95] M. Cho,[79] J. H. Chow,[25] N. Christensen,[75,70] Q. Chu,[68] A. J. K. Chua,[13] S. Chua,[74] A. K. W. Chung,[96] S. Chung,[68] G. Ciani,[5,55,56] R. Ciolfi,[97,98] C. E. Cirelli,[53] A. Cirone,[83,63] F. Clara,[48] J. A. Clark,[80] P. Clearwater,[99] F. Cleva,[70] C. Cocchieri,[11] E. Coccia,[17,18] P.-F. Cohadon,[74] D. Cohen,[28] A. Colla,[100,35] C. G. Collette,[101] L. R. Cominsky,[102] M. Constancio Jr.,[16] L. Conti,[56] S. J. Cooper,[62] P. Corban,[7] T. R. Corbitt,[2] I. Cordero-Carrión,[103] K. R. Corley,[52] N. Cornish,[104] A. Corsi,[86] S. Cortese,[30]

C. A. Costa,[16] M. W. Coughlin,[75,1] S. B. Coughlin,[92] J.-P. Coulon,[70] S. T. Countryman,[52] P. Couvares,[1] P. B. Covas,[105] E. E. Cowan,[80] D. M. Coward,[68] M. J. Cowart,[7] D. C. Coyne,[1] R. Coyne,[86] J. D. E. Creighton,[21] T. D. Creighton,[106] J. Cripe,[2] S. G. Crowder,[107] T. J. Cullen,[29,2] A. Cumming,[47] L. Cunningham,[47] E. Cuoco,[30] T. Dal Canton,[51] G. Dálya,[57] S. L. Danilishin,[22,10] S. D'Antonio,[33] K. Danzmann,[22,10] A. Dasgupta,[108] C. F. Da Silva Costa,[5] V. Dattilo,[30] I. Dave,[64] M. Davier,[28] D. Davis,[45] E. J. Daw,[109] B. Day,[80] S. De,[45] D. DeBra,[53] J. Degallaix,[26] M. De Laurentis,[17,4] S. Deléglise,[74] W. Del Pozzo,[62,23,24] N. Demos,[15] T. Denker,[10] T. Dent,[10] R. De Pietri,[59,60] V. Dergachev,[38] R. De Rosa,[82,4] R. T. DeRosa,[7] C. De Rossi,[26,30] R. DeSalvo,[110] O. de Varona,[10] J. Devenson,[27] S. Dhurandhar,[19] M. C. Díaz,[106] T. Dietrich,[38] L. Di Fiore,[4] M. Di Giovanni,[111,98] T. Di Girolamo,[52,82,4] A. Di Lieto,[23,24] S. Di Pace,[100,35] I. Di Palma,[100,35] F. Di Renzo,[23,24] Z. Doctor,[94] V. Dolique,[26] F. Donovan,[15] K. L. Dooley,[11] S. Doravari,[10] I. Dorrington,[36] R. Douglas,[47] M. Dovale Álvarez,[62] T. P. Downes,[21] M. Drago,[10] C. Dreissigacker,[10] J. C. Driggers,[48] Z. Du,[85] M. Ducrot,[8] R. Dudi,[36] P. Dupej,[47] S. E. Dwyer,[48] T. B. Edo,[109] M. C. Edwards,[75] A. Effler,[7] H.-B. Eggenstein,[38,10] P. Ehrens,[1] J. Eichholz,[1] S. S. Eikenberry,[5] R. A. Eisenstein,[15] R. C. Essick,[15] D. Estevez,[8] Z. B. Etienne,[42] T. Etzel,[1] M. Evans,[15] T. M. Evans,[7] M. Factourovich,[52] V. Fafone,[32,33,17] H. Fair,[45] S. Fairhurst,[36] X. Fan,[85] S. Farinon,[63] B. Farr,[94] W. M. Farr,[62] E. J. Fauchon-Jones,[36] M. Favata,[112] M. Fays,[36] C. Fee,[87] H. Fehrmann,[10] J. Feicht,[1] M. M. Fejer,[53] A. Fernandez-Galiana,[15] I. Ferrante,[23,24] E. C. Ferreira,[16] F. Ferrini,[30] F. Fidecaro,[23,24] D. Finstad,[45] I. Fiori,[30] D. Fiorucci,[39] M. Fishbach,[94] R. P. Fisher,[45] M. Fitz-Axen,[46] R. Flaminio,[26,113] M. Fletcher,[47] H. Fong,[93] J. A. Font,[88,114] P. W. F. Forsyth,[25] S. S. Forsyth,[80] J.-D. Fournier,[70] S. Frasca,[100,35] F. Frasconi,[24] Z. Frei,[57] A. Freise,[62] R. Frey,[73] V. Frey,[28] E. M. Fries,[1] P. Fritschel,[15] V. V. Frolov,[7] P. Fulda,[5] M. Fyffe,[7] H. Gabbard,[47] B. U. Gadre,[19] S. M. Gaebel,[62] J. R. Gair,[115] L. Gammaitoni,[43] M. R. Ganija,[76] S. G. Gaonkar,[19] C. Garcia-Quiros,[105] F. Garufi,[82,4] B. Gateley,[48] S. Gaudio,[37] G. Gaur,[116] V. Gayathri,[117] N. Gehrels,[51,†] G. Gemme,[63] E. Genin,[30] A. Gennai,[24] D. George,[12] J. George,[64] L. Gergely,[118] V. Germain,[8] S. Ghonge,[80] Abhirup Ghosh,[20] Archisman Ghosh,[20,14] S. Ghosh,[69,14,21] J. A. Giaime,[2,7] K. D. Giardina,[7] A. Giazotto,[24] K. Gill,[37] L. Glover,[110] E. Goetz,[119] R. Goetz,[5] S. Gomes,[36] B. Goncharov,[6] G. González,[2] J. M. Gonzalez Castro,[23,24] A. Gopakumar,[120] M. L. Gorodetsky,[65] S. E. Gossan,[1] M. Gosselin,[30] R. Gouaty,[8] A. Grado,[121,4] C. Graef,[47] M. Granata,[26] A. Grant,[47] S. Gras,[15] C. Gray,[48] G. Greco,[122,123] A. C. Green,[62] E. M. Gretarsson,[37] P. Groot,[69] H. Grote,[10] S. Grunewald,[38] P. Gruning,[28] G. M. Guidi,[122,123] X. Guo,[85] A. Gupta,[67] M. K. Gupta,[108] K. E. Gushwa,[1] E. K. Gustafson,[1] R. Gustafson,[119] O. Halim,[18,17] B. R. Hall,[72] E. D. Hall,[15] E. Z. Hamilton,[36] G. Hammond,[47] M. Haney,[124] M. M. Hanke,[10] J. Hanks,[48] C. Hanna,[67] M. D. Hannam,[36] O. A. Hannuksela,[96] J. Hanson,[7] T. Hardwick,[2] J. Harms,[17,18] G. M. Harry,[125] I. W. Harry,[38] M. J. Hart,[47] C.-J. Haster,[93] K. Haughian,[47] J. Healy,[61] A. Heidmann,[74] M. C. Heintze,[7] H. Heitmann,[70] P. Hello,[28] G. Hemming,[30] M. Hendry,[47] I. S. Heng,[47] J. Hennig,[47] A. W. Heptonstall,[1] M. Heurs,[10,22] S. Hild,[47] T. Hinderer,[69] W. C. G. Ho,[126] D. Hoak,[30] D. Hofman,[26] K. Holt,[7] D. E. Holz,[94] P. Hopkins,[36] C. Horst,[21] J. Hough,[47] E. A. Houston,[47] E. J. Howell,[68] A. Hreibi,[70] Y. M. Hu,[10] E. A. Huerta,[12] D. Huet,[28] B. Hughey,[37] S. Husa,[105] S. H. Huttner,[47] T. Huynh-Dinh,[7] N. Indik,[10] R. Inta,[86] G. Intini,[100,35] H. N. Isa,[47] J.-M. Isac,[74] M. Isi,[1] B. R. Iyer,[20] K. Izumi,[48] T. Jacqmin,[74] K. Jani,[80] P. Jaranowski,[127] S. Jawahar,[66] F. Jiménez-Forteza,[105] W. W. Johnson,[2] N. K. Johnson-McDaniel,[13] D. I. Jones,[126] R. Jones,[47] R. J. G. Jonker,[14] L. Ju,[68] J. Junker,[10] C. V. Kalaghatgi,[36] V. Kalogera,[92] B. Kamai,[1] S. Kandhasamy,[7] G. Kang,[40] J. B. Kanner,[1] S. J. Kapadia,[21] S. Karki,[73] K. S. Karvinen,[10] M. Kasprzack,[2] W. Kastaun,[10] M. Katolik,[12] E. Katsavounidis,[15] W. Katzman,[7] S. Kaufer,[22] K. Kawabe,[48] F. Kéfélian,[70] D. Keitel,[47] A. J. Kemball,[12] R. Kennedy,[109] C. Kent,[36] J. S. Key,[128] F. Y. Khalili,[65] I. Khan,[17,33] S. Khan,[10] Z. Khan,[108] E. A. Khazanov,[129] N. Kijbunchoo,[25] Chunglee Kim,[130] J. C. Kim,[131] K. Kim,[96] W. Kim,[76] W. S. Kim,[132] Y.-M. Kim,[95] S. J. Kimbrell,[80] E. J. King,[76] P. J. King,[48] M. Kinley-Hanlon,[125] R. Kirchhoff,[10] J. S. Kissel,[48] L. Kleybolte,[34] S. Klimenko,[5] T. D. Knowles,[42] P. Koch,[10] S. M. Koehlenbeck,[10] S. Koley,[14] V. Kondrashov,[1] A. Kontos,[15] M. Korobko,[34] W. Z. Korth,[1] I. Kowalska,[77] D. B. Kozak,[1] C. Krämer,[10] V. Kringel,[10] B. Krishnan,[10] A. Królak,[133,134] G. Kuehn,[10] P. Kumar,[93] R. Kumar,[108] S. Kumar,[20] L. Kuo,[90] A. Kutynia,[133] S. Kwang,[21] B. D. Lackey,[38] K. H. Lai,[96] M. Landry,[48] R. N. Lang,[135] J. Lange,[61] B. Lantz,[53] R. K. Lanza,[15] S. L. Larson,[92] A. Lartaux-Vollard,[28] P. D. Lasky,[6] M. Laxen,[7] A. Lazzarini,[1] C. Lazzaro,[56] P. Leaci,[100,35] S. Leavey,[47] C. H. Lee,[95] H. K. Lee,[136] H. M. Lee,[137] H. W. Lee,[131] K. Lee,[47] J. Lehmann,[10] A. Lenon,[42] E. Leon,[29] M. Leonardi,[111,98] N. Leroy,[28] N. Letendre,[8] Y. Levin,[6] T. G. F. Li,[96] S. D. Linker,[110] T. B. Littenberg,[138] J. Liu,[68] X. Liu,[21] R. K. L. Lo,[96] N. A. Lockerbie,[66] L. T. London,[36] J. E. Lord,[45] M. Lorenzini,[17,18] V. Loriette,[139] M. Lormand,[7] G. Losurdo,[24] J. D. Lough,[10] C. O. Lousto,[61] G. Lovelace,[29] H. Lück,[22,10] D. Lumaca,[32,33] A. P. Lundgren,[10] R. Lynch,[15] Y. Ma,[49] R. Macas,[36] S. Macfoy,[27] B. Machenschalk,[10] M. MacInnis,[15] D. M. Macleod,[36] I. Magaña Hernandez,[21] F. Magaña-Sandoval,[45] L. Magaña Zertuche,[45] R. M. Magee,[67] E. Majorana,[35] I. Maksimovic,[139] N. Man,[70] V. Mandic,[46] V. Mangano,[47]

G. L. Mansell,[25] M. Manske,[21,25] M. Mantovani,[30] F. Marchesoni,[54,44] F. Marion,[8] S. Márka,[52] Z. Márka,[52] C. Markakis,[12] A. S. Markosyan,[53] A. Markowitz,[1] E. Maros,[1] A. Marquina,[103] P. Marsh,[128] F. Martelli,[122,123] L. Martellini,[70] I. W. Martin,[47] R. M. Martin,[112] D. V. Martynov,[15] J. N. Marx,[1] K. Mason,[15] E. Massera,[109] A. Masserot,[8] T. J. Massinger,[1] M. Masso-Reid,[47] S. Mastrogiovanni,[100,35] A. Matas,[46] F. Matichard,[1,15] L. Matone,[52] N. Mavalvala,[15] N. Mazumder,[72] R. McCarthy,[48] D. E. McClelland,[25] S. McCormick,[7] L. McCuller,[15] S. C. McGuire,[140] G. McIntyre,[1] J. McIver,[1] D. J. McManus,[25] L. McNeill,[6] T. McRae,[25] S. T. McWilliams,[42] D. Meacher,[67] G. D. Meadors,[38,10] M. Mehmet,[10] J. Meidam,[14] E. Mejuto-Villa,[9] A. Melatos,[99] G. Mendell,[48] R. A. Mercer,[21] E. L. Merilh,[48] M. Merzougui,[70] S. Meshkov,[1] C. Messenger,[47] C. Messick,[67] R. Metzdorff,[74] P. M. Meyers,[46] H. Miao,[62] C. Michel,[26] H. Middleton,[62] E. E. Mikhailov,[141] L. Milano,[82,4] A. L. Miller,[5,100,35] B. B. Miller,[92] J. Miller,[15] M. Millhouse,[104] M. C. Milovich-Goff,[110] O. Minazzoli,[70,142] Y. Minenkov,[33] J. Ming,[38] C. Mishra,[143] S. Mitra,[19] V. P. Mitrofanov,[65] G. Mitselmakher,[5] R. Mittleman,[15] D. Moffa,[87] A. Moggi,[24] K. Mogushi,[11] M. Mohan,[30] S. R. P. Mohapatra,[15] I. Molina,[29] M. Montani,[122,123] C. J. Moore,[13] D. Moraru,[48] G. Moreno,[48] S. Morisaki,[84] S. R. Morriss,[106] B. Mours,[8] C. M. Mow-Lowry,[62] G. Mueller,[5] A. W. Muir,[36] Arunava Mukherjee,[10] D. Mukherjee,[21] S. Mukherjee,[106] N. Mukund,[19] A. Mullavey,[7] J. Munch,[76] E. A. Muñiz,[45] M. Muratore,[37] P. G. Murray,[47] A. Nagar,[89,144,145] K. Napier,[80] I. Nardecchia,[32,33] L. Naticchioni,[100,35] R. K. Nayak,[146] J. Neilson,[110] G. Nelemans,[69,14] T. J. N. Nelson,[7] M. Nery,[10] A. Neunzert,[119] L. Nevin,[1] J. M. Newport,[125] G. Newton,[47,‡] K. K. Y. Ng,[96] P. Nguyen,[73] T. T. Nguyen,[25] D. Nichols,[69] A. B. Nielsen,[10] A. Nitz,[10] A. Noack,[10] F. Nocera,[30] D. Nolting,[7] C. North,[36] L. K. Nuttall,[36] J. Oberling,[48] G. D. O'Dea,[110] G. H. Ogin,[147] J. J. Oh,[132] S. H. Oh,[132] F. Ohme,[10] M. A. Okada,[16] M. Oliver,[105] P. Oppermann,[10] Richard J. Oram,[7] B. O'Reilly,[7] R. Ormiston,[46] L. F. Ortega,[5] R. O'Shaughnessy,[61] S. Ossokine,[38] D. J. Ottaway,[76] H. Overmier,[7] B. J. Owen,[86] A. E. Pace,[67] J. Page,[138] M. A. Page,[68] A. Pai,[117,148] S. A. Pai,[64] J. R. Palamos,[73] O. Palashov,[129] C. Palomba,[35] A. Pal-Singh,[34] Howard Pan,[90] Huang-Wei Pan,[90] B. Pang,[49] P. T. H. Pang,[96] C. Pankow,[92] F. Pannarale,[36] B. C. Pant,[64] F. Paoletti,[24] A. Paoli,[30] M. A. Papa,[38,21,10] A. Parida,[19] W. Parker,[7] D. Pascucci,[47] A. Pasqualetti,[30] R. Passaquieti,[23,24] D. Passuello,[24] M. Patil,[134] B. Patricelli,[149,24] B. L. Pearlstone,[47] M. Pedraza,[1] R. Pedurand,[26,150] L. Pekowsky,[45] A. Pele,[7] S. Penn,[151] C. J. Perez,[48] A. Perreca,[1,111,98] L. M. Perri,[92] H. P. Pfeiffer,[93,38] M. Phelps,[47] O. J. Piccinni,[100,35] M. Pichot,[70] F. Piergiovanni,[122,123] V. Pierro,[9] G. Pillant,[30] L. Pinard,[26] I. M. Pinto,[9] M. Pirello,[48] M. Pitkin,[47] M. Poe,[21] R. Poggiani,[23,24] P. Popolizio,[30] E. K. Porter,[39] A. Post,[10] J. Powell,[47,41] J. Prasad,[19] J. W. W. Pratt,[37] G. Pratten,[105] V. Predoi,[36] T. Prestegard,[21] M. Prijatelj,[10] M. Principe,[9] S. Privitera,[38] R. Prix,[10] G. A. Prodi,[111,98] L. G. Prokhorov,[65] O. Puncken,[10] M. Punturo,[44] P. Puppo,[35] M. Pürrer,[38] H. Qi,[21] V. Quetschke,[106] E. A. Quintero,[1] R. Quitzow-James,[73] F. J. Raab,[48] D. S. Rabeling,[25] H. Radkins,[48] P. Raffai,[57] S. Raja,[64] C. Rajan,[64] B. Rajbhandari,[86] M. Rakhmanov,[106] K. E. Ramirez,[106] A. Ramos-Buades,[105] P. Rapagnani,[100,35] V. Raymond,[38] M. Razzano,[23,24] J. Read,[29] T. Regimbau,[70] L. Rei,[63] S. Reid,[66] D. H. Reitze,[1,5] W. Ren,[12] S. D. Reyes,[45] F. Ricci,[100,35] P. M. Ricker,[12] S. Rieger,[10] K. Riles,[119] M. Rizzo,[61] N. A. Robertson,[1,47] R. Robie,[47] F. Robinet,[28] A. Rocchi,[33] L. Rolland,[8] J. G. Rollins,[1] V. J. Roma,[73] J. D. Romano,[106] R. Romano,[3,4] C. L. Romel,[48] J. H. Romie,[7] D. Rosińska,[152,58] M. P. Ross,[153] S. Rowan,[47] A. Rüdiger,[10] P. Ruggi,[30] G. Rutins,[27] K. Ryan,[48] S. Sachdev,[1] T. Sadecki,[48] L. Sadeghian,[21] M. Sakellariadou,[154] L. Salconi,[30] M. Saleem,[117] F. Salemi,[10] A. Samajdar,[146] L. Sammut,[6] L. M. Sampson,[92] E. J. Sanchez,[1] L. E. Sanchez,[1] N. Sanchis-Gual,[88] V. Sandberg,[48] J. R. Sanders,[45] B. Sassolas,[26] B. S. Sathyaprakash,[67,36] P. R. Saulson,[45] O. Sauter,[119] R. L. Savage,[48] A. Sawadsky,[34] P. Schale,[73] M. Scheel,[49] J. Scheuer,[92] J. Schmidt,[10] P. Schmidt,[1,69] R. Schnabel,[34] R. M. S. Schofield,[73] A. Schönbeck,[34] E. Schreiber,[10] D. Schuette,[10,22] B. W. Schulte,[10] B. F. Schutz,[36,10] S. G. Schwalbe,[37] J. Scott,[47] S. M. Scott,[25] E. Seidel,[12] D. Sellers,[7] A. S. Sengupta,[155] D. Sentenac,[30] V. Sequino,[32,33,17] A. Sergeev,[129] D. A. Shaddock,[25] T. J. Shaffer,[48] A. A. Shah,[138] M. S. Shahriar,[92] M. B. Shaner,[110] L. Shao,[38] B. Shapiro,[53] P. Shawhan,[79] A. Sheperd,[21] D. H. Shoemaker,[15] D. M. Shoemaker,[80] K. Siellez,[80] X. Siemens,[21] M. Sieniawska,[58] D. Sigg,[48] A. D. Silva,[16] L. P. Singer,[51] A. Singh,[38,10,22] A. Singhal,[17,35] A. M. Sintes,[105] B. J. J. Slagmolen,[25] B. Smith,[7] J. R. Smith,[29] R. J. E. Smith,[1,6] S. Somala,[156] E. J. Son,[132] J. A. Sonnenberg,[21] B. Sorazu,[47] F. Sorrentino,[63] T. Souradeep,[19] A. P. Spencer,[47] A. K. Srivastava,[108] K. Staats,[37] A. Staley,[52] M. Steinke,[10] J. Steinlechner,[34,47] S. Steinlechner,[34] D. Steinmeyer,[10] S. P. Stevenson,[62,41] R. Stone,[106] D. J. Stops,[62] K. A. Strain,[47] G. Stratta,[122,123] S. E. Strigin,[65] A. Strunk,[48] R. Sturani,[157] A. L. Stuver,[7] T. Z. Summerscales,[158] L. Sun,[99] S. Sunil,[108] J. Suresh,[19] P. J. Sutton,[36] B. L. Swinkels,[30] M. J. Szczepańczyk,[37] M. Tacca,[14] S. C. Tait,[47] C. Talbot,[6] D. Talukder,[73] D. B. Tanner,[5] M. Tápai,[118] A. Taracchini,[38] J. D. Tasson,[75] J. A. Taylor,[138] R. Taylor,[1] S. V. Tewari,[151] T. Theeg,[10] F. Thies,[10] E. G. Thomas,[62] M. Thomas,[7] P. Thomas,[48] K. A. Thorne,[7] K. S. Thorne,[49] E. Thrane,[6] S. Tiwari,[17,98] V. Tiwari,[36] K. V. Tokmakov,[66] K. Toland,[47] M. Tonelli,[23,24] Z. Tornasi,[47] A. Torres-Forné,[88] C. I. Torrie,[1] D. Töyrä,[62] F. Travasso,[30,44] G. Traylor,[7] J. Trinastic,[5] M. C. Tringali,[111,98]

L. Trozzo,[159,24] K. W. Tsang,[14] M. Tse,[15] R. Tso,[1] L. Tsukada,[84] D. Tsuna,[84] D. Tuyenbayev,[106] K. Ueno,[21] D. Ugolini,[160] C. S. Unnikrishnan,[120] A. L. Urban,[1] S. A. Usman,[36] H. Vahlbruch,[22] G. Vajente,[1] G. Valdes,[2] M. Vallisneri,[49] N. van Bakel,[14] M. van Beuzekom,[14] J. F. J. van den Brand,[78,14] C. Van Den Broeck,[14] D. C. Vander-Hyde,[45] L. van der Schaaf,[14] J. V. van Heijningen,[14] A. A. van Veggel,[47] M. Vardaro,[55,56] V. Varma,[49] S. Vass,[1] M. Vasúth,[50] A. Vecchio,[62] G. Vedovato,[56] J. Veitch,[47] P. J. Veitch,[76] K. Venkateswara,[153] G. Venugopalan,[1] D. Verkindt,[8] F. Vetrano,[122,123] A. Viceré,[122,123] A. D. Viets,[21] S. Vinciguerra,[62] D. J. Vine,[27] J.-Y. Vinet,[70] S. Vitale,[15] T. Vo,[45] H. Vocca,[43,44] C. Vorvick,[48] S. P. Vyatchanin,[65] A. R. Wade,[1] L. E. Wade,[87] M. Wade,[87] R. Walet,[14] M. Walker,[29] L. Wallace,[1] S. Walsh,[38,10,21] G. Wang,[17,123] H. Wang,[62] J. Z. Wang,[67] W. H. Wang,[106] Y. F. Wang,[96] R. L. Ward,[25] J. Warner,[48] M. Was,[8] J. Watchi,[101] B. Weaver,[48] L.-W. Wei,[10,22] M. Weinert,[10] A. J. Weinstein,[1] R. Weiss,[15] L. Wen,[68] E. K. Wessel,[12] P. Weßels,[10] J. Westerweck,[10] T. Westphal,[10] K. Wette,[25] J. T. Whelan,[61] S. E. Whitcomb,[1] B. F. Whiting,[5] C. Whittle,[6] D. Wilken,[10] D. Williams,[47] R. D. Williams,[1] A. R. Williamson,[69] J. L. Willis,[1,161] B. Willke,[22,10] M. H. Wimmer,[10] W. Winkler,[10] C. C. Wipf,[1] H. Wittel,[10,22] G. Woan,[47] J. Woehler,[10] J. Wofford,[61] K. W. K. Wong,[96] J. Worden,[48] J. L. Wright,[47] D. S. Wu,[10] D. M. Wysocki,[61] S. Xiao,[1] H. Yamamoto,[1] C. C. Yancey,[79] L. Yang,[162] M. J. Yap,[25] M. Yazback,[5] Hang Yu,[15] Haocun Yu,[15] M. Yvert,[8] A. Zadrożny,[133] M. Zanolin,[37] T. Zelenova,[30] J.-P. Zendri,[56] M. Zevin,[92] L. Zhang,[1] M. Zhang,[141] T. Zhang,[47] Y.-H. Zhang,[61] C. Zhao,[68] M. Zhou,[92] Z. Zhou,[92] S. J. Zhu,[38,10] X. J. Zhu,[6] A. B. Zimmerman,[93] M. E. Zucker,[1,15] and J. Zweizig[1]

(LIGO Scientific Collaboration and Virgo Collaboration)

[1]*LIGO, California Institute of Technology, Pasadena, California 91125, USA*
[2]*Louisiana State University, Baton Rouge, Louisiana 70803, USA*
[3]*Università di Salerno, Fisciano, I-84084 Salerno, Italy*
[4]*INFN, Sezione di Napoli, Complesso Universitario di Monte S.Angelo, I-80126 Napoli, Italy*
[5]*University of Florida, Gainesville, Florida 32611, USA*
[6]*OzGrav, School of Physics & Astronomy, Monash University, Clayton 3800, Victoria, Australia*
[7]*LIGO Livingston Observatory, Livingston, Louisiana 70754, USA*
[8]*Laboratoire d'Annecy-le-Vieux de Physique des Particules (LAPP), Université Savoie Mont Blanc, CNRS/IN2P3, F-74941 Annecy, France*
[9]*University of Sannio at Benevento, I-82100 Benevento, Italy and INFN, Sezione di Napoli, I-80100 Napoli, Italy*
[10]*Max Planck Institute for Gravitational Physics (Albert Einstein Institute), D-30167 Hannover, Germany*
[11]*The University of Mississippi, University, Mississippi 38677, USA*
[12]*NCSA, University of Illinois at Urbana-Champaign, Urbana, Illinois 61801, USA*
[13]*University of Cambridge, Cambridge CB2 1TN, United Kingdom*
[14]*Nikhef, Science Park, 1098 XG Amsterdam, Netherlands*
[15]*LIGO, Massachusetts Institute of Technology, Cambridge, Massachusetts 02139, USA*
[16]*Instituto Nacional de Pesquisas Espaciais, 12227-010 São José dos Campos, São Paulo, Brazil*
[17]*Gran Sasso Science Institute (GSSI), I-67100 L'Aquila, Italy*
[18]*INFN, Laboratori Nazionali del Gran Sasso, I-67100 Assergi, Italy*
[19]*Inter-University Centre for Astronomy and Astrophysics, Pune 411007, India*
[20]*International Centre for Theoretical Sciences, Tata Institute of Fundamental Research, Bengaluru 560089, India*
[21]*University of Wisconsin-Milwaukee, Milwaukee, Wisconsin 53201, USA*
[22]*Leibniz Universität Hannover, D-30167 Hannover, Germany*
[23]*Università di Pisa, I-56127 Pisa, Italy*
[24]*INFN, Sezione di Pisa, I-56127 Pisa, Italy*
[25]*OzGrav, Australian National University, Canberra, Australian Capital Territory 0200, Australia*
[26]*Laboratoire des Matériaux Avancés (LMA), CNRS/IN2P3, F-69622 Villeurbanne, France*
[27]*SUPA, University of the West of Scotland, Paisley PA1 2BE, United Kingdom*
[28]*LAL, Univ. Paris-Sud, CNRS/IN2P3, Université Paris-Saclay, F-91898 Orsay, France*
[29]*California State University Fullerton, Fullerton, California 92831, USA*
[30]*European Gravitational Observatory (EGO), I-56021 Cascina, Pisa, Italy*
[31]*Chennai Mathematical Institute, Chennai 603103, India*
[32]*Università di Roma Tor Vergata, I-00133 Roma, Italy*
[33]*INFN, Sezione di Roma Tor Vergata, I-00133 Roma, Italy*
[34]*Universität Hamburg, D-22761 Hamburg, Germany*
[35]*INFN, Sezione di Roma, I-00185 Roma, Italy*

[36]Cardiff University, Cardiff CF24 3AA, United Kingdom

[37]Embry-Riddle Aeronautical University, Prescott, Arizona 86301, USA

[38]Max Planck Institute for Gravitationalphysik (Albert Einstein Institute), D-14476 Potsdam-Golm, Germany

[39]APC, AstroParticule et Cosmologie, Université Paris Diderot, CNRS/IN2P3, CEA/Irfu, Observatoire de Paris, Sorbonne Paris Cité,
F-75205 Paris Cedex 13, France

[40]Korea Institute of Science and Technology Information, Daejeon 34141, Korea

[41]OzGrav, Swinburne University of Technology, Hawthorn VIC 3122, Australia

[42]West Virginia University, Morgantown, West Virginia 26506, USA

[43]Università di Perugia, I-06123 Perugia, Italy

[44]INFN, Sezione di Perugia, I-06123 Perugia, Italy

[45]Syracuse University, Syracuse, New York 13244, USA

[46]University of Minnesota, Minneapolis, Minnesota 55455, USA

[47]SUPA, University of Glasgow, Glasgow G12 8QQ, United Kingdom

[48]LIGO Hanford Observatory, Richland, Washington 99352, USA

[49]Caltech CaRT, Pasadena, California 91125, USA

[50]Wigner RCP, RMKI, H-1121 Budapest, Konkoly Thege Miklós út 29-33, Hungary

[51]NASA Goddard Space Flight Center, Greenbelt, Maryland 20771, USA

[52]Columbia University, New York, New York 10027, USA

[53]Stanford University, Stanford, California 94305, USA

[54]Università di Camerino, Dipartimento di Fisica, I-62032 Camerino, Italy

[55]Università di Padova, Dipartimento di Fisica e Astronomia, I-35131 Padova, Italy

[56]INFN, Sezione di Padova, I-35131 Padova, Italy

[57]Institute of Physics, Eötvös University, Pázmány P. s. 1/A, Budapest 1117, Hungary

[58]Nicolaus Copernicus Astronomical Center, Polish Academy of Sciences, 00-716, Warsaw, Poland

[59]Dipartimento di Scienze Matematiche, Fisiche e Informatiche, Università di Parma, I-43124 Parma, Italy

[60]INFN, Sezione di Milano Bicocca, Gruppo Collegato di Parma, I-43124 Parma, Italy

[61]Rochester Institute of Technology, Rochester, New York 14623, USA

[62]University of Birmingham, Birmingham B15 2TT, United Kingdom

[63]INFN, Sezione di Genova, I-16146 Genova, Italy

[64]RRCAT, Indore MP 452013, India

[65]Faculty of Physics, Lomonosov Moscow State University, Moscow 119991, Russia

[66]SUPA, University of Strathclyde, Glasgow G1 1XQ, United Kingdom

[67]The Pennsylvania State University, University Park, Pennsylvania 16802, USA

[68]OzGrav, University of Western Australia, Crawley, Western Australia 6009, Australia

[69]Department of Astrophysics/IMAPP, Radboud University Nijmegen, P.O. Box 9010, 6500 GL Nijmegen, Netherlands

[70]Artemis, Université Côte d'Azur, Observatoire Côte d'Azur, CNRS, CS 34229, F-06304 Nice Cedex 4, France

[71]Institut FOTON, CNRS, Université de Rennes 1, F-35042 Rennes, France

[72]Washington State University, Pullman, Washington 99164, USA

[73]University of Oregon, Eugene, Oregon 97403, USA

[74]Laboratoire Kastler Brossel, UPMC-Sorbonne Universités, CNRS, ENS-PSL Research University,
Collège de France, F-75005 Paris, France

[75]Carleton College, Northfield, Minnesota 55057, USA

[76]OzGrav, University of Adelaide, Adelaide, South Australia 5005, Australia

[77]Astronomical Observatory Warsaw University, 00-478 Warsaw, Poland

[78]VU University Amsterdam, 1081 HV Amsterdam, Netherlands

[79]University of Maryland, College Park, Maryland 20742, USA

[80]Center for Relativistic Astrophysics, Georgia Institute of Technology, Atlanta, Georgia 30332, USA

[81]Université Claude Bernard Lyon 1, F-69622 Villeurbanne, France

[82]Università di Napoli "Federico II", Complesso Universitario di Monte S.Angelo, I-80126 Napoli, Italy

[83]Dipartimento di Fisica, Università degli Studi di Genova, I-16146 Genova, Italy

[84]RESCEU, University of Tokyo, Tokyo, 113-0033, Japan

[85]Tsinghua University, Beijing 100084, China

[86]Texas Tech University, Lubbock, Texas 79409, USA

[87]Kenyon College, Gambier, Ohio 43022, USA

[88]Departamento de Astronomía y Astrofísica, Universitat de València, E-46100 Burjassot, València, Spain

[89]Museo Storico della Fisica e Centro Studi e Ricerche Enrico Fermi, I-00184 Roma, Italy

[90]National Tsing Hua University, Hsinchu City, 30013 Taiwan, Republic of China

[91]Charles Sturt University, Wagga Wagga, New South Wales 2678, Australia

[92]Center for Interdisciplinary Exploration & Research in Astrophysics (CIERA), Northwestern University,
Evanston, Illinois 60208, USA

[93]*Canadian Institute for Theoretical Astrophysics, University of Toronto, Toronto, Ontario M5S 3H8, Canada*
[94]*University of Chicago, Chicago, Illinois 60637, USA*
[95]*Pusan National University, Busan 46241, Korea*
[96]*The Chinese University of Hong Kong, Shatin, NT, Hong Kong*
[97]*INAF, Osservatorio Astronomico di Padova, I-35122 Padova, Italy*
[98]*INFN, Trento Institute for Fundamental Physics and Applications, I-38123 Povo, Trento, Italy*
[99]*OzGrav, University of Melbourne, Parkville, Victoria 3010, Australia*
[100]*Università di Roma "La Sapienza", I-00185 Roma, Italy*
[101]*Université Libre de Bruxelles, Brussels 1050, Belgium*
[102]*Sonoma State University, Rohnert Park, California 94928, USA*
[103]*Departamento de Matemáticas, Universitat de València, E-46100 Burjassot, València, Spain*
[104]*Montana State University, Bozeman, Montana 59717, USA*
[105]*Universitat de les Illes Balears, IAC3—IEEC, E-07122 Palma de Mallorca, Spain*
[106]*The University of Texas Rio Grande Valley, Brownsville, Texas 78520, USA*
[107]*Bellevue College, Bellevue, Washington 98007, USA*
[108]*Institute for Plasma Research, Bhat, Gandhinagar 382428, India*
[109]*The University of Sheffield, Sheffield S10 2TN, United Kingdom*
[110]*California State University, Los Angeles, 5151 State University Drive, Los Angeles, California 90032, USA*
[111]*Università di Trento, Dipartimento di Fisica, I-38123 Povo, Trento, Italy*
[112]*Montclair State University, Montclair, New Jersey 07043, USA*
[113]*National Astronomical Observatory of Japan, 2-21-1 Osawa, Mitaka, Tokyo 181-8588, Japan*
[114]*Observatori Astronòmic, Universitat de València, E-46980 Paterna, València, Spain*
[115]*School of Mathematics, University of Edinburgh, Edinburgh EH9 3FD, United Kingdom*
[116]*University and Institute of Advanced Research, Koba Institutional Area, Gandhinagar Gujarat 382007, India*
[117]*IISER-TVM, CET Campus, Trivandrum Kerala 695016, India*
[118]*University of Szeged, Dóm tér 9, Szeged 6720, Hungary*
[119]*University of Michigan, Ann Arbor, Michigan 48109, USA*
[120]*Tata Institute of Fundamental Research, Mumbai 400005, India*
[121]*INAF, Osservatorio Astronomico di Capodimonte, I-80131, Napoli, Italy*
[122]*Università degli Studi di Urbino "Carlo Bo" I-61029 Urbino, Italy*
[123]*INFN, Sezione di Firenze, I-50019 Sesto Fiorentino, Firenze, Italy*
[124]*Physik-Institut, University of Zurich, Winterthurerstrasse 190, 8057 Zurich, Switzerland*
[125]*American University, Washington, DC 20016, USA*
[126]*University of Southampton, Southampton SO17 1BJ, United Kingdom*
[127]*University of Białystok, 15-424 Białystok, Poland*
[128]*University of Washington Bothell, 18115 Campus Way NE, Bothell, Washington 98011, USA*
[129]*Institute of Applied Physics, Nizhny Novgorod, 603950, Russia*
[130]*Korea Astronomy and Space Science Institute, Daejeon 34055, Korea*
[131]*Inje University Gimhae, South Gyeongsang 50834, Korea*
[132]*National Institute for Mathematical Sciences, Daejeon 34047, Korea*
[133]*NCBJ, 05-400 Świerk-Otwock, Poland*
[134]*Institute of Mathematics, Polish Academy of Sciences, 00656 Warsaw, Poland*
[135]*Hillsdale College, Hillsdale, Michigan 49242, USA*
[136]*Hanyang University, Seoul 04763, Korea*
[137]*Seoul National University, Seoul 08826, Korea*
[138]*NASA Marshall Space Flight Center, Huntsville, Alabama 35811, USA*
[139]*ESPCI, CNRS, F-75005 Paris, France*
[140]*Southern University and A&M College, Baton Rouge, Louisiana 70813, USA*
[141]*College of William and Mary, Williamsburg, Virginia 23187, USA*
[142]*Centre Scientifique de Monaco, 8 quai Antoine Ier, MC-98000, Monaco*
[143]*Indian Institute of Technology Madras, Chennai 600036, India*
[144]*INFN Sezione di Torino, I-10125 Torino, Italy*
[145]*Institut des Hautes Etudes Scientifiques, F-91440 Bures-sur-Yvette, France*
[146]*IISER-Kolkata, Mohanpur, West Bengal 741252, India*
[147]*Whitman College, 345 Boyer Avenue, Walla Walla, Washington 99362 USA*
[148]*Indian Institute of Technology Bombay, Powai, Mumbai, Maharashtra 400076, India*
[149]*Scuola Normale Superiore, Piazza dei Cavalieri 7, I-56126 Pisa, Italy*
[150]*Université de Lyon, F-69361 Lyon, France*
[151]*Hobart and William Smith Colleges, Geneva, New York 14456, USA*
[152]*Janusz Gil Institute of Astronomy, University of Zielona Góra, 65-265 Zielona Góra, Poland*

[153]University of Washington, Seattle, Washington 98195, USA

[154]King's College London, University of London, London WC2R 2LS, United Kingdom

[155]Indian Institute of Technology, Gandhinagar Ahmedabad Gujarat 382424, India

[156]Indian Institute of Technology Hyderabad, Sangareddy, Khandi, Telangana 502285, India

[157]International Institute of Physics, Universidade Federal do Rio Grande do Norte, Natal RN 59078-970, Brazil

[158]Andrews University, Berrien Springs, Michigan 49104, USA

[159]Università di Siena, I-53100 Siena, Italy

[160]Trinity University, San Antonio, Texas 78212, USA

[161]Abilene Christian University, Abilene, Texas 79699, USA

[162]Colorado State University, Fort Collins, Colorado 80523, USA

[†]Deceased, February 2017.
[‡]Deceased, December 2016.

Effect of elevated substrate temperature deposition on the mechanical losses in tantala thin film coatings

G. Vajente[1], R. Birney[2,3], A. Ananyeva[1], S. Angelova[2,3], R. Asselin[7], B. Baloukas[4], R. Bassiri[5], G. Billingsley[1], M. M. Fejer[5], D. Gibson[3], L. J. Godbout[7], E. Gustafson[1], A. Heptonstall[1], J. Hough[8], S. MacFoy[2,3], A. Markosyan[5], I. W. Martin[8], L. Martinu[4], P. G. Murray[8], S. Penn[6], S. Roorda[7], S. Rowan[8], F. Schiettekatte[7], R. Shink[7], C. Torrie[1], D. Vine[3], S. Reid[2,3], R. X. Adhikari[1]

[1] LIGO Laboratory, California Institute of Technology, Pasadena (CA) USA

[2] SUPA, Department of Biomedical Engineering, University of Strathclyde, UK

[3] SUPA, Institute of Thin Films, Sensors and Imaging, University of the West of Scotland, Paisley, UK

[4] École Polytechnique de Montréal, Montréal, Quebec, Canada

[5] Stanford University, Stanford (CA) USA

[6] Hobart and William Smith Colleges, Geneva (NY) USA

[7] Université de Montréal, Montréal, Quebec, Canada

[8] SUPA, Institute for Gravitational Research, University of Glasgow, Glasgow, UK.

E-mail: `vajente@caltech.edu, ross.birney@strath.ac.uk`

Abstract. Brownian thermal noise in dielectric multilayer coatings limits the sensitivity of current and future interferometric gravitational wave detectors. In this work we explore the possibility of improving the mechanical losses of tantala, often used as the high refractive index material, by depositing it on a substrate held at elevated temperature. Promising results have been previously obtained with this technique when applied to amorphous silicon. We show that depositing tantala on a hot substrate reduced the mechanical losses of the as-deposited coating, but subsequent thermal treatments had a larger impact, as it reduced the losses to levels previously reported in literature. We also show that the reduction in mechanical loss correlates with increased medium range order in the atomic structure of the coatings using x-ray diffraction and Raman spectroscopy. Finally, a discussion is included on our results, which shows that the elevated temperature deposition of pure tantala coatings does not appear to reduce mechanical loss in a similar way to that reported in the literature for amorphous silicon; and we suggest possible future research directions.

1. Introduction

The recent detections of gravitational wave signals from the coalescence of black holes [1, 2, 3, 4] and neutron stars [5] opened a new era in astronomy, and renewed the interest in the design and development of techniques to improve the sensitivity of the present generation of gravitational wave detectors such as Advanced LIGO [6], Advanced Virgo [7] and KAGRA [8].

The design sensitivity of Advanced LIGO is limited, in its most sensitive frequency range (20-300 Hz), by an equal contribution of quantum noise and thermal noise [6]. The dominant contribution to thermal noise is due to Brownian motion of the highly reflective, multilayer dielectric coatings deposited on the surfaces of the interferometer test masses [9]. Therefore, to further improve the sensitivity of the detectors in the present facilities, it is necessary to reduce the coating Brownian noise [10].

The Advanced LIGO high reflectivity multilayer coatings use alternating layers of silica (SiO_2) and titania-doped tantala (TiO_2-Ta_2O_5) [11, 12], where silica is the low refractive index material and titania-doped-tantala is the high refractive index material. The dominant contribution to the coating thermal noise comes from Brownian motion, which is directly related to the internal mechanical losses of the two materials [13, 14, 15]. In the state-of-the-art ion-beam-sputtered coatings used today, the measured mechanical loss angle for silica is 4×10^{-5} radians [16, 12], while for doped tantala it is 2.4×10^{-4} radians [11, 17]. Thus, the titania-doped-tantala layers are the dominant source of thermal noise.

There are many approaches under development to reduce the coating thermal noise: crystalline coatings [18], employing different materials and doping [19], or using different deposition and heat treatment techniques [20]. The goal for a medium term upgrade of Advanced LIGO (called Advanced LIGO+ [10]) is to improve the sensitivity by a factor of about two. This corresponds to a reduction of mechanical loss in the coating by a factor of four. For coatings of the dimensions needed for the Advanced LIGO core optics, no single approach has, as of today, provided a viable method to reduce mechanical losses by this factor.

In this work we discuss the exploration of one promising technique to deposit low loss coatings, by heating the substrate during the deposition process. It has been known for some time that post-deposition annealing reduces mechanical losses [20]. Recently, experimental studies performed with amorphous silicon [21] showed a reduction of 2-3 orders of magnitude in the mechanical losses, by depositing the thin film on a substrate heated to about 85% of the glass transition temperature. Similar results were obtained with different deposition techniques and materials [22]. Keeping the substrate at an elevated temperature increases the mobility of the atoms incident on the surface, which results in a more stable glass [23] and a reduced density of two-level tunnelling states [24, 25]; factors which have been shown to be correlated with mechanical losses in amorphous thin films. We should note here that post-deposition annealing at high temperature also allows an exploration of the energy landscape and a reduction of

the mechanical losses. However, both theoretical arguments and experimental results indicate that an elevated temperature during deposition allow a larger set of degrees of freedom to be explored by each atom that hits the surface, before being buried by the following layers.

We focused our first experimental efforts on the study of thin films made of undoped tantalum pentoxide (tantala). The lowest mechanical loss angle measured on thin films of this material after a post-deposition heat treatment is in the range 2.6×10^{-4} to 4.7×10^{-4} radians, depending on the deposition conditions [17, 26, 27, 28, 29, 30]. In this work we explored elevated temperature deposition using two different techniques that were readily available to us: magnetron sputtering and ion-beam sputtering [31].

Section 2 describes in detail both deposition techniques, as well as the substrates that were used. Section 3 describes the post-deposition heat treatment which was performed (annealing). Section 4 briefly describes the techniques used to measure the mechanical losses. Section 5 discusses the results of the measurements and Section 7 describes the structural studies that were carried out to try to understand the evolution of the coatings' microscopic structure.

2. Deposition techniques

We deposited undoped tantalum pentoxide thin films using two different techniques and substrates.

2.1. Magnetron sputtering deposition

A first set of depositions consisted of 1-μm-thick layers of tantala, deposited using magnetron sputtering (MS) [31], on a fused silica disk (Corning 7980), 75 mm in diameter and 1-mm-thick. The depositions were carried out at the École Polytechnique de Montréal and the Université de Montréal. The surfaces of the disk were polished, while the edge of the disk was simply ground. It has been shown that mechanical losses in fused silica substrates are limited by the surfaces that are not polished [32]. The disks have two flat cuts on opposite sides, to break the degeneracy of the resonant modes. The measurable vibrational modes of the disks had frequencies between 1.1 kHz and 30 KHz. The substrates were heat treated for 9 hours at 900°C in air before deposition. This step ensures that all the substrates have an equivalent low mechanical loss angle, and that residual stresses due to the machining process are reduced [33].

A total of 12 disk samples were coated using magnetron sputtering: four at room temperature (in reality approximately 50°C, due to the substrate heating up from the deposition process), and two disks at each of the following temperatures: 150°C, 250°C, 400°C and 480°C.

The magnetron-sputtered tantalum pentoxide films were deposited in a high vacuum CMS-18 process chamber built by Kurt J. Lesker Co. Ltd, equipped with a 7.62 cm diameter tantalum target of 99.95% purity located ∼25 cm beneath the substrate

holder. Prior to deposition, the base pressure was below 10^{-7} Torr.

The 1-mm-thick fused-silica substrates were installed one at a time on a 15-cm-diameter rotating stainless steel holder, designed with a 7.62-cm-diameter hole in the middle, and supported at the edges by a 1-mm ledge. A 3-mm-thick Macor® puck of the same diameter as the substrate was placed on its backside and thus directly exposed to the halogen heating lamps positioned above the substrate holder. The high emissivity of Macor® (0.93 according to [34]) helped increase mid-infrared radiation in order to reach the highest temperature of 480°C. The surface temperature of the substrates was pre-calibrated by installing a thermocouple in direct contact with a substrate's surface before the deposition. The thermocouple was not installed during the actual deposition.

Each deposition run began by setting the desired temperature, increasing it at a rate of 5°C/min and allowing it to stabilize for 30 minutes once reached. The sample was then subjected to a radio-frequency plasma cleaning procedure for 10 minutes in an Ar and O_2 gas mixture (2:1 Ar to O_2 ratio) at a pressure of 8 mTorr and a bias voltage between 90 and 100 V (the discharge power was maintained between 6 and 8 W). The tantalum target was then precleaned for 3 minutes in a pure Ar plasma at a discharge power of 440 W. Oxygen was then introduced into the chamber (60% O_2:Ar ratio at a pressure of 2 mTorr) and the discharge allowed to stabilize for 20 minutes to ensure steady-state conditions (bias cathode voltage of approximately -210 V). The main shutter was then opened and the film deposition started. It is important to note that the process itself typically heats the sample by 30 to 40°C when depositing at room temperature; this temperature increase is expected to be smaller for samples heated to higher temperatures. The deposition time was kept constant for all samples and the deposition rate was seen to decrease from 2.27 Å/s to 2.07 Å/s as the temperature was increased. Following the deposition, the samples were cooled down to room temperature at a rate of 10°C/min.

Rutherford backscattering spectrometry (RBS) confirms the expected stoichiometry of the films, and reveals the presence of Ar and H impurities at levels of 3% and 1.5% respectively. By combining RBS and ellipsometry measurements, we found the average density of the layers produced by MS to be $(7.5 \pm 0.3) \times 10^{22}$ atoms/cm³. The combined uncertainty on the RBS and ellipsometry measurements did not allow us to find a correlation between the density and the loss angle or X-ray diffraction peak width (see also Section 7). The refractive index of the tantala layer has also been measured. For all samples, except the one deposited at the highest temperature (480°C), the refractive index is 2.14 ± 0.01. The sample deposited at 480°C instead has a refractive index of 2.24 ± 0.01, however this sample showed signs of crystallization (see also Section 7).

2.2. Ion beam sputtering deposition

A further set of depositions consisted of ~0.5µm-thick layers of tantala, deposited using ion beam sputtering (IBS) [31], on fused silica cantilevers. The depositions were carried out at SUPA, Institute of Thin Films, Sensors and Imaging, University of the

West of Scotland. The samples were fabricated by dicing $\sim$ 150-µm-thick fused silica wafers (JGS1 material, 100-mm-diameter) into 45-mm-long strips, 5-mm-wide. These were then flame welded to a 3.1-mm-thick clamping block, of the same silica material, with area 10×10 mm^2, using a hydrogen-oxygen flame, on the 5 mm edge. The cantilevers were subsequently placed in boiling H_2O_2 (30 % w/w in H_2O) with 1 mol/l KOH dissolved, in order to clean the sample surface and to remove silica particulates associated with the welding process. Finally, the samples were annealed at 900°C in air for 1 hour. Further high temperature annealing did not change the substrate mechanical losses. The measurable vibrational modes of the cantilevers were between $\sim$300 Hz and $\sim$11 kHz.

A set of 5 cantilevers were coated by sputtering from a circular 4" diameter pure tantalum metal target of 0.125" thickness, purity 99.9% (Pi-Kem, UK), at room temperature and at elevated temperatures 100°C, 200°C, 300°C and 400°C. A further set of 6 cantilevers were then coated by sputtering from a 4" pure tantalum pentoxide target (Pi-Kem, UK), purity 99.99%, at room temperature and at elevated temperatures 100°C, 200°C, 300°C, 400°C and 500°C (the maximum possible with the current setup). Additional JGS1 silica witness samples, of 20 mm diameter and 0.5 mm thickness, for optical and structural characterization, were coated in separate deposition runs using nominally identical conditions.

The IBS system was custom-built and uses a single electron cyclotron resonance (ECR) ion source developed by Polygon Physics [35], as shown in Figure 1. The source uses a small $\lambda/4$ microwave (2.4 GHz) cavity, which is held at 11.7 kV in order to extract argon ions through a single aperture, which are focused into a near-parallel beam using electrostatic optics placed in front of the ECR cavity. The deposition system was specifically developed to be more flexible than standard (typically RF) ion beam sputtering, in addition to being potentially 'cleaner' due to the gridless extraction of the ions. However, the ion current is very low, typically in the range of $\sim$0.2$\rightarrow$0.5 mA, which limits the deposition rate in this geometry to within a range of 1$\rightarrow$10 Å/min. The base vacuum pressure was around 0.8×10^{-6} Torr or better prior to deposition, with the pressure rising to 6×10^{-5} Torr when injecting the required level of argon into the plasma cavity; finally increasing to 9×10^{-5} Torr once the reactive oxygen gas was fed into the chamber (introduced directly above the substrates being coated).

The temperature during deposition was monitored on the copper substrate holder, with calibration runs conducted by gluing PT100 resistance thermometers to silica cantilevers under identical conditions (the correction of the cantilever temperature with respect to the substrate holder was typically 20 $\rightarrow$ 40 °C, depending on deposition temperature). As with the magnetron coating process, the temperature was allowed to stabilize for a minimum of 30 mins before the deposition was commenced. The samples were allowed to cool naturally after deposition, with a maximum cooldown rate of 30°C/s for the 500°C deposition run, and slower cooldown rates for lower deposition temperatures.
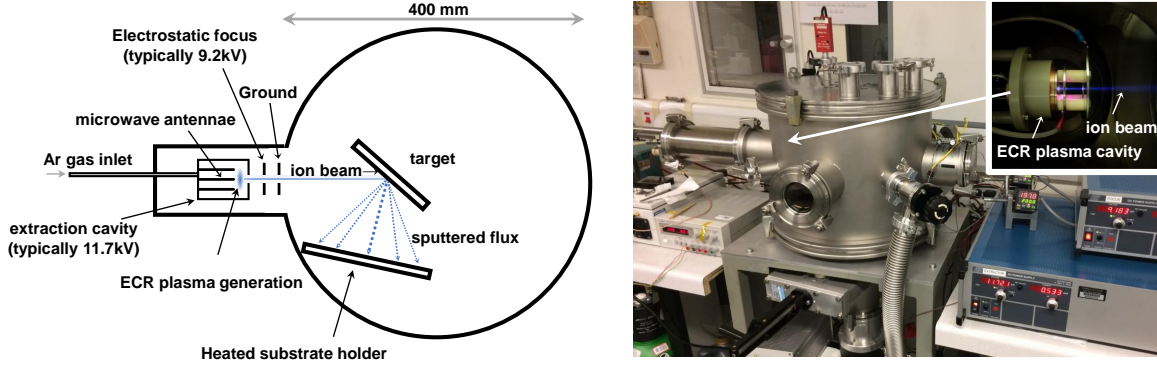
Figure 1. Schematic diagram (left) showing the configuration and geometry of the ion beam sputtering system, with images (right) of the chamber and ion source during operation (inset).

3. Post-deposition heat treatments

After deposition, the mechanical losses of all samples were measured using the techniques described below in Section 4. Additional structural measurements, described below in Section 7, were also performed. Afterwards, a subset of the samples were subjected to a heat treatment cycle (annealing). In the case of the magnetron-sputtered samples, we first annealed them at 300°C for 3 hours, then at 400°C for 3 hours, and finally at 500°C for 3 hours, carrying out mechanical loss and structural measurements after each heat treatment cycle. In each case the samples were heated up at a rate of about 1°C/min, and allowed to cool down at the same rate.

Similarly, the IBS samples were annealed for 5 hours in air, at increasing temperatures of 100, 200, 300, 400, 500, 600 and 650°C, and again allowed to cool naturally in the oven (maximum ramp-up rate 4°C/s, maximum ramp-down rate 3°C/s. Mechanical loss measurements were performed after each annealing step.

The small difference in annealing time for the MS and IBS samples does not significantly affect the measured loss angle. Longer annealing times have been tested by the authors on a subset of the samples, and the measured loss angles found to be comparable.

4. Measurement of mechanical losses

The mechanical loss angle of each sample was measured by exciting its resonant modes and tracking the amplitude of the motion at the mode peak frequency over time. The ring-down time is directly linked to the total mechanical loss angle of the sample ϕ_{total}, including contributions from both the substrate losses and the coating layer losses:

$$A(t) = A(0)e^{-t\pi f\phi_{\text{total}}} \tag{1}$$

where f is the frequency of one of the resonant modes of the sample. To disentangle the two contributions, we built finite element models of the coated substrates. The models

	Silica	Tantala
Young's modulus [GPa]	73.2 [12]	140 [36]
Poisson ratio	0.164 [12]	0.28 [36]
Density [kg/m^3]	2200 [12]	8200 [36]

Table 1. Material parameters used in finite element models.

are based on the values for the Young's modulus, density and Poisson ratio of silica and tantala listed in Table 1. The models are first tuned to accurately predict the resonant frequencies of the uncoated substrate. Afterwards, the coating thickness is tuned to the mean value over the whole surface measured by ellipsometry. Finally, the model can be used to extract the distribution of elastic energy in the substrate and in the coating. The ratio of the energy in the coating divided by the energy in the substrate is known as the dilution factor. It can be used to extract the coating loss angle from the total measured loss angle:

$$\phi_{\text{total}}^{(i)} = D^{(i)}\phi_{\text{coating}}^{(i)} + (1 - D^{(i)})\phi_{\text{substrate}}^{(i)} \tag{2}$$

where the subscript (i) refers to the vibrational modes, since the dilution factor differs from mode to mode. Also, in general, the loss angle may be frequency dependent. To accurately extract the coating loss angle, a measurement of the substrate loss is needed; this can be obtained by measuring the ring-down time of the uncoated sample, assuming that the deposition does not affect the substrate properties in a significant way. Typical numbers for the fused silica disks used in our experiments are $\phi_{\text{substrate}} \sim 10^{-7}$ and $\phi_{\text{total}} \sim 3 \times 10^{-6}$. The mechanical losses of the uncoated substrates used here are larger than what is expected for fused silica bulk [33], and they are limited by surface loss on the unpolished sides [32].

The coating loss angle could in principle be different for shear and bulk deformations [37]. Our finite element simulations show that most of the elastic energy is in shear. Moreover, recent results suggest that ϕ_{shear} and ϕ_{bulk} [38] are not largely different. Therefore, in the analysis presented here we do not make this distinction. This approach also makes it simpler to compare our measurements with previous results reported in the literature, which also do not take into account the distinction between shear and bulk losses. Moreover, our main goal is to determine if there is any change in the mechanical loss that is deposition-process dependent, and therefore using a single loss angle is sufficient.

The samples coated by magnetron sputtering (75-mm-diameter disks) were measured at the LIGO Laboratory (Caltech) using a system based on the Gentle Nodal Suspension [39, 40]. The fused silica substrate is supported at its center by a curved silicon surface, relying on gravity and friction between the sample and the support. This nodal suspension allows the measurements of all resonant modes between 1 kHz and 30 kHz with negligible clamping losses for all modes that have a node of non-motion at the center of the disk [41]. Four disks are mounted into one vacuum chamber, which allows

the parallel measurement of four samples. The disks are excited using an electrostatic comb drive [42], and the motion is read-out with an optical lever system; a HeNe laser beam is reflected off the disk surface, close to the edge, and the beam displacement is measured with a quadrant photo-detector (QPD). The output signals are sampled at 65 kHz and saved to disk to be processed offline. This excitation and data acquisition system allows the simultaneous measurement of the ring downs of all resonant modes of four samples. More details on the measurement system can be found in [40].

In the case of the coatings deposited on cantilevers by IBS, each sample was measured before and after coating using a readout technique similar to the one described above, but with a few notable differences. The silica cantilevers were each secured inside a vacuum chamber by fixing the clamping block in place with a stainless steel clamp. A He-Ne laser outside the chamber was then directed through a chamber window, incident upon the edge of the cantilever, and passed through a second window onto a split photodiode detector, again outside the chamber. The cantilever creates a shadow on the laser spot, the displacement of which (due to excitation of the cantilever) is then measured; each mode was measured and recorded individually by an automated LabView program for offline analysis. The mechanical losses were then calculated in the same way as with the disk samples, using eq. 2, with dilution factors obtained from finite element models of the cantilever geometry.

5. Results

The coating loss angle measured for all 12 MS samples is shown in Figure 2. For each sample, several resonant modes could be measured, with frequencies between 1 kHz to more than 20 kHz. All samples were measured after deposition, and before any additional treatment. Then, 5 samples (two deposited at room temperature and one for each of the other deposition temperatures) were treated with annealing cycles, at increasing temperatures of 300, 400 and 500°C. The results of all mechanical loss measurements, for all the frequencies, are shown in Figure 2.

For the majority of samples, the dependence of the loss angle upon the mode frequency is rather weak and, in most cases, a clear trend is difficult to identify. For these reasons, and to facilitate easier comparison between samples, the loss angle has been averaged over frequency for each sample; the results are shown in Figure 3. One can first observe that there is a reduction of mechanical losses in the as-deposited samples, when the substrate is at an elevated temperature during deposition. However, the measured losses further improved with post-deposition annealing, reaching a level as low as 4.5×10^{-4} rad; comparable with what is reported in the literature for annealed pure tantala [27, 30, 29].

For the IBS coatings, Figure. 4 shows the measured loss angles for all resonant modes and all samples. Again, the dependence of loss angle upon mode frequency is quite weak in most cases; therefore, the loss angles were again averaged over all resonant frequencies for ease of comparison between different samples (see Figure 5).
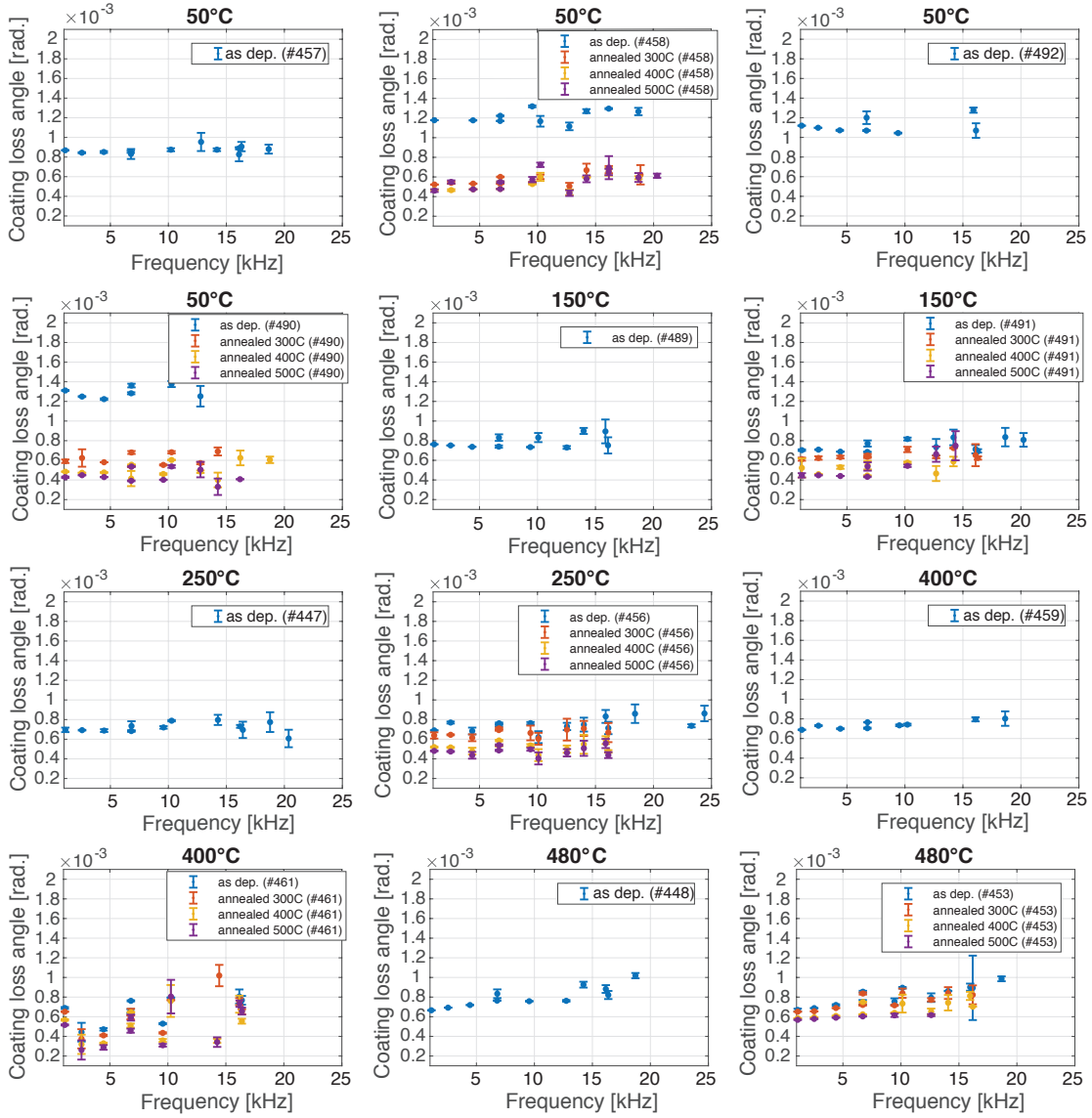
Figure 2. Summary of all measurements performed on the magnetron sputtered samples. Each panel corresponds to a different sample. The title shows the temperature at which the coating was deposited, while the different traces (if present) in each panel refer to the coating as-deposited or after subsequent annealing treatments. The numbers in the legend are unique identification numbers for each substrate. The error bars at each frequency are 95% confidence intervals computed from the standard deviation of repeated measurements.
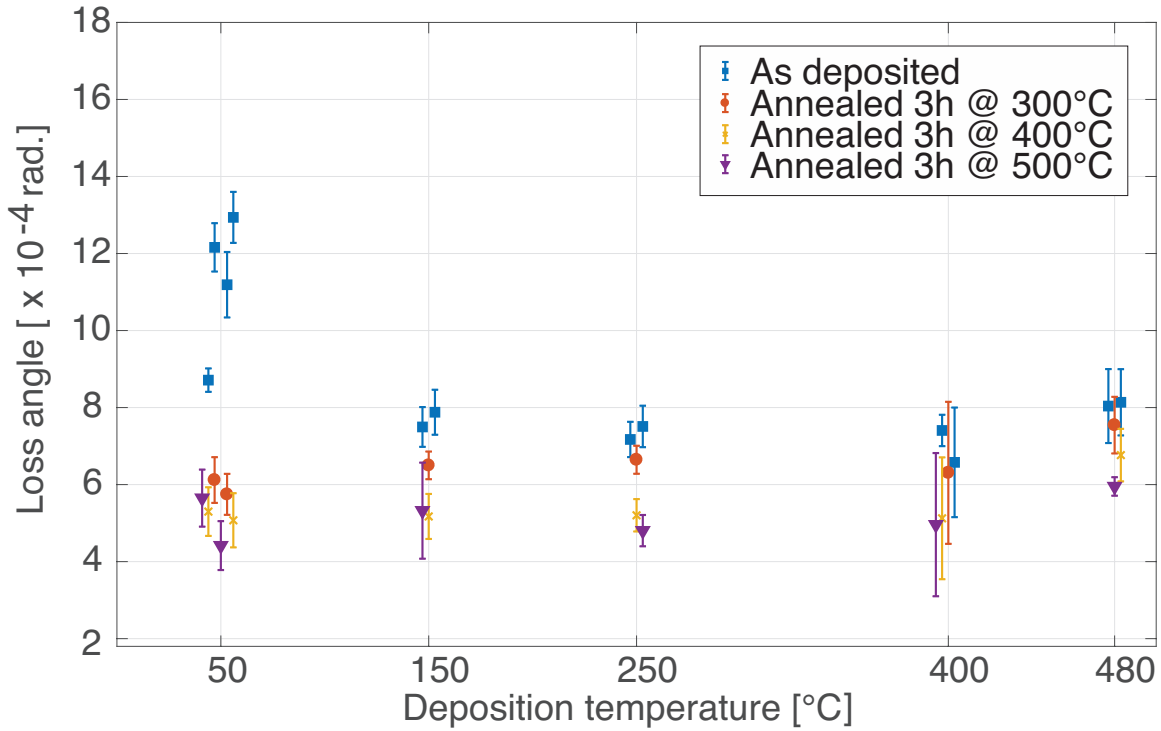
Figure 3. Averaged mechanical loss angle for magnetron sputtered tantala. The values shown here are obtained by averaging the results shown in Figure 2, over all frequencies. The error bars are 95% confidence intervals computed from the standard deviation of the loss angles measured for the different modes for each sample (the uncertainty in the single frequency measurements are negligible). A random horizontal shift of the points have been added to improve the readability of the plot.

The IBS coatings showed broadly similar results to the magnetron sputtered coatings, in that mechanical loss is reduced by elevated temperature deposition. However, the measured losses further improved with post-deposition annealing, with the average loss reaching $2.7 \pm 0.8 \times 10^{-4}$ rad, which is in line with the lower end of previously reported measurements [26], and also close to the loss angle measured on the titania-doped-tantala used in the Advanced LIGO coatings [17]. It should be noted that there are two significant differences between the ECR ion beam sputtering process employed in this work and current industry standard processes: a significantly slower deposition rate and a higher extraction potential. Further investigations of these factors, in relation to the achievable levels of mechanical loss, are therefore worth exploring.

In summary, the mechanical loss of as-deposited tantala improves with the deposition temperature up to about 250°C and then remains roughly constant, although at a value better than that measured on room-temperature-deposited samples. However, high temperature annealing erases the deposition history of the coating. The main remaining difference is the fact that coatings deposited by IBS have about 1.6 times lower mechanical loss angle than the coatings deposited by MS. It is worth noting that
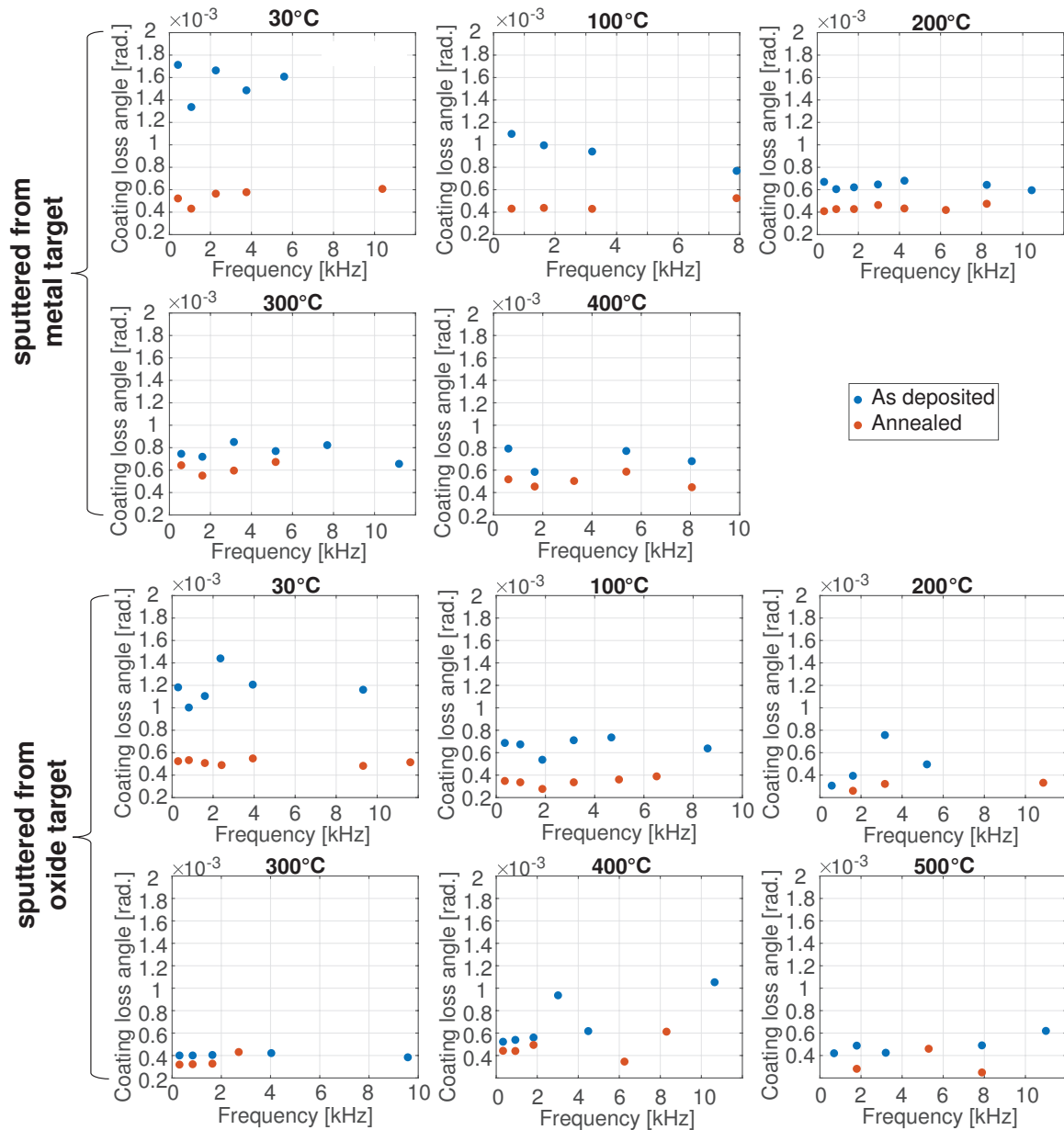
Figure 4.   Summary of all the measurements performed on ion beam sputtered samples. Each panel corresponds to a different sample. The title shows the temperature at which the coating was deposited, with separate traces to show the mechanical loss as-deposited and post annealing treatment (all at 600°C for 1 hr). The uncertainty for all data points is about 1%, and not visible in the plot.
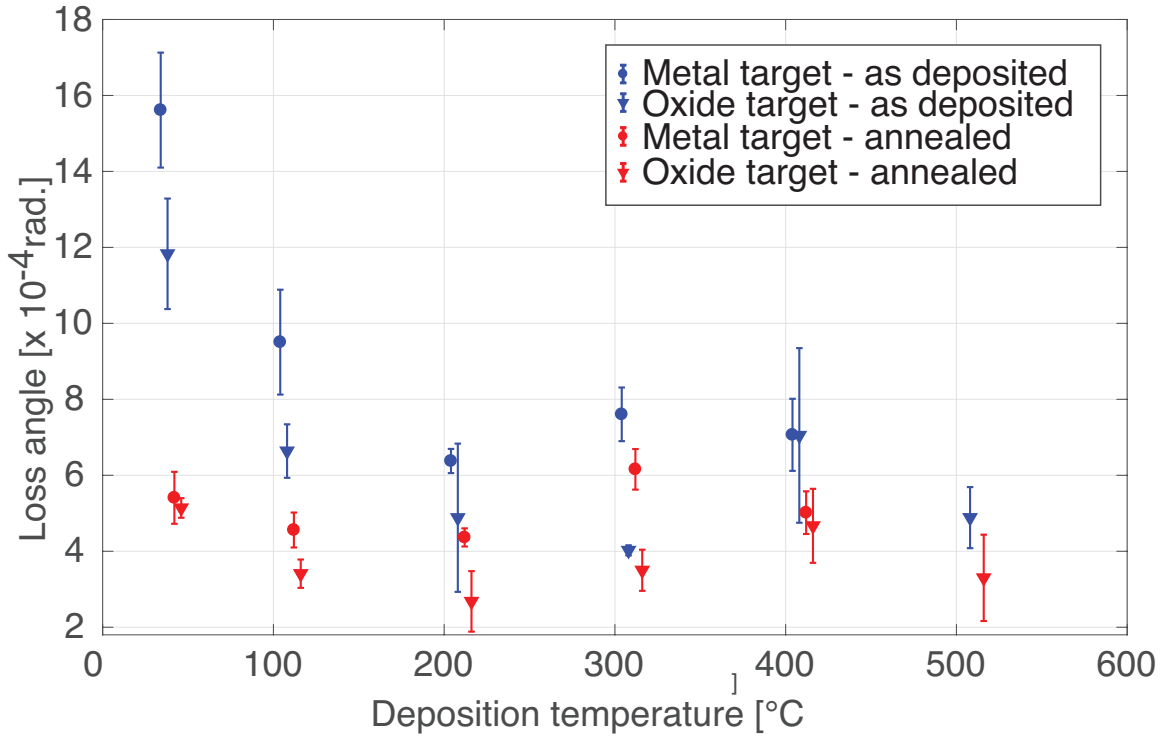
Figure 5. Averaged mechanical loss angle for ion beam sputtered tantala. The values shown here are obtained by averaging the results shown in Figure 4 over all frequencies. The error bars show the standard error associated with the spread in the measured mechanical losses. The slight change in deposition temperature between the metal and oxide target sputtered coatings are associated with improvements in the calibration of the temperature readout carried out between these sets of coating runs.

a small discrepancy has been observed in the past between mechanical loss measurements performed on disk with gentle nodal suspension systems and cantilevers. However, as shown in [12], the mechanical loss measured on disks were lower than the mechanical losses measured on cantilever. Therefore we believe that the larger difference in our samples is due to the deposition techniques.

6. Structural characterization : measurement techniques

6.1. X-ray diffraction

X-ray diffraction study of all MS samples was carried out on a PANalytical X'Pert PRO x-ray diffraction system in parallel beam mode at the Stanford Nano Shared Facilities. For these measurements, in order to obtain maximum scattered intensity from the deposited thin films, while minimizing the contribution from the substrate, the incident x-ray beam angle was fixed at 1.5° while the detector was scanned from 10° to 90°. The angle of divergence for the incident and diffracted beams was 0.04° and 0.27°, respectively. For polycrystalline samples, such a scan results in the same Bragg

peaks as a standard θ-2θ scan but with slightly different relative peak intensities. In amorphous thin films, one would not observe sharp Bragg peaks but broad diffraction peaks. Once properly reduced (i.e. expressed as oscillations about the structure factor versus scattering vector) a Fourier transform of these broad structures gives the atomic radial distribution function (see, e.g., ref. [43]. Therefore, increased medium range order in the atomic structure of an amorphous material usually results in sharper (less broad) diffraction features.

6.2. Raman spectroscopy

Raman spectroscopy was performed using a Renishaw Invia Reflex Raman microscope employing an Argon laser operating at 514 nm, non-polarized in a backscattering geometry. The 25.0 mW laser beam was focused to a circular spot of 2 μm diameter. Rayleigh scattering was removed by an edge filter with a 90 cm^{-1} cut-off. A 1800 l/mm grating spectrometer dispersed the scattered light onto 1040 $\times$ 256 pixel CCD resulting in a spectral resolution of 1.0 cm^{-1}. Three measurements were carried out at different locations on each sample, and the average is plotted in the figure. Individual measurements were also analyzed to check for non-uniformity; no obvious effect was found. The Raman spectrum of an amorphous material resembles its vibrational density of states, since the selection rules that affect the Raman scattering in crystalline materials is not operative. The shape of the Raman spectrum can be described in an ad-hoc fashion, as a combination of lorentzian curves each representing one band in the (crystalline) phonon dispersion diagram or from a molecular dynamics simulation of the material. For the case of Ta_2O_5, the first approach requires 19 lorentzians ref. [44]; the vibrational density of states deduced from molecular dynamics was reported by ref. [45].

7. Structural studies: results

Several structural studies (X-ray diffraction (XRD) and Raman spectroscopy) were carried out to gain more insights into the effect of deposition temperature and annealing, and to look for residual differences between coatings deposited at different substrate temperatures.

7.1. X-ray diffraction

As a first step, XRD measurements were performed for all samples to check for possible crystallization, both immediately after deposition and after subsequent heat treatment cycles. Figure 6 shows the resulting diffraction patterns for the IBS samples and the MS samples. In the case of IBS samples, XRD scans were performed on the samples as deposited, and after the last annealing step at 600°C. No crystallization was detected for any deposition temperature in IBS samples, while the MS coating deposited on a substrate at 480°C showed clear signs of crystallization. Crystallization in MS thin

films was already observed at deposition temperatures above 450°C [46, 47]. No further crystallization was induced by the post-deposition annealing cycles. The IBS deposition is likely to produce denser coating, thus suppressing crystallization; other workers have also reported crystallisation of amorphous thin films to increase with increasing packing density [48].
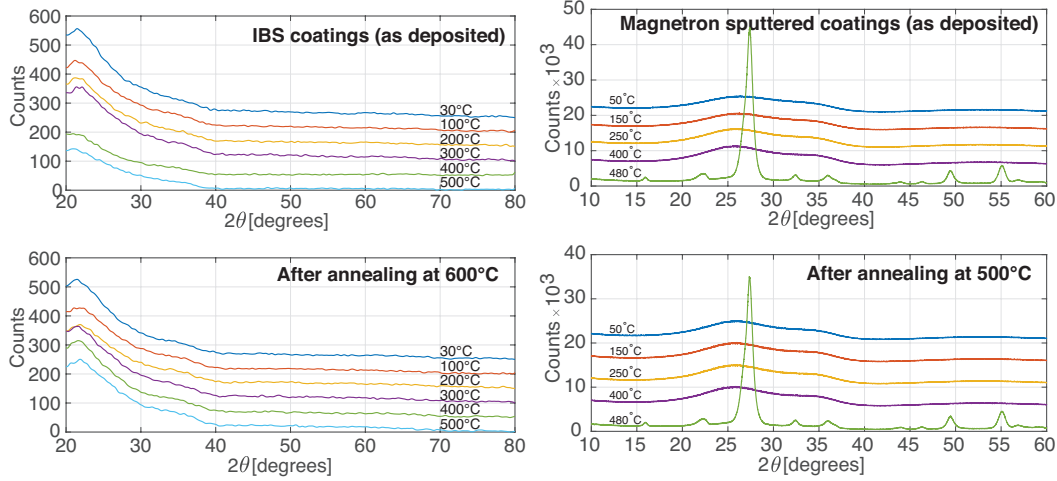

Figure 6. **Left.** XRD diffraction patterns for ion beam deposited tantalum pentoxide films, sputtered from an oxide target, before (top) and after (bottom) annealing at 600°C. The temperatures listed in the graph correspond to the different substrate temperature during deposition. XRD scans were carried out using a Siemens D5000 X-ray diffractometer at room temperature with Cu K$_{\alpha}$ radiation (λ = 0.154 nm) in the range of 2θ between 20° and 80° (2 seconds per scan, step size = 0.02°. **Right.** X-ray diffraction curves for a selection of the magnetron sputtered samples, before (top) and after (bottom) annealing. In each panel, the curves corresponding to different deposition temperatures have been shifted vertically by an arbitrary amount for readability.

7.2. Medium range order and loss angle

XRD measurements were also used to characterize more subtle changes in the microscopic structure of the coatings. In particular, medium range order (the local atomic structure in the range of 0.5 - 5 nm) in amorphous covalent glasses can be characterized by the *first sharp diffraction peak* (FSDP) in the XRD spectrum [49]. Both the position and width of the FSDP provide information on the statistical distribution of bond angles [50]. We have therefore attempted to correlate the loss angle measurements with the width and position of the FSDP on the MS samples. Since in Ta$_2$O$_5$ the FSDP is very asymmetric with a large shoulder on the high-angle side, we selected an angular range of 2θ between 16 and 28 degrees and fit the data with a Gaussian peak plus a constant offset. Figure 7 shows the results for the as-deposited and post-annealing MS coatings. The width of the FSDP is correlated with the deposition temperature, as

visible in the left panel of Figure 7: for both the as-deposited samples and the annealed samples, the peak width decreases with increasing deposition temperature. The effect of annealing is also important: annealed samples show narrower peaks with respect to the corresponding as-deposited sample.

The correlation between the loss-angle measurements and the FSDP-peak widths is shown in the right panel of Figure 7. The anneal temperature in all cases was 500°C. Very similar results are obtained when comparing the loss angle measurements to the FSDP position instead of width (not shown here). There is a weak linear correlation (correlation coefficient $r = 0.78$) between the FSDP width and the mechanical loss angle: lower loss angles correspond to narrower peaks.

In view of the good linear fit for most data points, we can speculate that a narrower FSDP, corresponding to an increased medium range order, is correlated to lower loss angle. However, for two samples (as deposited, 250°C and 400°C), another mechanism inhibited low loss angles in spite of good medium range order. This could be caused by, for example, a strain mismatch between substrate and deposited layer, or some other issue that can be remedied with the post-deposition anneal. Still, aiming at low loss angles one should strive for increased medium range order [51]. This suggests that the deposition should be carried out at as high a deposition temperature as possible, and post-deposition annealing should be carried out at as high a temperature as possible. Indeed, in the case of pure amorphous silicon, high medium range order, as characterized by X-ray diffraction and Raman spectroscopy, was obtained by a short, high temperature flash anneal [52]; crystallization was avoided by limiting the anneal time to a few seconds. It is therefore worthwhile to investigate the loss angle in samples deposited at temperatures above 400°C (but below 480°C which results in partly crystalline MS films) and subsequently heat treat at higher anneal temperatures, perhaps using rapid thermal annealing.

7.3. Raman spectroscopy and loss angle

Raman spectroscopy is a powerful tool to detect structural relaxation, as shown in amorphous silicon in [53]. This type of structural relaxation, or change in the medium range ordering, involves a thermally activated atomic rearrangement of the otherwise static atomic structure. Based on our XRD observations, we surmise that the dynamical relaxation or internal friction mechanisms which we try to minimize in the Ta_2O_5 layers are reduced somewhat in materials that have undergone such a structural relaxation of the permanent atomic structure. In other words, the mechanical loss angle in Ta_2O_5 may be correlated to medium range order, and in turn the medium range order in amorphous Ta_2O_5 can perhaps be detected by Raman spectroscopy. Therefore we decided to measure the Raman spectrum of all the samples for which the mechanical loss angle had also been measured. The Raman spectrum of Ta_2O_5 is much more complicated than that of amorphous silicon: in the case of silicon, there are only four main bands (TO-, TA-, LA-, LO -like) relatively well separated, so that one can determine the
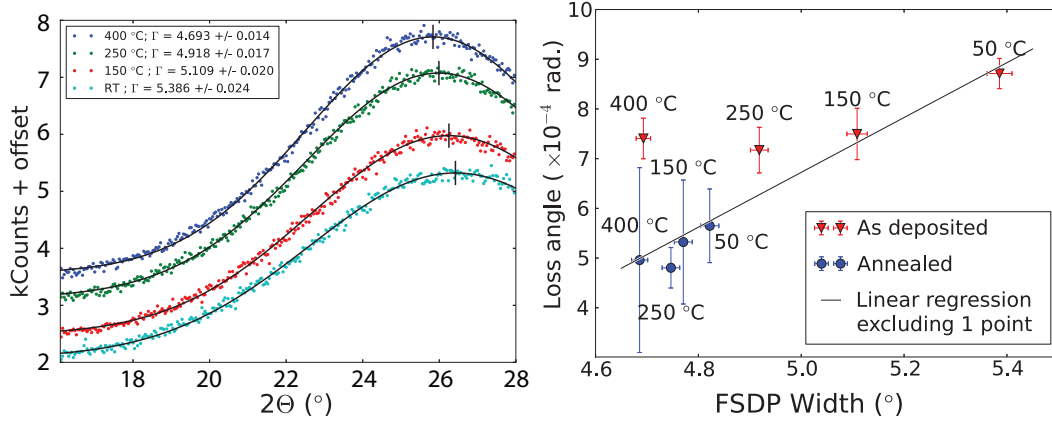
Figure 7. **Left.** First sharp diffraction peak (small angle side only) of four magnetron sputtered samples, before annealing. Spectra have been offset vertically for clarity. From top to bottom : deposited at 400°C, 250°C, 150°C, and at room temperature. The solid lines show a gaussian fit to the experimental data. The peak positions determined by the fit are shown as vertical lines across the maximum of each curve, and the peak widths are reported in the legend. The quoted uncertainty corresponds to the 1-sigma increase in chi-squared as determined by the fitting routine. **Right.** Mechanical loss angle as a function of the FSDP width for magnetron sputtered samples, before (red triangles) and after (blue circles) annealing at 500°C . The solid line is a linear fit to all datapoints, excluding the one deposited at 400° C before annealing.

width, position, and relative intensity of each band. In particular, the width of the amorphous silicon TO-like band has been shown to depend on the average distortion of the tetrahedral bond angle, and hence to be a good indicator of medium range order [54]. In the case of Ta_2O_5, the Raman spectra of the crystalline and amorphous phases can be described with a fit containing essentially 19 Lorentzian curves [44], and most of those are overlapping. This makes it difficult to reliably extract the width of any single band from the Ta_2O_5 Raman spectrum.

The left panel in Figure 8 shows the Raman spectrum measured for each of the magnetron sputtered samples, after annealing. The main feature in all spectra is a large peak centered near 700 cm^{-1}, which is due to at least 4 separate bands according to the fit described in [44]. Molecular dynamics ([45]) indicate this frequency range corresponds to bending and stretching movements involving 3 Ta coordinated oxygen atoms. One spectrum (deposition temperature = 480°C) also shows a peak near 200 cm^{-1} indicative of crystallization [44], as already noticed in the XRD analysis (see Figure 6). The right panel in Figure 8 compares the mechanical loss angles of all samples with the Raman peak width. As can be observed, this analysis is inconclusive: lower mechanical losses are weakly correlated to narrower peaks (correlation coefficient $r = 0.71$), similarly to what was already determined in the XRD analysis. We have extracted many more parameters from the Raman spectra, such as the relative intensity of the bands at 90 and 650 cm^{-1} or the mean position rather than FWHM of the main peak, and evaluated their behavior
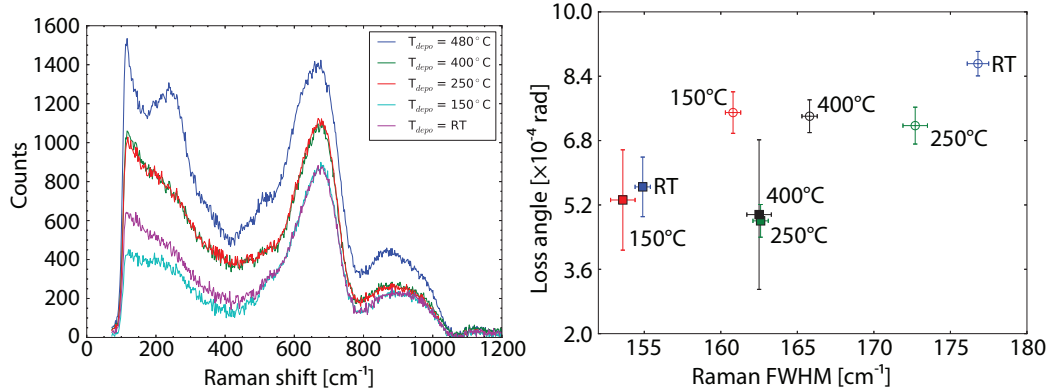
Figure 8. **Left.** Raman spectra of five magnetron sputtered samples, after annealing. From top to bottom: deposited at 480 °C, 400 °C nearly overlapping with the one deposited at 250°C, 150°C, and at room temperature. **Right.** Loss angle as a function of the full width at half maximum (FWHM) of the main peak of the Raman spectrum, for the magnetron sputtered samples. Open circles correspond to measurements performed on samples as-deposited, while solid squares to measurements performed on samples annealed at 500°C. The substrate temperature during deposition is written next to each data point.

versus the loss angle or anneal temperature. So far, no parameter measured by Raman spectroscopy shows a clear correlation with the mechanical loss angle even though in all samples the anneal treatment leads to both a decrease in Raman peak width and mechanical loss angle. Further efforts are needed, especially from a simulation point of view, in order to interpret the features of these spectra.

8. Discussion of the results

In this work, we explored the effect of deposition on a substrate held at elevated temperature on the mechanical loss of pure tantala. The results obtained from two different deposition techniques agree quite well: depositing the coating on a hot substrate improves the mechanical loss. However, the as-deposited coatings did not show a significant improvement of mechanical loss with respect to previous results for room-temperature-deposited films after optimal post-deposition annealing. Additionally, heat treatment after deposition appears to have a much larger effect than elevated temperature deposition: after annealing at about 400°C all coatings, regardless of the deposition technique or the substrate temperature, show mechanical loss in the range $2.7 - 4 \times 10^{-4}$ radians, in line with previous results. It is worth noting that post annealing the IBS films exhibit about 1.6 times lower loss angle than the MS films: further investigations are needed to confirm if this difference is due to the deposition technique, or that the IBS coatings were deposited at a significantly lower rate.

Structural studies were carried out to correlate the mechanical loss with increased medium range order. Lower mechanical losses are correlated with a narrower width of

the first diffraction peak in X-ray measurements and, more weakly, with the width of the main Raman spectrum peak. Although the substrate temperature during deposition played a role in determining the peak widths as well as the mechanical loss, the effect of post-deposition heat treatment is much more significant: annealed samples systematically showed lower loss angles and more relaxed structure (narrower peaks).

In conclusion, we could not achieve for tantala the same level of reduction in mechanical loss angle observed in amorphous silicon [21]. From a theoretical point of view, mechanical losses are associated with low-energy excitations usually modeled as two-level systems (TLS). The structure of the energy landscape in glasses depends on the fabrication history: a detectable change in the glass structure is expected to happen when the deposition is carried out at a significant fraction (85%) of the glass transition temperature [24, 25]. This was indeed observed in amorphous silicon. If, as expected from experiments and models, the fraction of the glass transition temperature at which the density of TLS reduces is universal, we might expect any effect to be visible in tantala for temperatures much higher than those explored in this study, which was limited by the incipient crystallization of the thin film. It is possible that the glass transition temperature of tantala is too high to be practically reachable before crystallization of the coating is induced. A strategy that will be explored in the future is the prevention of crystallization, either geometrically, with nano-layers [55], or chemically, with the addition of dopants to tantala, for example titania [11] or zirconia [17].

Further investigations are needed to better understand the microscopic structure of tantala coatings. Future planned experiments will use X-ray scattering [56] and electron diffraction [57], combined with atomic deposition modeling [58], to perform a detailed analysis of the medium range order. Such studies could elucidate the atomic structure motifs that play a significant role in the mechanical loss, in particular with elevated temperature deposition and post-deposition heat treatment of tantala and other oxides.

The results reported here indicate that elevated temperature deposition of pure tantala might not be a viable solution for low mechanical loss coatings for future gravitational wave detectors. We do not have enough data to generalize these results to other materials, or to doped tantala. Future investigations will therefore focus on doping, other oxides with lower melting temperatures, and alternative deposition techniques, such as ion-beam-assisted IBS and lower deposition rates.

Acknowledgements

[1] B P Abbott et al. Observation of gravitational waves from a binary black hole merger. *Phys. Rev. Lett.*, 116:061102, 2016.

[2] B P Abbott et al. GW151226: Observation of gravitational waves from a 22-solar-mass binary black hole coalescence. *Phys. Rev. Lett.*, 116:241103, 2016.

[3] B P Abbott et al. GW170104: Observation of a 50-solar-mass binary black hole coalescence at redshift 0.2. *Phys. Rev. Lett.*, 118:221101, 2017.

[4] B P Abbott et al. GW170814: A three-detector observation of gravitational waves from a binary black hole coalescence. *Phys. Rev. Lett.*, 119:141101, 2017.

[5] B P Abbott et al. GW170817: Observation of gravitational waves from a binary neutron star inspiral. *Phys. Rev. Lett.*, 119:161101, 2017.

[6] B P Abbott et al. The advanced LIGO detectors in the era of first discoveries. *Phys. Rev. Lett.*, 116:131103, 2016.

[7] F Acernese et al. Advanced virgo: a second-generation interferometric gravitational wave detector. *Class. Quantum Grav.*, 32:024001, 2015.

[8] T. Akutsu et al. Large-scale cryogenic gravitational-wave telescope in japan: KAGRA. *Journal of Physics: Conference Series*, 610:012016, 2015.

[9] G M Harry et al. Thermal noise in interferometric gravitational wave detectors due to dielectric optical coatings. *Class. Quantum Grav.*, 19:897, 2002.

[10] J Miller et al. Prospects for doubling the range of Advanced LIGO. *Phys. Rev. D*, 91:062005, 2015.

[11] G M Harry et al. Titania-doped tantala/silica coatings for gravitational-wave detectors. *Class. Quantum Grav.*, 24:405, 2007.

[12] M. Granata et al. Mechanical loss in state-of-the-art amorphous optical coatings. *Phys. Rev. D*, 93:012007, 2017.

[13] Y T Liu and K S Thorne. Thermoelastic noise and homogeneous thermal noise in finite sized gravitational-wave test masses. *Phys. Rev. D*, 62:122002, 2000.

[14] Y Levin. Internal thermal noise in the LIGO test masses: A direct approach. *Phys. Rev. D*, 57:659, 1998.

[15] Y Levin. Fluctuation-dissipation theorem for thermo-refractive noise. *Phys. Lett. A*, 372:1941, 2008.

[16] S D Penn et al. Mechanical loss in tantala/silica dielectric mirror coatings. *Class. Quantum Grav.*, 20:2917, 2003.

[17] R Flaminio et al. A study of coating mechanical and optical losses in view of reducing mirror thermal noise in gravitational wave detectors. *Class. Quantum Grav.*, 27:084030, 2010.

[18] G D Cole et al. High-performance near- and mid-infrared crystalline coatings. *Optica*, 3(6):647, 2016.

[19] S Reid et al. Development of mirror coatings for gravitational wave detectors. *Coatings*, 6:61,

2016.

[20] I W Martin et al. Effect of heat treatment on mechanical dissipation in Ta$_2$O$_5$ coatings. *Class. Quantum Grav.*, 27:225020, 2010.

[21] X Liu et al. Hydrogen-free amorphous silicon with no tunneling states. *Phys. Rev. Lett.*, 113:025503, 2014.

[22] T Pérez-Castañeda et al. Suppression of tunneling two-level systems in ultrastable glasses of indomethacin. *PNAS*, 111:11275, 2014.

[23] L Berthier and M D Ediger. Facets of glass physics. *Physics Today*, 69:40, 2016.

[24] W A Phillips. Tunneling states in amorphous solids. *J. Low Temp. Phys.*, 7:351, 1972.

[25] A J Leggett and D C Vural. Tunneling two-level systems model of the low-temperature properties of glasses: are smoking gun tests possible? *J. Phys. Chem. B*, 117:12966, 2013.

[26] I W Martin et al. Comparison of the temperature dependence of the mechanical dissipation in thin films of Ta$_2$O$_5$ and Ta$_2$O$_5$ doped with TiO$_2$. *Class. Quantum Grav.*, 26:155012, 2009.

[27] D R M Crooks et al. Experimental measurements of mechanical dissipation associated with dielectric coatings formed using SiO$_2$, Ta$_2$O$_5$ and Al$_2$O$_3$. *Class. Quantum Grav.*, 23:4953, 2006.

[28] E Cesarini et al. Silica as a key material for advanced gravitational wave detectors. *J. of Non Cryst. Sol.*, 357:2005, 2011.

[29] T Li et al. Measurements of mechanical thermal noise and energy dissipation in optical dielectric coatings. *Phys. Rev. D*, 89:092004, 2014.

[30] M Principe et al. Material loss angles from direct measurements of broadband thermal noise. *Phys. Rev. D*, 91:022005, 2015.

[31] J L Vossen. *Thin Film Processes*. Elsevier, 1978.

[32] G. Cagnoli et al. Mode-dependent mechanical losses in disc resonators. *Phys. Lett. A*, in press, 2017.

[33] S. Penn et al. Frequency and surface dependence of the mechanical loss in fused silica. *Phys. Lett. A*, 352:3, 2006.

[34] G M Carlomagno and G Cardone. Infrared thermography for convective heat transfer measurements. *Exp. Fluids*, 49:1187, 2010.

[35] Polygon physics.

[36] E Çetinörgü et al. Mechanical and thermoelastic characteristics of optical thin films deposited by dual ion beam sputtering. *Appl. Opt.*, 48:4536, 2009.

[37] T. Hong, H. Yang, E. Gustafson, R. Adhikari, and Y. Chen. Brownian thermal noise in multilayer coated mirrors. *Phys. Rev. D*, 87:26, 2012.

[38] M. Abernathy et al. Bulk and shear mechanical loss of titania-doped tantala. *Phys. Lett A*, in press, 2017.

[39] E Cesarini et al. A gentle nodal suspension for measurements of the acoustic attenuation in materials. *Rev. Sci. Instrum.*, 80:053904, 2009.

[40] G Vajente et al. A high throughput instrument to measure mechanical losses in thin film coatings. *Rev. Sci. Instrum.*, 88:073901, 2017.

[41] M. Granata et al. Internal friction and young's modulus measurements on SiO$_2$ and Ta$_2$O$_5$ films done with an ultra-high Q silicon-wafer suspension. *Arch. Metall. Mater.*, 60:365, 2016.

[42] A Cadez et al. Measuring high mechanicai quality factors of bodies made of bare insulating materials. *J. Phys. E: Sci. Instrum.*, 21:453, 1988.

[43] S. R. Elliott. *Physics of amorphous Materials*. Longman, 1983.

[44] C. Joseph, P. Bourson, and M.D. Fontana. Amorphous to crystalline transformation in Ta$_2$O$_5$ studied by raman spectroscopy. *Journal of Raman Spectroscopy*, 43:1146–1150, 2012.

[45] T. Damart et al. Numerical study of the structural and vibrational properties of amorphous Ta$_2$o$_5$ and TiO$_2$-doped Ta$_2$O$_5$. *J. Appl. Phys.*, 119:175106, 2016.

[46] Y Nakagawa, Y Gomi, and Okada T. Deposition of new piezoelectric Ta$_2$O$_5$ thin films and their surface acoustic?wave properties. *J. Applied Phys.*, 61:5012, 1987.

[47] Chen Guoping, Li Lingzhen, Zhang Suixin, and Zhang Haokang. Structures and properties of

a Ta$_2$O$_5$ thin film deposited by dc magnetron reactive sputtering in a pure O$_2$ atmosphere. *Vacuum*, 41(4):1204 – 1206, 1990. Selected proceedings of the 11th international vacuum congress (IVC-11) 7th international conference on solid surfaces (ICSS-7).

[48] H-C Chen, K-S Lee, and C-C Lee. Annealing dependence of residual stress and optical properties of TiO$_2$ thin film deposited by different deposition methods. *Appl. Opt.*, 47(13), May 2008.

[49] S.R. Elliot. Origin of the first sharp diffraction peak in the structure factor of covalent glasses. *Phys. Rev. Lett.*, 67:711, 1991.

[50] G. Lucovsky and J.C. Phillips. Nano-regime length scales extracted from the first sharp diffraction peak in non-crystalline SiO$_2$ and related materials: Device applications. *Nanoscale Res. Lett.*, 5:550, 2010.

[51] R. Bassiri et al. Correlations between the mechanical loss and atomic structure of amorphous TiO$_2$-doped Ta$_2$O$_5$ coatings. *Acta Materialia*, 61:1070, 2013.

[52] L. de Wit, S Roorda, W.C. Sinke, F.W. Saris, A.J.M. Berntsen, and W.F. van der Weg. Structural relaxation of amorphous Si induced by high temperature annealing. *Mater. Res. Soc. Symp. Proc.*, 205:3, 1992.

[53] R. Tsu, J. Gonzalez-Hernandez, and F.H. Pollack. Determination of energy barrier for structural relaxation in a-Si and a-Ge by Raman scattering. *J. Non-Cryst. Solids*, 66:109, 1984.

[54] D. Beeman, R. Tsu, and M.F. Thorpe. Structural information from the Raman spectrum of amorphous silicon. *Physical Review B*, 32:874, 1985.

[55] Huang-Wei Pan et al. Thickness-dependent crystallization on thermal anneal for titania/silica nm-layer composites deposited by ion beam sputter method. *Opt. Expr.*, 22:29847, 2014.

[56] B. Shyam et al. Measurement and modeling of short and medium range order in amorphous Ta$_2$O$_5$ thin films. *Scientific Reports*, 6:32170, 2016.

[57] M. J. Hart et al. Medium range structural order in amorphous tantala spatially resolved with changes to atomic structure by thermal annealing. *J. Non-cryst. solids*, 438:10, 2016.

[58] F. Grigoriev et al. Computational experiments on atomistic modeling of thin-film deposition. *Appl. Optics*, 56:C87, 2017.

High precision detection of change in intermediate range order of amorphous zirconia-doped tantala thin films due to annealing

Kiran Prasai,[1,][*] Jun Jiang,[2] Alec Mishkin,[2] Svetoslava Angelova,[3] Ross Birney,[3] David A Drabold,[4]
Mariana Fazio,[5] Eric Gustafson,[6] Gregory Harry,[7] Sarah Hoback,[7] Carl Lévesque,[8] Ian MacLaren,[9] Iain W Martin,[9]
Carmen S Menoni,[5] Steven Penn,[10] Stuart Reid,[3] Raymond Robie,[9] François Schiettekatte,[8] Rosalie Shink,[8]
Badri Shyam,[11] Gabriele Vajente,[6] Hai-Ping Cheng,[2] Martin M Fejer,[1] Apurva Mehta,[12] and Riccardo Bassiri[1,][†]

[1]*E. L. Ginzton Laboratory, Stanford University, Stanford, California 94305, USA*
[2]*Department of Physics and Quantum Theory Project,*
University of Florida, Gainesville, Florida 32611, USA
[3]*SUPA, Department of Biomedical Engineering, University of Strathclyde, Glasgow G1 1QE, United Kingdom*
[4]*Department of Physics and Astronomy, Ohio University, Athens, Ohio 45701, USA*
[5]*Department of Electrical and Computer Engineering,*
Colorado State University, Fort Collins, Colorado 80523, USA
[6]*LIGO Laboratory, California Institute of Technology, Pasadena, California 91125, USA*
[7]*Department of Physics, American University, Washington, DC 20016, USA*
[8]*Department of Physics, Université de Montréal, Québec H3T 1J4, Canada*
[9]*SUPA, School of Physics and Astronomy, University of Glasgow, Glasgow G12 8QQ, UK*
[10]*Department of Physics, Hobart and William Smith Colleges, Geneva, New York 14456, USA*
[11]*University of Dayton Research Institute, Dayton, Ohio 45469, USA*
[12]*SLAC National Accelerator Laboratory, Menlo Park, California 94025, USA*
(Dated: January 18, 2019)

Intermediate range order (IRO) of amorphous thin films is difficult to measure and unambiguously interpret. Through x-ray scattering measurements on thin films of amorphous zirconia-doped-tantala (ZrO_2-Ta_2O_5), we present high precision detection of the change in the IRO as a function of post-deposition heat treatment (annealing). We present an integrated atomic modeling approach and show for the first time that the annealing-induced changes seen in measured pair distribution function (PDF) can be captured in atomic models with high accuracy. Structural analysis shows that the material has building blocks of metal-centred polyhedra and the effect of annealing is to alter the way the polyhedra connect with each other. We explain the observed changes in IRO in terms of a shift in the ratio of corner-sharing to edge-sharing polyhedra as a function of annealing. We compute the degree of orientational order in metal-metal correlations and speculate on the correlations between the observed changes in the IRO and measured mechanical loss of thin films.

A scientific and technological grand challenge lies in the ability to understand the atomic structure properties that govern the performance of functional amorphous materials, and enabling the accelerated discovery and development of improved materials. Amorphous thin film coatings, in particular, are technologically important materials that often limit the performance of a variety of precision measurements. For example, Brownian thermal noise, due to mechanical loss, is a significant impairment in thin film coatings used in atomic clocks [1] and interferometric gravitational-wave detectors [2], such as the Laser Interferometer Gravitational-wave Observatory (LIGO), Virgo and KAGRA. The research presented here is driven by the critical importance in developing thin-film coatings with lower mechanical losses, and hence lower Brownian thermal noise, to the performance of future generations of interferometric gravitational-wave detectors [3].

In general, the atomic structure of amorphous materials can be described in terms of short- and intermediate-range order (SRO and IRO, respectively); the long-range order (LRO), characteristic of crystals, is unambiguously absent [4, 5]. SRO generally describes the structural

order up to the first coordination sphere measured as the first peak in the pair distribution function (PDF), which often resembles the amorphous material's crystalline counterpart. Despite the general agreement on the concept, the definition of distance boundaries in SRO can vary in the literature [6]. In this letter, we study zirconia-doped tantala and use the SRO to describe the order up to ~ 2.9 Å, which is where the first coordination polyhedra of the material end. The IRO describes the structural organization that is *intermediate* between the discrete chemical bonds described in the SRO and the periodic lattice described in the LRO, and is the highest level of structural organization in amorphous materials. However, the IRO is less well understood than the SRO, and is more dependent on the details of how the material was synthesized or deposited.

Post-deposition annealing of amorphous thin films has been shown induce changes in both the atomic structure and mechanical loss [7, 8]. The structural changes associated with post-deposition annealing are often observed beyond the first coordination sphere, and lie in the IRO [9]. Even with tools that are best suited to probe the IRO, such as fluctuation electron microscopy (FEM) and

x-ray or neutron PDFs, the observed structural changes can be small and difficult to interpret. Accurate atomic modeling is required to capture the small changes in the atomic structure, and probe the IRO in detail.

In this paper, we demonstrate high precision atomic structure measurements and modeling of amorphous zirconia-doped tantala thin films that show small, but systematic, changes in IRO as a function of post-deposition annealing. We use grazing-incidence PDF (GIPDF) measurements and unprecedentedly sensitive atomic structure modeling that captures the local order changes accurately up to 15 Å. Finally, we discuss the implications of this increased understanding of the atomic structure and its relation to our efforts to reduce mechanical loss.

GIPDF data was collected from thin films of zirconia-doped tantala deposited by MLD Technologies (Mountain View, CA), were deposited by ion-beam sputtering with a $Zr/(Zr+Ta) \simeq 0.48$, ~ 590 nm in thickness (see [10]) on fused silica substrates. The target materials were pure metals in a partially pressurized oxygen environment, and the ambient temperature during deposition was less than 100°C. Post-deposition annealing of three different samples was carried out at 300, 600 and 800°C in air for 12 hours. GIPDF data was collected at the dedicated X-ray scattering beamline 10-2 at the Stanford Synchrotron Radiation Lightsource (SSRL), with q-range of 21 Å^{-1}. This unique GIPDF capability allows us to overcome a significant difficulty in measuring PDFs from thin films: a grazing incidence angle can be chosen that will enable the collection of X-rays scattered from the coatings and not the substrate. In addition, there is no destructive sample preparation, ensuring that the observed changes in the measured atomic structure do not result from the sample preparation process, which is especially relevant when looking at small structural changes due to annealing. Further details on the GIPDF data collection method are discussed in Refs [11–13]. The total scattering data was reduced to the normalized structure factor after applying corrections for air scattering, absorption, Compton scattering, polarization effects and geometric effects due to the detector footprint [13, 14].

The measured PDFs for one as-deposited and the three annealed samples are plotted in figure 1. At a first glance, all PDFs appear largely similar; all show a sharp first peak at 2.0(2) Å, a bifurcated second peak between 2.9(0) and 4.3(0) Å, and a series of smaller peaks between 5 Å and 15 Å. A closer look reveals a number of changes among the PDFs; the major changes, for example marked by letters a to f in figure 1, lie in the IRO. These include an increase in intensity of the peaks, appearance of new peaks, shifts in the position of the peaks and a deepening of the troughs. In most cases, the change is *systematic* with respect to the annealing temperature, an example is highlighted in the inset.

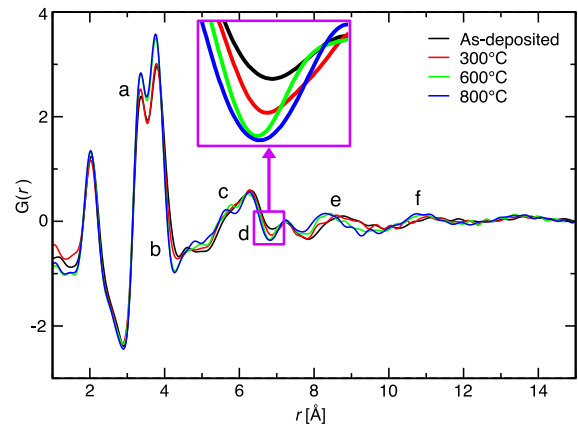In order to better understand the annealing-induced

FIG. 1. **Detection of annealing induced changes:** Measured pair distribution functions (PDFs) of four thin films of zirconia-doped tantala are shown. The thin films differed only in annealing history: as-deposited, 300, 400, 600 and 800°C. The differences among the PDFs are the result of annealing-induced change to the atomic structure. The letters represent sections of PDF where the most significant changes are observed: (a), (b) and (d) change in intensity, (c) new peaks appearing, (e) and (f) shift in peak positions. Section (d) is magnified in the inset to highlight the systematic change as a function of annealing temperature.

atomic level processes that cause the changes seen in the PDFs, it is essential to develop atomic models that are sensitive enough to capture the observed changes in PDFs. A common method of choice is to follow a regression algorithm that fits atomic coordinates with the measured PDFs, e.g. simulated annealing [15] or reverse Monte Carlo (RMC) [16] etc. However, the changes caused by annealing are subtle even for the two extreme ends of annealing (viz as-deposited and 800°C annealed) and hence one faces an interesting problem and requirement: how to reliably generate two slightly different structural solutions of an otherwise identical disordered system? Conventional modeling techniques often fail to resolve subtle changes in atomic structure with high fidelity, especially in the IRO, which makes it difficult to give definitive statements about the changes in structure.

We follow an integrated modeling approach that seeks to maximally constrain the solution space by using all *a priori* information. In this work, the set of *a priori* information consisted of density-functional-theory-based atomic models, a classical two-body force field, density and composition measurements on thin films, and the X-ray GIPDF measurements. These data are used to guide an RMC-based high-throughput modeling routine. In order to have the correct atomic ratio and supercell size in our models, we measured the composition and density in our samples using Rutherford Back-scattering Spectrometry (RBS) and used the results to constrain the composition and density of the models (see [10]). The measured PDFs show some structure up to a distance of ~ 15 Å and
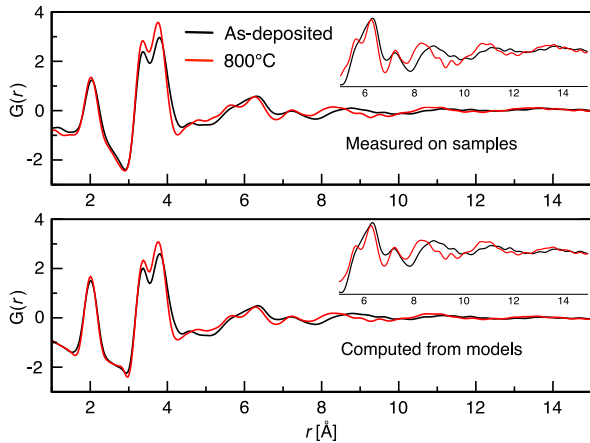
FIG. 2. **Measured and computed PDFs:** The measured
PDFs from two samples (top) are compared with PDFs com-
puted from atomic models (bottom). The PDFs are grouped
to highlight that the atomic models are able to closely track
the annealing-induced changes in PDFs. Computed PDFs in
the bottom plot are averages of over 1000 independent mod-
els. The 5 Å to 15 Å section of PDFs in each plot are shown
in higher resolution in insets. See [10] for plot involving all
four samples.

accordingly the supercell size of the model is chosen to be
able to compute $G(r)$ up to 15 Å. Using the composition
and density from the RBS measurements, we generated
starting configurations of zirconia-doped tantala by em-
ploying melt-quench molecular dynamics (MD) simula-
tions where we used two-body empirical potentials from
[18, 19]. These configurations are then modified using
RMC until the computed PDF matches with the GIPDF
data. However, it is well known that a traditional RMC
produces non-physical solutions, even in elemental sys-
tems [20]. We used *ab initio* molecular dynamics (AIMD)
to generate smaller models (190 atoms) of the same sys-
tem, and the distribution of bond-lengths present in the
AIMD models was used as a constraint to RMC. This was
done by requiring that the metal-oxygen bond distances
lie in the range predicted by the partial PDFs of AIMD
models (see [10]). Furthermore, following the "FEAR"
method [21], RMC moves were interspersed with energy
minimization moves iteratively until the desired agree-
ment with experiments was obtained. The entire mod-
eling algorithm was repeated to get 1000 independent
atomic models corresponding to each of the four samples
i.e. as-deposited, 300°C annealed, 600°C annealed and
800°C annealed. All the properties reported hereafter
are computed by averaging over 1000 models. Figure 2
shows the ability of the models to capture the changes on
measured PDF up to 15 Å; to the best of our knowledge,
it is the first demonstration that atomic models can cap-
ture changes in IRO up to 15 Å with such a high accuracy.
It should be emphasized here that the models reported
in this work are chemically realistic i.e. they contain no

non-physical metal-metal chemical bonds. The models,
by construction, have density and composition that are
representative of the IBS coatings. In the following, we
show that the deductions made from the models agree
with experiments and the structural features computed
from the models show a systematic trend with anneal-
ing temperature. A plot showing the fit of the structure
factor $S(q)$ and $G(r)$ along with additional information
on the modeling method is given in the supplementary
material [10].

In the following, we present a discussion of the struc-
ture of a-Ta_2O_5:ZrO_2 based on the models we obtained.
As in many glass-forming materials like silica, the struc-
ture of a-Ta_2O_5:ZrO_2 can be described as a 3-dimensional
network of metal (M)-centred coordination polyhedra
that have oxygen (O) atoms at their corners. The M-O
correlation gives rise to the first peak. The polyhedra are
predominantly distorted octahedra ($\sim$80% for Ta, $\sim$60%
for Zr, [10]). It has been shown that the first peak of $G(r)$
for pure a-Ta_2O_5 closely resembles to the corresponding
peak of crystalline Ta_2O_5 [13]. We find that the coordi-
nation of Ta by O (n_{TaO}) is 6.13 whereas n_{ZrO} is 6.14;
both values are for un-annealed sample. The measured
value of n_{TaO} using ^{17}O NMR studies on IBS deposited
pure a-Ta_2O_5 is 6.1(3) [22, 23]. The M-O bond distance
peaks at 2.0(2) Å and it is comprised of a Ta-O sub-
peak at 1.98 Å and and a Zr-O sub-peak at 2.06 Å. The
slight difference in Ta-O and Zr-O bond distances is also
consistent with *ab initio* models; it is likely that this dif-
ference is helpful in frustrating the crystallization of tan-
tala [24]. As a result of annealing, coordination of M by
O (n_{MO}) shows a small but consistent trend to smaller
values, and a corresponding change, although small, in
the M-O bond distance towards a lower value is observed
in the total $G(r)$ (see figure 10 in [10]). The structure
within the first coordination sphere of tantala has been
extensively characterized [7, 13, 25, 26].

The polyhedra link with each other through O-atoms
at each corner. Each O-atom is at least 2-coordinated
with metal atoms. The ratio of 2-coordinated to 3-
coordinated O-atoms is $\sim$ 1:2, which is notably differ-
ent from pure tantala where the value measured using
NMR is 2:3 [22, 23]. The difference comes from O-
atoms bonding preferentially 3-fold with Zr; the mean
O-coordination by M is 2.7 (see inset of figure 3(e)).
The correlation between two metal atoms connected by
at least one O-atom gives rise to the second peak in to-
tal $G(r)$. It is interesting to note the bifurcation in the
M-M peak into two sub-peaks at 3.35 Å and 3.75 Å since
similar measurements in pure tantala show the first sub-
peak at 3.35 Å at much reduced intensity [13, 25]. Its
much more pronounced presence in the mixed phase is
an effect of doping by zirconia and has structural impli-
cations in that the first and second peaks originate from
correlations of edge-sharing (ES) and corner-sharing (CS)
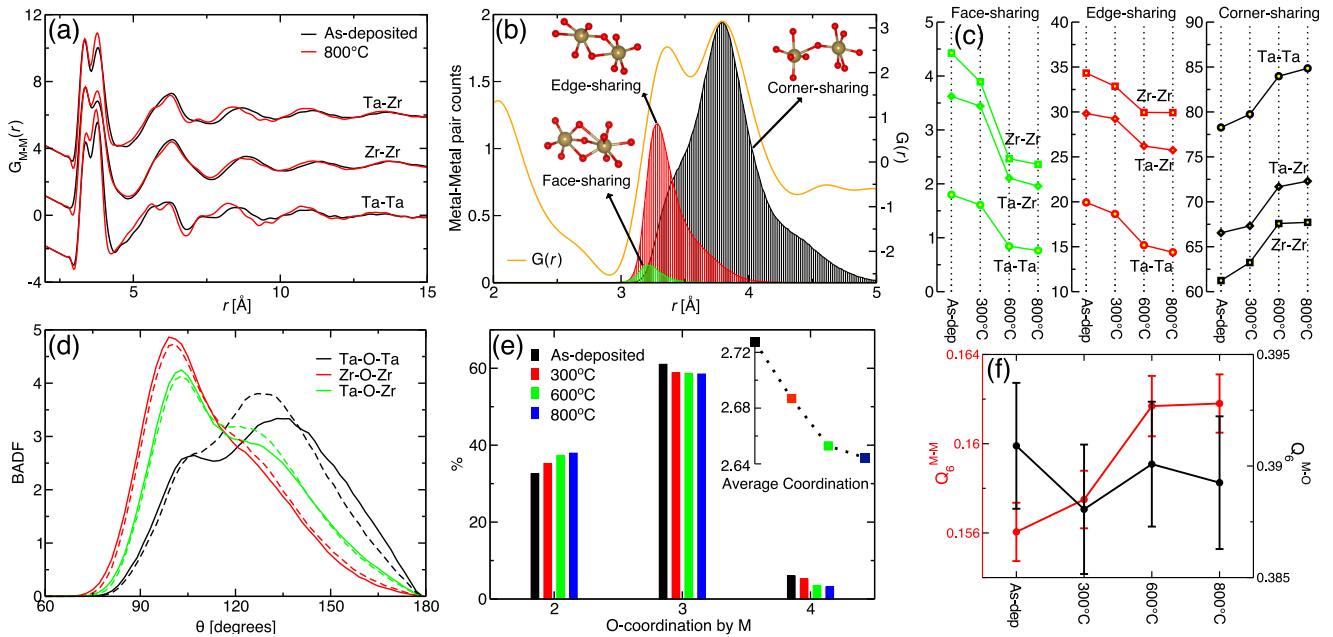polyhedra respectively (figure 3(b)). For the as-deposited

FIG. 3. **Structural fingerprints of annealing:** Plots of major structural trends in the models. All results are averages over 1000 models. When it applies, an M-O bond cutoff distance of 2.9 Å is used. This distance is the minimum directly after the first peak in total G(r). (a) Partial PDFs for M-M pairs are plotted. (b) Origin of the double hump in G(r) as correlations between corner and edge shared M-M pairs. The orange line represents total G(r). The shaded regions represent the distribution of M-M pair distances separated on the basis of the number of O-atoms they share. A shared O-atom is the one that lies within the bond cutoff distance from both M-atoms. (c) The evolution percentages of corner-, edge-, and face- shared M-M pairs with annealing. (d) BADF from the as deposited (the dashed lines) and 800°C annealed models (e) Distribution of O-coordination by M for samples with different annealing history. Inset shows the averaged coordination vs annealing temperature. (f) BOO parameters (Q$_6$) [17] as a function of annealing temperature. The black and red dots show the Q$_6$ for M-O and M-M correlations. The error bars are standard deviations. The dots are connected to guide the eyes.

sample, the ratio of CS to ES correlations is 3.93 for Ta-Ta, 2.23 for Ta-Zr, and 1.78 for Zr-Zr. There is also a small concentration of face-sharing (FS) polyhedra where the polyhedra share 3 O-atoms between them.

The effect of annealing is much more pronounced beyond the first M-O peak and all the way to 15 Å. Many of the changes observed in the total G(r) can be explained by considering the partial M-M correlation (figure 3(a)), where changes are observed from ∼3 Å all the way up to 15 Å. First of all, the peaks become narrower and sharper suggesting that annealing increases the order in M-M correlation lengths. Since the bifurcated M-M peak represents the correlations between the polyhedra, the annealing induced change in the peak signifies that annealing alters the mode by which polyhedra connect with each other. An analysis presented in figure 3(c) shows that the concentration of CS polyhedra increases as a result of annealing whereas it decreases for ES and FS polyhedra. The effect of the overall decrease of density of ES and FS polyhedra is that the average O-coordination by M decreases as a function of annealing temperature (see figure 3(e)). A decrease in O-coordination upon annealing was also observed for pure tantala using ^{17}O NMR studies in [23]. An analysis of the M-O-M bond angle dis-

tribution function (BADF) shows that BADF, in general, narrows and shows a more defined peak upon annealing 3(d). However, there is a more characteristic change in BADF that is worth noting: each M-O-M BADF curve shows a double peak and the peak around 120° to 130° increases with annealing. Further analysis shows that the characteristic two-peak BADF arises from the presence of ES and CS polyhedra; the increase in M-O-M BADF around 120° to 130° is caused by increase in the ratio of CS to ES polyhedra (see figure 9 in [10]).

We use the bond orientational order (BOO) parameter Q$_6$ [17] to quantify the degree of disorder present in the models. The BOO parameter corresponding to M-O bonds, denoted by Q$_6^{\text{M-O}}$ in figure 3(f), shows that there is no significant effect of annealing in the M-O coordination sphere. We also probed the degree of order among the polyhedral units by computing Q$_6^{\text{M-M}}$ among the metal atoms and the values suggest an increase in BOO with annealing, a trend clearly seen in the measured G(r). To the extent Q$_6^{\text{M-M}}$ is a measure of IRO among the polyhedral units, it is noteworthy to observe an inverse correlation of Q$_6^{\text{M-M}}$ with measured values of mechanical loss at room temperature (see figure 1 in [10]). Future modeling experiments are planned to directly compute the

mechanical loss on these structures [27], which will help elucidate the role of IRO in mechanical loss.

The experimental observations, atomistic models, and resulting atomic structure analysis suggest the following consequences of annealing:

1. There is evidence of subtle change in first co-ordination sphere around M-atoms in that M-coordination by O decreases upon annealing and M-O bond distance trends to a smaller value.

2. The major effect of annealing is found to be the change in the way the polyhedral units organize themselves in the film. The ratio of edge-sharing to corner-sharing M-M polyhedra decreases upon annealing and, as a corollary, the average O-coordination by M decreases.

3. There is a hint of an increased order in M-M correlation as indicated by narrowing and sharpening of M-M peaks in partial PDFs and increase in the computed values of $Q_6^{\text{M-M}}$.

It is observed experimentally that as a result of annealing tantala-based coatings the mechanical loss at room temperature decreases [8, 10, 28, 29]. The dissipation mechanism for mechanical loss is often conceptualized as two-level systems (TLSs) which are asymmetric double-wells separated by an energy barrier. TLSs arise from subtle rearrangements of clusters of atoms [27, 30]. The observed trends in mechanical loss with annealing suggests that ES-polyhedra are more likely associated with TLSs that contribute to room temperature mechanical loss, whereas the CS-polyhedra that form lower barrier height TLSs contribute to low temperature mechanical loss. This conjecture is bolstered by the observation that silica, which has nearly 100% CS polyhedra has low loss in room temperature and high loss at low temperature [31]. If this conjecture is correct, then in order to reduce mechanical loss at room temperature one would aim to have a material that produces less ES-polyhedra and more CS-polyhedra. Conversely, a material with less CS-polyhedra and more ES-polyhedra would likely reduce mechanical loss at low temperature. As doping with zirconia helps suppress the crystallization but increases the ratio of ES-polyhedra, the doping percentage of zirconia is a key variable to optimize in order to reduce mechanical loss at room temperature. In particular, a lower concentration of zirconia that is just enough to suppress the crystallization would be desirable. Indeed, in a study by Tewg et al. [24], lower zirconia doping concentrations in tantala were observed to suppress crystallization, with a highest crystallization temperature measured from a sample with $\text{Zr}/(\text{Zr+Ta}) \simeq 0.33$. Investigations are currently underway for thin films with varying levels of zirconia doping concentrations.

In conclusion, we have presented a detailed study on the effect of annealing on zirconia-doped tantala amorphous thin films using a combination of experimental data and modeling routines. Upon annealing, there are subtle changes observed in the SRO, but the most significant change is the increase in IRO. The GIPDF measurement method and the modeling scheme employed in this work represent a significant step forward for the detailed study of the atomic structure of amorphous thin films, providing a powerful tool capable of accurately capturing subtle changes in the atomic structure up to 15 Å. Important to the particular usage case of reducing thermal noise in interferometric gravitational-wave detectors, caused by mechanical loss in the mirror coatings, our analysis and interpretation suggests that, compared to the $\text{Zr}/(\text{Zr+Ta}) \simeq 0.48$ measured here, lowering the zirconia doping concentration merits further study and is the subject of ongoing research.

* prasai@stanford.edu
† rbassiri@stanford.edu

[1] N. Hinkley, J. Sherman, N. Phillips, M. Schioppo, N. Lemke, K. Beloy, M. Pizzocaro, C. W. Oates, and A. Ludlow, Science **341**, 1215 (2013).
[2] G. M. Harry, H. Armandula, E. Black, D. Crooks, G. Cagnoli, J. Hough, P. Murray, S. Reid, S. Rowan, P. Sneddon, et al., Applied optics **45**, 1569 (2006).
[3] S. Hild, Classical and Quantum Gravity **29**, 124006 (2012).
[4] S. R. Elliott, Longman Group, Longman House, Burnt Mill, Harlow, Essex CM 20 2 JE, England, 1983. (1983).
[5] S. R. Elliott, Nature **354**, 445 (1991).
[6] L. Červinka, Journal of Non-Crystalline Solids **106**, 291 (1988).
[7] R. Bassiri, K. Borisenko, D. Cockayne, J. Hough, I. MacLaren, and S. Rowan, Applied Physics Letters **98**, 031904 (2011).
[8] I. W. Martin, R. Bassiri, R. Nawrodt, M. Fejer, A. Gretarsson, E. Gustafson, G. Harry, J. Hough, I. MacLaren, S. Penn, et al., Classical and Quantum Gravity **27**,

225020 (2010).

[9] M. J. Hart, R. Bassiri, K. B. Borisenko, M. Véron, E. F. Rauch, I. W. Martin, S. Rowan, M. M. Fejer, and I. MacLaren, Journal of Non-Crystalline Solids **438**, 10 (2016).

[10] See supplementary information for additional information on the simulation method and further numerical results.

[11] P. Fuoss and A. Fischer-Colbrie, Physical Review B **38**, 1875 (1988).

[12] A. Fischer-Colbrie, A. Bienenstock, P. Fuoss, and M. A. Marcus, Physical Review B **38**, 12388 (1988).

[13] B. Shyam, K. H. Stone, R. Bassiri, M. M. Fejer, M. F. Toney, and A. Mehta, Scientific Reports **6**, 32170 (2016).

[14] X. Qiu, J. W. Thompson, and S. J. Billinge, Journal of Applied Crystallography **37**, 678 (2004).

[15] S. Kirkpatrick, C. D. Gelatt, and M. P. Vecchi, Science **220**, 671 (1983).

[16] D. Keen and R. McGreevy, Nature **344**, 423 (1990).

[17] P. J. Steinhardt, D. R. Nelson, and M. Ronchetti, Physical Review B **28**, 784 (1983).

[18] J. Trinastic, R. Hamdan, Y. Wu, L. Zhang, and H.-P. Cheng, The Journal of Chemical Physics **139**, 154506 (2013).

[19] J. Yu, R. Devanathan, and W. J. Weber, Journal of Materials Chemistry **19**, 3923 (2009).

[20] D. Drabold, The European Physical Journal B **68**, 1 (2009).

[21] A. Pandey, P. Biswas, and D. A. Drabold, Scientific Reports **6**, 33731 (2016).

[22] N. Kim and J. F. Stebbins, Chemistry of Materials **23**, 3460 (2011).

[23] N. Kim and J. F. Stebbins, Journal of Non-Crystalline Solids **378**, 158 (2013).

[24] J.-Y. Tewg, Y. Kuo, and J. Lu, Electrochemical and Solid-state Letters **8**, G27 (2005).

[25] O. L. Alderman, C. Benmore, J. Neuefeind, E. Coillet, A. Mermet, V. Martinez, A. Tamalonis, and R. Weber, Physical Review Materials **2**, 043602 (2018).

[26] R. Bassiri, F. Liou, M. R. Abernathy, A. C. Lin, N. Kim, A. Mehta, B. Shyam, R. L. Byer, E. K. Gustafson, M. Hart, *et al.*, APL Materials **3**, 036103 (2015).

[27] J. P. Trinastic, R. Hamdan, C. Billman, and H.-P. Cheng, Physical Review B **93**, 014105 (2016).

[28] G. Vajente, R. Birney, A. Ananyeva, S. Angelova, R. Asselin, B. Baloukas, R. Bassiri, G. Billingsley, M. Fejer, D. Gibson, *et al.*, Classical and Quantum Gravity **35**, 075001 (2018).

[29] G. M. Harry, M. R. Abernathy, A. E. Becerra-Toledo, H. Armandula, E. Black, K. Dooley, M. Eichenfield, C. Nwabugwu, A. Villar, D. Crooks, *et al.*, Classical and Quantum Gravity **24**, 405 (2006).

[30] P. Fedders and D. Drabold, Physical Review B **53**, 3841 (1996).

[31] K. Topp and D. G. Cahill, Zeitschrift für Physik B Condensed Matter **101**, 235 (1996).

Supplementary information: High precision detection of change in intermediate range order of amorphous zirconia-doped tantala thin films due to annealing

Kiran Prasai,[1, *] Jun Jiang,[2] Alec Mishkin,[2] Svetoslava Angelova,[3] Ross Birney,[3] David A Drabold,[4] Mariana Fazio,[5] Eric Gustafson,[6] Gregory Harry,[7] Sarah Hoback,[7] Carl Lévesque,[8] Ian MacLaren,[9] Iain W Martin,[9] Carmen S Menoni,[5] Steven Penn,[10] Stuart Reid,[3] Raymond Robie,[9] François Schiettekatte,[8] Rosalie Shink,[8] Badri Shyam,[11] Gabriele Vajente,[6] Hai-Ping Cheng,[2] Martin M Fejer,[1] Apurva Mehta,[12] and Riccardo Bassiri[1, †]

[1]E. L. Ginzton Laboratory, Stanford University, Stanford, California 94305, USA
[2]Department of Physics and Quantum Theory Project,
University of Florida, Gainesville, Florida 32611, USA
[3]SUPA, Department of Biomedical Engineering, University of Strathclyde, Glasgow G1 1QE, United Kingdom
[4]Department of Physics and Astronomy, Ohio University, Athens, Ohio 45701, USA
[5]Department of Electrical and Computer Engineering,
Colorado State University, Fort Collins, Colorado 80523, USA
[6]LIGO Laboratory, California Institute of Technology, Pasadena, California 91125, USA
[7]Department of Physics, American University, Washington, DC 20016, USA
[8]Department of Physics, Université de Montréal, Québec H3T 1J4, Canada
[9]SUPA, School of Physics and Astronomy, University of Glasgow, Glasgow G12 8QQ, UK
[10]Department of Physics, Hobart and William Smith Colleges, Geneva, New York 14456, USA
[11]University of Dayton Research Institute, Dayton, Ohio 45469, USA
[12]SLAC National Accelerator Laboratory, Menlo Park, California 94025, USA
(Dated: January 18, 2019)

S1. Motivations for studying zirconia-doped tantala

The work presented in this letter is a part of research directed at identifying low Brownian thermal noise optical coatings for the test masses of the LIGO gravitational wave detectors. The current generation of the LIGO detectors use highly reflective dielectric coatings for its coreoptics, which consist of alternating layers of amorphous silica and titania-doped-tantala. At the most sensitive frequency range ($\sim 40\text{-}200$ Hz), these coatings give rise to a limit in the detector sensitivity due to Brownian thermal noise. The dominant source of Brownian thermal noise arises from the mechanical loss in the high-refractive index titania-doped-tantala layers, with a mechanical loss of $\sim 2 \times 10^{-4}$. For the Advanced LIGO + upgrade, planned to start commissioning in 2021, a coating with at least a factor of two improvement in mechanical loss is required (mechanical loss $\leq 1 \times 10^{-4}$).

The current coatings for LIGO optics are deposited using ion-beam sputtering (IBS). One of the ways of reducing the thermal noise at room temperature of thin film coatings is post-deposition annealing. It has been shown that post-deposition annealing of tantala up to the temperatures of 600°C, prior to the onset of crystallization, reduces the room temperature mechanical loss of the coatings [1]. Doping amorphous tantala with zirconia at a ratio of $Zr/(Ta+Zr) = 0.33$ can suppress crystallization, allowing the films to remain amorphous after annealing up to 800°C [2].

The mechanical loss was measured at room temperature as a function of post-deposition annealing temperature from similar coatings used for GIPDF analysis of zirconia-doped tantala ($Zr/(Ta+Zr) \simeq 0.48$) coat-

ings. The results shown in figure 1 indicate that, as with pure tantala, the mechanical loss of zirconia-doped tantala decreases with increasing post-deposition annealing temperature. As indicated in figure 1, the annealing time is extended for temperatures at 600°C and above, but appears to have little effect at 600°C compared to the annealing temperature. Interestingly, the 800°C annealed sample has a loss of 1.8×10^{-4}, which is slightly below the currently employed titania-doped tantala coatings, and demonstrates that zirconia-doped tantala is a promising coating material system that warrants further study as a potential Advanced LIGO + coating.
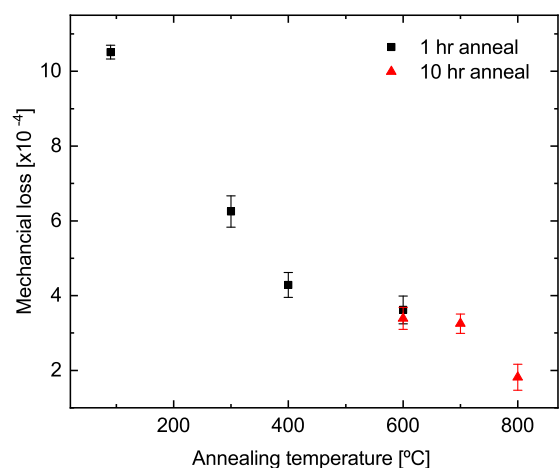

FIG. 1. Mechanical loss at room temperature for zirconia doped tantala as a function of annealing temperature. For details of the measurement process see Refs. [3].

S2. Density and composition of samples

We measured the composition, density and thickness of two of the four samples used in GIPDF measurements. Those two samples are as-deposited and 800°C annealed. The composition was determined using Rutherford Backscattering Spectrometry (RBS) [4] analysis where the samples were exposed to a beam of α particles at an energy of 2.9 MeV at normal incidence and the back-scattered particles were detected at 170°. Atomic concentrations were determined by fitting a simulated spectra to the measured spectra. The best fit was obtained at the concentrations given in table I.

TABLE I. **Composition measurements using RBS**

| Element | Atomic Concentration (%) | |
	As deposited	800°C annealed
Ta	16.00±0.15	15.50±0.15
Zr	14.8±0.3	14.8±0.3
O	66.4±1.5	67.0±1.5
Ar	2.8±0.4	2.7±0.4

Areal densities of the samples were also obtained from RBS to be $4370\pm90 \times 10^{15}$ atoms/cm^2 for both as-deposited and 800°C annealed samples. The thicknesses of the samples were measured, using combinations of stylus profilometry and ellipsometry [5, 6] measurements, to be 589±4 nm and 587±10 nm for as-deposited and 800°C annealed samples respectively. Thickness measurements, combined with areal density and composition measurements from RBS, enabled us to calculate mass densities of the samples to be 6.53±0.15 gm/cm^3 for as-deposited sample and 6.53±0.18 gm/cm^3 for 800°C sample.

Following these measurements, we used a stoichiometric ratio of 15:67.5:15 for Ta, O and Zr respectively for all our models. We have not included Ar atoms in our models because the x-ray scattering signature of ∼2.5% Ar is low (see figure 2) and because our separate DFT based calculations (not shown here) indicate that Ar atoms have a negligible effect on the structure of the material itself. We used a density of 6.53 gm/cm^3 for our models, but we did take into account a mass of 2.5% Ar to obtain the effective box-size for our models. After considering the mass of Ar atoms, the effective density in our models is 6.41 gm/cm^3. The size of our models is chosen to enable computation of G(r) up to 15 Å which is the distance up to which measured GIPDF shows some degree of IRO. With all of these considerations in place, our final models have 400 Ta, 1800 O and 400 Zr in a cubic box of dimension 32.92 Å.
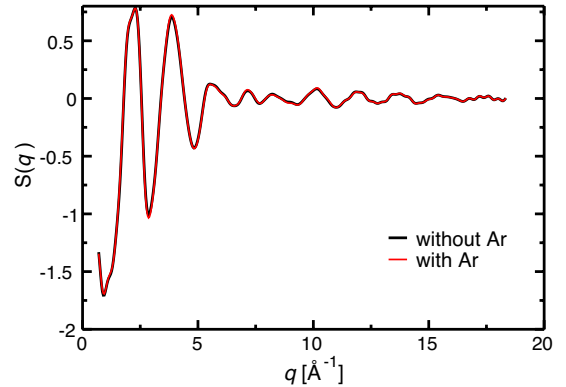
FIG. 2. The x-ray structure factors, S(q), computed from the models. The red curve is from a model which has Ta, O, Zr and Ar atoms in the ratio 15:67.5:15:2.5. The black curve represents when the Ar atoms were removed from the model.

S3. Integrated modeling approach

The modeling scheme that is used to obtain the atomic models presented in this work is further illustrated here. The flowchart in figure 3(a) shows the sequence of steps followed to obtain the final models. The modeling algorithm starts by considering 1000 independent systems where each system has 2600 randomly positioned atoms in a cubic supercell; a threshold distance of 1.9 Å between is maintained between the atoms even for random positions. The atomic ratio and density are chosen as discussed in section S2 and are kept fixed. These models are taken through a conventional melt-quench MD modeling cycle (as discussed in section S5). The final configurations from MD serve as the starting configuration for the RMC models. RMC moves are set to fit to the measured S(q) and are constrained by enforcing a distance window of 1.5 Å to 2.9 Å for Ta-O bond distance and of 1.5 Å to 3.2 Å for Zr-O bond distance. M-M lower cutoff of 2.9 Å and O-O lower cutoff of 2.0 Å were also used to constrain the RMC moves. These distances correspond to the lower and upper cutoff of the corresponding partial PDFs of AIMD-based models (see discussion in section S4 and figure 5). RMC moves and energy minimization moves are iterated back and forth until a convergence in chi-squared (degree of misfit) and a convergence in the total energy are reached. This iterative approach was first proposed as force enhanced atomic relaxation (FEAR) in [7, 8]. The final models from this process are considered as representative of the samples on which the GIPDF measurements were made. To get a better statistical accuracy, we repeat the process for 1000 independent models and take an average for all quantities reported in the paper. The plot of the fitted structure factor (S(q)) and the corresponding plot in real space is presented in figure 3(b) and (c).
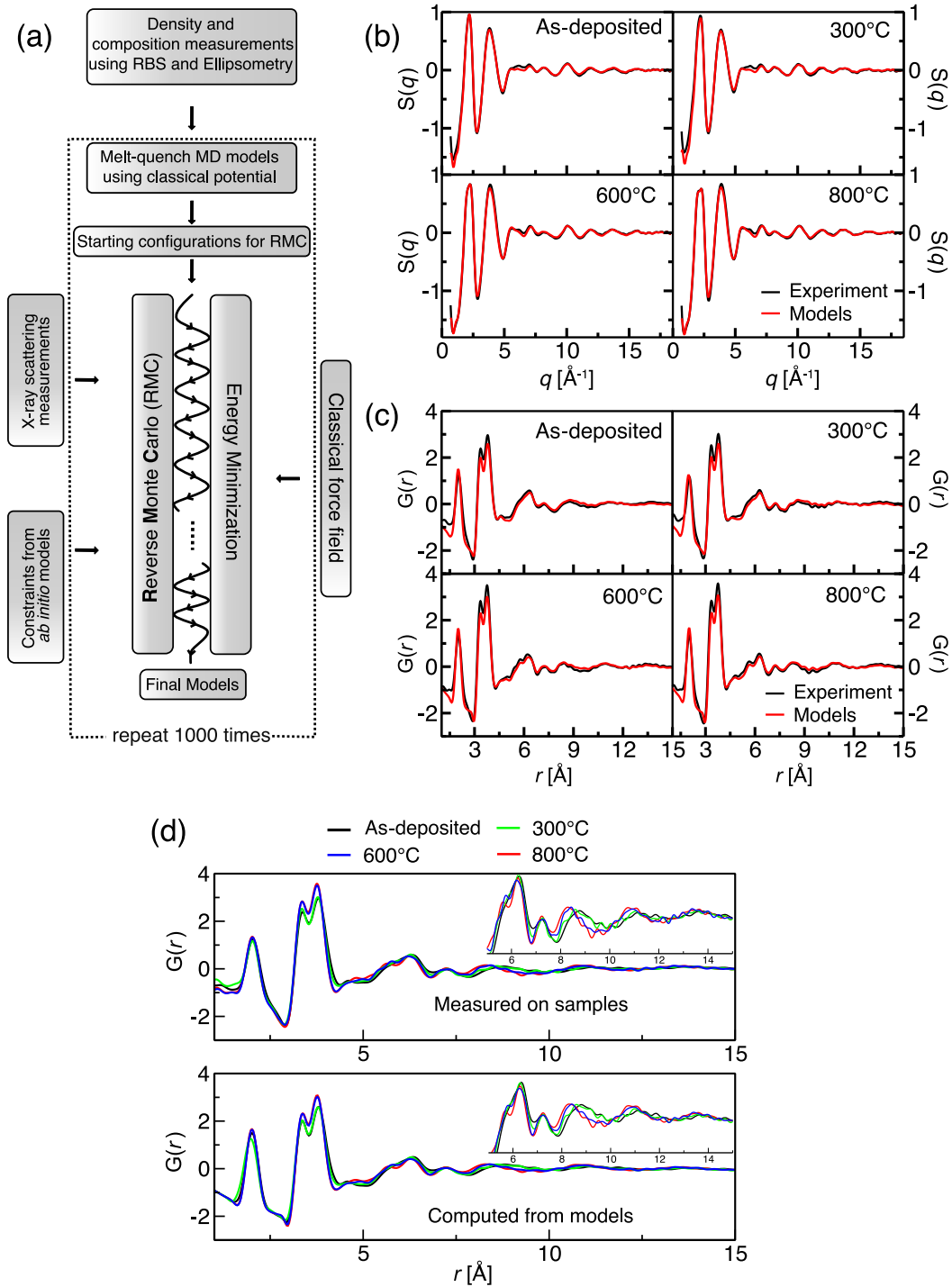
FIG. 3. **More on the modeling approach and results** (a) The integrated modeling approach: Illustration of how *ab initio* MD, classical MD, RMC based on measure GIPDF data and density and composition measurements of thin films are combined together to obtain models that are realistic and sensitive to annealing induced changes in the structure. (b) Goodness of fit: The structure factor, S(q), measured on samples is compared the corresponding fitted models. The computed S(q) are averages over 1000 models. (c) The computed G(r) on models are compared with G(r) obtained from GIPDF measurements. The computed G(r) are averages over 1000 models. (d) The ability of the computed models to track the changes in IRO seen in the measured G(r) at different annealing temperature. This figure is the complete version of figure 2 in main paper.

S4. Melt-quench models using *ab initio* molecular dynamics (AIMD)
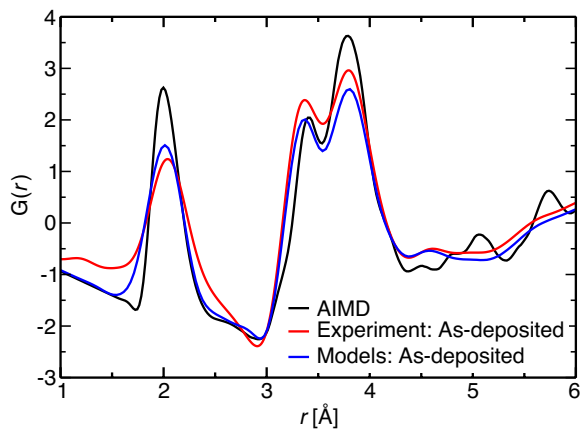
FIG. 4. The total G(r) of AIMD models is compared with measured G(r) and the computed G(r) from RMC based models.
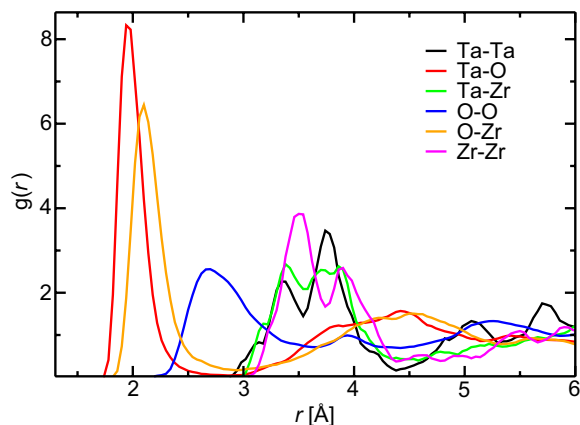
FIG. 5. The partial G(r) computed on AIMD models. Note that the definition of G(r) used in this plot is different the definition of G(r) used in the paper. In this case, $g_{\alpha\beta} = \frac{V}{4\pi r^2 N_\alpha} \frac{dn_{\alpha\beta}}{dr}$, where V is volume of supercell, N_α is number of species α, and $dn_{\alpha\beta}$ is the number of β atoms at distance r to $r+dr$ from α atom. This definition of G(r) is useful to help infer the cutoffs for atomic correlations. Additionally, the area under the partial G(r) give the corresponding coordinations as a function of r.

We performed *ab initio* molecular dynamics (AIMD) to obtain smaller atomic models of zirconia-doped tantala. The purpose of this exercise was to provide geometrical constraints to bond distances during RMC modeling and also to enable basic sanity checks on our main models. 30 Ta atoms, 30 Zr atoms and 135 O atoms are taken in a cubic supercell of dimensions 13.78 Å and periodic boundary conditions were applied. This is equivalent to a bulk mass density of 6.55 gm/cm^3. In order to create the starting configuration for AIMD, the system is first

taken through a melt-quench molecular dynamics cycle employing an empirical force field [9, 10] over a total time period of 1.15 ns. LAMMPS simulation software was used [11]. The starting configuration obtained is then taken through an AIMD melt-quench cycle using Vienna *ab initio* software package (VASP) [12, 13]. PBE functionals were used [14, 15] and valence electrons were treated using plane waves of upto 400 eV. The system was equilibrated at 4000 K, then at 2500 K, then quenched to 300 K, and then again equilibrated at 300 K. Total simulation time for the melt-quench dynamics was 104.6 ps, wherein time steps of 2 fs were used throughout the simulation. The computed G(r) from AIMD models is compared with measured G(r) and computed G(r) from RMC-based models in figure 4.

S5. Melt-quench models using classical molecular dynamics (CMD)
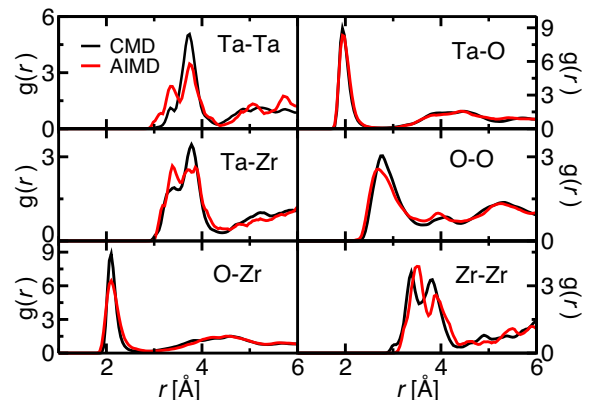
FIG. 6. Partial PDF from MD models: The partial PDFs obtained from the melt-quench MD modeling described in section S4 and S5 are plotted here for comparison. CMD denotes the models using classical molecular dynamics as described in section S5. AIMD denotes the *ab initio* molecular dynamics described in section S4. The partial PDFs from CMD are averages of 1000 snapshots of the model over 100 ps of MD at 300 K; each model contains 975 atoms. The partial PDFs from AIMD are averages of 7844 snapshots of the model over 15.7 ps of MD at 300 K; each model contains 195 atoms.

We use a unified classical two-body potential from references [9, 10] to perform the energy minimization component of our modeling (see figure 3). To investigate the ability of the potential to predict basic structural features, we carried out melt-quench molecular dynamics simulation in the framework of the classical potential. We used the LAMMPS simulation program [11] as follows: A random collection of 975 atoms (of type Ta, O and Zr atoms in the ratio discussed in section S2) in a supercell of size determined by the density is taken. Constant pressure (NPT) MD simulations were carried out at various starting densities (viz 6.0, 6.3, 6.55, 6.7, 7.0 and

7.5 gm/cm^3). For all simulations, the system was taken to a high temperature of 6000 K, equilibrated at that temperature, then cooled down to 300 K and equilibrated again at 300 K. The total number of steps was more than 1.3×10^6 which corresponds to more than 1.3 ns of simulated time. The structures were finally relaxed to its minimum energy configurations using conjugate gradient algorithm. The final density of all the models converged to $\sim$6.8 gm/cm^3. In figure 6, we compare the partial PDFs of these models with the AIMD generated models (described in section S4). We find that the CMD predicts the basic features of the partial PDF correctly, although the M-M correlations are not predicted very well. The energy minimization with respect to the referenced force-field is a useful constraint, however one needs to be careful about how it interferes with the overall models. Note that the melt-quench MD used to generate the starting configurations for RMC modeling follows the same routine as described in this section, except that those models contain 2600 atoms and constant volume (NVT) ensemble is used for MD.

S6. Further plots on coordinations and bond angle distributions
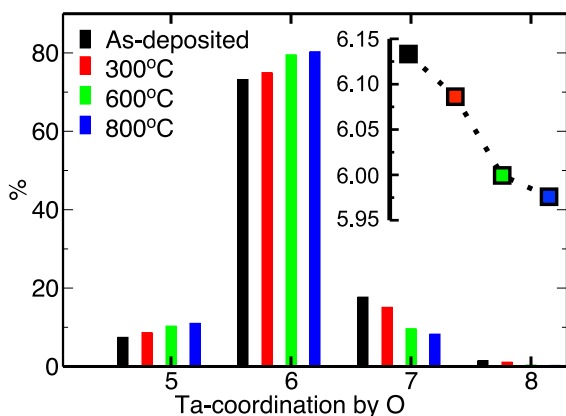
FIG. 7. The distribution of Ta-coordination by O atoms in our models. The bond cutoff is taken to be 2.90 Å which is the first minimum of total G(r). The coordination values are averages over 1000 models. The inset shows the average coordination number for the four samples.
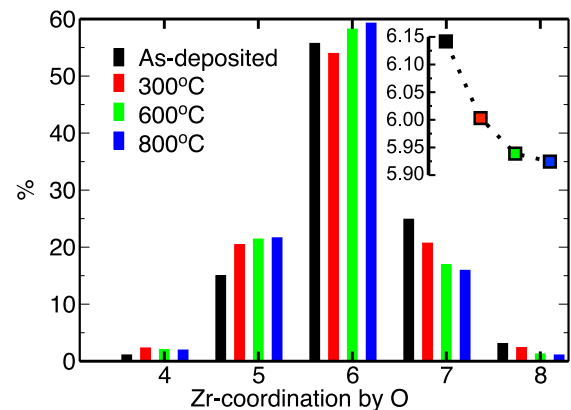
FIG. 8. The distribution of Zr-coordination by O atoms in our models. The bond cutoff is taken to be 2.90 Å which is the first minimum of total G(r). The coordination values are averages over 1000 models. The inset shows the average coordination number for the four samples.
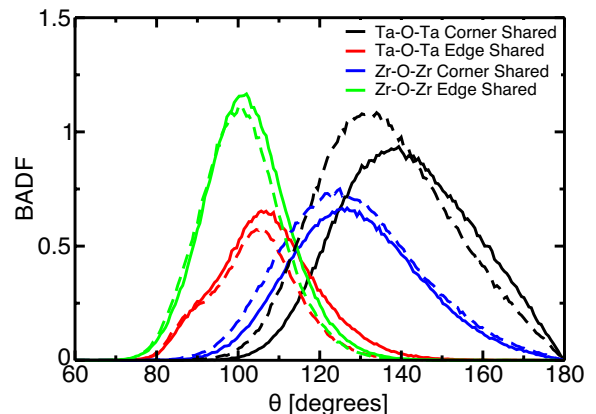
FIG. 9. BADF resolved into edge-sharing and corner-sharing polyhedra for Ta-O-Ta and Zr-O-Zr. Solid line represents as deposited sample and dashed line represents 800°C annealed sample.
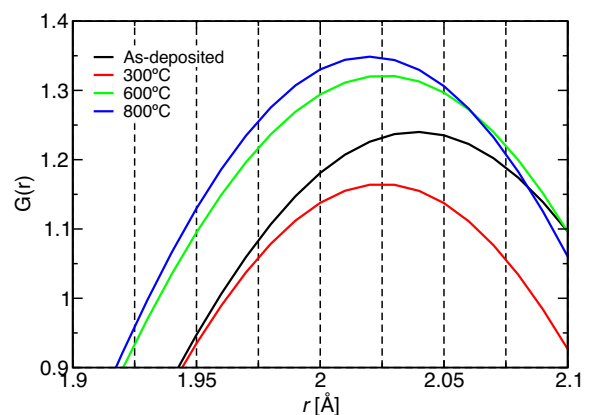
FIG. 10. The first peak in G(r) in high resolution. The positions of first peak correspond to M-O bond lengths.

* prasai@stanford.edu

† rbassiri@stanford.edu

[1] G. Vajente, R. Birney, A. Ananyeva, S. Angelova, R. Asselin, B. Baloukas, R. Bassiri, G. Billingsley, M. Fejer, D. Gibson, *et al.*, Classical and Quantum Gravity **35**, 075001 (2018).

[2] J.-Y. Tewg, Y. Kuo, and J. Lu, Electrochemical and Solid-state Letters **8**, G27 (2005).

[3] G. Vajente, A. Ananyeva, G. Billingsley, E. Gustafson, A. Heptonstall, E. Sanchez, and C. Torrie, Review of Scientific Instruments **88**, 073901 (2017).

[4] W.-K. Chu, *Backscattering spectrometry* (Elsevier, 2012).

[5] A. Piegari and E. Masetti, Thin solid films **124**, 249 (1985).

[6] H. Fujiwara, *Spectroscopic ellipsometry: principles and applications* (John Wiley & Sons, 2007).

[7] A. Pandey, P. Biswas, and D. A. Drabold, Scientific Reports **6**, 33731 (2016).

[8] A. Pandey, P. Biswas, and D. Drabold, Physical Review B **92**, 155205 (2015).

[9] J. Trinastic, R. Hamdan, Y. Wu, L. Zhang, and H.-P. Cheng, The Journal of Chemical Physics **139**, 154506 (2013).

[10] J. Yu, R. Devanathan, and W. J. Weber, Journal of Materials Chemistry **19**, 3923 (2009).

[11] S. Plimpton, Journal of Computational Physics **117**, 1 (1995).

[12] G. Kresse and J. Hafner, Physical Review B **47**, 558 (1993).

[13] G. Kresse and J. Furthmüller, Physical Review B **54**, 11169 (1996).

[14] P. E. Blöchl, Physical Review B **50**, 17953 (1994).

[15] J. P. Perdew, K. Burke, and M. Ernzerhof, Physical Review Letters **77**, 3865 (1996).

Appendix

Fig. 7.1 - 7.5 present internal loss measurements of elevated temperature depositions of tantulum pentoxide films from a metallic Ta target.

Fig. 7.6 - 7.11 present internal loss measurements of elevated temperature depositions of tantulum pentoxide films from an oxide Ta_2O_5 target.

Fig. 7.12 - 7.14 present internal loss measurements of elevated temperature depositions of zirconia doped tantulum pentoxide coatings from an oxide Ta_2O_5 target with Zr foil attached to its surface.

Fig. 7.15 - 7.20 present internal loss measurements of zirconia doped tantulum pentoxide coatings deposited from Ta_2O_5 and ZrO_2 targets.
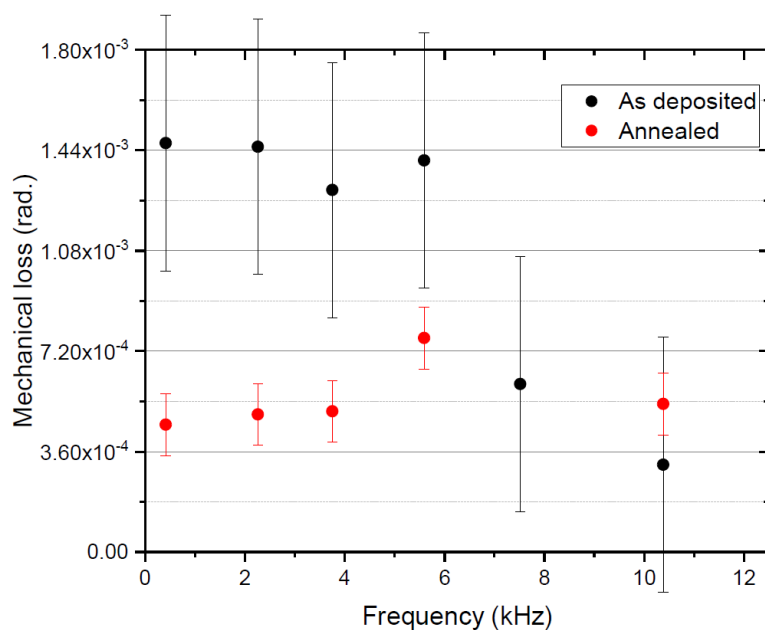
Figure 7.1: Tantulum pentoxide film deposited at room temperature utilising a Ta metal target. Film had been annealed at a temperature of 600° C.
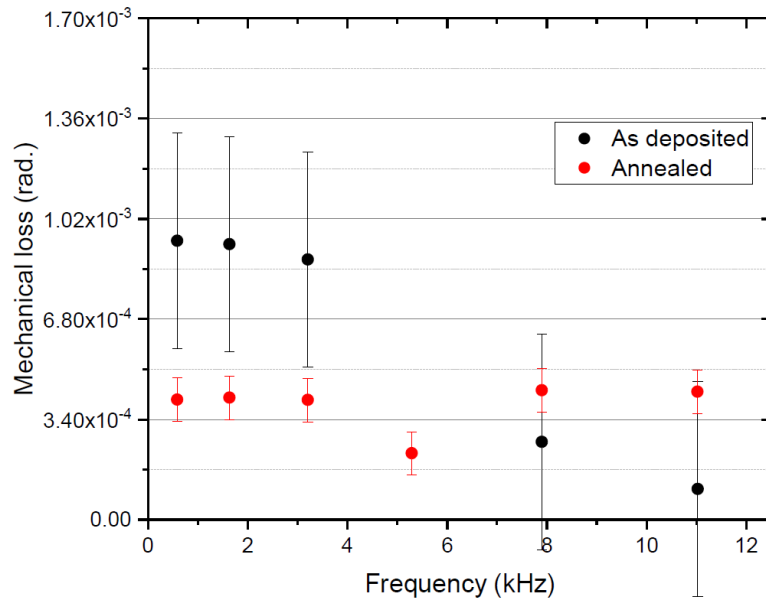
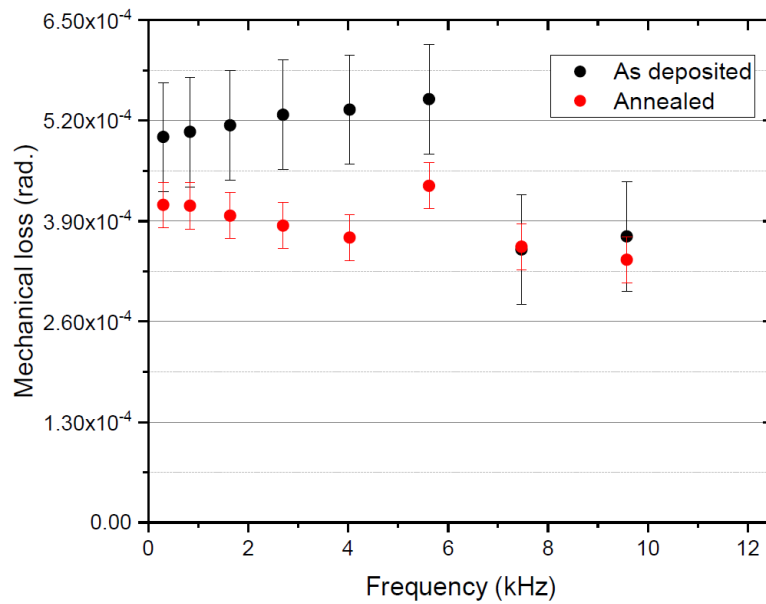Figure 7.2: Tantulum pentoxide film deposited at 100° C utilising a Ta metal target. Film had been annealed at a temperature of 600° C.
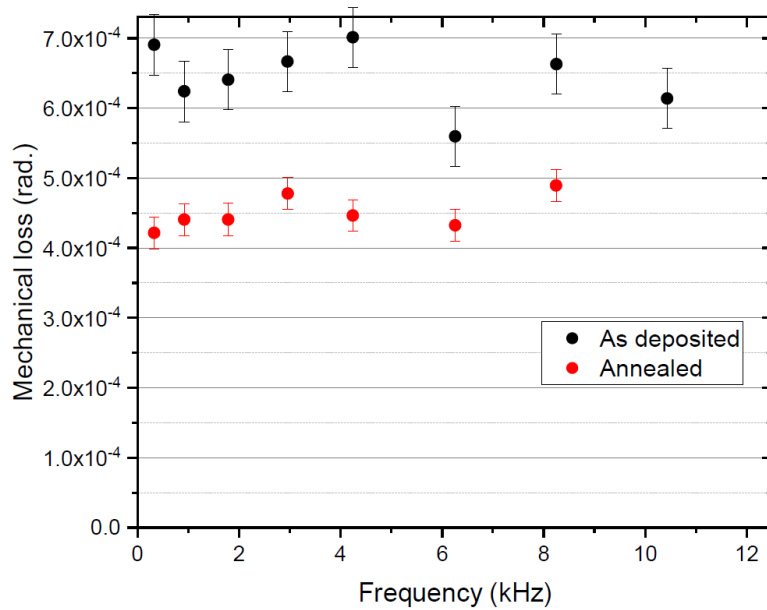
Figure 7.3: Tantulum pentoxide film deposited at 200° C utilising a Ta metal target. Film had been annealed at a temperature of 600° C.
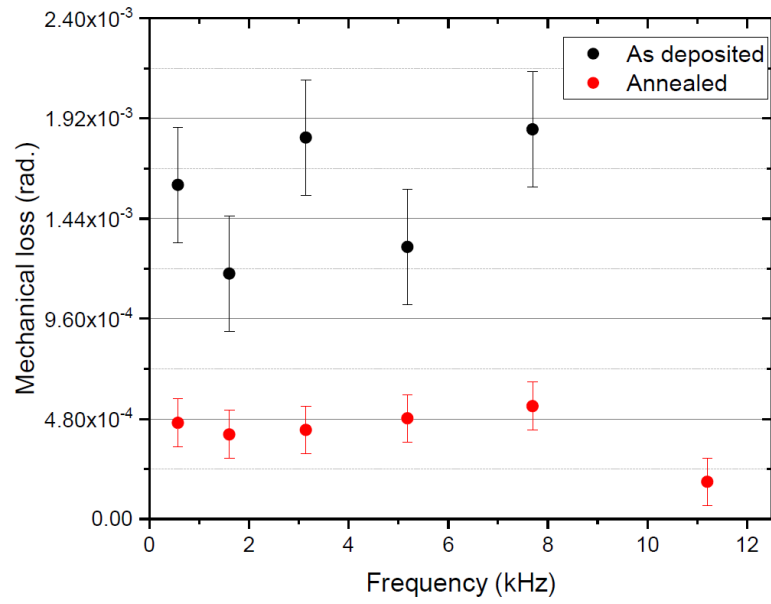
Figure 7.4: Tantulum pentoxide film deposited at 300° C utilising a Ta metal target. Film had been annealed at a temperature of 600° C.
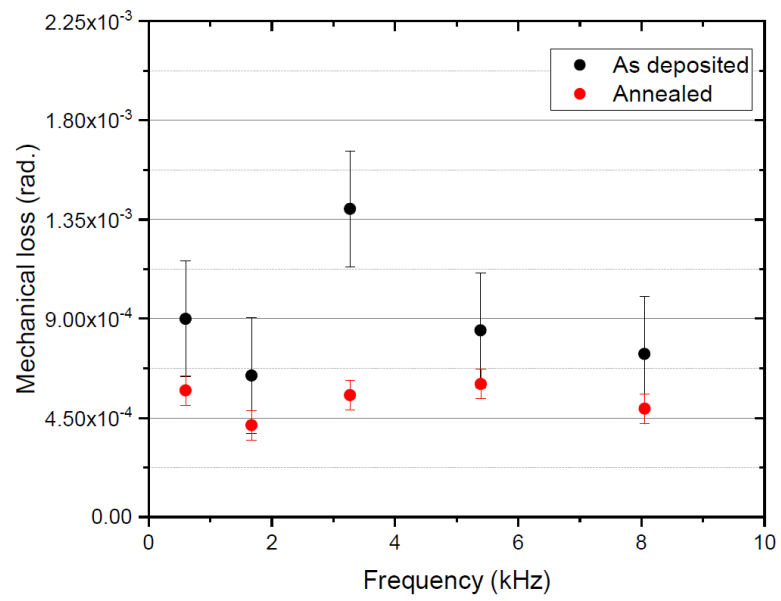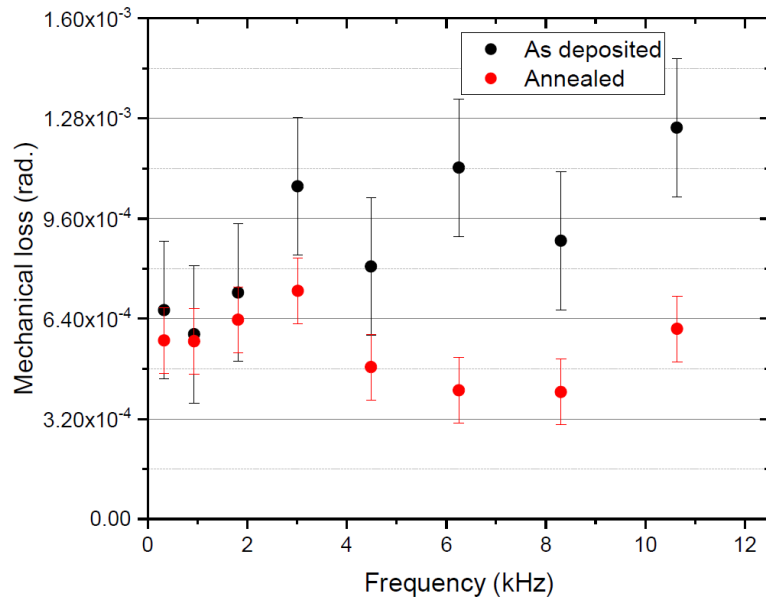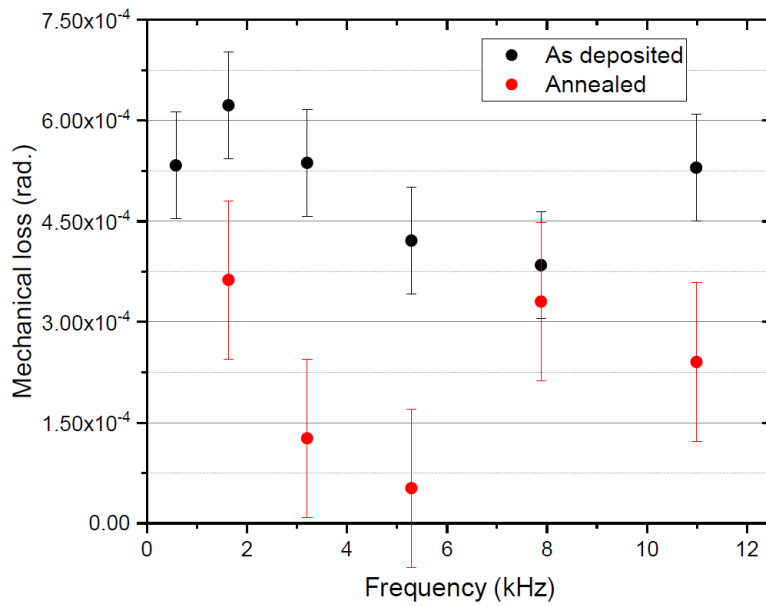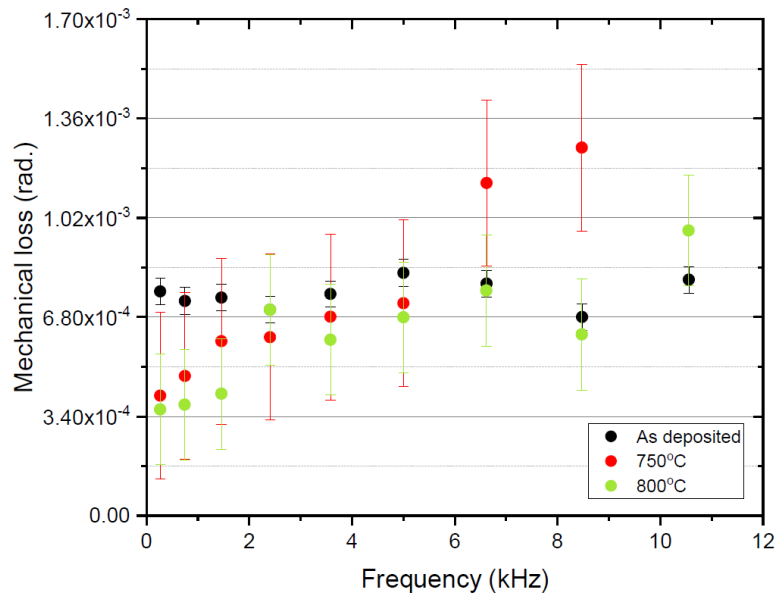

Figure 7.5: Tantulum pentoxide film deposited at 400° C utilising a Ta metal target. Film had been annealed at a temperature of 600° C.
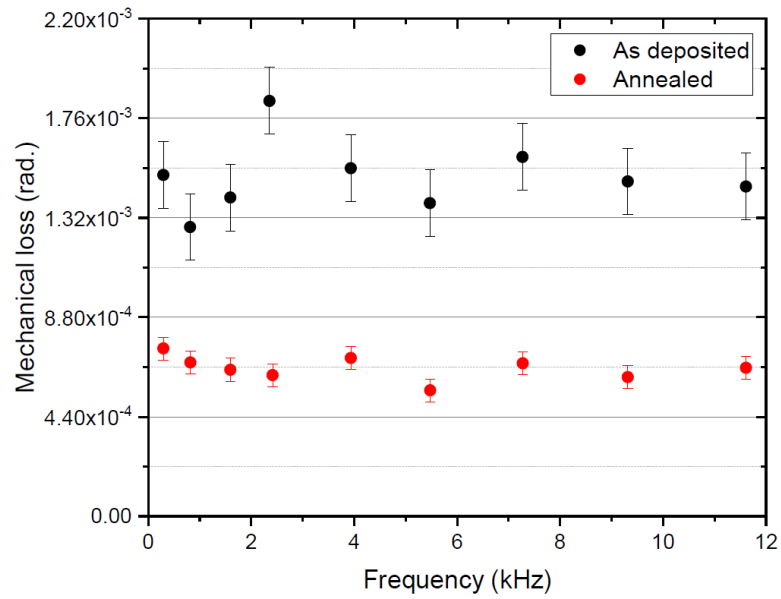
Figure 7.6: Tantulum pentoxide film deposited at room temperature utilising a Ta_2O_5 oxide target. Film had been annealed at a temperature of 600° C.
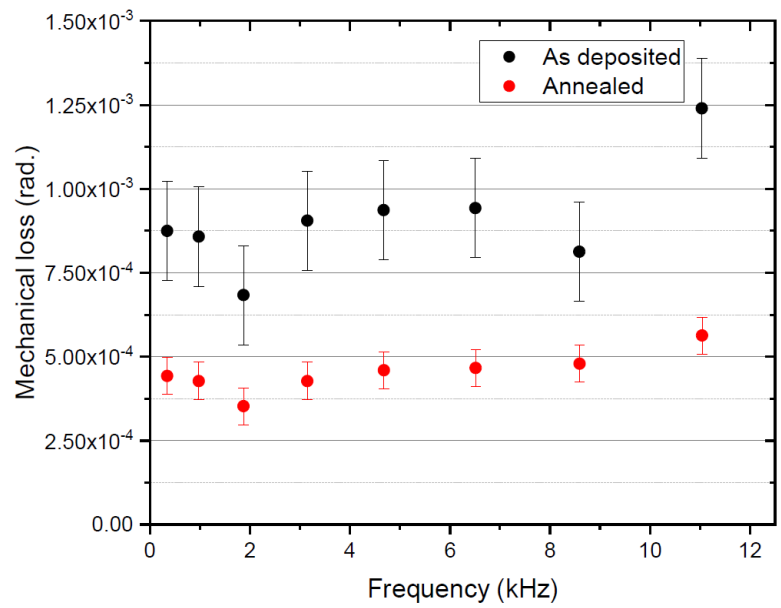
Figure 7.7: Tantulum pentoxide film deposited at 100° C utilising a Ta_2O_5 oxide target. Film had been annealed at a temperature of 600° C.

221
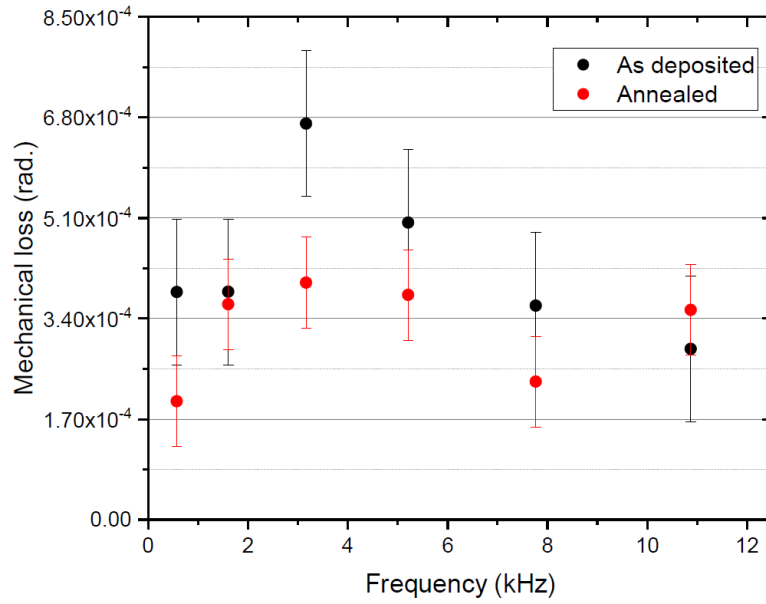
Figure 7.8: Tantulum pentoxide film deposited at 200° C utilising a Ta_2O_5 oxide target. Film had been annealed at a temperature of 600° C.

Figure 7.9: Tantulum pentoxide film deposited at 300° C utilising a Ta_2O_5 oxide target. Film had been annealed at a temperature of 600° C.

Figure 7.10: Tantulum pentoxide film deposited at 400° C utilising a Ta_2O_5 oxide target. Film had been annealed at a temperature of 600° C.

Figure 7.11: Tantulum pentoxide film deposited at 500° C utilising a Ta_2O_5 oxide target. Film had been annealed at a temperature of 600° C.

Figure 7.12: Zirconia doped tantulum pentoxide film deposited at 400° C utilising a Ta_2O_5 target with Zr foil attached to its surface. Film had been annealed up to a temperature of 800° C.
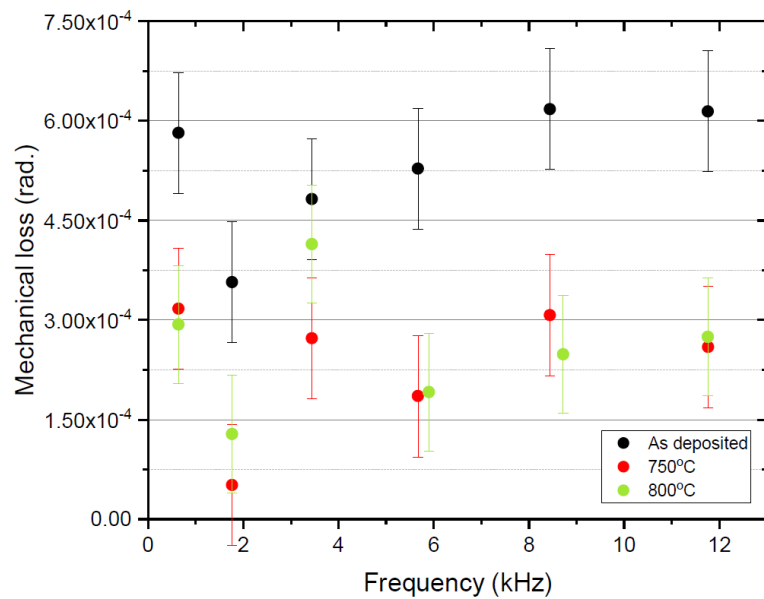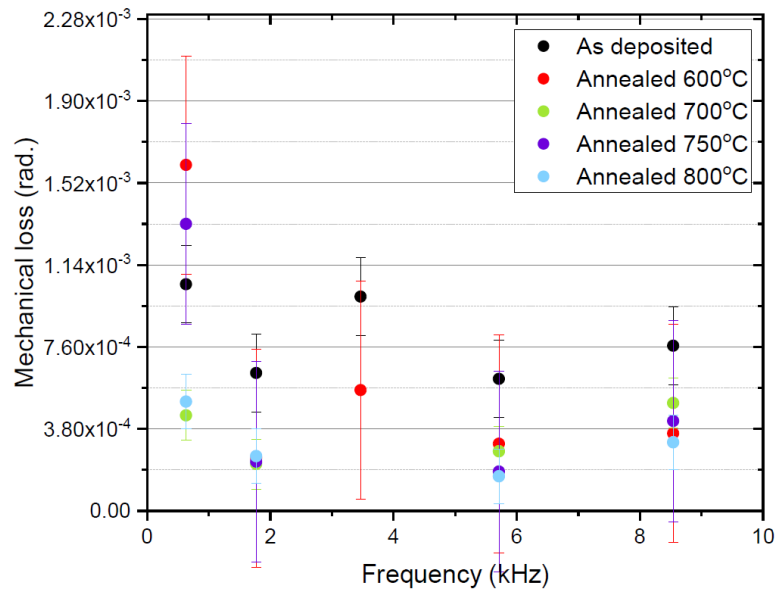

Figure 7.13: Zirconia doped tantulum pentoxide film deposited at 400° C utilising a Ta_2O_5 target with Zr foil attached to its surface. Film had been annealed up to a temperature of 800° C.
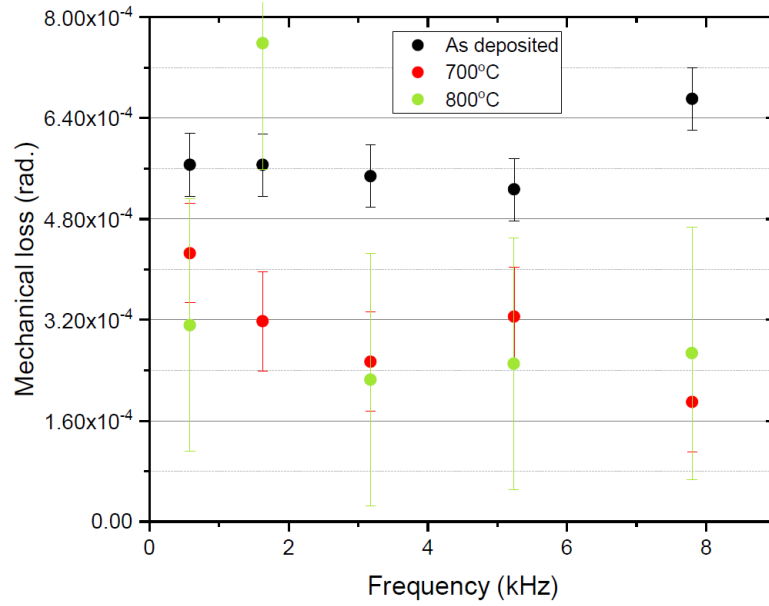
Figure 7.14: Zirconia doped tantulum pentoxide film deposited at 500° C utilising a Ta_2O_5 target with Zr foil attached to its surface. Film had been annealed up to a temperature of 800° C.

Figure 7.15: Zirconia doped tantulum pentoxide film deposited at RT utilising a Ta_2O_5 and ZrO_2 targets. Coating performed on multi - sourced system at an inclination of 0°. Film had been annealed up to a temperature of 800° C.
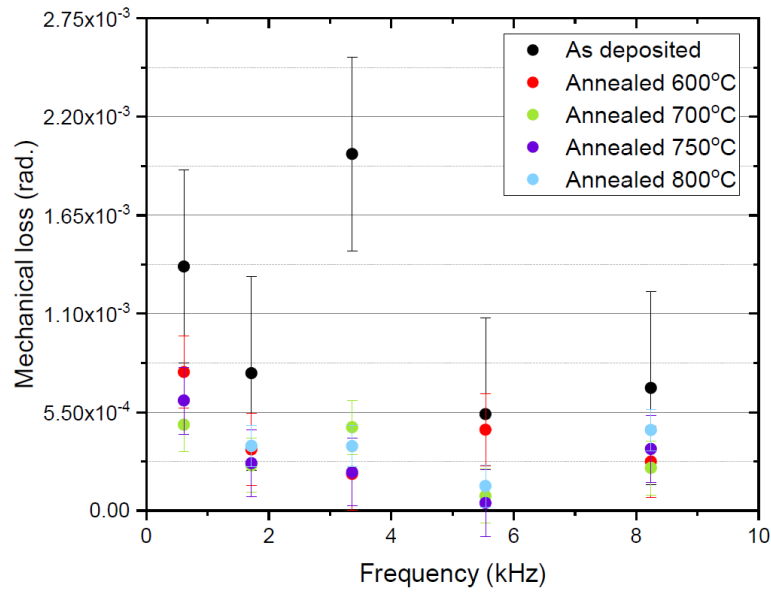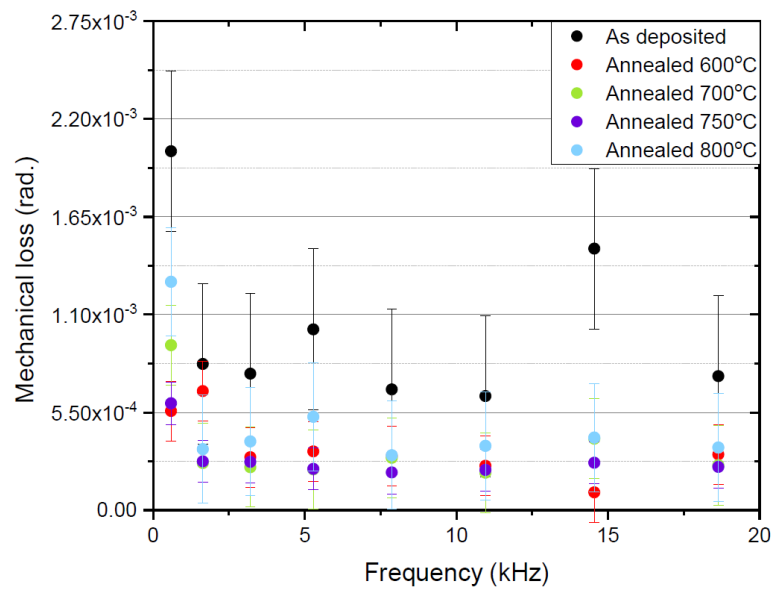
Figure 7.16: Zirconia doped tantulum pentoxide film deposited at RT utilising a Ta_2O_5 and ZrO_2 targets. Coating performed on multi - sourced system at an inclination of 30° (27°). Film had been annealed up to a temperature of 800° C.
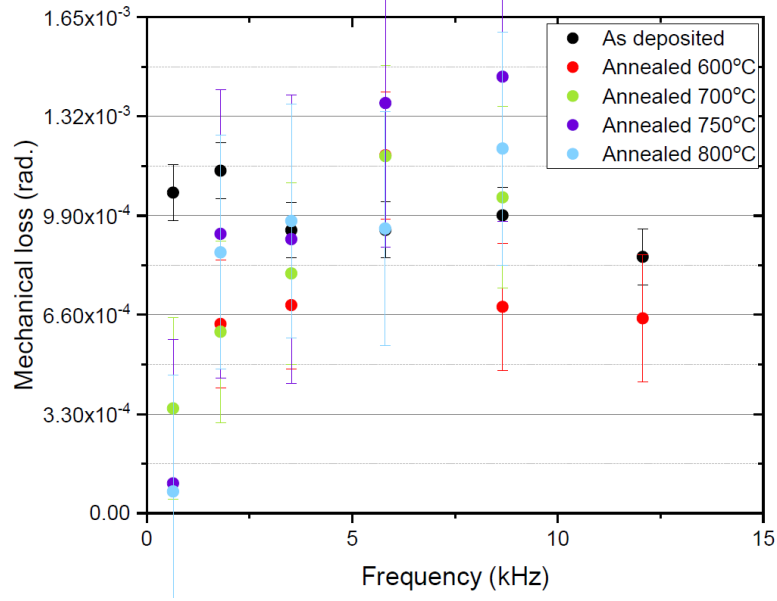

Figure 7.17: Zirconia doped tantulum pentoxide film deposited at RT utilising a Ta_2O_5 and ZrO_2 targets. Coating performed on multi - sourced system at an inclination of 15° (12°). Film had been annealed up to a temperature of 800° C.

226

Figure 7.18: Zirconia doped tantulum pentoxide film deposited at RT utilising a Ta_2O_5 and ZrO_2 targets. Coating performed on multi - sourced system at an inclination of 0°. Film had been annealed up to a temperature of 800° C.
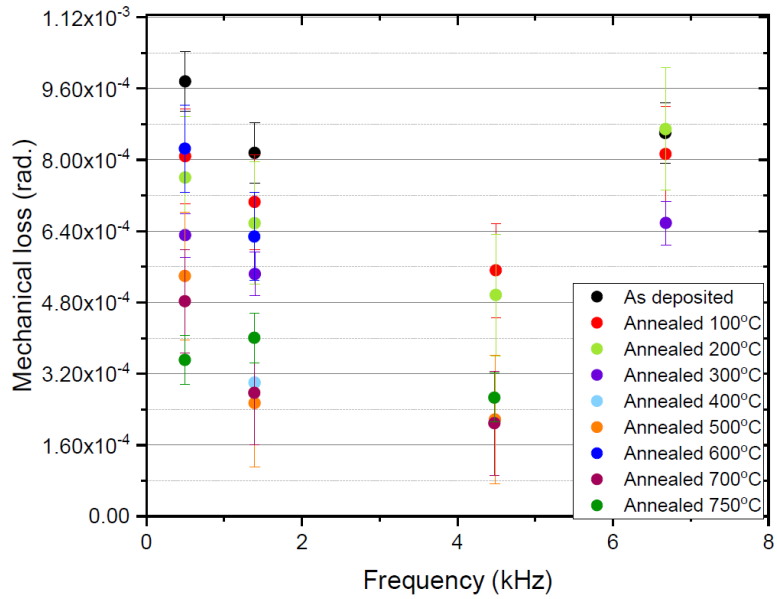

Figure 7.19: Zirconia doped tantulum pentoxide film deposited at RT utilising a Ta_2O_5 and ZrO_2 targets (1/2). Film annealed at steps of 100° C, up to a temperature of 750° C. Cracking on coating surface appeared after heat treatments at 500° C.
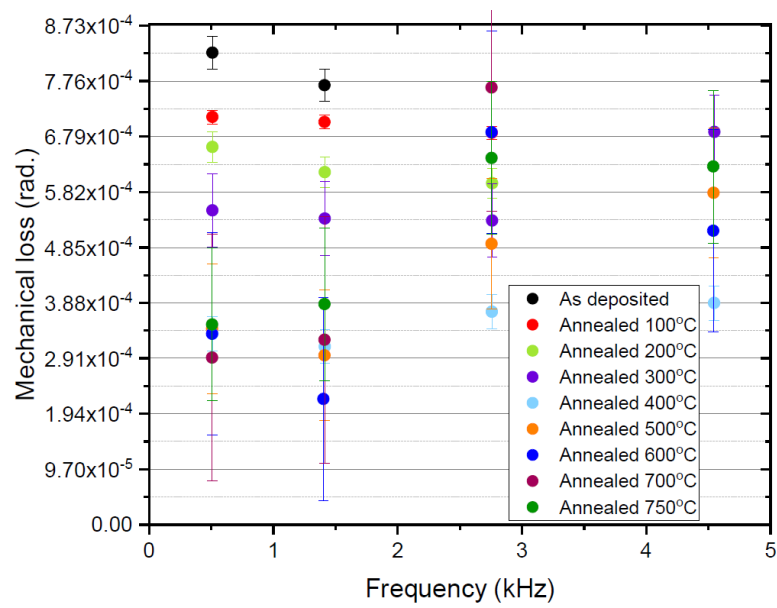
Figure 7.20: Zirconia doped tantulum pentoxide film deposited at RT utilising a Ta_2O_5 and ZrO_2 targets (2/2). Film annealed at steps of 100° C, up to a temperature of 750° C. Cracking on coating surface appeared after heat treatments at 500° C.